



HAL
open science

Satellite image restoration by nonlinear statistical filtering techniques

Bassel Marhaba

► **To cite this version:**

Bassel Marhaba. Satellite image restoration by nonlinear statistical filtering techniques. Automatic Control Engineering. Université du Littoral Côte d'Opale, 2018. English. NNT : 2018DUNK0502 . tel-02094292

HAL Id: tel-02094292

<https://theses.hal.science/tel-02094292>

Submitted on 9 Apr 2019

HAL is a multi-disciplinary open access archive for the deposit and dissemination of scientific research documents, whether they are published or not. The documents may come from teaching and research institutions in France or abroad, or from public or private research centers.

L'archive ouverte pluridisciplinaire **HAL**, est destinée au dépôt et à la diffusion de documents scientifiques de niveau recherche, publiés ou non, émanant des établissements d'enseignement et de recherche français ou étrangers, des laboratoires publics ou privés.

École doctorale n° 072 : Sciences Pour l'Ingénieur
Unité de recherche : LISIC

THESE

Présentée par :

Bassel MARHABA

Pour obtenir le grade de

Docteur de l'Université du Littoral Côte d'Opale

Spécialité : Automatique, Génie informatique, Traitement du Signal et des Image

Titre de la thèse

Restauration d'images Satellitaires par des techniques de filtrage statistique non linéaire

Soutenu le 21 Novembre 2018, devant le jury composé de :

Président du jury

Mme. Christine Fernandez-Maloigne, Professeur à l'Université de Poitiers

Rapporteurs

M. Yassine Ruichek, Professeur à l'Université de Technologie de Belfort-Montbéliar

M. Stéphane Derrode, Professeur à l'École Centrale de Lyon

Examineurs

M. Abdelmalik Taleb-Ahmed, Professeur à l'IUT de Valenciennes

M. Ayman Al Falou, Professeur à Yncréa Ouest/ISEN

Directeur de thèse

M. Mourad Zribi, Maître de Conférences HDR à l'ULCO

École doctorale n° 072: Sciences Pour l'Ingénieur SPI
Research Unit: LISIC

THESE

presented by:

Bassel MARHABA

To obtain the grade of

Doctor from the Université du Littoral Côte d'Opale

Specialty: Automatic, Computer Engineering, Signal and Image Processing.

Thesis Title

Satellite image restoration by nonlinear statistical filtering techniques

Defended on November 21st, 2018, in front of the jury composed of:

President of the jury

Mrs. Christine Fernandez-Maloigne, professor at the University of Poitiers

Rapporteurs

Mr. Yassine Ruichek, Professor at Belfort-Montbéliar University of Technology

Mr. Stéphane Derrode, professor at the Ecole Centrale de Lyon

Examiners

Mr. Abdelmalik Taleb-Ahmed, professor at the IUT of Valenciennes

Mr. Ayman Al Falou, Professor at Yncrea West / ISEN

Thesis supervisor

Mr. Mourad Zribi, Associate Professor HDR at the ULCO

Résumé

Le traitement des images satellitaires est considéré comme l'un des domaines les plus intéressants dans les domaines de traitement d'images numériques. Les images satellitaires peuvent être dégradées pour plusieurs raisons, notamment les mouvements des satellites, les conditions météorologiques, la dispersion et d'autres facteurs. Plusieurs méthodes d'amélioration et de restauration des images satellitaires ont été étudiées et développées dans la littérature. Les travaux présentés dans cette thèse se concentrent sur la restauration des images satellitaires par des techniques de filtrage statistique non linéaire. Dans un premier temps, nous avons proposé une nouvelle méthode pour restaurer les images satellitaires en combinant les techniques de restauration aveugle et non aveugle. La raison de cette combinaison est d'exploiter les avantages de chaque technique utilisée. Dans un deuxième temps, de nouveaux algorithmes statistiques de restauration d'images basés sur les filtres non linéaires et l'estimation non paramétrique de densité multivariée ont été proposés. L'estimation non paramétrique de la densité à posteriori est utilisée dans l'étape de ré-échantillonnage du filtre Bayésien bootstrap pour résoudre le problème de la perte de diversité dans le système de particules. Enfin, nous avons introduit une nouvelle méthode de combinaison hybride pour la restauration des images basée sur la transformée en ondelettes discrète (TOD) et les algorithmes proposés à l'étape deux, et nous avons prouvé que les performances de la méthode combinée sont meilleures que les performances de l'approche TOD pour la réduction du bruit dans les images satellitaires dégradées.

Mots-clés : Image satellitaire, Restauration, techniques de restauration aveugle et non aveugle, filtre Bayésien bootstrap, estimation non paramétrique de densité multivariée, TOD.

Abstract

Satellite image processing is considered one of the more interesting areas in the fields of digital image processing. Satellite images are subject to be degraded due to several reasons, satellite movements, weather, scattering, and other factors. Several methods for satellite image enhancement and restoration have been studied and developed in the literature. The work presented in this thesis, is focused on satellite image restoration by nonlinear statistical filtering techniques. At the first step, we proposed a novel method to restore satellite images using a combination between blind and non-blind restoration techniques. The reason for this combination is to exploit the advantages of each technique used. In the second step, novel statistical image restoration algorithms based on nonlinear filters and the nonparametric multivariate density estimation have been proposed. The nonparametric multivariate density estimation of posterior density is used in the resampling step of the Bayesian bootstrap filter to resolve the problem of loss of diversity among the particles. Finally, we have introduced a new hybrid combination method for image restoration based on the discrete wavelet transform (DWT) and the proposed algorithms in step two, and, we have proved that the performance of the combined method is better than the performance of the DWT approach in the reduction of noise in degraded satellite images.

Key words: Satellite image, Restoration, blind and non-blind restoration techniques, Bayesian bootstrap filter, nonparametric multivariate density estimation, DWT.

Dans la vie, rien n'est gratuit. Pour obtenir quelque chose, vous devez payer pour cela. Ce travail dans vos mains - comme tout - n'était pas gratuit, le prix était le sacrifice, l'effort et les larmes.

In this life nothing is free. In order to get something, you have to pay for it. This work in your hands - like everything - was not for free, the price was sacrifice, effort, and tears.

Remerciements

Je voudrais exprimer ma profonde gratitude à mon directeur, M. Mourad **ZRIBI**. C'était une belle collaboration. Il était toujours là où il devrait être. J'ai beaucoup bénéficié de lui, non seulement dans le domaine scientifique, mais aussi dans de nombreux aspects de la vie. Avec ses connaissances et son attention, il était toujours le superviseur expert et le frère assistant. Sans son aide, je ne pourrais jamais terminer mes recherches.

Je remercie vivement mes rapporteurs de thèse, M. Yassine **RUICHEK** et M. Stéphane **DERRODE** pour le temps qu'ils ont consacré à la lecture ainsi que pour la qualité de leur expertise et de leurs critiques constructives qui ont grandement permis d'améliorer la version finale de ce travail.

Je suis très reconnaissant à Mme Christine **FERNANDEZ-MALOIGNE**, M. Abdelmalik **TALEB-AHMED** et M. Ayman **AI FALOU** pour prendre part à mon jury de thèse et de leurs conseils et je les remercie sincèrement.

Je voudrais également remercier tous mes **amis** du laboratoire pour la bonne ambiance qui a prévalu entre nous et qui a été un catalyseur supplémentaire. Merci à vous tous et je vous souhaite le meilleur dans votre vie scientifique et personnelle.

J'aimerais également remercier à tous les **membres** du laboratoire d'Informatique Signal et Image de la Côte d'Opale de l'Université du Littoral Côte d'Opale.

J'aimerais également remercier l'European Space Agency (**ESA**) pour avoir fourni des images satellitaires gratuitement.

Bien sûr, mes profonds remerciements à ma bonne famille. Mon père **Ghazi**, ma mère **Nawal**, mes enfants, **Zaynab**, **Mariam**, **Linah** et **Ghazi**, ma femme **Dina**, ma belle-mère **Bouchra**, mes **frères** et mes **beaux-frères**. Vos prières, votre amour et vos soins ont toujours été pour moi une source de force pour poursuivre ma thèse et ma vie. **Dina**, merci de tout cœur pour votre soutien, votre patience et votre véritable amour. Vous avez tous contribué à ce travail. Merci beaucoup.

Acknowledgement

I would like to express my deep gratitude to my director, Mr. Mourad **ZRIBI**. It was a beautiful and adorable collaboration. He was always where he should be. I benefited greatly from him, not only in the scientific field but also in many aspects of life. With his knowledge and attention, he was always the expert supervisor and the assistant brother. Without his help, I could never finish my research.

I would like to thank my thesis reviewers, Mr. Yassine **RUICHEK** and Mr. Stéphane **DERRODE** for the time they have devoted to reading as well as for the quality of their expertise and their constructive criticism, which greatly improved the final version of this work.

I am very grateful to Mrs Christine **FERNANDEZ-MALOIGNE**, Mr Abdelmalik **TALEB-AHMED** and Mr Ayman **AI FALOU** for taking part in my thesis jury and their advices and I thank them sincerely.

I would also like to thank all my **friends** from the laboratory for the good atmosphere that has prevailed between us and which has been an additional catalyst. Thank you all and wish you the best in your scientific and personal life.

I would also like to thank all the **members** of the Signal and Image Computer Laboratory at the Côte d'Opale at the Côte d'Opale Coastal University.

I would also like to thank the European Space Agency (**ESA**) for providing free satellite images.

Of course, my deepest thanks to my good family. My father **Ghazi**, my mother **Nawal**, my children, **Zaynab**, **Mariam**, **Linah** and **Ghazi**, my wife **Dina**, my mother-in-law **Bouchra**, my **brothers** and my **brothers-in-law**. Your prayers, your love, and your care have always been a source of strength for me to pursue my thesis and my life. **Dina**, thank you wholeheartedly for your support, your patience and your true love. All of you have contributed to this work. Thank you so much.

Publications

During this thesis, 4 papers have been published in international conferences. In addition, 1 paper has been published in international journal.

Paper in International journal:

1. Bassel Marhaba, Mourad Zribi, Wassim Khoder, Image Restoration Using a Combination of Blind and Non-Blind Deconvolution Techniques, International Journal of Engineering Research & Science (IJOER), Vol. 2, No. 5, pp. 225–239, May 2016.

Papers in International conferences:

2. Bassel Marhaba, Mourad Zribi, Regularized bootstrap filter for image restoration, 11th International Conferences Computer Graphics, Visualization, Computer Vision and Image Processing and Big Data Analytics, Data Mining and Computational Intelligence, Lisbon, pp. 117-123, July 2017.
3. Bassel Marhaba, Mourad Zribi, The bootstrap Kernel-Diffeomorphism Filter for Satellite Image Restoration, IEEE 22nd International Symposium on Consumer Technologies, Russia, pp. 80 - 84, May 2018.
4. Bassel Marhaba, Mourad Zribi, Reduction of speckle noise in SAR images using hybrid combination of Bootstrap filtering and DWT, International Conference on Computer and Applications (ICCA), Beirut, pp. 377-382, July 2018.
5. Bassel Marhaba, Mourad Zribi, A Novel Combination Method for Image Restoration Based on Bootstrap Filter and DWT, Accepted in 5th International Francophone Congress of Advanced Mechanics (CIFMA), Beirut, November 2018.

Table of Contents

Résumé	v
Remerciements	ix
Acknowledgments	xi
Publications.....	xiii
Table of contents	xv
List of Figures	xvii
List of Tables	xxi
List of Line Charts	xxiii
General Introduction	1
Chapter 1 Modeling of degraded satellite images	5
Introduction	9
1.1 Satellite images.....	10
1.2 Reasons for image degradation	15
1.3 Image and degradation models.....	31
Conclusion.....	39
References	40
Chapter 2 Modeling of degraded satellite images	45
Introduction	49
2.1 Basic model of image restoration	50
2.2 Non-blind restoration technique	52
2.3 Blind Deconvolution Methods	59
2.4 Proposed method to restore the Sentinel images.....	67
Conclusion.....	101
References	103
Chapter 3 Importance sampling Monte Carlo filters for satellite images restoration.....	107
Introduction	111
3.1 Analytical methods for filtering	112
3.2 Monte Carlo methods for nonlinear filtering	125
3.3 Experimental results	137
Conclusion.....	146

References	147
Chapter 4 Reduction of speckle noise in SAR images	151
Introduction	155
4.1 Nonparametric multivariate density estimation	156
4.2 A proposed method to reduce the speckle noise	162
4.3 Experimental results	170
Conclusion.....	180
References	182
General Conclusions and Perspectives	187
Appendix	189

List of Figures

Figure 1.1: The Sentinel family.....	11
Figure 1.2: The Sentinel-1 Satellite.....	13
Figure 1.3: The Sentinel-2 satellite.	15
Figure 1.4: Satellite photography.	18
Figure 1.5: Images and histograms corresponding to motion blurring.	19
Figure 1.6: Images and histograms corresponding to out-of-focus blurring.	21
Figure 1.7: Images and histograms corresponding to atmospheric turbulence blurring.	23
Figure 1.8: Images and histograms corresponding to salt and pepper noising.....	25
Figure 1.9: Probability density function of Gaussian noise.	26
Figure 1.10: Images and Histograms corresponding to Gaussian noise.....	27
Figure 1.11: Probability density function of speckle noise.	28
Figure 1.12: Images and histograms corresponding to speckle noise.	29
Figure 1.13: Images and histograms corresponding to Poisson noise.....	31
Figure 1.14: The state vector $x(m, n)$	33
Figure 2.1: Image degradation model.....	50
Figure 2.2: Image restoration model.	51
Figure 2.3: Classification of restoration techniques.	52
Figure 2.4: General block diagram for image restoration.	52
Figure 2.5: Deblurring using Lucy-Richardson method.	54
Figure 2.6: Deblurring by Inverse Filter.	55
Figure 2.7: Deblurring by Wiener filter.	57
Figure 2.8: Deblurring by Regularized Filter.	58
Figure 2.9: Deblurring by Constrained Least-Squares filter.	59
Figure 2.10: Deblurring by different mean filters.	61
Figure 2.11: Deblurring by Median filter.	62
Figure 2.12: Deblurring by DWT filter.	64
Figure 2.13: Deblurring by bilateral filter.	65
Figure 2.14: Deblurring by adaptive local filter.....	66
Figure 2.15: Proposed method for image restoration diagram.	68
Figure 2.16: The resultant deblurred images by the non-blind deconvolution methods and the corresponding histogram for each deblurred image, for the motion blur case....	71

Figure 2.17: The resultant deblurred images by the blind deconvolution methods, and the corresponding histogram for each deblurred image, for the motion blur case....	73
Figure 2.18: The resultant deblurred images by the non-blind deconvolution methods, and the corresponding histogram for each deblurred image, for the out of focus blur case.	76
Figure 2.19: The resultant deblurred images by the blind deconvolution methods, and the corresponding histogram for each deblurred image, for the out of focus blur case.	78
Figure 2.20: The resultant deblurred images by the non-blind deconvolution methods and the corresponding histogram for each deblurred image, for the atmospheric turbulence blur case.	80
Figure 2.21: The resultant deblurred images by the blind deconvolution methods, and the corresponding histogram for each deblurred image, for the atmospheric turbulence blur case.....	82
Figure 2.22: The resultant denoised images by the non-blind deconvolution methods, for the salt & pepper noise.	84
Figure 2.23: The resultant denoised image by the blind deconvolution methods for the salt & pepper noise.	85
Figure 2.24: The resultant denoised images by the non-blind deconvolution methods, for the Gaussian noise.....	87
Figure 2.25: The resultant denoised image by the blind deconvolution methods, for the Gaussian noise.....	87
Figure 2.26: The resultant denoised images by the non-blind deconvolution methods, for the Speckle noise.....	89
Figure 2.27: The resultant denoised images by the blind deconvolution methods, for the Speckle noise.....	89
Figure 2.28: The resultant denoised images by the non-blind deconvolution methods, for the Poisson noise.	91
Figure 2.29: The resultant denoised image by the blind deconvolution methods, for the Poisson noise.....	91
Figure 2.30: The resultant restored images by the non-blind deconvolution methods, for the case of atmospheric turbulence blur and Speckle noise.....	93
Figure 2.31: The resultant restored image by the blind deconvolution methods, for the case of linear atmospheric turbulence blur and Speckle noise.	93

Figure 2.32: The resultant restored images for the case of motion blur.....	95
Figure 2.33: The resultant restored image for the out of focus blur.....	96
Figure 2.34: The resultant restored image, for the atmospheric turbulence blur.	97
Figure 2.35: The resultant restored image, for the salt & pepper noise.	98
Figure 2.36: The resultant restored image for the Gaussian noise.	99
Figure 2.37: The resultant restored image for the speckle noise.....	99
Figure 2.38: The resultant restored image for the Poisson noise.	100
Figure 2.39: The resultant restored image for the Speckle noise with atmospheric turbulence blur.....	101
Figure 3.1: Restoration of the French synergy image degraded by impulse noise.	139
Figure 3.2: Restoration of the Seville Spain image degraded by the impulse noise.	140
Figure 3.3: Restoration of the French synergy image degraded by the Gaussian noise.....	141
Figure 3.4: Restoration of the Seville Spain image degraded by the Gaussian noise.	142
Figure 3.5: Restoration of the Seville Spain image degraded by the Gaussian noise.	143
Figure 3.6: Restoration of the Seville Spain image degraded by the Gaussian noise.	144
Figure 4.1: Kernel density estimate with diagonal bandwidth for synthetic normal mixture data.	159
Figure 4.2: Estimation of pdf $f_{p,q}(x)$	161
Figure 4.3: The Proposed algorithm.....	163
Figure 4.4: ERS SAR image.....	164
Figure 4.5: Noised SAR image.....	165
Figure 4.6: Denoising of ‘Sydney, Australia’ image corrupted by speckle noise of variance of 0.08.....	174
Figure 4.7: Denoising of ‘city of Paris’ image corrupted by speckle noise of variance of 0.08.. ..	179

List of Tables

Table 2.1: The resultant metrics of the deblurred by non-blind deconvolution methods for the motion blur case.	74
Table 2.2: The resultant metrics of the deblurred by blind deconvolution methods for the motion blur case.....	74
Table 2.3: The resultant metrics of the deblurred by non-blind deconvolution methods, for the out of focus blur case.....	78
Table 2.4: The resultant metrics of the deblurred by blind deconvolution methods, for the out of focus blur case.....	78
Table 2.5: The resultant metrics of the deblurred by non-blind deconvolution methods, for the atmospheric turbulence blur case.	82
Table 2.6: The resultant metrics of the deblurred by blind deconvolution methods, for the atmospheric turbulence blur case.	83
Table 2.7: The resultant metrics of the denoised by non-blind deconvolution methods for the salt & pepper noise.	85
Table 2.8: The resultant metrics of the denoised by the blind deconvolution methods for the salt & pepper noise.....	85
Table 2.9: The resultant metrics of the denoised by non-blind deconvolution methods, for the Gaussian noise.	88
Table 2.10: The resultant metrics of the denoised by the blind deconvolution methods, for the Gaussian noise.	88
Table 2.11: The resultant metrics of the denoised by non-blind deconvolution methods, for the Speckle noise.....	90
Table 2.12: The resultant metrics of the denoised by the blind deconvolution methods, for the Speckle noise.	90
Table 2.13: The resultant metrics of the denoised by non-blind deconvolution methods, for the Poisson noise.....	92
Table 2.14: The resultant metrics of the denoised by the blind deconvolution methods, for the Poisson noise.	92
Table 2.15: The resultant metrics of the restoration with non-blind deconvolution methods, for the case of linear atmospheric turbulence blur and Speckle noise.	94

Table 2.16: The resultant metrics of the restoration with blind deconvolution methods, for the case of linear motion blur and Speckle noise.	94
Table 2.17: The resultant PSNR of the different methods for the case of motion blur.....	95
Table 2.18: The resultant PSNR of the different methods for the out of focus blur.	96
Table 2.19: The resultant PSNR of the different methods, for the atmospheric turbulence blur.	97
Table 2.20: The resultant PSNR of the different methods, for the salt & pepper noise.....	98
Table 2.21: The resultant PSNR of the different methods for the Gaussian noise.....	99
Table 2.22: The resultant PSNR of the different methods for the speckle noise.	99
Table 2.23: The resultant PSNR of the different methods for the Poisson noise.....	100
Table 2.24: The resultant PSNR of the different methods for the Speckle noise with atmospheric turbulence blur.	101
Table 3.1: The values of the images coefficients.	138
Table 3.2: The metric results obtained from the denoised French synergy image.....	145
Table 3.3: The metric results obtained from the denoised Seville Spain image.	145
Table 4.1: Model coefficients for the used SAR images.....	171
Table 4.2: Comparison of the ISNR resultant values of the proposed, NBBF, BBF and the other basic filters for denoising the SAR image of Sydney corrupted by Speckle noise.	175
Table 4.3: Comparison of the RMSE resultant values of the proposed, NBBF, BBF and the other basic filters for denoising the SAR image of Sydney corrupted by Speckle noise	175
Table 4.4: Comparison of the PSNR resultant values of the proposed, NBBF, BBF and the other basic filters for denoising the SAR image of Sydney corrupted by Speckle noise.	175
Table 4.5: Comparison of ISNR resultant values of the proposed, NBBF, BBF and other basic filters for denoising the SAR image of Paris corrupted by Speckle noise.	179
Table 4.6: Comparison of RMSE resultant values of the proposed, NBBF, BBF and other basic filters for denoising the SAR image of Paris corrupted by Speckle noise.	179
Table 4.7: Comparison of PSNR resultant values of the proposed, NBBF, BBF and other basic filters for denoising the SAR image of Paris corrupted by Speckle noise.	180

List of Line Charts

Line Chart 4.1: The PSNR results for denoising the SAR image of Sydney by the several filters.	176
Line Chart 4.2: The PSNR results for denoising the image of the city of Paris SAR image by the several filters.	180

General Introduction

Satellite imagery, space-borne photography, or remote sensing, are different names for the images of Earth or other planets collected by imaging satellites operated by governments and businesses around the world in order to obtain information about the regions been photographed. Then these companies sell images by licensing them to governments and other private organizations such as Apple Maps and Google Maps.

There are many different satellites scanning the Earth, each with its own unique purpose. Satellites use different kinds of sensors to collect electromagnetic radiation reflected from the Earth. Passive sensors collect radiation which the Sun emits and the Earth reflects, and do not require energy. Active sensors emit radiation themselves, and analyze it after it is reflected back from the Earth. Active sensors require a significant amount of energy to emit radiation, but they are useful because they can be used during any season and time of day (passive sensors cannot be used on a part of Earth that is in shadow) and because they can emit types of radiation that the Sun does not provide.

Satellite images are useful because different surfaces and objects can be identified by the way they react to radiation. For instance, smooth surfaces, such as roads, reflect almost all of the energy, which comes at them at a single direction. This is called specular reflection. Meanwhile, rough surfaces, such as trees, reflect energy in all directions. This is called diffuse reflection. Sensing different types of reflection is useful in measuring the density and amount of forests, and forest change. Also, objects react differently to different wavelengths of radiation. For instance, there is a frequency of infrared light, which can be used to determine plant health. Healthy leaves reflect this frequency well while unhealthy ones do not.

Satellite images are subject to distortion due to the presence of two disturbing factors that negatively affect the purity and clarity of the satellite images degraded by noise during image acquisition and transmission process. These two factors are blur and noise. There are many types of blur that affect satellite images, such as motion blur, out of focus blur and atmospheric turbulence blur. On the other hand, there are also several types of noise that affect the satellite images such as impulse noise, additive noise and multiplicative noise. The presence of blur and/or noise in the satellite images is a very disturbing issue since it has reduced the purity of the image and distorts the useful information in the image. These distorted images must be restored and the useful information must be recovered.

Reducing and eliminating noise and/or blur from the satellite images is a big challenge for the researchers in the domain digital image processing. The process of reducing the noise and/or blur from the satellite images and recovering the useful information in it is called; denoising in the presence of noise only, deblurring in the presence of blur only or restoration in the presence of both noise and blur which also can be called denoising, and deblurring. Anyhow, deblurring and denoising could be named restoration.

For several decades and until now, reducing noise and/or blur from the satellite images is a big hurdle for the researchers in digital image processing. Many methods were proposed and developed in the literature for restoring satellite images.

During our work in this thesis several contributions have been made. At the first step, we examined several blind and non-blind restoration techniques already exist in the literature. Blind image restoration techniques have no/or few knowledge about the point spread function that has degraded the original image. On the other hand, non-blind restoration techniques have a prior information about the point spread function, which has degraded the original image. During this step, we studied, tested and compared the behavior of these techniques through implementing it on restoration degraded satellite images. Here, the contribution is the fusion combination between the blind and non-blind restoration techniques based on the wavelet transform method. In the second step, we studied the Monte Carlo filters and the nonparametric multivariate density estimation for satellite image restoration. Here our first contribution is to adopt the recursive Bayesian Bootstrap filtering for image restoration. Bootstrap filter is a filtering method based on Bayesian state estimation and Monte Carlo method, which has the great advantage of being able to handle any functional non-linearity and system and/or measurement noise of any distribution. Due to the problem of degeneracy found in the (sequential importance sampling) particle filter, where after a few sampling steps all the particles except one will have a negligible weight, the bootstrap filter with a resampling step was introduced to solve the degeneracy problem. Although the resampling step in the Bayesian bootstrap filter has solved the degeneracy problem, but it has caused loss of diversity among the particles. This problem arises due to the fact that the particles are drawn from a discrete distribution. To solve this problem, we need to draw the particles from a continuous distribution. To achieve this solution, we propose to use nonparametric multivariate density estimation in the bootstrap resampling step. The second contribution is to use the nonparametric multivariate density estimation in the resampling step of the Bayesian bootstrap filter. Finally, to ameliorate the satellite image restoration using the new nonparametric filters, we have proposed a novel approach which combine the proposed filters and discrete wavelet transform (DWT). The DWT, is a robust approach and it is easy to be implemented in the image restoration field.

The thesis is instructed as follows

In chapter 1, we introduce satellite imagery and then we define the Sentinel family concept. After that, we describe the Sentinel 1 and 2 missions with some details about the satellites. Next, we describe the reason for the image degradation, and finally, we show the image model and the degradation model.

In chapter 2, we present a basic image restoration technique. We consider the restoration process as a two-dimensional convolution of true image and the point spread function. Subsequently, a strategy to reconstruct the true image given the blurred image and the point spread function is presented. Moreover, we give an overview of blind and non-blind restoration techniques, two topics that are regarded in more details in this chapter. To ameliorate the results obtained by the two techniques, we propose a new method of restoration which consists of fusion combination of the two techniques.

In chapter 3, we describe the Monte Carlo filters. First we review the analytical method for filtering, for example Kalman filter. In the second step, a comparative study of the different filters has been realized for the satellite image restoration. Finally, in this chapter, we are interested in Monte Carlo methods for nonlinear filtering and in particular the Bayesian bootstrap filter. Here, we have adopted the filter to the problem of satellite image restoration.

In chapter 4, we have treated the problem of the speckle noise of synthetic aperture radar images using Bayesian bootstrap filtering. First, we review the nonparametric multivariate density estimation. Secondly, we have noticed that resampling step in the Bayesian bootstrap filter which reduces the degeneracy problem introduced loss of diversity among the particles. This arises due to the fact that in the resampling step, samples are drawn from a discrete distribution. To resolve this problem, we have proposed to draw samples from an approximation method using nonparametric multivariate density estimation which allowed us to have new filters called nonparametric Bayesian bootstrap filtering. Finally, we proposed another hybrid combination method based on the nonparametric Bayesian bootstrap filter and the discrete wavelet transform (DWT) to reduce the speckle noise of synthetic aperture radar images.

Chapter 1

Modeling of degraded satellite images

Table of Contents

Introduction	9
1.1 Satellite images.....	10
1.1.1 Sentinel family	10
1.1.2 Sentinel-1	12
1.1.3 Sentinel-2	14
1.2 Reasons for image degradation	15
1.2.1 Reasons for blurring.....	16
1.2.1.1 Motion blur	17
1.2.1.2 Out-of-focus blur.....	19
1.2.1.3 Atmospheric turbulence blur.....	21
1.2.2 Reasons for noise	23
1.2.2.1 Impulse noise	24
1.2.2.2 Additive noise	25
1.2.2.3 Multiplicative noise.....	27
1.2.2.4 Poisson noise.....	29
1.3 Image and degradation models	31
1.3.1 Image model.....	32
1.3.2 Degradation models	33
1.3.2.1 Linear space-invariant blur models.....	34
1.3.2.2 Space-variant blur models.....	34
1.3.3 Estimation of image model coefficients	35
1.3.3.1 Least squares method	35
1.3.3.2 Yule-Walker equations	36
1.3.4 Measures of image restoration quality	37
1.3.4.1 Improvement Signal-to-noise ratio (ISNR) improvement	37
1.3.4.2 Mean Square Error (MSE)	38
1.3.4.3 Root Mean Square Error (RMSE).....	38
1.3.4.4 Peak signal-to-noise ratio (PSNR).....	38
Conclusion.....	39
References	40

Introduction

Satellite image processing is one of the leading fields in computer research. Scientists and researchers benefit from satellite images variety of fields such as meteorology, oceanography, fisheries, agriculture, biodiversity conservation, forestry, landscapes, astronomy, geology and more [Lia05][Was14][Zhe13][Yi11]. Images acquired from satellites degraded due to many effects, such as climate, weather and some other factors [Rav13]. In satellite image processing, images received from satellites contain large amounts of data for further processing or analysis. Satellite images are usually captured under a variety of situations. Each captured satellite image is, in a sense, a degraded version of the scene [Hua04]. Sources of degradation can be blur, noise aliasing and atmospheric turbulence, which have usually defective effects in its nature. However, the acquired image always represents a degraded version of the original scene due to defects in imaging and acquisition process. Removing these defects is important for most subsequent image processing tasks. There are different types of damage to take into consideration, such as noise, geometric degradation (pincushion deformation), imperfections in lighting and color (under/over exposure, saturation), and blurring. Due to defective image formation, blurring is a form of ideal image bandwidth reduction. The relative motion between the camera and the original scene, or an out of focus optical system may cause this blur. When producing aerial photographs for remote sensing, several factors will affect the images, like atmospheric turbulence, aberrations in the optical system, and relative motion between the camera and the ground, one/all of those factors will introduce blur in the images. An additional defect besides blur is noise, which affects any captured image. Noise can occur by the media which is producing the image (random absorption or dispersion effects), by recording media (sensor noise), by errors in measurement caused by the limited accuracy of the acquiring system and digital storage quantization of the data. Sudden changes in atmospheric temperature, external disturbances, and lack of acquisition of earth sensors, are another causes to add different types of noise to the acquired images [Kum14]. There are several types of earth satellites such as, NOAA, Metop and SAR, which are sending images to the satellite receivers. These images contain a fixed resolution depending on the application. The density, size, and length of the pixels are useful for analyzing information [Par99].

We start the first chapter with a state-of-the-art of satellite images, and in particular sentinel 1 and sentinel 2 images, in Section 1.1. In Section 1.2, we present a brief review of

reasons for image degradation. In Section 1.3, we describe the image and degradation models with non-symmetric half-plane (NSHP) regions of support.

1.1 Satellite images

Satellite imagery is indeed one of the eminent, robust and essential tools used by meteorologists. Actually, we can consider it as an eye in the sky. These images help forecasters to know the fluctuations in the climate and the changes expected to be achieved in the atmosphere as they provide a clear, precise and correct description of the events and how it is unfolding. Without satellites, predicting the weather and conducting research will be a hard challenge. Data collected at stations across the country are limited in terms of atmospheric performance. Although it is still possible to get a reasonable analysis of the data obtained, there will be a great opportunity to lose valuable pieces of information because hundreds of kilometers separate the earth stations. Satellite images help to show things that cannot be measured or seen. In addition, the satellite image is considered the truth. The data provided by the satellite images can be interpreted "firsthand". Satellite images may well reflect what is happening around the world, especially in the vast ocean of data. The data cannot be collected in some parts of the world, but without these data, the prediction will be as difficult as without satellites. There are two types of satellites in orbit around the Earth, polar and terrestrial. The geostationary satellite operating environment satellite (GOES) is still located at a fixed position on the Earth's surface at about 22,500 kilometers above the equator. Because satellites spin with the earth, they always see the same part of the earth. In contrast, polar-orbiting satellites have their orbits at lower altitudes (800-900 km). Their path is 2400 km wide centered on the path of the track. Polar-orbiting satellites are observing a new path in each orbit. Polar satellites are not useful for meteorologists because they do not observe the same area. Geostationary satellites allow meteorologists to observe the process of developing meteorology by observing the same area. As part of its plan to contribute to the Space Segment of Global Environmental and Security Monitoring (GMES), European Space Agency (ESA) is undertaking a high-resolution Optical Earth Observation mission. In the rest of this section, we will present a summary of sentinel images.

1.1.1 Sentinel family

ESA has developed a new family of missions called Sentinels specifically for the operational needs of the Copernicus program. Each Sentinel mission is based on a

constellation of two satellites to fulfil revisit and coverage requirements, providing robust datasets for Copernicus Services. These missions carry a range of technologies, such as radar and multi-spectral imaging instruments for land, ocean and atmospheric monitoring:

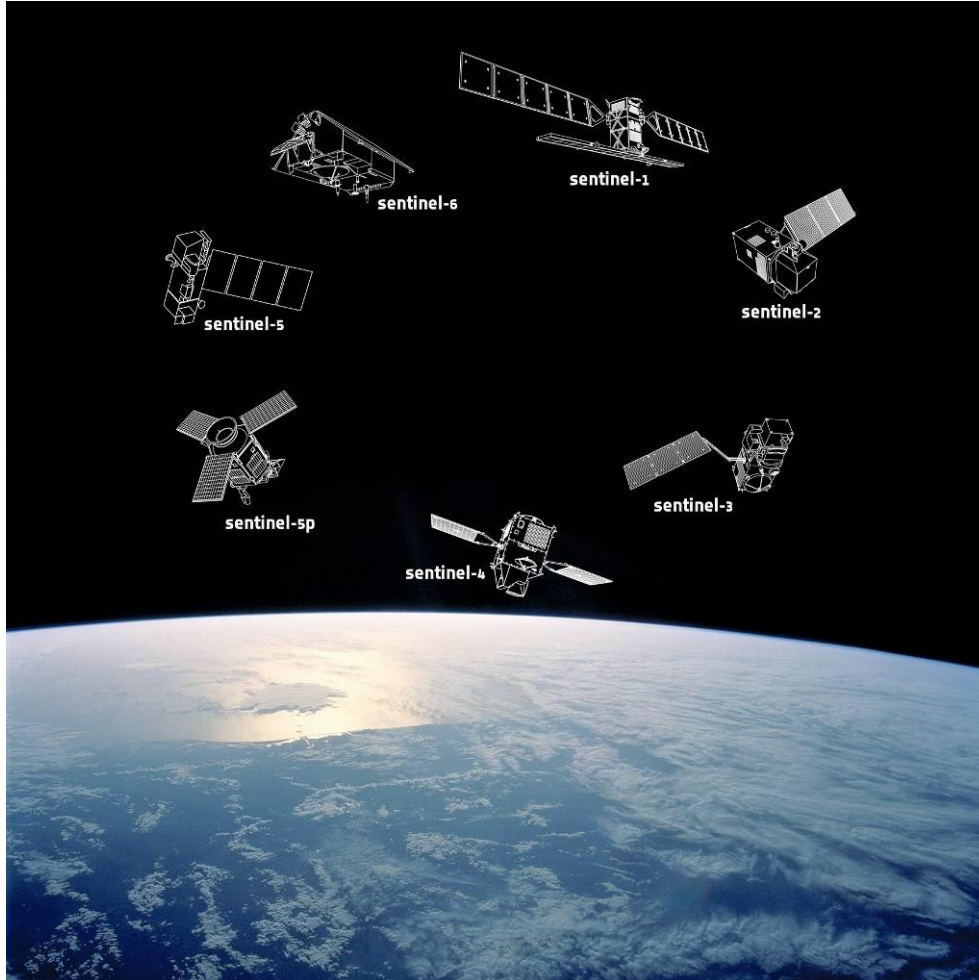


Figure 1.1: The Sentinel family.

- Sentinel-1 is a polar-orbiting, all-weather, day-and-night radar imaging mission for land and ocean services. Sentinel-1A was launched on 3 April 2014 and Sentinel-1B on 25 April 2016. Both were taken into orbit on a Soyuz rocket from Europe's Spaceport in French Guiana.
- Sentinel-2 is a polar-orbiting, multispectral high-resolution imaging mission for land monitoring to provide, for example, imagery of vegetation, soil and water cover, inland waterways and coastal areas. Sentinel-2 can also deliver information for emergency services. Sentinel-2A was launched on 23 June 2015 and Sentinel-2B followed on 7 March 2017.

- Sentinel-3 is a multi-instrument mission to measure sea-surface topography, sea- and land-surface temperature, ocean color and land color with high-end accuracy and reliability. The mission will Support Ocean forecasting systems, as well as environmental and climate monitoring. Sentinel-3A was launched on 16 February 2016.
- Sentinel-4 is a payload devoted to atmospheric monitoring that will be embarked upon a Meteosat Third Generation-Sounder (MTG-S) satellite in geostationary orbit.
- Sentinel-5 Precursor – also known as Sentinel-5P – is the forerunner of Sentinel-5 to provide timely data on a multitude of trace gases and aerosols affecting air quality and climate. It has been developed to reduce data gaps between the Envisat satellite – in particular the Sciamachy instrument – and the launch of Sentinel-5. Sentinel-5P was taken into orbit on a Rocket launcher from the Plesetsk Cosmodrome in northern Russia on 13 October 2017.
- Sentinel-5 is a payload that will monitor the atmosphere from polar orbit aboard a MetOp Second Generation satellite.
- Sentinel-6 carries a radar altimeter to measure global sea-surface height, primarily for operational oceanography and for climate studies.

In our work, we were particularly interested in the first two as data for the restoration problem. We will first start with the description of sentinel-1 and then sentinel-2.

1.1.2 Sentinel-1

The first in the series, Sentinel-1, carries an advanced radar instrument to provide an all-weather, day-and-night supply of imagery of Earth's surface. As a constellation of two satellites orbiting 180° apart, the mission images the entire Earth every six days. As well as transmitting data to a number of ground stations around the world for rapid dissemination, Sentinel-1 also carries a laser to transmit data to the geostationary European Data Relay System for continual data delivery.

Sentinel-1A was launched on 3 April 2014 and Sentinel-1B on 25 April 2016. Both were taken into orbit on a Soyuz rocket from Europe's Spaceport in French Guiana. The C-band Synthetic Aperture Radar (SAR) is built on ESA's and Canada's heritage SAR systems on ERS-1, ERS-2, Envisat and Radarsat.



Figure 1.2: The Sentinel-1 Satellite.

Sentinel-1 is an observatory polar-orbiting European radar providing continuity of SAR data for operational applications. These applications include: monitoring sea ice zones and the arctic environment surveillance of marine environment monitoring land surface motion risks mapping of land surfaces; forest, water and soil, agriculture mapping in support of humanitarian aid in crisis situations. The design of Sentinel-1 with its focus on reliability, operational stability, global coverage and quick data delivery is expected to enable the development of new applications and meet the evolving needs of Copernicus. Sentinel-1 is the result of close collaboration between the ESA, the European Commission, industry, service providers and data users. Designed and built by a consortium of around 60 companies led by Thales Alenia Space and Airbus Defence and Space, it is an outstanding example of Europe's technological excellence. Sentinel-1 is an imaging radar mission providing continuous all weather, day-and-night imagery at C-band. The Sentinel-1 constellation provides high reliability, improved revisit time, geographical coverage and rapid data dissemination to support operational applications in the priority areas of marine monitoring, land monitoring and emergency services. Sentinel-1 potentially images all global landmasses, coastal zones and shipping routes in European waters in high resolution and covers the global oceans at regular intervals. Having a primary operational mode over land and another over Open Ocean allows for a pre-programmed conflict-free operation. The main operational mode features a wide swath (250 km) with high geometric (typically 20 m Level-1 product resolution) and

radiometric resolutions, suitable for most applications. The Sentinel-1 Synthetic Aperture Radar (SAR) instrument may acquire data in four exclusive modes:

- Stripmap (SM) - A standard SAR stripmap-imaging mode where the ground swath is illuminated with a continuous sequence of pulses, while the antenna beam is pointing to a fixed azimuth and elevation angle.
- Interferometric Wide swath (IW) - Data is acquired in three swaths using the Terrain Observation with Progressive Scanning SAR (TOPSAR) imaging technique. In IW mode, bursts are synchronized from pass to pass to ensure the alignment of interferometric pairs. IW is Sentinel-1's primary operational mode over land.
- Extra Wide swath (EW) - Data is acquired in five swaths using the TOPSAR imaging technique. EW mode provides very large swath coverage at the expense of spatial resolution.
- Wave (WV) - Data is acquired in small stripmap scenes called "vignettes", situated at regular intervals of 100 km along track. The vignettes are acquired by alternating, acquiring one vignette at a near range incidence angle while the next vignette is acquired at a far range incidence angle. WV is Sentinel-1's operational mode over Open Ocean.

More details about sentinel-1 are given in appendix 1.A.

1.1.3 Sentinel-2

Sentinel-2 is a satellite system consisting of two polar-orbiting satellites, will help improve continuity and SPOT and Landsat multispectral range of tasks and ensure the high quality data and applications for a land monitoring operation, Services emergency and security intervention. The Sentinel line of satellites is planned to delivering land remote sensing data that are central to the European Commission's Copernicus program; in late 2015, the Sentinel line became operational. The Sentinel-2 mission emerged as a result of close cooperation between the ESA, the European Commission, data users, service providers, and industry. The mission has been designed and built by a consortium of around 60 companies led by Airbus Defense and Space, and supported by the CNES French space agency to optimize image quality and by the DLR German Aerospace Centre to improve data recovery using optical communications.

The Sentinel-2 mission consists of two satellites developed to support vegetation, land cover, and environmental monitoring. The Sentinel-2A satellite was launched by ESA on June

23 2015, and operated in a sun-synchronous orbit with a 10-day repeat cycle. The current Sentinel-2A acquisition priorities are focused primarily on Europe. A second identical satellite (Sentinel-2B) was launched on March 7, 2017 and is expected to be operational for data acquisitions in 3-4 month. Together they will cover all Earth's land surfaces, large islands, and inland and coastal waters every five days.



Figure 1.3: The Sentinel-2 satellite.

More details about sentinel 2 are given in appendix 1.B.

1.2 Reasons for image degradation

There are several modalities used to capture images, and for each modality, there are many ways to construct images. Therefore, there are many reasons and sources for image degradation. Images acquired through any modern sensors consist of variety of noises (such as thermal noise, amplifier noise, photon noise, quantization noise and cross talk), resulting from stochastic variations and deterministic distortions or shading. In addition to inherent reasons, blurring occurs in many image formation systems due to limited performance of both optical and electronic systems. The shutter speed, for example, is the main factor deciding the amount of motion blur. As blurring can significantly degrade the visual quality of images.

In digital image processing, in general, discrete model for a linear degradation caused by blurring and additive noise can be given by the following superposition summation,

$$g(x, y) = \sum_k^M \sum_l^N h(x-k, y-l) f(x, y) + n(x, y) \quad (1.1)$$

where $f(x, y)$ represents an original image with size of $M \times N$ pixels, $g(x, y)$ is the degraded image which is acquired by the imaging system, $n(x, y)$ represents an additive noise introduced by the system, and $h(x-k, y-l)$ is the two-dimensional point spread function (PSF) of the imaging system, which, in general, can be spatially varying. More detail of PSF is given in Appendix 2.A.

In the following of this section, we will study the reasons for image degradation on French synergy image [URL16]. A sentinel-2 image Figure 1.5 (a) shows La Rochelle - the capital of the Charente-Maritime department in western France - and surroundings. At the center, we can see clearly the 2.9 km long bridge connecting the city with the Île de Ré. The white lines represent the sandy beaches of the coastal area. Between the water line and the beach, silt layers and darker sand are shown, which are presented in this image captured during low tide. The La Rochelle- Île de Ré airport is visible at the north of the city. Also at top-right, it is the visible part of the Natural Reserve of the Bay of Aiguillon. It hosts hundreds of thousands of migratory water birds every year. It is an area of synergy between sea and land, freshwater and saltwater, and between humankind and nature. Since 23 June 2015, the Sentinel-2 has been in orbit as a polar-orbiting, high-resolution land monitoring satellite, supplying imagery of soil and water cover, vegetation, coastal areas and inland waterways. The size of this image is $2953 \times 4016 \times 3$.

1.2.1 Reasons for blurring

Blurring in an image occurs because of a localized averaging of pixels, and results in the smoothing of image content. It can be caused by a number of phenomena including, relative motion between the camera and the imaged scene, defocusing or atmospheric turbulence. Blurring is usually modeled as a convolution of the image with the point spread function (PSF). We will form the blurring process model in the following way:

$$g(x, y) = (h * f)(x, y) + n(x, y) \quad (1.2)$$

Let us consider each component in a more detailed way. As for functions $f(x, y)$ and $g(x, y)$, everything is quite clear with them. However, as for the blurring function $h(x, y)$ we need to say a couple of words. In the process of blurring each pixel of a source image turns into a spot

in case of defocusing and into a line segment (or some path) in case of a usual blurring due to movement. Alternatively, we can say otherwise, that each pixel of a blurred image is "assembled" from pixels of some nearby area of a source image. All those overlap each other, which fact results in a blurred image. The principle, according to which one pixel becomes spread, is called the blurring function.

1.2.1.1 Motion blur

Image blur can result from the subject moving while the shutter is open. Such movement results in the subject only being blurred. Most satellite imaging systems do not remain fixed over a target because they are in orbit around Earth or the Moon. Regarding the ordinary digital photos, the movement of our subject will cause blur in the image which we don't want to happen. For satellite photography, it is unavoidable that the satellite in its orbit or the Target are in motion (Figure 1.4). Once we have determined the resolution that our satellite camera needs to study a Target, we also have to keep track of image and Target motion, which can also blur the image. To avoid blurring, we do not want the scene being photographed to move by more than one pixel during the exposure time. Motion blurring can significantly degrade the visual quality of images. Motion blurring is usually modeled as a spatially invariant convolution process. The general form of motion blur function h is given as follows [Reg97]:

$$h(x, y) = \begin{cases} \frac{1}{L} & \text{if } \sqrt{x^2 + y^2} \leq \frac{L}{2} \text{ and } \frac{x}{y} = -\tan(\theta) \\ 0 & \text{otherwise} \end{cases} \quad (1.3)$$

where L and θ are the length and angle of the blur, respectively.

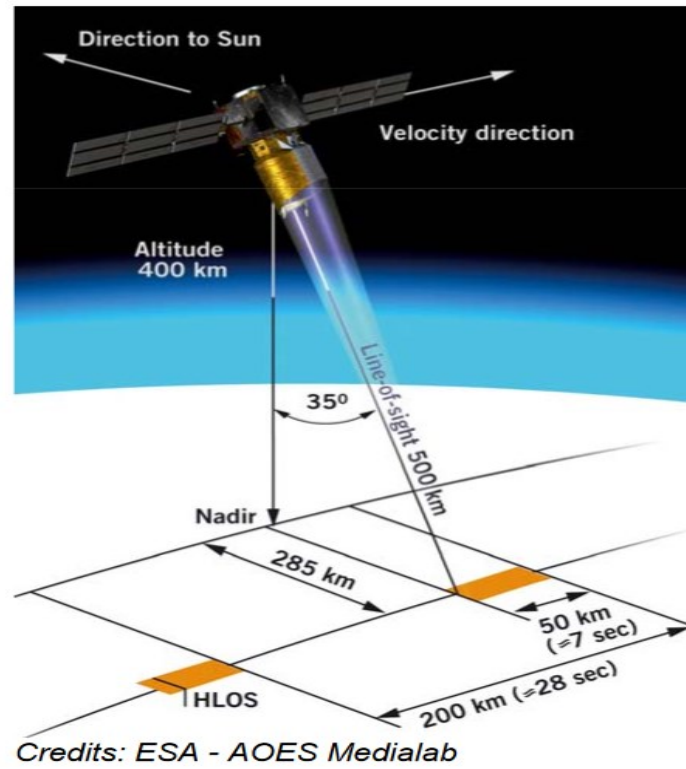


Figure 1.4: Satellite photography.

We present in Figure 1.5 a satellite image corrupted by linear motion blur with $L=20$ pixels and $\theta=45^\circ$.

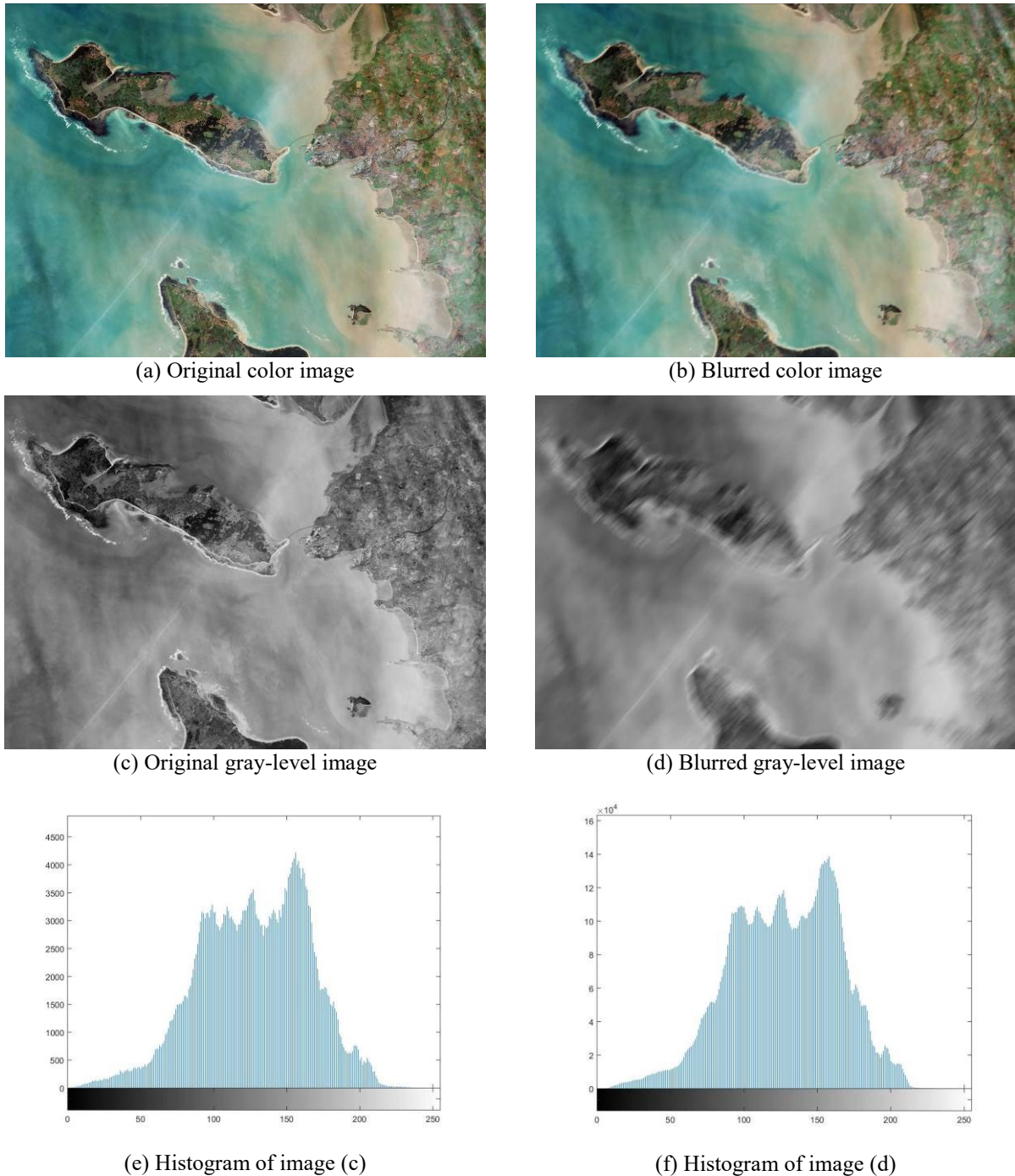


Figure 1.5: Images and histograms corresponding to motion blurring.

1.2.1.2 Out-of-focus blur

To reduce noise in short exposures, the aperture size can be increased to allow more light into the camera. Increasing the aperture size reduces the depth of field portion of image that is in-focus, however, it increases the portion of the image that will be out-of-focus. For a circular aperture, a point source in a scene will be projected onto the sensor as a circular disc.

This disc is known as the circle of confusion. The diameter of the circle depends on the focal length, aperture number and the distance between the lens and the object being imaged [Bov05]. If an object is out-of-focus, the lens will behave like a low pass filter, removing high frequency image content. If the PSF is large relative to the wavelengths being imaged, it can be modeled using the following spatially-invariant blur,

$$h(x, y) = \begin{cases} \frac{1}{\pi r^2} & \text{if } \sqrt{x^2 + y^2} \leq r \\ 0 & \text{otherwise} \end{cases} \quad (1.4)$$

where r is the radius of the out-of-focus blur.

We present in Figure 1.6 a satellite image corrupted by out-of-focus blur with $r=45^\circ$.

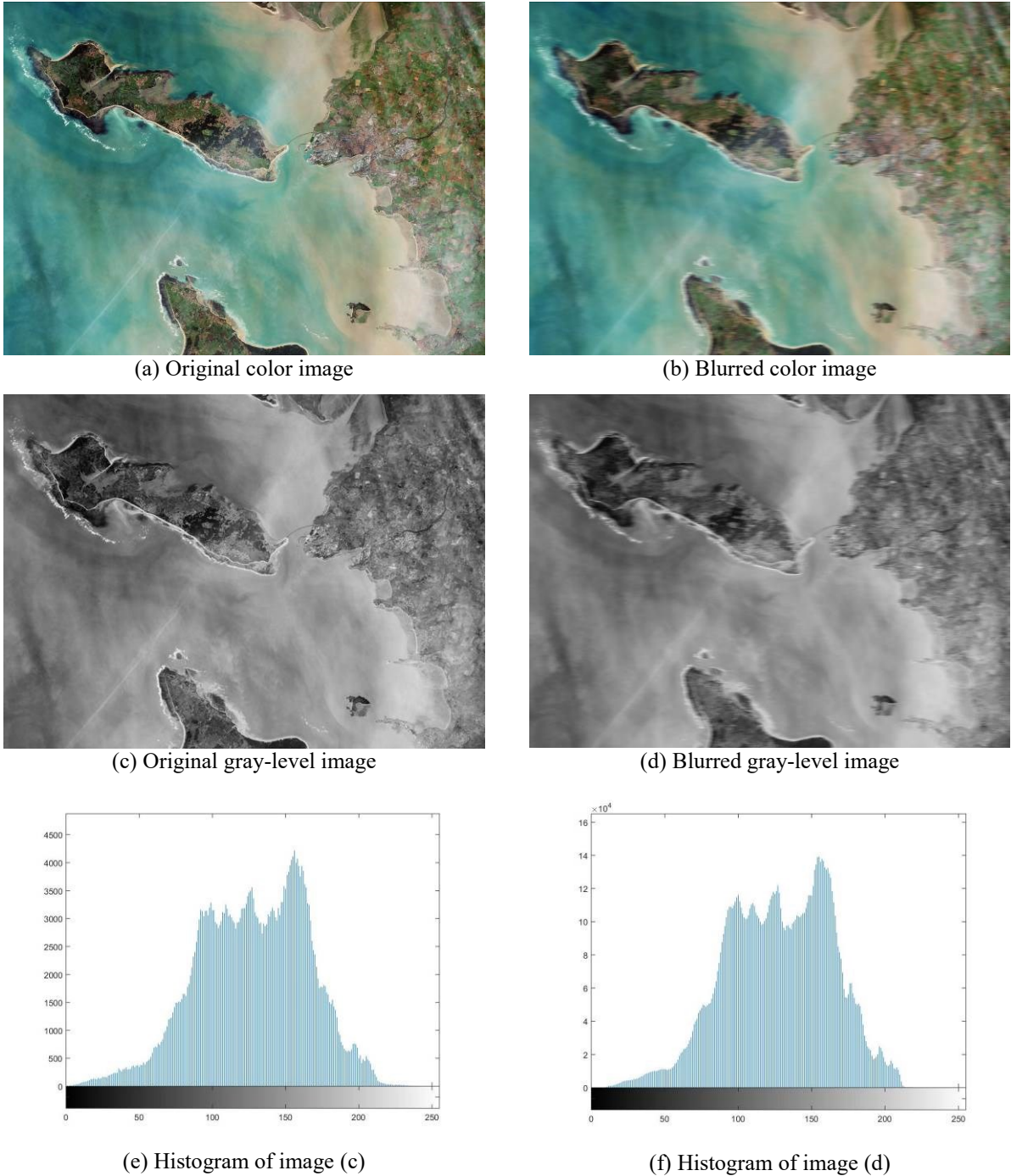


Figure 1.6: Images and histograms corresponding to out-of-focus blurring.

1.2.1.3 Atmospheric turbulence blur

Satellite images through the atmosphere are blurred, distorted, and have reduced contrast relative to their source. There are atmospheric phenomena that give rise to attenuation of the irradiance of the propagating image, thus reducing the contrast of the final image. Absorption

and large angle scattering by aerosols attenuate images propagating through the atmosphere [Li07]. They are blurred by small angle scattering caused by aerosols, and by optical turbulence. Image blur through the atmosphere [Li08] involves both turbulence and small angle forward scatter of light by aerosols, which is also called the adjacency effect, since it causes photons to be imaged in pixels adjacent to those in which they ought to have been imaged.

Common in remote sensing and aerial imaging, the blur due to long-term exposure through the atmosphere can be modeled by a Gaussian PSF,

$$h(x, y) = K \exp\left(-\frac{x^2 + y^2}{2\sigma^2}\right) \quad (1.5)$$

where K is a normalizing constant ensuring that, the blur is of unit volume, and σ^2 is the variance that determines the severity of the blur.

We present in Figure 1.7 a satellite image corrupted by atmospheric turbulence with $\sigma^2=5$.



(a) Original color image



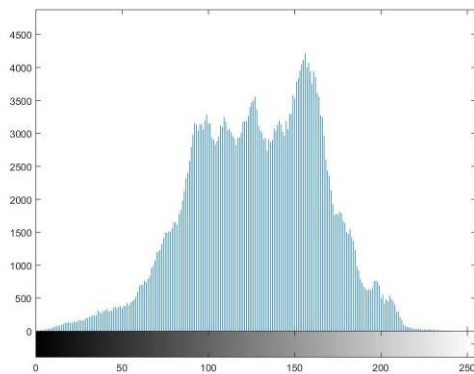
(b) Blurred color image



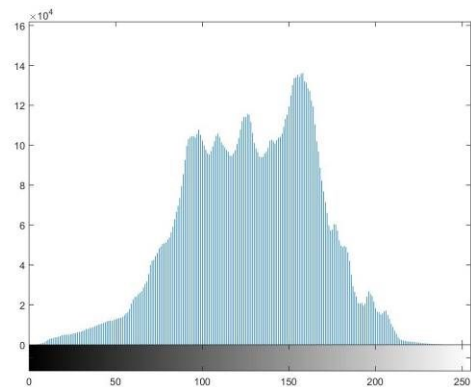
(c) Original gray-level image



(d) Blurred gray-level image



(e) Histogram of image (c)



(f) Histogram of image (d)

Figure 1.7: Images and histograms corresponding to atmospheric turbulence blurring.

1.2.2 Reasons for noise

Digital images are prone to a variety of types of noise. Noise is the result of errors in the image acquisition process that result in pixel values that do not reflect the true intensities of the real scene [Gag96][Fed17]. There are several ways that noise can be introduced into an image, depending on how the image is created. For example, if the image is scanned from a photograph made on film, the film grain is a source of noise. Noise can also be the result of

damage to the film, or be introduced by the scanner itself. If the image is acquired directly in a digital format, the mechanism for gathering the data (such as a CCD detector) can introduce noise. Electronic transmission of image data can introduce noise. Noise is deemed to be each or any measurement that is not part of the phenomena of importance. In imagery, we can categorize the noise into two categories as image data independent noise and image data dependent noise. Noise could be added systematically introduced into images. As types of noise, there are three types which are mostly represented to be added to the image; impulse, additive and multiplicative noise [Sub11].

1.2.2.1 Impulse noise

Impulse noise [Har10][Ric17] corruption is very common in digital images. Impulse noise is always independent and uncorrelated to the image pixels and is randomly distributed over the image. Hence unlike Gaussian noise, for an impulse noise corrupted image all the image pixels are not noisy, a number of image pixels will be noisy and the rest of pixels will be noise free. There are different types of impulse noise namely salt and pepper type of noise and random valued impulse noise. In salt and pepper type of noise the noisy pixels take either salt value (gray level-225) or pepper value (grey level-0) and it appears as black and white spots on the images. If p is the total noise density then, salt noise and pepper noise will have a noise density of $p/2$. This can be mathematically represented by:

$$g(i, j) = \begin{cases} 0 \text{ or } 255 & \text{with probability } p \\ f(i, j) & \text{with probability } 1 - p \end{cases} \quad (1.6)$$

where $g(i, j)$ represents the noisy image pixel, p is the total noise density of impulse noise and $f(i, j)$ is the uncorrupted image pixel.

At times the salt noise and pepper noise may have different noise densities p_1 and p_2 and the total noise density will be $p=p_1+p_2$. In case of random valued impulse noise, noise can take any gray level value from 0 to 225. In this case, also, noise is randomly distributed over the entire image and probability of occurrence of any gray level value as noise will be same. We can mathematically represent random valued impulse noise as:

$$g(i, j) = \begin{cases} n(i, j) & \text{with probability } p \\ f(i, j) & \text{with probability } 1 - p \end{cases} \quad (1.7)$$

where $n(i, j)$ is the gray level value of the noisy pixel.

We present in Figure 1.8 a satellite image noised by salt and pepper noise with $p=0.1$.

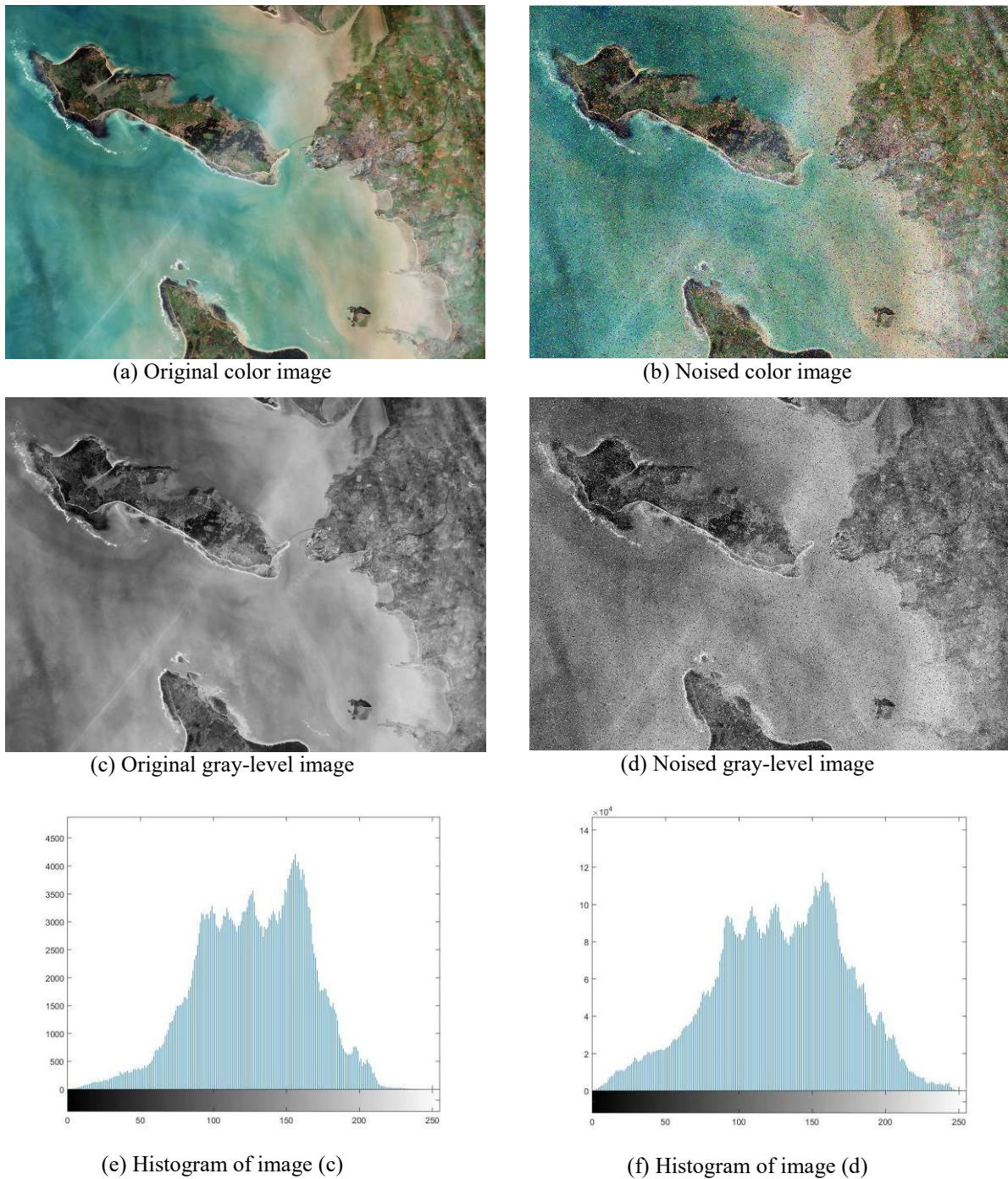


Figure 1.8: Images and histograms corresponding to salt and pepper noising.

1.2.2.2 Additive noise

In the additive noise, we can decompose the corrupted image g as:

$$g(i, j) = f(i, j) + n(i, j), \text{ where } 1 \leq i \leq M, 1 \leq j \leq N \quad (1.8)$$

where, f is the original image and n is the noise component. We assumed n to be white, i.e. every realization is independent from the others, in other words, corresponds to say that it is spatially uncorrelated which mean that the noise for each pixel is independent. Some examples of additive noise are Gaussian noise, uniform noise, Laplacian noise and Cauchy noise [Sci17]. Identification of Gaussian noises are very easy identified using skewness and kurtosis, the distribution of pixel is equally spread over the entire pixel, it's shown very less symmetry compared with others, the kurtosis is also very minimum, because of it is uniformly distributed entire the region. Gaussian noise is evenly distributed over signal. This means that each pixel in the noisy image is the sum of the true pixel value and a random Gaussian distributed noise value. The noise is independent of intensity of pixel value at each point. A special case is white Gaussian noise, in which the values at any pair of times are identically distributed and statistically independent. White noise draws its name from white light. Principal sources of Gaussian noise in digital images arise during acquisition, for example sensor noise caused by poor illumination or high temperature or transmission. Gaussian noise is statistical noise having a probability density function equal to that of the normal distribution, which is also known as the Gaussian distribution. In other words, the values that the noise can take on are Gaussian-distributed.

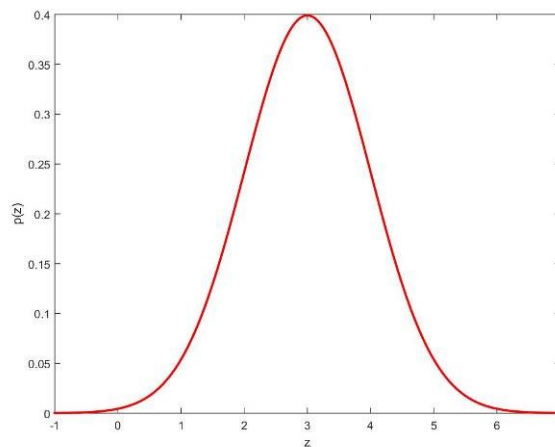


Figure 1.9: Probability density function of Gaussian noise.

The probability density function p of a Gaussian random variable z is given by:

$$p(z) = \frac{1}{\sqrt{2\pi}\sigma} e^{-(z-\mu)^2/2\sigma^2} \quad (1.9)$$

where z represents the grey level, μ the mean value and σ the standard deviation.

We present in Figure 1.10 a satellite image noised by a Gaussian noise with zero mean and variance of 0.1.

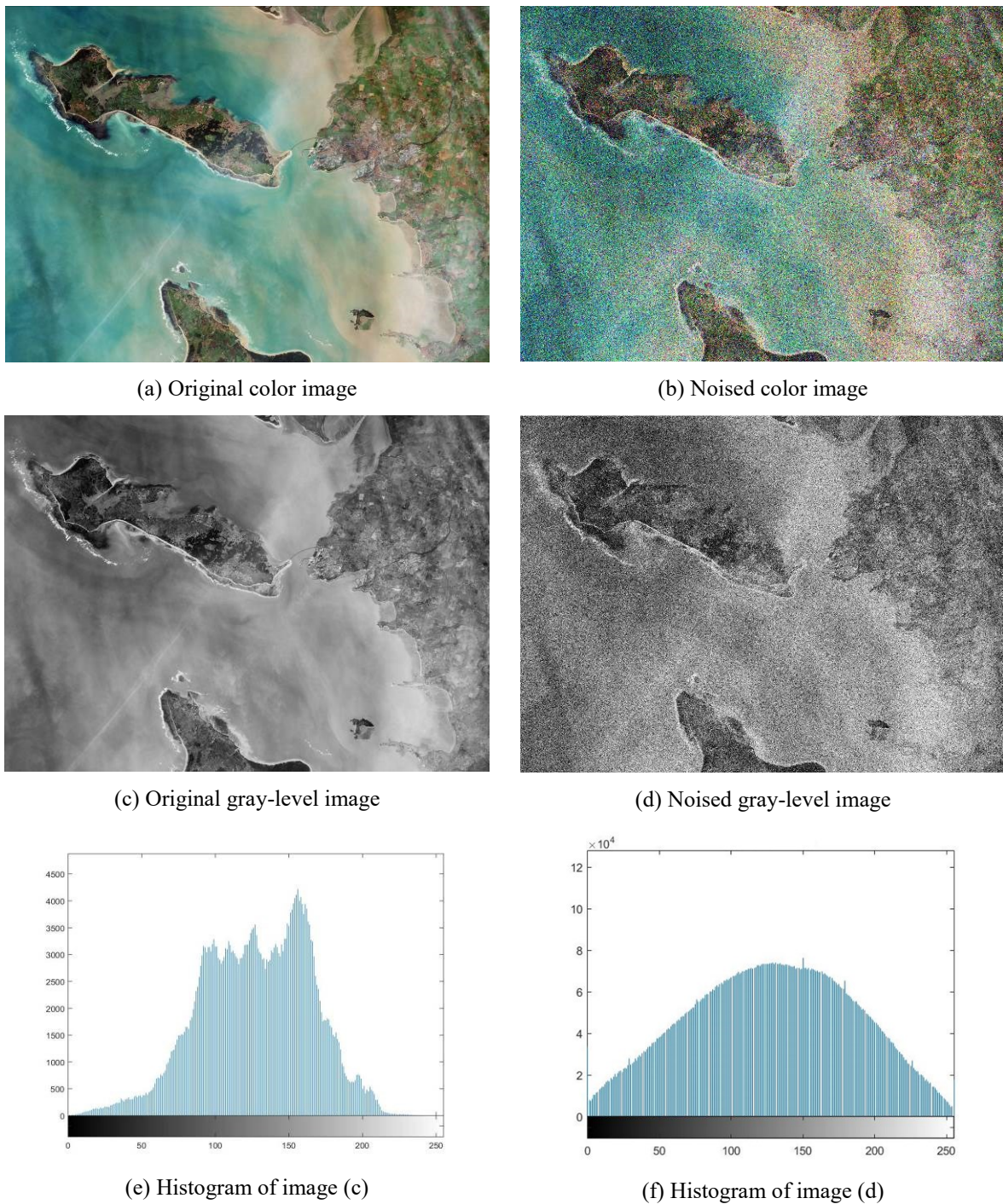


Figure 1.10: Images and Histograms corresponding to Gaussian noise.

1.2.2.3 Multiplicative noise

The multiplicative noise that is also, known as Speckle noise. Speckle noise is commonly observed in radar sensing system, although it may appear in any type of remotely sensed

image utilizing coherent radiation. Like the light from a laser, the waves emitted by active sensors travel in phase and interact minimally on their way to the target area. Speckle noise in image is serious issue, causing difficulties for image representation [Pal13]. Coherent processing of backscattered signals from multiple distributed targets causes it. Speckle noise is a multiplicative noise, which occurs in the coherent imaging, while other noises are additive noise. Speckle is caused by interference between coherent waves that, back scattered by natural surfaces, arrive out of phase at the sensor [Gag97]. Speckle can be described as random multiplicative noise. The source of this noise is a form of multiplicative noise in which the intensity values of the pixels in the image are multiplied by random values. Speckle noise is multiplicative noise unlike the Gaussian and salt pepper noise. The probability distribution function for speckle noise is given by gamma distribution

$$p(z) = \frac{z^{\alpha-1}}{(\alpha-1)!a^\alpha} e^{-z/a} \quad (1.10)$$

where z , α and a represent respectively the gray level, the shape parameter and the scale parameter.

The probability density function of speckle noise is graphically represented in Figure 1.11.

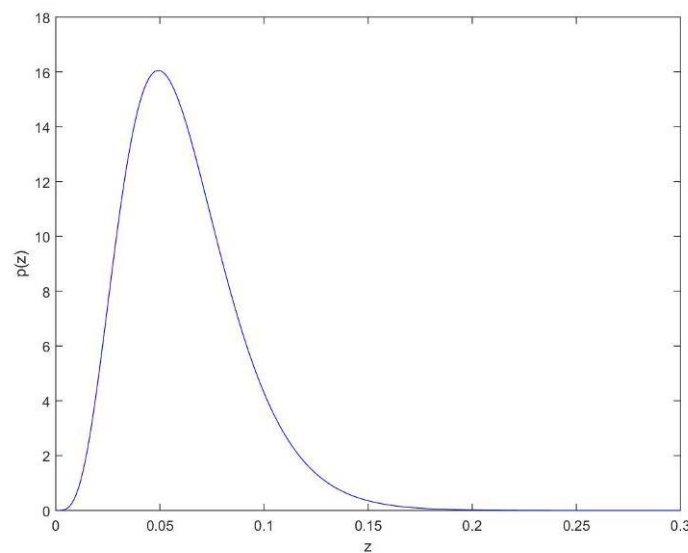


Figure 1.11: Probability density function of speckle noise.

We present in Figure 1.12 a satellite image noised by a zero mean speckle noise with variance is equal to 0.3.



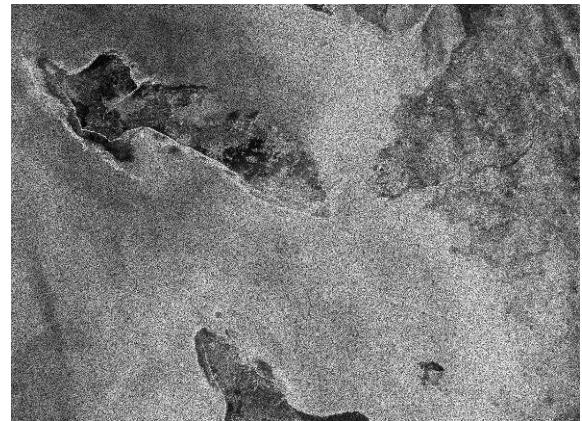
(a) Original color image



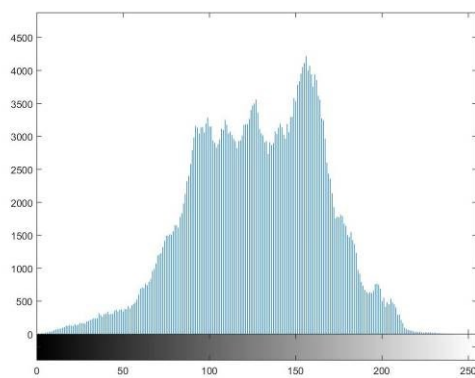
(b) Noised color image



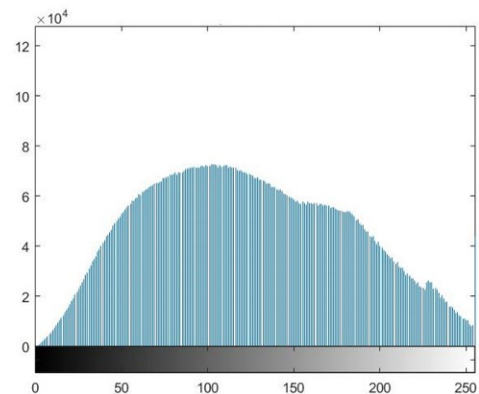
(c) Original gray-level image



(d) Noised gray-level image



(e) Histogram of image (c)



(f) Histogram of image (d)

Figure 1.12: Images and histograms corresponding to speckle noise.

1.2.2.4 Poisson noise

Poisson noise, also known as Photon noise, is a basic form of uncertainty associated with the measurement of light, inherent to the quantized nature of light and the independence of photon detections. In computer vision, a widespread approximation is to model image noise as signal independent, often using a zero-mean additive Gaussian. Though this simple model suffices for some applications, it is physically unrealistic. In real imaging systems, photon

noise and other sensor-based sources of noise contribute in varying proportions at different signal levels, leading to noise that is dependent on scene brightness. Understanding photon noise and modeling it explicitly is especially important for low-level computer vision tasks treating noisy images [Foi08], and for the analysis of imaging systems that consider different exposure levels or sensor gains [Has10].

Let I denote an image that does not include noise and the number of the photons $\lambda(i)$ for pixel value $I(i)$ at pixel i , which is expressed as [Ima16]

$$\lambda(i) = rI(i) \quad (1.11)$$

where r is a coefficient indicating the photons for a tone level of 1. Then, the noise in the pixel is Poisson distributed with probability function

$$P(k) = \frac{\lambda(i)^k e^{-\lambda(i)}}{k!} \quad (1.12)$$

where, k is the gray level.

A characteristic of the Poisson distribution is that the variance is equal to the mean, so that for each pixel the noise depends on the number of photons.

We present in Figure 1.13 a satellite image noised by a Poisson noise. The satellite image is coded on 8 bits. For example, if a pixel has the value of 10, then the corresponding output pixel will be generated from a Poisson distribution with mean 10.



(a) Original color image



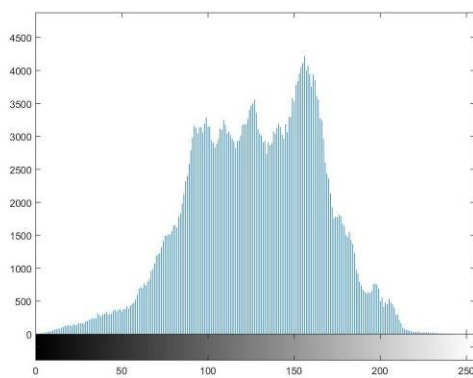
(b) Noised color image



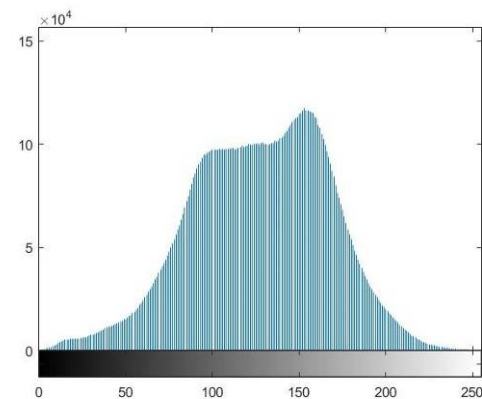
(c) Original gray-level image



(d) Noised gray-level image



(e) Histogram of image (c)



(f) Histogram of image (d)

Figure 1.13: Images and histograms corresponding to Poisson noise.

1.3 Image and degradation models

Two-dimensional (2-D) autoregressive (AR) models have many applications in image processing and analysis. For instance, they have been applied to image restoration [Kau91], to texture analysis [Sar94], to fine arts painting analysis [Hei87], and to 2-D spectrum estimation [Sha86].

1.3.1 Image model

In establishing the fundamentals for mathematical image modeling, we will assume that any interesting image can be defined on mapping of pixel coordinates into density values over a discrete 2D square region consisting of a $N \times N$ regularly spaced lattice, i.e., with N^2 different picture elements or pixels. A conventional raster type scan from left to right and from top to bottom will be followed. Space-invariant image models assume that the image is a realization of a homogeneous random field. A causality is introduced in the representation of images by the scanning process. We assume previous information that the real image structure can be described by a 2D independent auto regressive (AR) model with zero-mean homogeneous Gaussian noise $w(m, n)$ with covariance $\sigma_w^2(m, n)$ [Arb04]. The model equation is

$$s(m, n) = \sum_{(k,l) \in \Gamma} c_{k,l} s(m-k, n-l) + w(m, n) \quad (1.11)$$

where $c_{k,l}$ are the image model coefficients (assumed stationary), $s(m, n)$ is the present pixel estimated in the original image from past pixels in the range Γ , and the range Γ is the pixels belonging to the non-symmetric half plane (NSHP), which were defined as past.

When the range is limited to an M by M pixel size, then

$$\Gamma = \left\{ \begin{array}{l} (m-k, n-l) : (1 \leq k < M, 0 \leq l < M) \\ \cup (-M \leq k \leq 0, 1 \leq l \leq M) \end{array} \right\} \quad (1.12)$$

where M is empirically defined according to the image correlation.

By lexicographically ordering of the image data [And77] we can use the more compact matrix-vector notation:

$$s = Cs + w \quad (1.13)$$

A general state-space difference equation representation is of the form:

$$x(m, n) = Cx(m-1, n) + Eu(m, n) + Dw(m, n) \quad (1.14)$$

where $x(m, n)$ is the state at (m, n) ; u denotes a deterministic input, w denotes additive noise independent of x , and C , D , and E are system matrices. The deterministic input term, u , has not been used previously for image restoration.

The representation of (1.14) is a one-dimensional state-space difference equation where "one-dimensional" implies one direction of state propagation, either horizontally or vertically. In order to represent (1.11) in the form of (1.14), the one-dimensional (horizontal) state-space representation requires the state to be defined as follows:

$$x(m, n) = \begin{bmatrix} s(m, n), s(m-1, n), \dots, s(1, n); \\ s(N, n-1), \dots, s(1, n-1); \dots; \\ s(N, n-M), \dots, s(m-M, n-M) \end{bmatrix}^T \quad (1.15)$$

This state was determined assuming an image of N pixels wide and scanned from left to right, top to bottom. The pixels contained in the state vector are shown pictorially in Figure 1.14. It is obvious that the size of the state vector will remain constant in a given column.

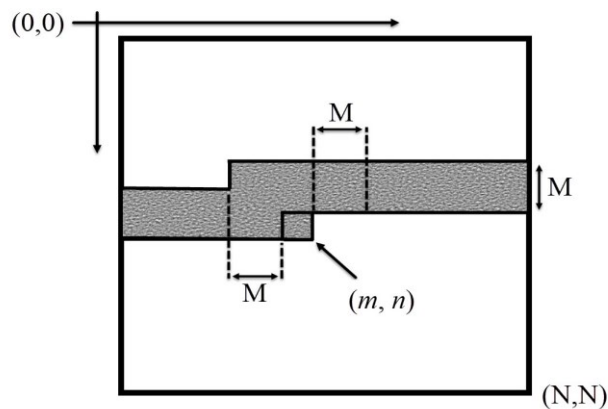


Figure 1.14: The state vector $x(m, n)$.

1.3.2 Degradation models

The deterministic component of the degradations, called blur, is modeled by a mapping $f(m, n; s(o, p))$ of the scene $s(o, p)$ to the image plane coordinates (m, n) . In its most general form, this mapping is non-linear and space-variant [And77]. Images are also subject to statistical degradations, commonly called noise, which for practical purposes can be modeled as an additive white, Gaussian random field, $v(m, n)$, with zero-mean and variance σ_v^2 [Woo77][Ros82][Zha89]. Hence, the observation model becomes:

$$y(m, n) = f(m, n; s(o, p)) + v(m, n) \quad (1.16)$$

We will now investigate some simplified blur models.

1.3.2.1 Linear space-invariant blur models

The mapping $f(m, n; s(o, p))$ becomes the point spread function (PSF) if $s(o, p)$ is substituted by the unit impulse $\delta(m, n)$ indicating a point source for the scene. Assuming a linear degradation system, in the limit of representing the scene with a spatial distribution of an infinite number of point sources, the resulting image plane intensity distribution, $b(m, n)$, is given by the following superposition rule:

$$b(m, n) = \sum_{(o, p) \in \Psi} h(m, n; o, p) s(o, p) \quad (1.17)$$

where $h(m, n; o, p)$ is the PSF and Ψ denotes the PSF support.

Further simplification of (1.17) is possible due to the nature of some blurs. If the blur is considered as space-invariant, then (1.17) becomes a discrete convolution summation as follows:

$$b(m, n) = \sum_{(k, l) \in \Psi} h(k, l) s(m - k, n - l) \quad (1.18)$$

where $h(k, l) = h(m - o, n - p)$.

Unlike the image model support, the support of the PSF does not to be causal, and in general, almost all realistic blurs are modeled with non-causal PSFs. The blurring PSF which is modeled by this way is an $(M \times M)^{th}$ order finite impulse response (FIR) filter. The conservation of energy assumption implies that a point source of light should result in no loss of energy, i.e.,

$$\sum_{(k, l) \in \Psi} h(k, l) = 1. \quad (1.19)$$

1.3.2.2 Space-variant blur models

In some cases, a space-invariant blur model is not appropriate as explained in the introduction. The most general case of space-variant blurs is modeled by equation (1.16). However, under some assumptions, it is possible to approximate the space-variant blur model with a piecewise space-invariant PSF. In other words, we can assume that the space-variant blur can be represented by a collection of L distinct point spread functions, where L is a pre-

determined number, such that at each pixel one of the L point spread functions will be more-or-less matched to the observed data. Then (1.17) simplifies to:

$$b(m, n) = \sum_{(k, l) \in \Psi} h(k, l) (\theta(m, n)) s(m - k, n - l) \quad (1.20)$$

where $\theta(m, n)$ is a random variable that indicates the blur model acting at (m, n) .

The space-variant blur identification problem then reduces to a detection problem, at each pixel, over a finite-population set of possible point spread functions. Real life examples of image-blurs that can approximately be modeled by (1.20) are given below.

1.3.3 Estimation of image model coefficients

The problem of two-dimensional (2D) autoregressive modeling is very important in many signal-processing applications. This problem has applications in image processing, radar, sonar, and communications. In image processing, it has been applied to image modeling [Zha08], texture analysis [Oe93], and hyperspectral imagery [He13]. In radar and sonar, it can be included in direction finding, model based detection, and spectral estimation [Han90]. Modeling of 2D AR processes with various regions of support is considered in [Cho07]. We will briefly review the procedure for estimating the image model coefficients.

1.3.3.1 Least squares method

The method of least squares is a standard approach in regression analysis to the approximate solution of overdetermined systems, i.e., sets of equations in which there are more equations than unknowns. "Least squares" means that the overall solution minimizes the sum of the squares of the residuals made in the results of every single equation.

Alternatively, (1.11) can be written as follows:

$$s(m, n) = C^T s_1(m-1, n) + w(m, n) \quad (1.21)$$

where $s_1(m-1, n)$ is as in [Kau83], a vector consisting of those pixels in Γ , and C is a vector containing the corresponding coupling coefficients.

The most straightforward procedure for estimating the coefficient vector C is to perform a least-squares fit of (1.21) over a representative block Ω of data using the observations $y(m, n)$ in place of the true densities $s(m, n)$. That is, \hat{C} would be determined so as to minimize:

$$J = \sum_{(m,n) \in \Omega} \left(y(m,n) - C^T y_1(m-1,n) \right)^2 \quad (1.22)$$

where, $y_1(m-1,n) = s_1(m-1,n) + v_1(m-1,n)$.

Setting to zero the gradient of J with respect to C results in:

$$\hat{C} = \left[\sum_{(m,n) \in \Omega} \left(y_1(m-1,n) y_1^T(m-1,n) \right) \right]^{-1} \times \left[\sum_{(m,n) \in \Omega} \left(y_1(m-1,n) y(m,n) \right) \right] \quad (1.23)$$

It should be noted, however, that since y_1 , the term that multiplies C in (1.22), contains noise, the estimate will be significantly biased in the sense that $E(\hat{C}) \neq C$.

An approximate method for reducing this bias can be realized by first recognizing that the true unbiased estimate would be:

$$\hat{C}_0 = \left[\sum_{(m,n) \in \Omega} \left(s_1(m-1,n) s_1^T(m-1,n) \right) \right]^{-1} \times \left[\sum_{(m,n) \in \Omega} \left(s_1(m-1,n) s(m,n) \right) \right] \quad (1.24)$$

If the sums in (1.23) is regarded as expectation approximation, then (1.24) can be rewritten as:

$$\hat{C}_0 = \left[E(s_1 s_1^T) \right]^{-1} \times \left[E(s_1 s) \right] \quad (1.25)$$

1.3.3.2 Yule-Walker equations

The image model coefficients and the related modeling variance σ_w^2 can be obtained immediately by the 2D Yule-Walker equations [Yul27][Wal31], because the autocorrelation coefficients can be computed directly from the original image s . The term $w(m,n)$ can also be regarded as the modeling error between the image and its predicted value. Specifically, we obtain the AR coefficients $c(k,l)$ by solving the Yule-Walker equations:

$$\begin{aligned} r_{m,n} &= \sum_{(k,l) \in \Gamma} c_{k,l} r_{m-k,n-l} & \forall (m,n) \in \Gamma \\ \sigma_w^2 &= r_{0,0} - \sum_{(k,l) \in \Gamma} c_{k,l} r_{k,l} \end{aligned} \quad (1.26)$$

where σ_w^2 is variance of the state noise and $r_{m,n}$ is the $(m,n)^{\text{th}}$ auto-correlation coefficient

of the original (or its prototype) image computed as:

$$r_{m,n} = \frac{1}{(N-m)(N-n)} \sum_{\{(i,j),(i-m,j-n)\} \in S} s(i,j)s(i-m,j-n) \quad (1.27)$$

1.3.4 Measures of image restoration quality

In applications of image restoration, image quality usually refers to the image's fidelity to its original. To measure the image restoration quality thus means to measure the amount of improvement in image quality due to restoration. There are two classes of objective quality assessment of images. The first are the mathematically defined measures such as the mean square error (MSE), peak signal to noise ratio (PSNR), root mean square error (RMSE), and improvement signal to noise ratio (ISNR). The second class of measurement methods depend on the characteristics of the human visual system (HVS) in an attempt to incorporate perceptual quality measures. Of the two methods, the mathematically defined measures are most widely used. This is because of simplicity of implementation. Most error sensitivity methods are based on the mean square error (MSE). In most circumstances, they are "equivalent metrics". The MSE is parameter-free, easy to compute and the samples in an image are considered to be independent. The MSE allows a clear physical meaning.

1.3.4.1 Improvement Signal-to-noise ratio (ISNR) improvement

In image restoration, the improvement in quality of the restored image over the recorded blurred one is measured by the improvement signal-to-noise ratio (ISNR) improvement which is defined as follows in decibels (dB). For an image of size $M \times N$ pixels, ISNR is given by:

$$ISNR = 10 \log_{10} \frac{\sum_{i=1}^M \sum_{j=1}^N (x(i,j) - y(i,j))^2}{\sum_{i=1}^M \sum_{j=1}^N (x(i,j) - \hat{x}(i,j))^2} \quad (1.28)$$

where x , y and \hat{x} are the original image, the degraded image and the restored image, respectively. This objective measure is usually applied to evaluate restoration performance, and is widely adopted in the comparative study of restoration algorithms [Kat91][Lag91].

The improvement in ISNR is a measure that expresses the reduction of disagreement with the ideal image when comparing the distorted and restored images. Note that all of the above signal-to-noise measures can only be computed in case the ideal image is available, i.e., in an experimental setup or in a design phase of the restoration algorithm.

1.3.4.2 Mean Square Error (MSE)

Mean Square Error (*MSE*) is a quality measure, which quantitatively recognize the strength of error signal. *MSE* is commonly used because it has a simple mathematical structure and easy to implement. If x is an input image and its desired or restored image is \hat{x} then, Mean Square Error may be defined as:

$$MSE = \frac{1}{M \times N} \sum_{i=1}^M \sum_{j=1}^N (x(i, j) - \hat{x}(i, j))^2 \quad (1.29)$$

1.3.4.3 Root Mean Square Error (RMSE)

The Root Mean Square Error (RMSE) is the root square of MSE:

$$RMSE = \sqrt{MSE} \quad (1.30)$$

1.3.4.4 Peak signal-to-noise ratio (PSNR)

The term peak signal-to-noise ratio (*PSNR*) is an expression for the ratio between the maximum possible value (power) of a signal and the power of distorting noise that affects the quality of its representation. Because many signals have a very wide dynamic range, (ratio between the largest and smallest possible values of a changeable quantity) the *PSNR* is usually expressed in terms of the logarithmic decibel scale. Image enhancement or improving the visual quality of a digital image can be subjective. Saying that one method provides a better quality image could vary from person to person. For this reason, it is necessary to establish quantitative/empirical measures to compare the effects of image enhancement algorithms on image quality. Using the same set of tests images, different image enhancement algorithms can be compared systematically to identify whether a particular algorithm produces better results. The metric under investigation is the peak-signal-to-noise ratio. If we can show that an algorithm or set of algorithms can enhance a degraded known image to more closely resemble the original, then we can more accurately conclude that it is a better algorithm. The mathematical representation of the *PSNR* for gray scale image is as follows:

$$PSNR = 10 \log_{10} \left[\frac{255^2}{MSE} \right] \quad (1.31)$$

Conclusion

In this chapter, we have recalled the main characteristics of sentinel family satellite images, as well as their different phases of treatment, also, we recalled their contributions in the various fields of human activity. We have also presented the reasons for image degradation, which consists of two distinct phenomenon's blur and noise. The blur occurs due to a number of reasons such as motion, defocusing and atmospheric turbulence. The noise may originate in the following process, the image formation process and the transmission process or the combination of these two. We described the mathematical models for the image and degradation that we will adopt for the restoration of satellite images. It is assumed that the original image can be represented by the output of a 2-D autoregressive process and the noisy blurred image can be modeled by the 2-D convolution summation.

References

- [And77] H. C. Andrews and B. R. Hunt, *Digital Image Restoration*, Prentice-Hall, Englewood Cliffs, N J, 1977.
- [Arb04] D. Arbel et al, *Landsat TM Satellite Image Restoration Using Kalman Filters*, *Photogrammetric Engineering & Remote*, Vol. 70, No. 1, pp. 91–100, 2004.
- [Bov05] A. Bovik, *Handbook of image and video processing*, 2nd ed. Elsevier Academic Press, 2005.
- [Boy15] A. K. Boyat, B. K. Joshi, *A Review Paper: Noise Models In Digital Image Processing*, *Signal & Image Processing: An International Journal (SIPIJ)*, Vol.6, No.2, April 2015.
- [Cho07] B. Choi and D. N. Politis, *Modeling 2-D AR processes with various regions of support*, *IEEE Transactions on Signal Processing*, Vol. 55, no. 5, pp. 1696–1707, 2007.
- [Esa11] S. Esakkirajan, T. Veerakumar, Adabala N. Subramanyam, C. H. PremChand, *Removal of High Density Salt and Pepper Noise Through Modified Decision Based Unsymmetric Trimmed Median Filter*, *IEEE Signal Processing Letters*, Vol. 18, Issue: 5, pp. 287 – 290, May 2011.
- [Fed17] S. Federica, D. Yiqiu and H. Per Christian, *Image reconstruction under non-Gaussian noise*, Kgs. Lyngby: Technical University of Denmark (DTU), 2017.
- [Foi08] A. Foi, M. Trimeche, V. Katkovnik, and K. Egiazarian, *Practical Poissonian-Gaussian noise modeling and fitting for single-image raw-data*, *IEEE Transactions on Image Processing*, Vol. 17, 11: pp. 1737-1754, 2008.
- [Gag96] L. Gagnon and F.D. Smaili, *Speckle Noise Reduction of Airborne SAR Images with Symmetric Daubechies Wavelets*, *SPIE Proc.* pp. 1424, 1996.
- [Gag97] L. Gagnon., A. Jouan, *Speckle filtering of SAR images: A comparative study between complex-wavelet based and standard filters*, *In SPIE Proc.*, pp. 80–91, 1997.
- [Han90] R. R. Hansen Jr. and R. Chellappa, *Noncausal 2-D spectrum estimation for direction finding*, *IEEE Transactions on Information Theory*, Vol. 36, No. 1, pp. 108–125, 1990.
- [Har10] J. Harikiran, B. Saichandana, B. DivakarImpulse, *Noise Removal in Digital Images*, *International Journal of Computer Applications*, Vol. 10 No. 8, pp. 39-42, 2010.

- [Has10] S. W. Hasinoff, F. Durand, and W. T. Freeman, Noise-optimal capture for high dynamic range photography, In Proc. IEEE Conference on Computer Vision and Pattern Recognition, pp. 553-560, 2010.
- [Hei87] F. Heitz, H. Maitre and C. de Couessian, Application of autoregressive models to fine arts painting analysis,” Signal Processing, Vol. 13, pp. 1-14, 1987.
- [He13] L. He, Z. Yu, Z. Gu, and Y. Li, Long-tail distribution based multiscale-multiband autoregressive detection for hyperspectral imagery, Multidimensional Systems and Signal Processing, Vol. 24, No. 1, pp. 65–85, 2013.
- [Hua04] X. Huang, A. C. Madoc, A. D. Cheetham, Multi-noise removal from images by wavelet-based Bayesian estimator, Multimedia Software Engineering, Proceedings. IEEE Sixth International Symposium, pp. 258-264, 2004.
- [Ima16] K. Imamura et al., Image denoising using non-local means for Poisson Noise, In Proceeding ISPACS, pp. 1-6, 2016.
- [Jai14] A. Jain, S. G. Kerhalkar, and M. Ahmed, Review on Denoising techniques for the AWGN signal introduced in a stationary image, International Journal of Engineering Science Invention, Vol. 3, Issue 4, pp. 01-10, 2014.
- [Kat91] A. K. Katsaggelos, Digital Image restoration, Springer-Verlag, Berlin, New York, pp. 17-18, 1991.
- [Kauf83] H. Kaufman, J. W. Woods, S. Dravida, A. M. Tekalp, Estimation and identification of two-dimensional images, IEEE Trans. Automat. Control, Vol. AC-28, pp. 7, 1983.
- [Kau91] H. Kaufman and A. M. Tekalp, Survey of estimation techniques in image restoration, IEEE Control Systems Magazine, Vol. 11, No, 1, pp. 16-24, 1991.
- [Kum14] A. Kumari, P. D. Chadha, A Survey on Filtering Technique for Denoising Images in Digital Image Processing, International Journal of Advanced Research in Computer Science and Software Engineering, ISSN: 2277 128X, pp. 612-614 , 2014.
- [Lag91] R. Lagendijk and J. Biemond, Iterative identification and restoration of images, Kluwer Academic Publishers, Boston, 1991.
- [Li07] D. Li, Restoration of Atmospheric Turbulence Degraded Video Using Kurtosis Minimization And Motion Compensation, Georgia Institute of Technology, May 2007.
- [Li08] D. Li and S. Simske, Atmospheric Turbulence Degraded Image by Kurtosis Minimization, IEEE Geoscience and Remote Sensing Letters, December, 2008.

- [Lia05] D. Y. Liao, Y. T. Yang, Satellite imaging order scheduling with stochastic weather condition forecast Systems, Man and Cybernetics, IEEE International Conference, pp. 2524-2529, 2005.
- [Oe93] S. Oe, Texture segmentation method by using two-dimensional AR model and Kullback information, Pattern Recognition, Volume 26, Issue 2, pp. 237-244, 1993.
- [Pal13] S. Palwinder and L. Jain, "Noise reduction in ultrasound images using wavelet and spatial filtering techniques", IEEE conference IMKE-2013, pp. 57, 2013.
- [Par99] J. M. Park, W. J. Pearlman, Speckle filtering of SAR images based on adaptive windowing, IEEE Proceedings on Vision, Image and Signal Processing, Vol. 146, No. 4, pp. 191-197, 1999.
- [Raj06] K. Rajesh et al, Satellite image restoration using statistical models, Signal Processing, Vol. 87, Issue 3, pp. 366-373, 2006.
- [Rav13] A. Ravinder, P. K. Reddy, N. Prasad, Detection of Wavelengths for Hail Identification Using Satellite Imagery of Clouds, Computational Intelligence, Communication Systems and Networks (CICSyN), Fifth International Conference, pp. 205-211, 2013.
- [Ros82] A. Rosenfeld, and A.C. Kak, Digital Picture Processing, Second Edition, Academic Press, New York, N.Y., 435 pp., 1982.
- [Reg97] L. Reginald, Basic Methods for Image Restoration and Identification, Information and Communication Theory Group, Delft University of Technology, Elsevier, Amstardam, 1997.
- [Ric17] R. D. Rickie and Odile Clavier, Impulsive noise: A brief review, Hearing Research Vol. 349, pp. 34-36, June 2017.
- [Sar97] A. Sarkar, K. M. S. Sharma and R. V. Sonak, A new approach for subset 2-D AR model identification for describing textures, IEEE Trans. Image Proc., Vol. 6, pp. 407-413, 1997.
- [Sci17] F. Sciacchitano, Image reconstruction under non-Gaussian noise, Kgs. Lyngby: Technical University of Denmark (DTU). DTU Compute PHD-2016, No. 426, 2017
- [Sha86] G. Sharma and R. Chellappa, Two-dimensional spectrum estimation using non causal autoregressive models, IEEE Trans. Information Theory, Vol. IT-32, No. 2, pp. 268-275, 1986.
- [Sub11] P. Subhashini, P.T. Bharat, Automatic Noise Identification in image using Statistical Features, International Journal of Computer Science and Technology, pp. 467-471, 2011.

- [URL16] http://www.esa.int/spaceinimages/Images/2016/02/French_synergy
- [Wal31] G. Walker, On Periodicity in Series of Related Terms, Proceedings of the Royal Society of London, Ser. A, Vol. 131, pp. 518-532, 1931.
- [Was14] S. A. Wasimi, K. K. Saha, An expert system to assess the landfall propensity of a tropical cyclone in Australia, Computer Science and Engineering (APWC on CSE), Asia-Pacific World Congress, pp. 1-6, 2014.
- [Woo77] J. W. Woods, and C.H. Radewan, *Kalman filtering in two dimensions*, IEEE Transactions on Information Theory, Vol. 23, N. 4, pp. 473–482, 1977.
- [Yi11] P. Yi, Y. Zhao, 3D landscape development based on the high-resolution satellite image, Remote Sensing, Environment and Transportation Engineering (RSETE), International Conference, pp. 8011-8014, 2011.
- [YLi07] Y. Li et al, Noise Removal for Degraded Images with Poisson Noise Using M-Transformation and BayesShrink Method, Electronics and Communications in Japan, Part 3, Vol. 90, No. 11, 2007
- [Yul27] G. Udny Yule, On a Method of Investigating Periodicities in Disturbed Series, with Special Reference to Wolfer's Sunspot Numbers, Philosophical Transactions of the Royal Society of London, Ser. A, Vol. 226, pp. 267-298, 1927.
- [Zha89] J.Y. Zhang, and W. Steenaart, High speed Kalman filtering for image restoration, Proceedings, Visual Communications and Image Processing IV , July, San Diego, California (SPIE, Bellingham, Washington), 1199: pp. 125–135, 1989.
- [Zha08] X. Zhang and X. Wu, Image Interpolation by Adaptive 2-D Autoregressive Modeling and Soft-Decision Estimation, IEEE Tran. On image processing, Vol. 17, NO. 6, pp. 887-896, 2008.
- [Zhe13] P. Zhenzhou, Y. Shinjae, D. Yu, D. Huang, Solar irradiance forecast system based on geostationary satellite, IEEE International Conference Smart Grid Communications, pp. 708-713, 2013.

Chapter 2

Comparative study of restoration techniques for satellite images

Table of Contents

Introduction	49
2.1 Basic model of image restoration	50
2.1.1 Image degradation model.....	50
2.1.2 Image restoration model	51
2.2 Non-blind restoration techniques	52
2.2.1 Deconvolution using Lucy Richardson Algorithm.....	53
2.2.2 Deconvolution using inverse filter.....	54
2.2.3 Deconvolution using Wiener filter	55
2.2.4 Deconvolution using Regularized Filtering.....	57
2.2.5 Deconvolution using Constrained Least-Squares Filtering	58
2.3 Blind Deconvolution Methods	59
2.3.1 Deconvolution using mean filter.....	60
2.3.2 Deconvolution using Median filter	61
2.3.3 Wavelet Deconvolution	62
2.3.4 Deconvolution using bilateral filter	64
2.3.5 Deconvolution using Adaptive local Filter.....	66
2.4 Proposed method to restore the Sentinel images.....	67
2.4.1 Result Analysis	68
2.4.1.1 Blur reduction in satellite images.....	70
2.4.1.2 Noise reduction in satellite images	83
2.4.1.3 Blur and noise reduction in satellite images	92
2.4.2 Evaluation of results and applying the proposed method.....	94
2.4.2.1 Cases for the blurred satellite images.....	95
2.4.2.2 Cases for the noised only satellite images.....	97
2.4.2.3 Cases for noised and blurred satellite images	100
Conclusion.....	101
References	103

Introduction

Satellite image processing is one of the thrust areas in the field of computer science research. In the satellite image processing, the image received from the satellite contains enormous amount of data for the further processing or analysis. The received satellite image always corrupted by blur and noise.

There are many types of blur that affect images, such as linear motion blur, out of focus blur and atmospheric turbulence blur. However, the atmospheric turbulence blur is the main source for blurring in the remote sensing imagery [Tom08]. In the satellite image, noise is introduced in many stages: transmission channel, quantization process, and measurement process. Moreover, lenses, digitizer, and cameras also contribute to the image degradation. The analysis of such degraded images will hamper the investigation part and may lead to wrong solutions. Such images have to be restored back to its original form to get the correct results.

The restoration of the image is an area that also deals with improving the appearance of an image [Kau12][Das15]. However, unlike image enhancement, which is subjective, the image restoration is objective in the sense that restoration techniques tend to be based on mathematical or probabilistic models of image degradation. Many restoration algorithms have been developed but all of them having its own advantages and disadvantages [Gan13]. The selection of the appropriate algorithm depends on the targeted application. For example, the restoration algorithm developed for a medical image is not suitable for the satellite or any other images [Ras17].

Image restoration is the process of any form of image degradation reduction. Image restoration algorithms can be broadly divided into blind [Can76] and non-blind techniques. If the degradation function or point spread function (PSF) is known, then the algorithm is said to be non-blind whereas if the PSF is unknown then the algorithm is a blind image restoration technique. Image restoration techniques are the methods that attempt the inversion of some degrading process. Image restoration technique can be broadly classified into two types depending upon the knowledge of degradation. If the prior knowledge about degradation is known, then the deterministic method of image restoration can be applied. If it is not known, then the stochastic method of image restoration has to be employed.

The aim of this chapter is to compare and understand some of the popular image restoration algorithms for different images that are obtained from various different imaging fields and to develop a more powerful restoration technique, which can fulfill the desire to have satellite image as clear as possible. We organize this chapter as following. We start by introducing a

basic model of image restoration in Section 2.1. We described the non-blind and the blind restoration techniques respectively in Section 2.2 and Section 2.3. Finally, we introduce the proposed method in Section 2.4.

2.1 Basic model of image restoration

The main objective of image restoration is to recover the original image from a degraded image, which is affected by blur and/or noise. At first, the original image is degraded using degradation function, the noise is added to this generated output after that. At the next stage, the received degraded image is given to the restoration filter, which suppress the blur and/or noise, and produce the output image, which is compared to the original image.

2.1.1 Image degradation model

In the degradation model, the image is blurred using the degradation function h , and then the noise is added to the image. The image degradation model is given by:

$$g(x, y) = (h * f)(x, y) + n(x, y) \quad (2.1)$$

where, $h(x, y)$, $g(x, y)$, $f(x, y)$, and $n(x, y)$ represent respectively the degradation function, the observed or degraded image, the original image or input image and the additive noise respectively.

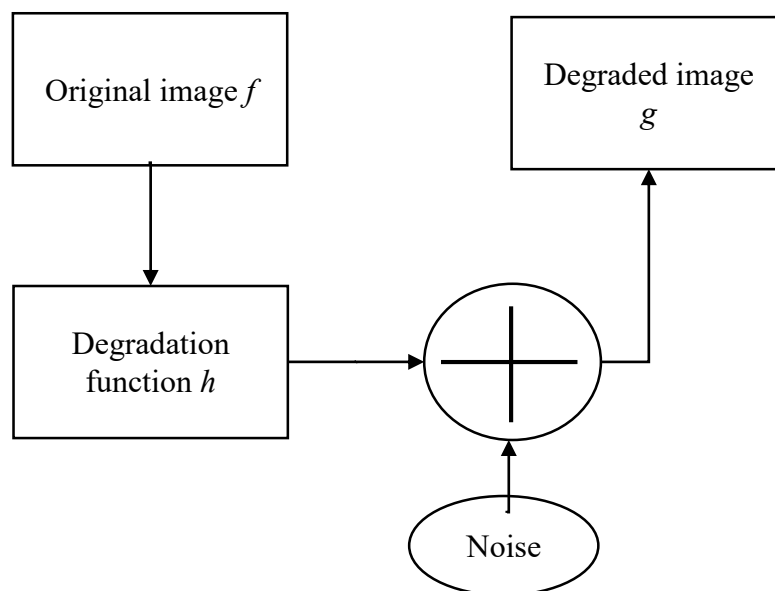


Figure 2.1: Image degradation model.

2.1.2 Image restoration model

In the image restoration model, the restored image $\hat{f}(x, y)$ is built back by the restoration filter from the degraded image $g(x, y)$. The restoration process is implemented by inverting the degradation process by removing the blur factor and the additive noise from the degraded image. We obtain an estimation of the original image after the restoration. The closer of the restored image $\hat{f}(x, y)$ to the original image $f(x, y)$ the more efficient is the filter.

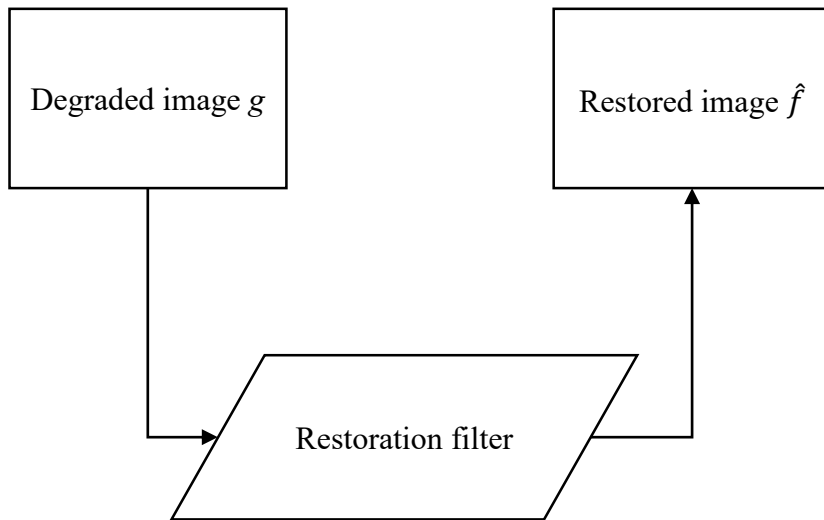


Figure 2.2: Image restoration model.

The domain of image restoration (which is sometimes referred to as image deconvolution or image de-blurring) is concerned in the reconstruction or estimation of the uncorrupted image from a blurred and/or noisy image. Basically, restoration techniques are classified into blind restoration techniques and non-blind restoration techniques [Tha16]. Blind and non-blind restoration techniques are further more divided into linear restoration methods and non-linear restoration methods [Sum09]. Figure 2.3 shows classification of restoration techniques.

We will discuss the non-blind restoration techniques at first in this chapter. A non-blind technique depends on the estimation of Point Spread Function (PSF), which should be priory known. Based on the PSF estimation, the input image will be restored. As we mentioned before, there are two types of non-blind techniques. First, the linear restoration methods, such as Weiner filter, Inverse filter, regularized filter and constrained least square filter. The second type is the non-linear type such as Lucy-Richardson algorithm restoration method.

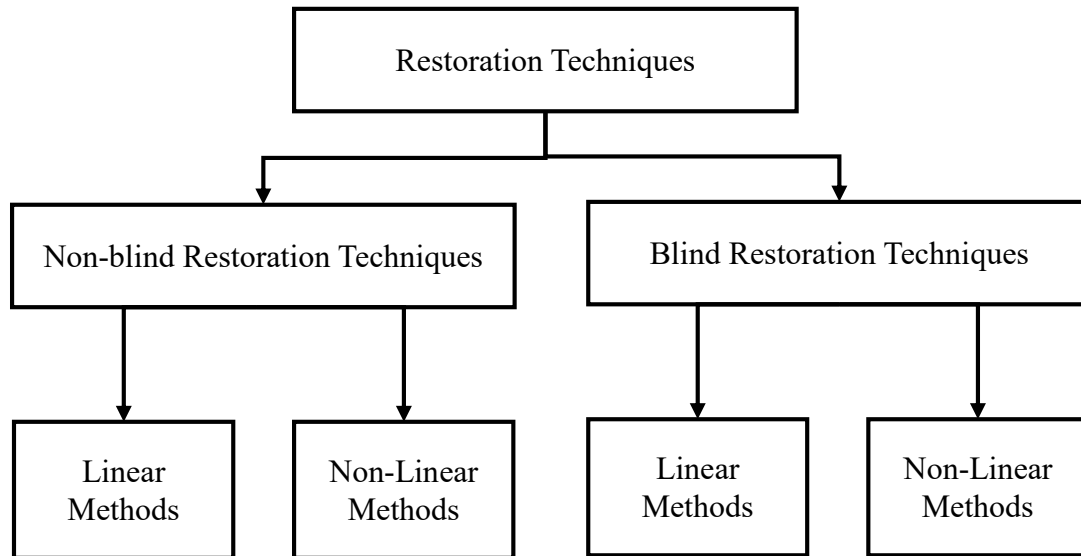


Figure 2.3: Classification of restoration techniques.

The general system design describing the image restoration process is represented in a block diagram given below in Figure 2.4.

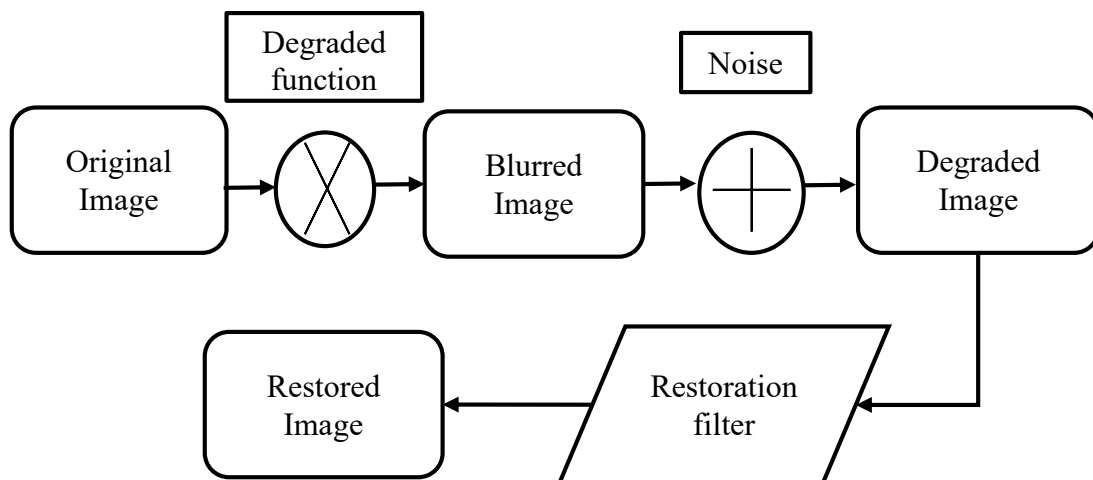


Figure 2.4: General block diagram for image restoration process.

2.2 Non-blind restoration techniques

In this section, we will describe briefly a number of non-blind restoration techniques for the case of blurred images when we have a prior knowledge about the PSF. In addition, we will illustrate a practical example for the performance of each technique.

2.2.1 Deconvolution using Lucy Richardson Algorithm

The first technique that we will describe and examine is the Lucy-Richardson algorithm. W.H. Richardson (1972) and L.B. Lucy (1974) have introduced together this procedure. Initially Leon Lucy and William Richardson derived it on the basis of the Bayesian theorem in the early 1970's [WHI94]. The Richardson-Lucy Algorithm (LRA), which is also known as Lucy-Richardson deconvolution, is an iterative technique for restoring a degraded image that has been distorted by a known point spread function.

The LRA can be used successfully if the PSF (blur kernel) is known, but limited or no information is given for the noise. The iterative and accelerated LRA repairs the blurred and noisy images. The additional optical system such as camera features can be used as input parameters to recover the quality of the image restoration.

The algorithm requires an appropriate estimation of the process by which the image was corrupted in order to assure an accurate restoration as much as possible. The degradation in the image can be in many ways and of many sources, such as subject movement, out-of-focus lenses, or atmospheric turbulence, and is been determined by the system PSF. We can represent the observed image pixels in terms of the degraded image and the PSF as follows:

$$d_i = \sum_j p_{ij} u_j \quad (2.2)$$

where p_{ij} is the PSF function (which is the light fraction that comes from a true location j , which is observed at a position i), u_j represent the pixel value at a location j in the degraded image, and d_i represent the observed value at location i .

The statistics are done under the consideration that u_j are Poisson distributed, which is relevant for photon noise distribution in the data. The main objective is to calculate the maximum likelihood estimation (MLE) for u_j with the presence of the observed d_i and the already known PSF p_{ij} as following:

$$u_j^{t+1} = u_j^t \sum_i \frac{d_i}{c_i} p_{ij} \quad (2.3)$$

with

$$c_i = \sum_j p_{ij} u_j^t \quad (2.4)$$

LRA is easy to implement, and it preserves edges due to its non-linearity, as it is a nonlinear method. Precisely, a big problem we face here is the noise amplification. When implementing a high number of L-R iterations on an image that may contain an extended object such as a galaxy, the extended emission usually develops a “Speckled” appearance [Bov09]. We present in Figure 2.5 the original image of Eiffel tower in gray level with dimensions of 256×256 pixels, the blurred image with atmospheric turbulence blurring with standard deviation of 5 and the deblurred resultant image obtained by Lucy-Richrdson method.

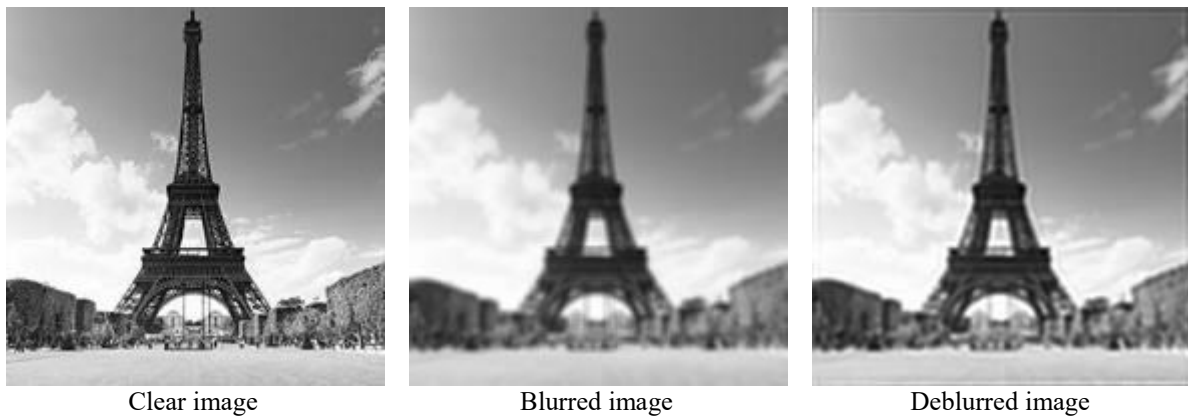


Figure 2.5: Deblurring using Lucy-Richardson method.

2.2.2 Deconvolution using inverse filter

The inverse filtering (IF) deconvolution is a restoration technique, i.e., if an image is blurred with a known low pass filter, the image can be restored using inverse filtering or generalized inverse filtering [Gon08]. In this technique, a Fourier transform estimate of the image $\hat{S}(u, v)$ is estimated by dividing the Fourier transform of the degraded image by the Fourier transform of the degradation function:

$$\hat{F}(u, v) = \frac{G(u, v)}{H(u, v)} \quad (2.5)$$

This technique will give a great result if the image was affected by blur effects only but not noise effects. However, if a noise was added to the blurred image then the result of the direct inverse filtering is very bad. Otherwise, the formula (2.5) will be,

$$\hat{F}(u, v) = F(u, v) + \frac{N(u, v)}{H(u, v)} \quad (2.6)$$

where $N(u, v)$ is usually unknown.

Sometimes, because of the fraction, we have to face the problem that the degradation function has zero or very small values. One way to solve the problem is to limit the filter frequencies to values near the origin, which is usually non-zero. Therefore, the probability of finding zero values will be diminished. In this experiment, we will center the Fourier transform of the original image, as well as the degradation function. The centered function is:

$$H(u, v) = e^{-k((M-u)^2 + (N-v)^2)^{\frac{5}{6}}} \quad (2.7)$$

where M and N are the size of the image.

Unfortunately, as the IF is a sort of high pass filter, inverse filtering reacts very badly in case of noise present in the image because the noise tends to be high frequency. Here we present in Figure 2.6 the original image of champs_élysées street in gray level with dimensions of 256×256 pixels, the blurred image with atmospheric turbulence blurring with standard deviation of 5 and the deblurred resultant image obtained by IF.



Figure 2.6: Deblurring by Inverse Filter.

2.2.3 Deconvolution using Wiener filter

In the 40's of the last century, Norbert Wiener has introduced the wiener deconvolution technique that was published in 1949. The Wiener technique is a non-blind deconvolution that rebuilds the degraded image with a previous knowledge of the PSF. The Wiener filter (WF) inverts the blur effect and at the same time removes the additive noise. It performs the deblur using invert technique as high pass filter and in the same time it eliminates noise with a compression operation as a low pass filter. The WF operates in the frequency domain; the goal is to minimize the influence of the noise at a poor signal to noise ratio frequencies. This

technique is based on recognizing images and noise as random operations. The goal is to find an appropriate estimate of \hat{f} for the original not degraded image f so that the mean square error between them is reduced. The WF is widely used in image deconvolution applications since the frequency spectrum can easily be estimated for the most of visual images. WF is one of the good methods to linear image restoration. It seeks an estimate \hat{f} that reduces the statistical error function:

$$e^2 = E\{(f - \hat{f})^2\} \quad (2.8)$$

where E is the expected value operator.

The solution to above expression in the frequency domain is:

$$\hat{F}(u, v) = \left[\frac{1}{H(u, v)} \frac{|H(u, v)|^2}{|H(u, v)|^2 + \frac{S_n(u, v)}{S_f(u, v)}} \right] G(u, v) \quad (2.9)$$

where $H(u, v)$ the degradation function, $S_n(u, v)$ the power spectrum of noise, $S_f(u, v)$ is the power spectrum of the original image and $G(u, v)$ is the degraded image.

We present in Figure 2.7 the original image of famous lena in gray level with dimensions of 256×256 pixels, the blurred image with atmospheric turbulence blurring with standard deviation of 5 and the deblurred resultant image obtained by WF. One of the major flaws of a WF is the mandatory for previous knowledge of power spectra for the original image and noise. In the case of random noise, it is difficult to estimate the typical restoration of the image.



Figure 2.7: Deblurring by Wiener filter.

2.2.4 Deconvolution using Regularized Filtering

Regularized filter (RF) is one of the non-blind convolution family, i.e. it de-blur an image with a prior knowledge of the blur function that blurred the image [Kau15]. This filter is considered an approximation for the WF, and it results with a close result to that of the Weiner filter. Anyway, the RF needs less information about the blurred function in order to restore the image. Regularized filtering is used in an effective way when few information is known about the additive noise. The RF uses constrained least square algorithm to restore the noisy and blurred image. It is usually classified as a discrete Laplacian filter. The RF is easy to implement and needs less information about the blurred function. However, it has to have a prior information about the blur function.

We present in Figure 2.8 the original image of famous barbara in gray level with dimensions of 256×256 pixels, the blurred image with atmospheric turbulence blurring with standard deviation of 5 and the deblurred resultant image obtained by RF.



Figure 2.8: Deblurring by Regularized Filter.

The RF is used in a better way when constraints like smoothness are applied on the recovered image and very less information is known about the additive noise. A constrained least-squares restoration algorithm that uses a RF regains the blurred and noisy image.

2.2.5 Deconvolution using Constrained Least-Squares Filtering

Constrained Least-Squares (CLS), is another non-blind method for image restoration, which was first introduced by Hunt [Hun73]. CLS is a linear image deconvolution method that maximizes the restored image smoothness subject to a constraint on the fidelity of the restored image. Constrained least squares estimation is a method that to solve the integral equations of the first kind. The problem of image restoration requires the solution of an integral equation of the first kind. However, applying the constrained least squares estimation to image restoration requires the solution of extremely large linear systems of equations. In the Wiener method, we use the power spectrum of the actual image and noise. In the CLS algorithm, we constrain the variation occurred in the image due to noise without actual knowledge of both power spectrums. The CLS method uses the Laplacian operator as a prior knowledge with decreasing the computational requirement by introducing the fast Fourier transform (FFT). The CLS restoration can be given by:

$$\hat{F}(u,v) = \left[\frac{1}{H(u,v)} \frac{|H(u,v)|^2}{|H(u,v)|^2 + \gamma |P(u,v)|^2} \right] G(u,v) \quad (2.10)$$

where, $\gamma = \frac{1}{\lambda}$ and λ is a Lagrange multiplier [Hun73], $P(u,v)$ represent the Fourier transform of the Laplacian filter:

$$p(x, y) = \begin{bmatrix} 0 & -1 & 0 \\ -1 & 4 & -1 \\ 0 & -1 & 0 \end{bmatrix} \quad (2.11)$$

The Fourier transform $P(u, v)$ has a great amplitude at high frequencies, where the noise tends to be dominant. Here the denominator will be modified in order to diminish the noise effects at high frequencies. Let $H(u, v)$ is the two-dimensional discrete Fourier transform of the degradation function $h(x, y)$ of the space-invariant degradation model, the corresponding constrained least-squares restoration filter $R_{CLS}(u, v)$ will be given as:

$$R_{CLS}(u, v) = \frac{1}{H(u, v)} \frac{|H(u, v)|^2}{|H(u, v)|^2 + \lambda |C(u, v)|^2} \quad (2.12)$$

where $C(u, v)$ is a high-pass filter and the parameter of regularization to managing the smoothness in the restored image [Gon08].

We present in Figure 2.9 the original image of peppers in gray level with dimensions of 256×256 pixels, the blurred image with atmospheric turbulence blurring with standard deviation of 5 and the deblurred resultant image obtained by CLS.



Figure 2.9: Deblurring by Constrained Least-Squares filter.

2.3 Blind Deconvolution Methods

In this section, we will describe the blind restoration methods for the case of blurred images. Blind deconvolution is a Blind technique of image restoration, which restore the blurred images without a prior knowledge of the PSF. In this deconvolution method, we allow the recovery of the degraded image from a single or set of infected images in the presence of a few or no

information about PSF. The first step in this method is to obtain an estimation of the blurring operator i.e. PSF and then using that estimate we will be able to deblur the image. Furthermore, the blind deconvolution method is a technique that could be executed iteratively as well as non-iteratively. In an iterative process, after each iteration, the estimation of the PSF will be improved and by using that estimated PSF, we can enhance the restored image repeatedly by bringing it as close as possible to the original image. In a non-iterative procedure, a single application of the algorithm on the base of exterior information will extract the PSF then this extracted PSF will be used to restore the original image from the degraded one.

2.3.1 Deconvolution using mean filter

The mean filter (MF) or the average linear filter [Nat13] is a nonlinear deconvolution method. In this technique, the filter calculates the average value of the corrupted image in a previously determined area, and then the center pixel intensity value is then replaced by that average value. This procedure is then repeated for all pixels in the degraded image. The algorithm is similar to the low pass filter algorithm.

The principal idea of this method is to deal with each pixel of the degraded image as following: It takes the pixel and the surrounded neighborhood pixels according to the window size that has been specified, then sums all the values and divide by the number of the elements. This is the average value; at last, the filter replaces the old pixel with the new average value and so on until all the pixels in the noisy image are replaced by the average value. The process now is completed; we have the filtered or resultant image. There are many types of mean filtering such as arithmetic, geometric, harmonic and contraharmonic mean filters. Information about these filters are given in the appendix (section 3.A). In Figure 2.10, we show the results for deblurring image of the Louvre using the different mean filters. The original image of Louvre is in gray level with dimensions of 256×256 pixels. The blurred image obtained using atmospheric turbulence with standard deviation of 5.

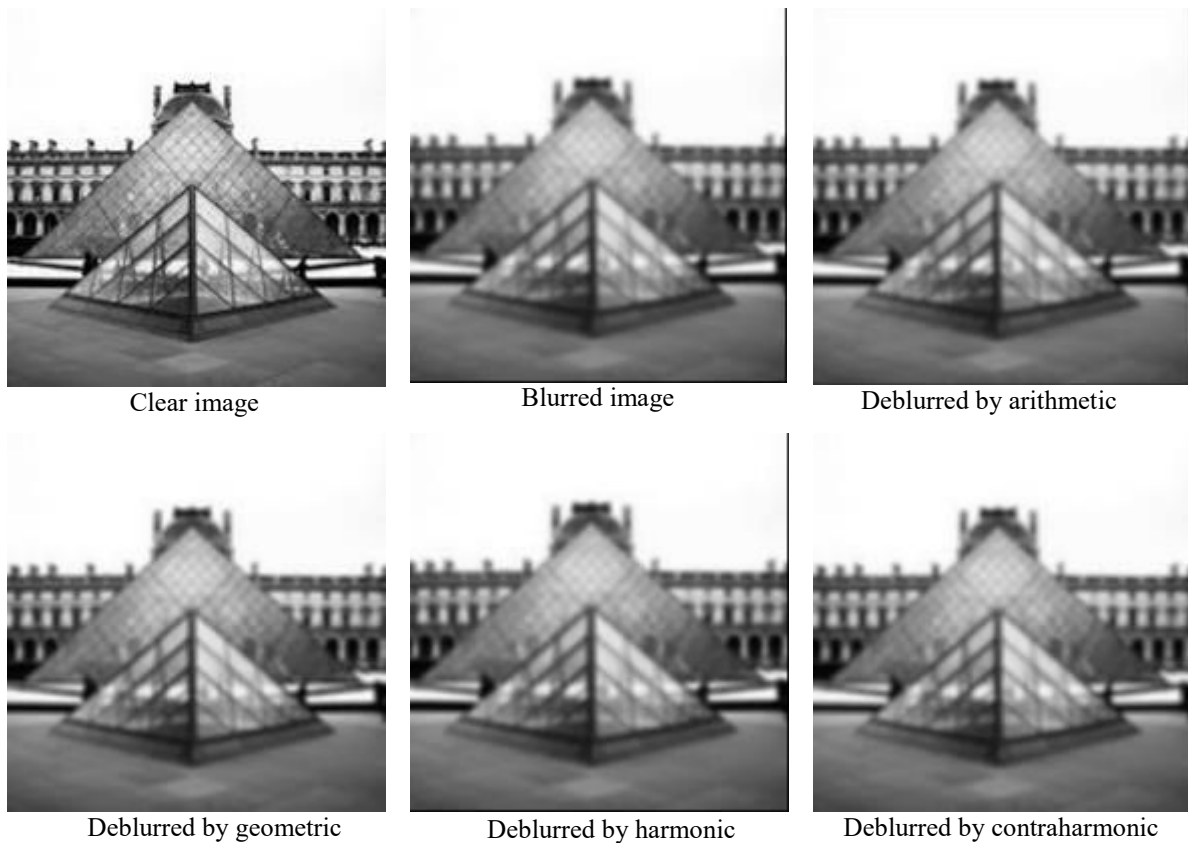


Figure 2.10: Deblurring by different mean filters.

In general, mean filtering has a simple algorithm and it is built easy but a single pixel value could fully affect the mean value of the average of the neighborhood pixels, which yields to a wrong value in the restored image pixel.

2.3.2 Deconvolution using Median filter

Median filtering (MeF) is a non-linear deconvolution broadly used to restore or smooth degraded images [Mah10][Zhu12]. The MeF is broadly used because it is very efficient at eliminating noise while preserving edges of the image. It is especially powerful at eliminating ‘salt and pepper’ type of noise. The MeF procedure is to move through the image pixel by pixel while replacing every value by the median value of neighboring pixels. The pattern of neighbors and its dimension is called the "window", which moves, pixel by pixel across the whole image. The median value is computed by sorting the values of each pixel within the median window into numerical order, after that, this middle (median) pixel value will be given to pixel under consideration.

When applying the MeF to grayscale images, which is a “neighborhood brightness-ranking algorithm”, it will arrange the brightness values of the pixels from every neighborhood in ascending order. The MeF will then choose the median value of that ordered sequence to be the

representative brightness value for that neighborhood. At the same time, every pixel in the restored image will be defined as the brightness median value of the related neighborhood in the original image [Ver13]. The MeF is the best-known “order-statistics” filter that works by replacing the pixel value by the median value of the gray levels in the neighborhood of that pixel:

$$\hat{f}(x, y) = \underset{(s,l) \in S_{xy}}{\text{median}}\{g(s, l)\} \quad (2.13)$$

The main difference between the MF and the MeF is that the original value of the pixel will be included in the MeF computation. The popularity of the MeF comes from its excellent restoration capabilities with less blurring than similar size linear smoothing filters. The MeF is effective mostly when both bipolar and unipolar impulse noises are present.

We present in Figure 2.11 the original image of centre Georges Pompidou in gray level with dimensions of 256×256 pixels, the blurred image with atmospheric turbulence blurring with standard deviation of 5 and the deblurred resultant image obtained by MeF.



Figure 2.11: Deblurring by Median filter.

2.3.3 Wavelet Deconvolution

The wavelet method is used widely in image processing fields' such as image compression, and in image restoration [Gup15]. Wavelet transforms are based on small waves, which are called wavelets. Wavelets, which means the little waves, such as Haar, Daubechies, Morlet, etc. are functions that are concentrated in the frequency domain and in time domain surrounding a fixed point. Wavelet transforms provide an efficient representation of the image by finely tuned to its intrinsic properties. By combining such representations with simple processing techniques in the transform domain, multiresolution analysis can accomplish remarkable performance and

efficiency for many image processing problems. We can summarize the method of restoration for an image by wavelet deconvolution technique into three main categories; wavelet transform or decomposition, threshold [Hed11], and lastly the noise removing (restoring) [Zho00]. The wavelet transform is computationally very fast and easy to perform. On the other hand, it is sensitive to every shift in frequency because the input-signal shifts produce unpredictable variations in the discrete wavelet transform (DWT) coefficients, further it requires the phase information that correctly represents non-stationary signal behavior.

Considering the estimation based on wavelet, the image f is usually represented in terms of an orthogonal wavelet expansion that provides a very sparse representation (some large coefficients and several very small ones). Let W express the DWT and let us write the image $f=W\theta$, where θ represent the vector of wavelet coefficients. Now, let us represent a maximum penalized likelihood estimator/maximum a posteriori (MPLE/MAP) criterion in terms of θ , the wavelet coefficients for the original image considering the likelihood function to be $p(g/\theta)$. Taking some penalty $pen(\theta)$ to emphasize sparsity of the DWT coefficients, the MPLE/MAP estimate is given by:

$$\hat{\theta} = \arg \max_{\theta} \{ \log p(g/\theta) - pen(\theta) \} \quad (2.14)$$

$$= \arg \max_{\theta} \left\{ -\frac{\|g - HW\theta\|^2}{2\sigma^2} - pen(\theta) \right\} \quad (2.15)$$

When $H=I$, which is considered for direct restoring problems, wavelet-based deconvolution is very effective due to the DWT fast implementations and to the orthogonality of (that is, $W^T W = W W^T = I$) which allows solving (2.14) using a coefficient-wise restoring rule; furthermore, these methods achieve state-of-the-art execution [Mih99][Mou99]. The superior performance of wavelet-based in image restoration is due to the adequacy of the underlying priors/models of real-world images. In spite of the fact that wavelets have shown effectiveness in image restoration problems [Ban96][Bel00], major obstacles arise, unlike H , which is block-circulant, HW is not block-circulant, i.e. it is not diagonalized by the discrete Fourier transform (DFT). Furthermore, HW is not orthogonal, unlike W , this will exclude the efficient coefficient-wise rules [Fig03].

We present in Figure 2.12 the original image of Henri Cartier Bresson foundation in gray level with dimensions of 256×256 pixels, the blurred image with atmospheric turbulence blurring with standard deviation of 5 and the deblurred resultant image obtained by DWT.

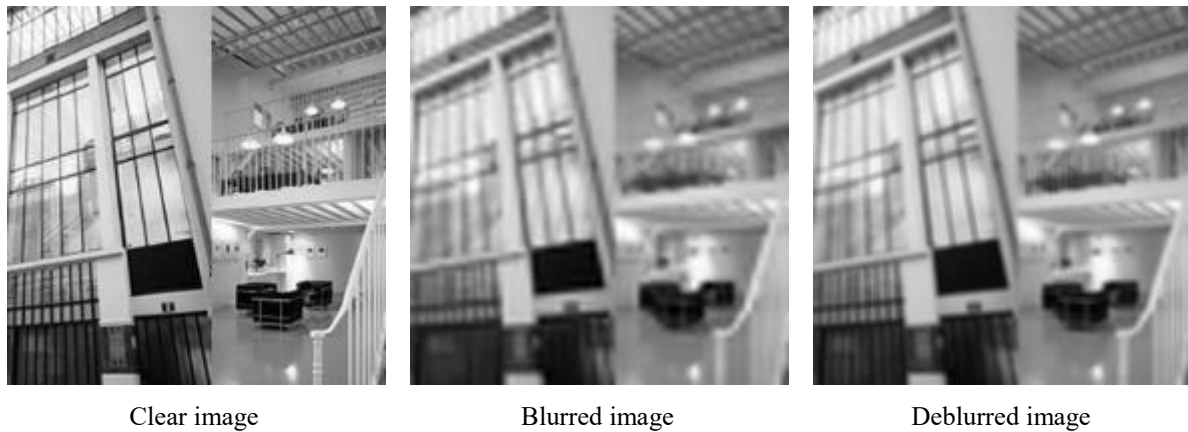


Figure 2.12: Deblurring by DWT filter.

2.3.4 Deconvolution using bilateral filter

The bilateral filter (BF) was firstly presented by Tomasi and Manduchi in 1998 [Tom98]. In addition, the BF concept was introduced as the SUSAN filter in [Smi97] and as the neighborhood filter in [Yar85]. The BF method is a non-iterative and non-linear image restoration algorithm that function in the spatial domain. It uses the spatial data and the intensity data between a point and its neighbors to restore the degraded images while well preserving the data in the edges. The BF is developed to achieve an important objective: to reduce noise while preserving the critical image details [Des15]. The BF algorithm is functioning on a register-transfer level. The unique feature of the BF design idea consists of changing the clock domain in a way, which assures the possibility of the kernel-based processing. That means the processing of the whole filter window at a one-pixel clock cycle. This characteristic of the kernel-based design is maintained by arranging the input data into groups in such a way that the internal clock of the design will be the multiple of the pixel clock specified by the targeted system. The BF deconvolution represents the concept of combining between both filtering methods domain and range. The domain filter functions as same as a low-pass filter since it computes the average of the nearby pixel values. The range filter plays the part of the non-linear filtering that has an important role in edge preserving. This combination provides averaging for only the similar pixel values, notwithstanding of their location in the filter window. If the pixel value in the filter window has diverged from the pixel value that been filtered by a particular value, then it will be skipped. Mathematically, given a pixel located at (x, y) which will be restored in a degraded image using its neighboring pixels, and the location of one of its neighboring pixels is at (s, l) then, the output of a BF is computed as follows:

$$\hat{f}(x, y) = \frac{1}{C} \sum_{(s, l) \in S_{xy}} e^{-\frac{(x-s)^2 + (y-l)^2}{2\sigma_d^2} - \frac{\|f(x, y) - f(s, l)\|^2}{2\sigma_r^2}} f(s, l) \quad (2.16)$$

where σ_d and σ_r are smoothing parameters controlling the fall-off of weights in spatial and intensity domains, respectively, S_{xy} is a spatial neighborhood, $f(x, y)$ and $f(s, l)$ are the intensity of pixels (x, y) and (s, l) respectively, and C is the normalization constant:

$$C = \sum_{(s, l) \in S_{xy}} e^{-\frac{(x-s)^2 + (y-l)^2}{2\sigma_d^2} - \frac{\|f(x, y) - f(s, l)\|^2}{2\sigma_r^2}} \quad (2.17)$$

When the intensity domain parameter σ_r increases, the BF approaches gradually Gaussian convolution more closely because the Gaussian range widens and flattens, which indicates that it becomes almost constant over the intensity interval of the image. As the spatial domain σ_d increases, the larger components are smoothed.

We present in Figure 2.13 the original image of Manufacture des Gobelins in gray level with dimensions of 256×256 pixels, the blurred image with atmospheric turbulence blurring with standard deviation of 5 and the deblurred resultant image obtained by BF.



Figure 2.13: Deblurring by bilateral filter.

The filter has been used for many applications such as texture removal, dynamic range compression, and photograph enhancement. The BF is a powerful method in removing high-density noise from the noisy images. On the other hand, it has a limited effect on the salt and pepper noise.

2.3.5 Deconvolution using Adaptive Local Filter

Adaptive local filter (ALF) [Ran14] is another type of blind filters, which is used to restore the degraded images that contain data of the original images affected by noise and/or blur. The restoration procedure in this filter rely on two statistical measurements mean and variance, using a specific $m \times n$ window:

$$\hat{f}(x, y) = g(x, y) - \left(\frac{\sigma_n^2}{\sigma_l^2} \right) [g(x, y) - m_l] \quad (2.18)$$

where, σ_n^2 , m_l , σ_l^2 , $g(x, y)$ and $\hat{f}(x, y)$ are respectively the local variance of the local region, the local mean, the variance of overall noise, the pixel value at the position (x, y) and the restored value.

The ALF is easy to implement and fast. However, it has weak results due to its slow convergence.

We present in Figure 2.14 the original image of Manufacture des Gobelins in gray level with dimensions of 256×256 pixels, the blurred image with atmospheric turbulence blurring with standard deviation of 5 and the deblurred resultant image obtained by ALF.

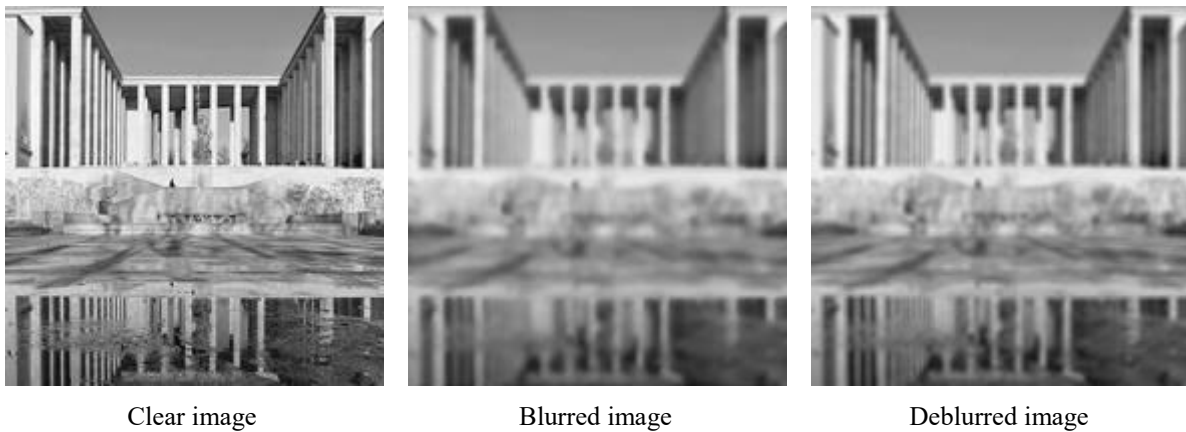


Figure 2.14: Deblurring by adaptive local filter.

2.4 Proposed method to restore the Sentinel images

Sentinel satellite images are very important in many applications as we mentioned before. However, these images are subject to quality reduction due to the effects of noise and blur in the stage of acquiring or transferring. Our objective in this section is to propose a new method to restore the sentinel satellite images based on combination techniques. The process of combining two or more images into a single image while retaining the important features of each image is called image fusion. In this section, the filtered images from the two different smoothing algorithms, the blind and non-blind, are fused to obtain a high quality restored image. Our method [Mar16] is to combine the image restored from the non-blind deconvolution method that has the best metrics results among the other non-blind deconvolution methods, with the best result of the same image restored by blind deconvolution in order to improve the quality of the restored image. We will use a combination method, to combine a two of resultant images and obtain an image that is better, this method called image fusion [Ufa12]. Image fusion [Cho14][Zho99] has several types such as the high pass filtering, which is the classic method. Other modern methods exist such as: fusion based on Laplacian pyramid, uniform rational filter bank, and discrete wavelet transform. We will implement the combination using fusion based on DWT [Sin13]. The process of the fusion method is illustrated in Figure 2.15. The effective work in the wavelet based image fusion is to combine the coefficients, in other words, is to find the most convenient way to integrate the coefficients in such a way to have the best quality of the fused image. There are many ways to achieve this goal; the simplest way is to calculate the average of the coefficients to be integrated [Paj04].

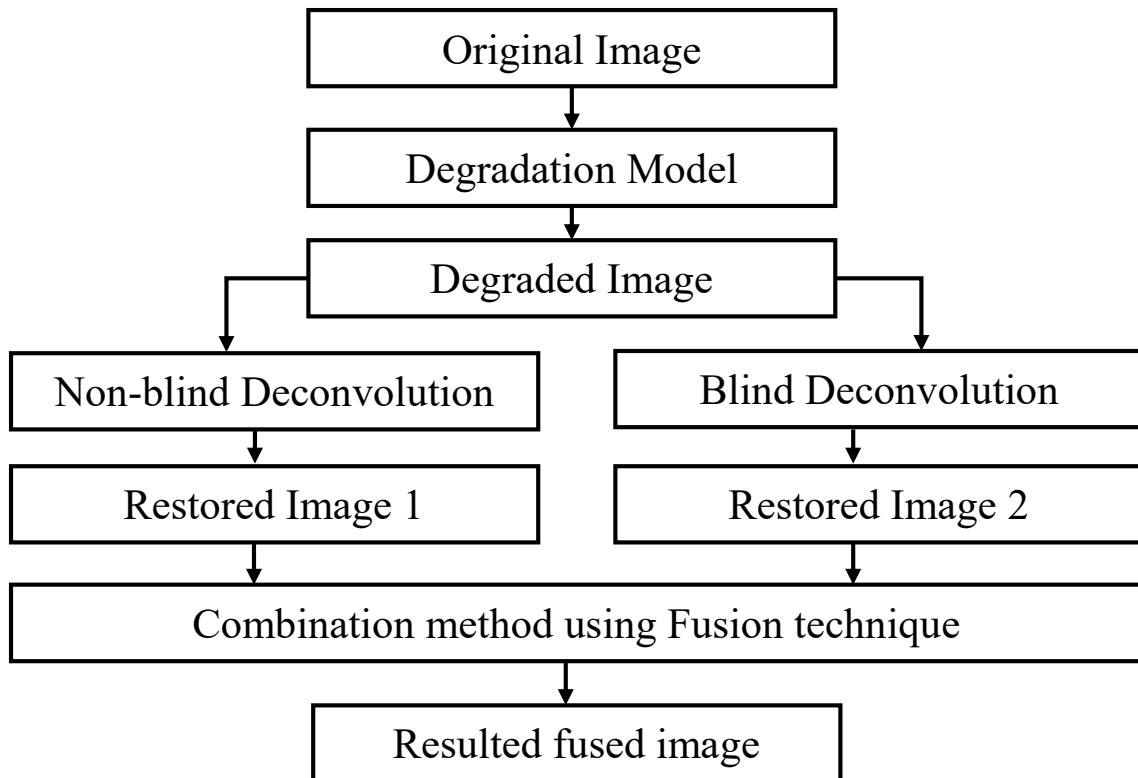


Figure 2.15: Proposed method for image restoration diagram.

2.4.1 Result Analysis

In order to show the effectiveness of our proposed method, we chose the satellite images and more particularly the sentinel images described in chapter 1 as the field of application. Satellite images are usually degraded by noise during image acquisition and transmission process. In the last several decades, numerous approaches for satellite image restoration has been proposed [Zha12][Gup15]. In this section, we will apply the proposed method [Bas16] to solve the problem of degraded sentinel images. The effectiveness of our method is illustrated by simulating the actual procedure of remote sensing satellite image restoration. We will use three Sentinel satellite images, given in figures 2.16, 2.22 and 2.30.

The first image in Figure 2.16 is obtained from sentinel-1 satellite. The original image “Radar image of the Netherlands” shown in Figure 2.16 is obtained from the site [URL14]. This image was acquired on 15 April with the radar operating in ‘strip map mode’, which provides coverage at a resolution of about 10 m. This image over the west coast of the Netherlands is one of the early radar scans by the Sentinel-1A satellite. In the sake of time conserving, we edited the dimensions of the image to be 512×898 pixels instead of the original 8811×14452 pixels. The second image shown in Figure 2.22 is obtained from sentinel-2 satellite. The original image of “Toulouse” shown in Figure 2.22 is obtained from the site [URL17]. The

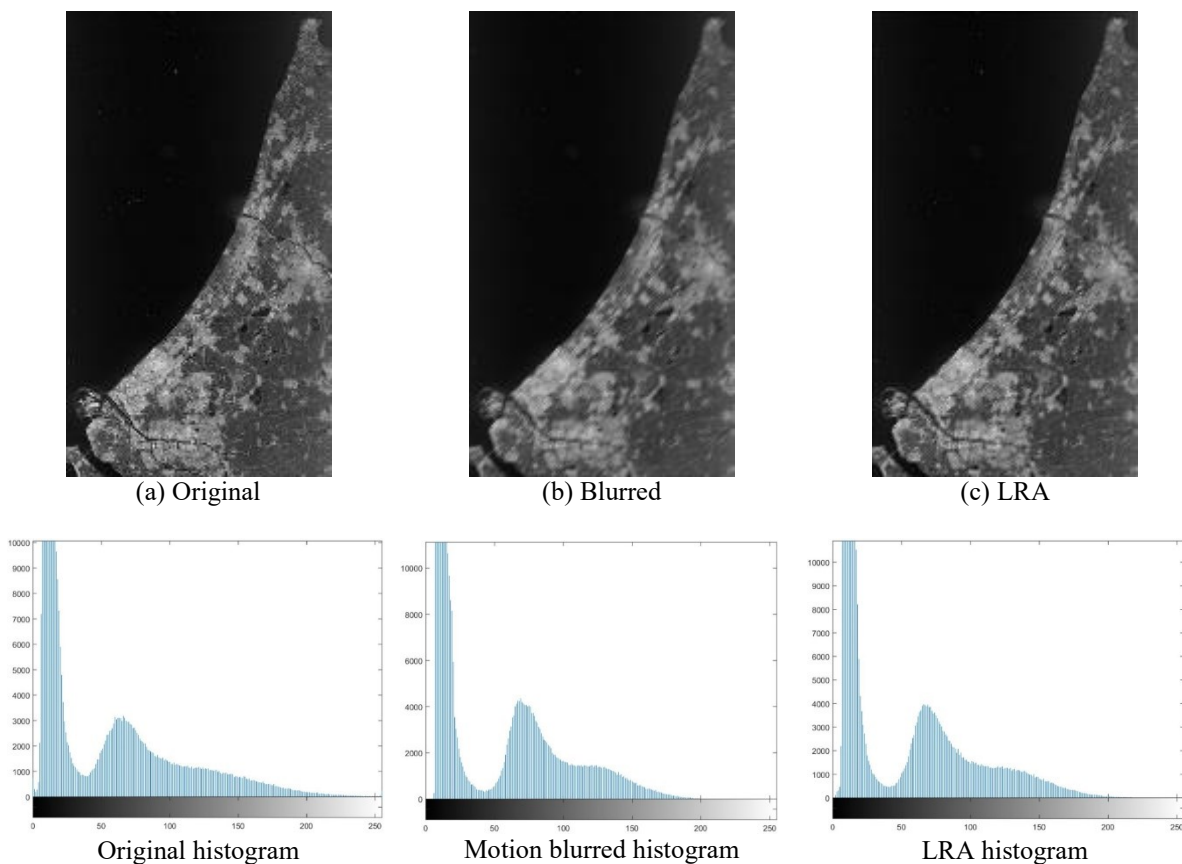
Copernicus Sentinel-2A satellite takes us over Toulouse in southern France and the surrounding agricultural landscape. Positioned on the banks of the River Garonne, the city is in France and it is the fourth largest. It is nicknamed the Ville Rose – pink city – owing to the color of the terracotta bricks commonly used in the local architecture. Even from space, the pinkish tint from the terracotta roof tiles is evident. In the upper left, we can see the runways of the Toulouse-Blagnac airport. The air route to the Paris Orly airport is one of the busiest in Europe. Fields blanketing the countryside dominate the image. In fact, France is the EU's leading agricultural power and is home to about a third of all agricultural land within the EU. While agriculture brings benefits for economy and food security, it puts the environment under pressure. Satellites can help to map and monitor land use, and the information they provide can be used to improve agricultural practices. This image was captured on 10 July 2017 by Sentinel-2's multispectral camera. Sentinel-2 is designed to provide images that can be used to distinguish between different crop types as well as data on numerous plant indices, such as leaf area, leaf chlorophyll and leaf water – all essential to monitor plant growth accurately. In the sake of time conserving we edited the dimensions of the image to be 512×427 pixels instead of the original 1920×1601 pixels. The third image shown in Figure 2.30 is obtained from sentinel-2 satellite. The original image “Southeast France”, shown in Figure 2.30, is obtained from the site [URL18]. “This Sentinel-1 radar image captures a stretch of southeast France, from the city of Lyon on the left to the Alps on the right the northeast part of the Auvergne-Rhone-Alps region. The image is made up of three satellite acquisitions from 13 July, 12 August and 11 September 2017 to highlight any changes on the ground. Grey tones, where there are mountains, towns for example depict no change, but red, green, and blue tones indicate where vegetation has changed as summer progressed. The highest mountain in the Alps, Mont Blanc, which is on the French–Italian border, is featured a little below half way down the right side of the image. To the north of the Alps, part of Lake Geneva can be seen with the Swiss city of Geneva at southwestern end of the lake. Further south and slightly west of the Alps, Lake Annecy and Lake Bourget are visible. To the west of these lakes the land gives way to gentle valleys with Lyon featured on the left side of the image”. The dimensions of the image “Southeast France” are 910×512 pixels. In our work, we used the software Matlab[®] 2015a. The window size for the mean and median filters were 3×3 . The DWT filter was single-level 2-D wavelet decomposition with respect to the wavelet Daubechies. In the bilateral filter, the spatial domain control parameter $\sigma_d = 3$ and the intensity domain control parameter $\sigma_r = 0.2$.

2.4.1.1 Blur reduction in satellite images

In this section we will test the behavior of the deconvolution techniques in deblurring the images in the case of blur only and no noise existing. The blur process is done with three PSF functions as mentioned before. Then after the deconvolution of the blurred image with the deconvolution techniques, we will choose the best result from the blind deconvolution techniques and the best result from the non-blind deconvolution techniques and propose the combination method of the two images in order to get a restored image with a better quality.

2.4.1.1.a Motion blur case

In this section, we will simulate the “Radar image of the Netherlands” with motion blur. We present in the Figures 2.16 (a), (b) and 2.17 (a), (b), the original “Radar image of the Netherlands” image and the corrupted image by linear motion blur with $L=20$ pixels and $\theta=45^\circ$ respectively. After that, we will deblur the blurred image using the blind and non-blind deconvolution methods. The final step will be to implement our proposed method by combining the best image resulted from the non-blind convolution methods with the best one obtained from the blind convolution methods by the fusion technique.



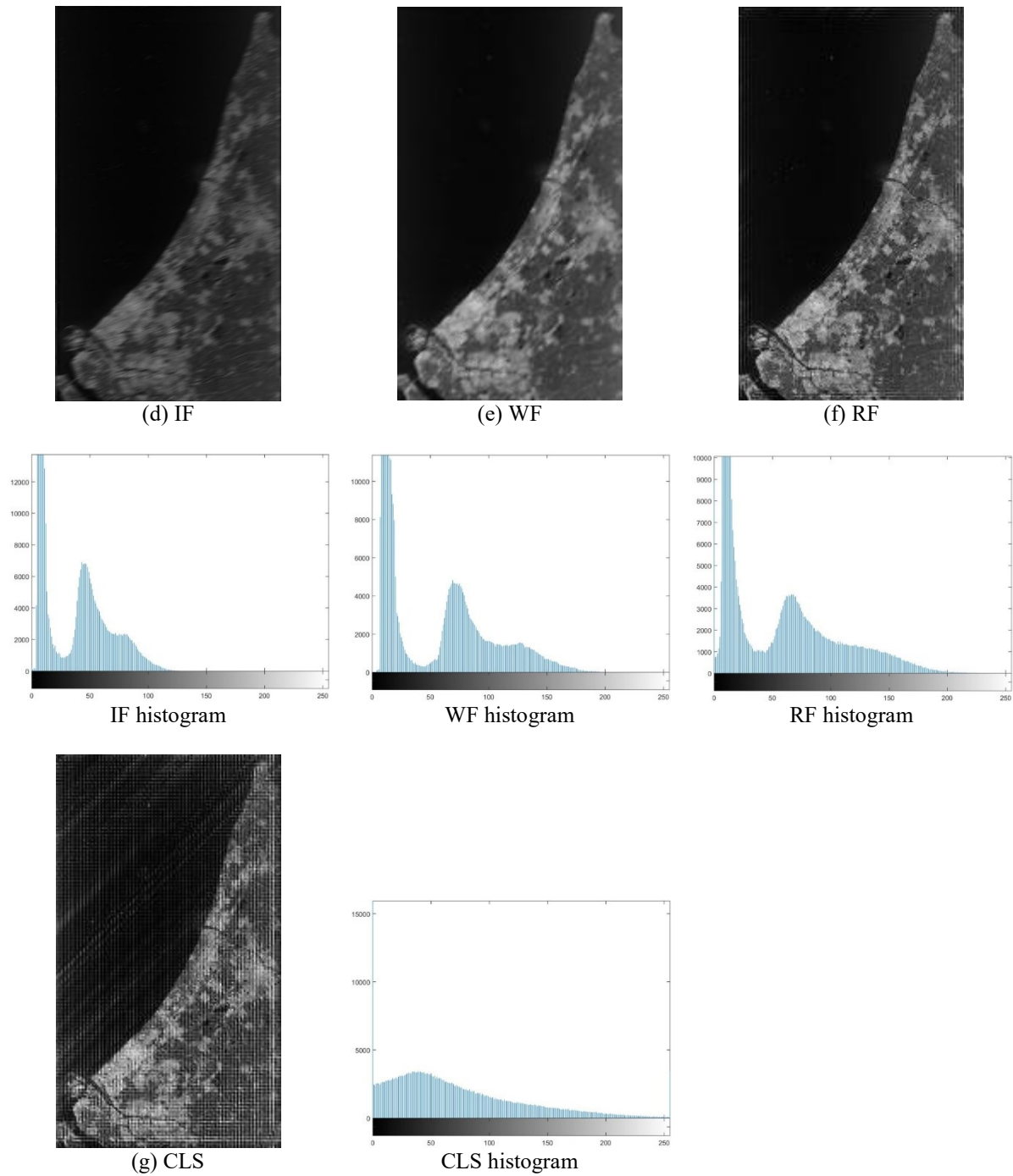
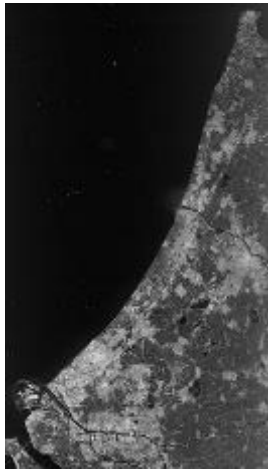
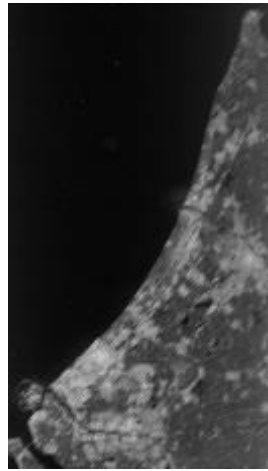


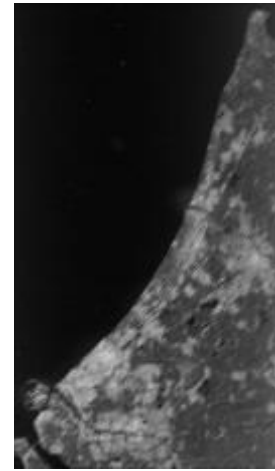
Figure 2.16: The resultant deblurred images by the non-blind deconvolution methods and the corresponding histogram for each deblurred image, for the motion blur case.



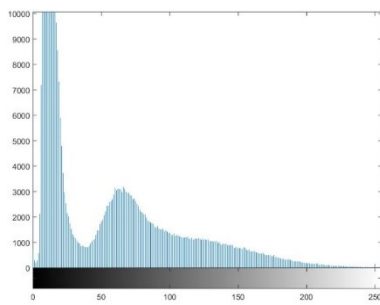
(a) original



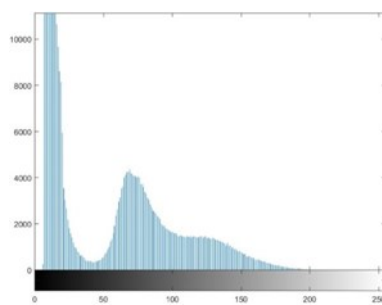
(b) Blurred



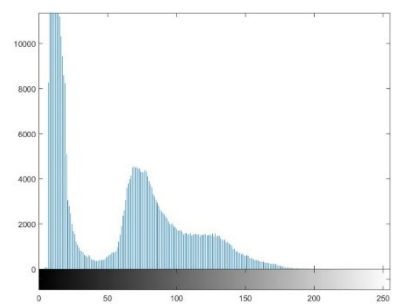
(c) AMF



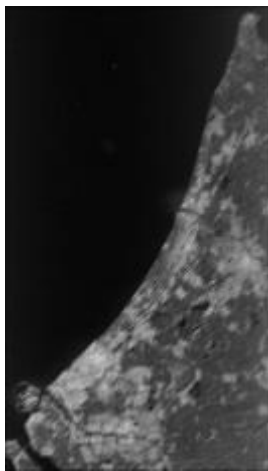
Original histogram



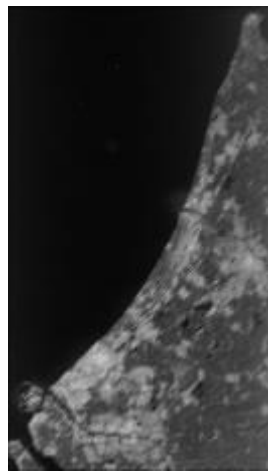
Motion blurred histogram



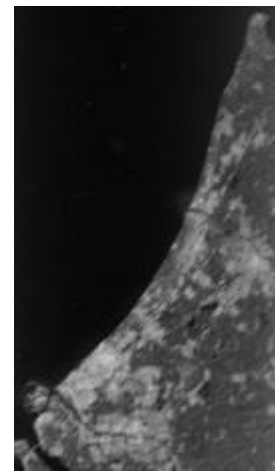
AMF histogram



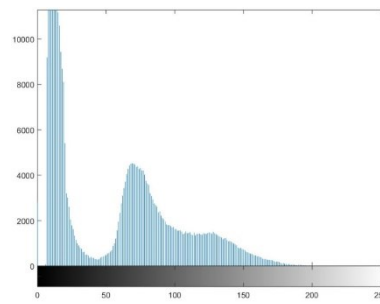
(d) GMF



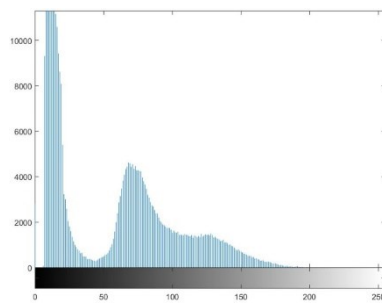
(e) HMF



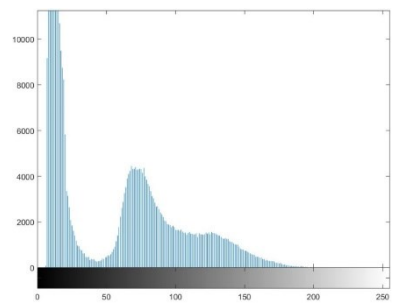
(f) CHMF



GMF histogram



HMF histogram



CHMF histogram

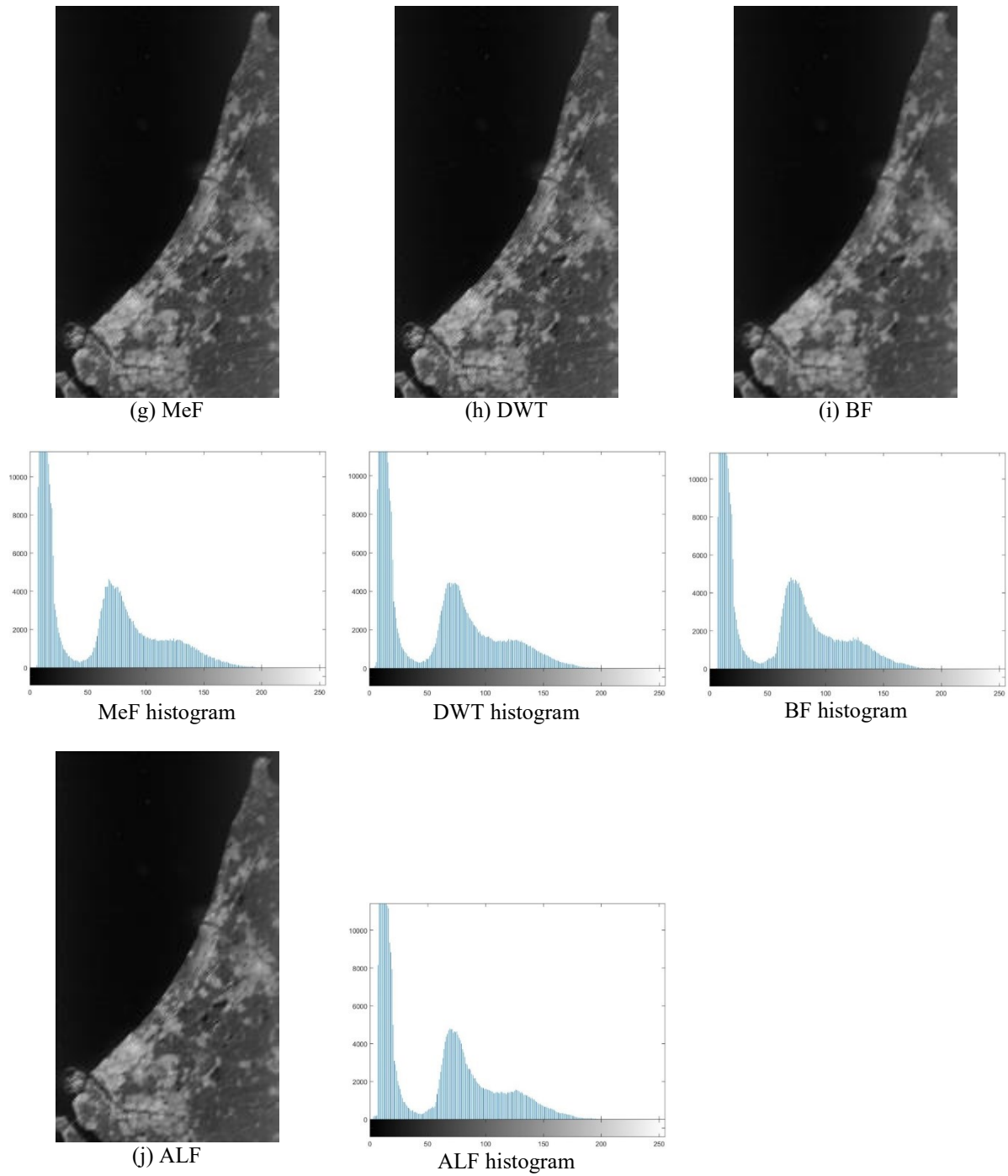


Figure 2.17: The resultant deblurred images by the blind deconvolution methods, and the corresponding histogram for each deblurred image, for the motion blur case.

Table 2.1: The resultant metrics of the deblurred by non-blind deconvolution methods for the motion blur case.

Netherlands	ISNR	RMSE	PSNR
LRA	1.22	17.84	23.07
IF	0.41	33.69	17.55
WF	0.93	20.45	21.88
RF	0.85	21.40	21.49
CLS	0.25	39.04	16.27

Table 2.2: The resultant metrics of the deblurred by blind deconvolution methods for the motion blur case.

Netherlands	ISNR	RMSE	PSNR
AMF	0.82	22.80	20.94
GMF	0.88	21.04	21.64
HMF	0.87	21.09	21.62
CHMF	0.92	20.54	21.85
MeF	0.95	20.14	22.02
DWT	0.91	20.63	21.81
BF	0.94	21.09	21.62
ALF	0.84	21.26	21.55

Regarding the results shown in Figure 2.16 and in Table 2.1 we can see that the LRA has shown the best results in visual and metrics, whereas the CLS has shown the worst results obtained among the rest non-blind methods introduced. Regarding the results shown in Figure 2.17 and in Table 2.2 we can see that the MeF has shown the best results in visual and metrics, whereas the AMF has shown the worst results obtained among the rest blind methods.

2.4.1.1.b Out of focus blur case

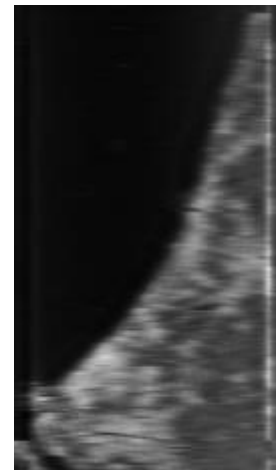
In this section, we will simulate the “Radar image of the Netherlands” with out of focus blur with $r=45^\circ$. We present in Figures 2.18 (a), (b) and 2.19 (a), (b), the original “Radar image of the Netherlands” and the corrupted image by the out of focus blur with $r=45^\circ$ respectively. After that, we will deblur the blurred image using the blind and non-blind deconvolution methods. The final step will be to implement our proposed method by combining the best image resulted from the non-blind convolution methods with the best one obtained from the blind convolution methods by the fusion technique.



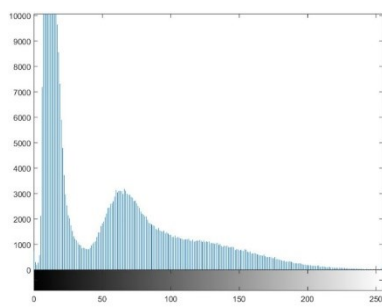
(a) original



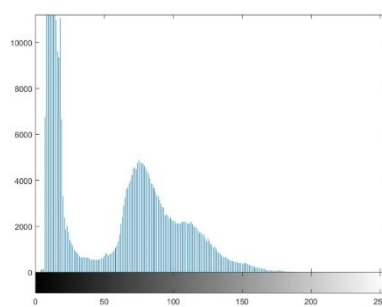
(b) Blurred



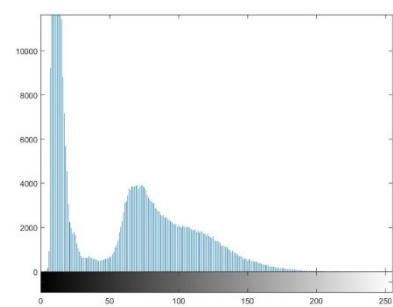
(c) LRA



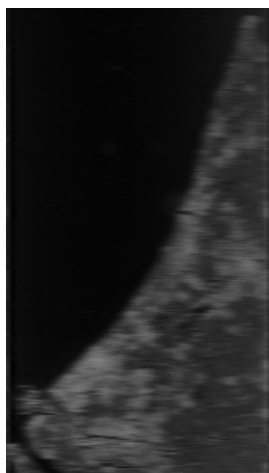
Original histogram



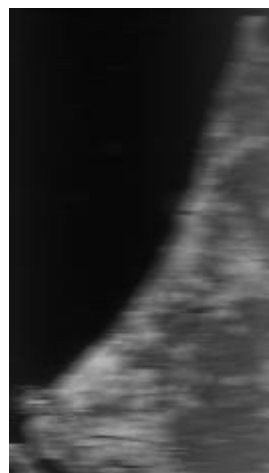
Out of focus blurred histogram



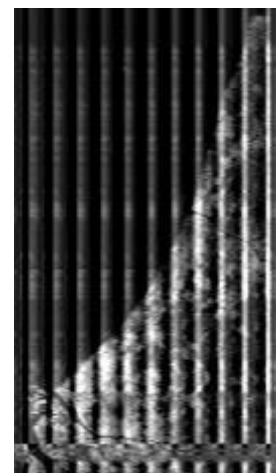
LRA histogram



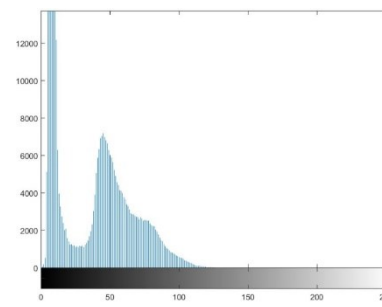
(d) IF



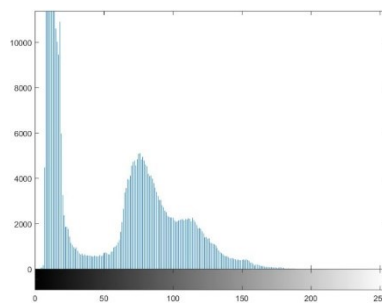
(e) WF



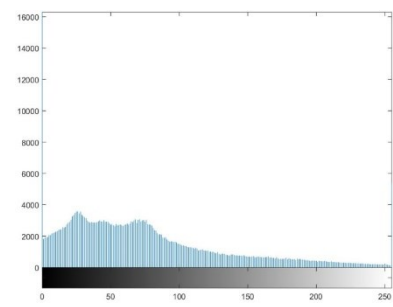
(f) RF



IF histogram



WF histogram



RF histogram

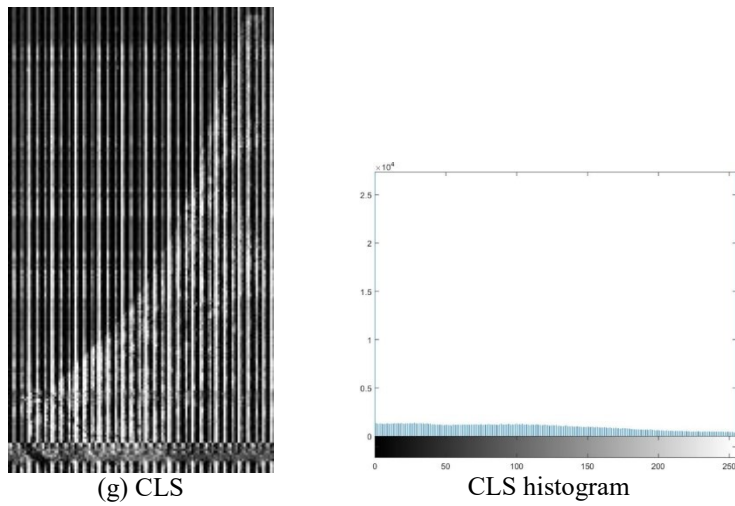
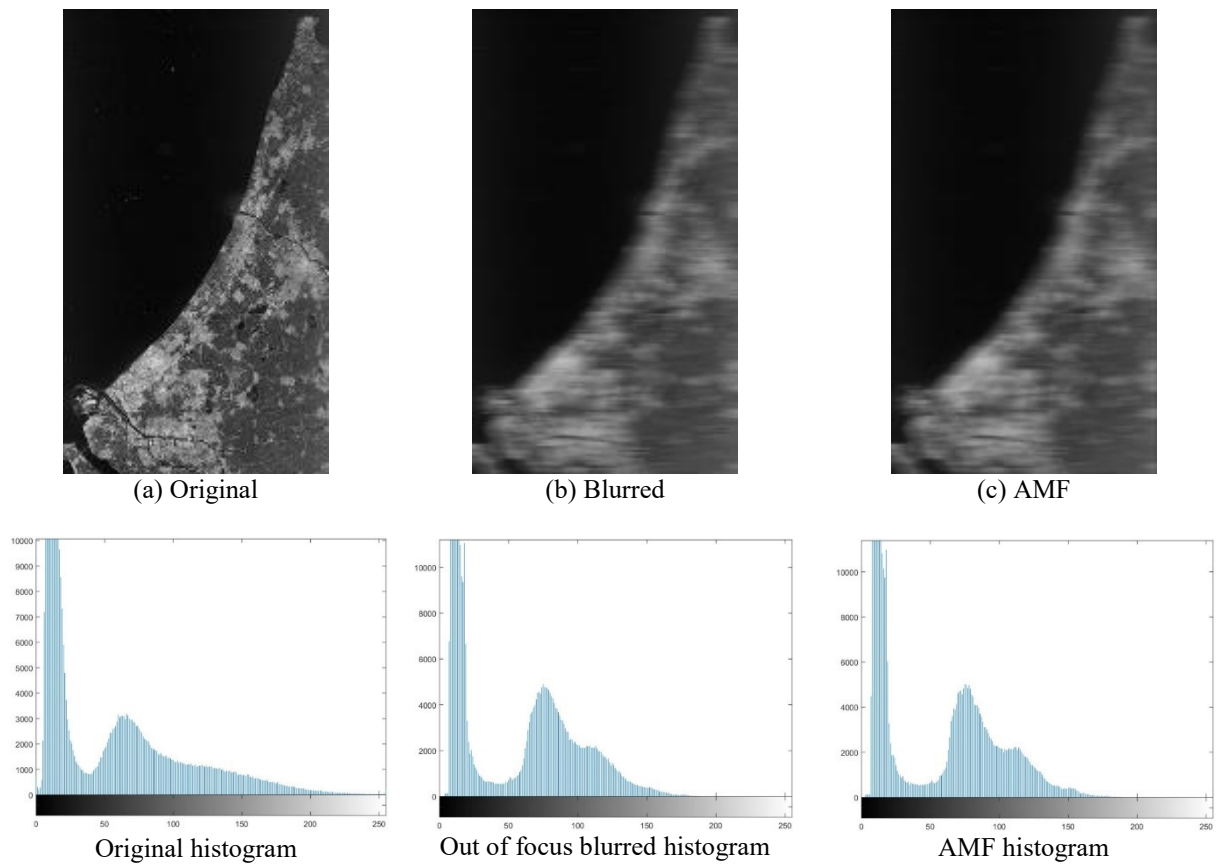
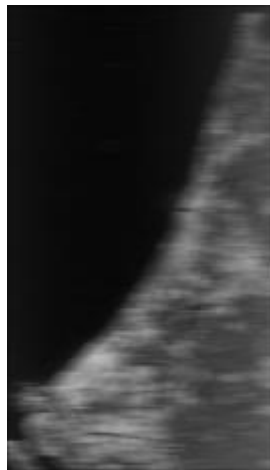


Figure 2.18: The resultant deblurred images by the non-blind deconvolution methods, and the corresponding histogram for each deblurred image, for the out of focus blur case.

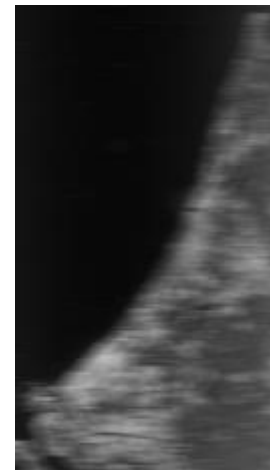




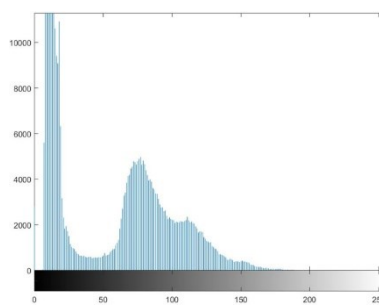
(d) GMF



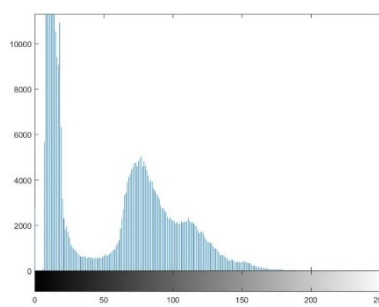
(e) HMF



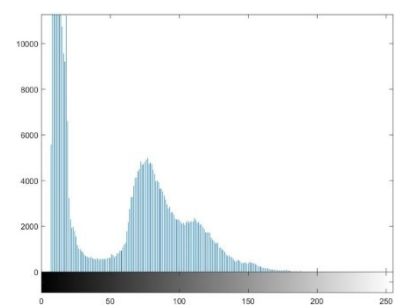
(f) CHMF



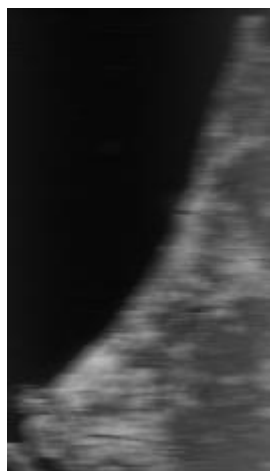
GMF histogram



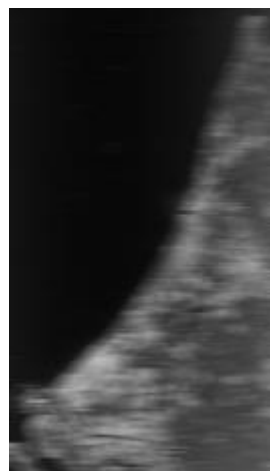
HMF histogram



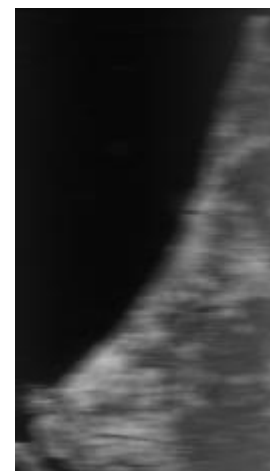
CHMF histogram



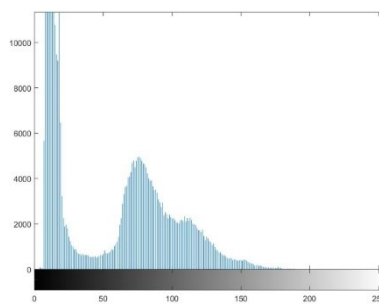
(g) MeF



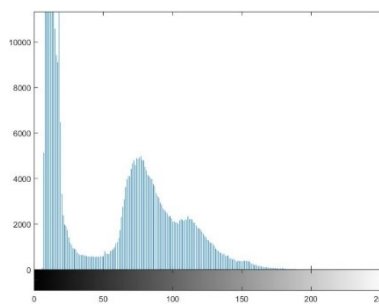
(h) DWT



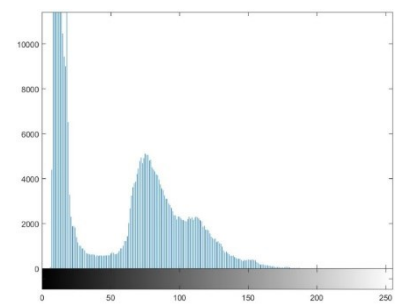
(i) BF



MeF histogram



DWT histogram



BF histogram

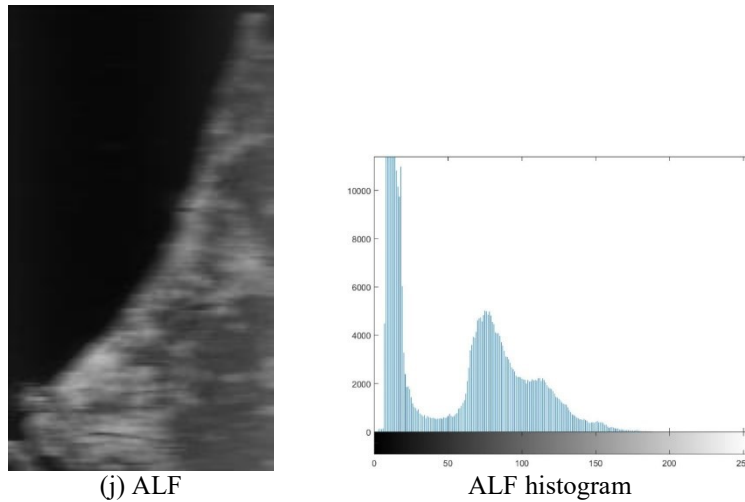


Figure 2.19: The resultant deblurred images by the blind deconvolution methods, and the corresponding histogram for each deblurred image, for the out of focus blur case.

Table 2.3: The resultant metrics of the deblurred by non-blind deconvolution methods, for the out of focus blur case.

Netherlands	ISNR	RMSE	PSNR
LRA	1.25	24.13	20.45
IF	0.48	34.32	17.39
WF	0.95	25.38	19.92
RF	0.22	25.53	19.96
CLS	0.07	94.30	8.61

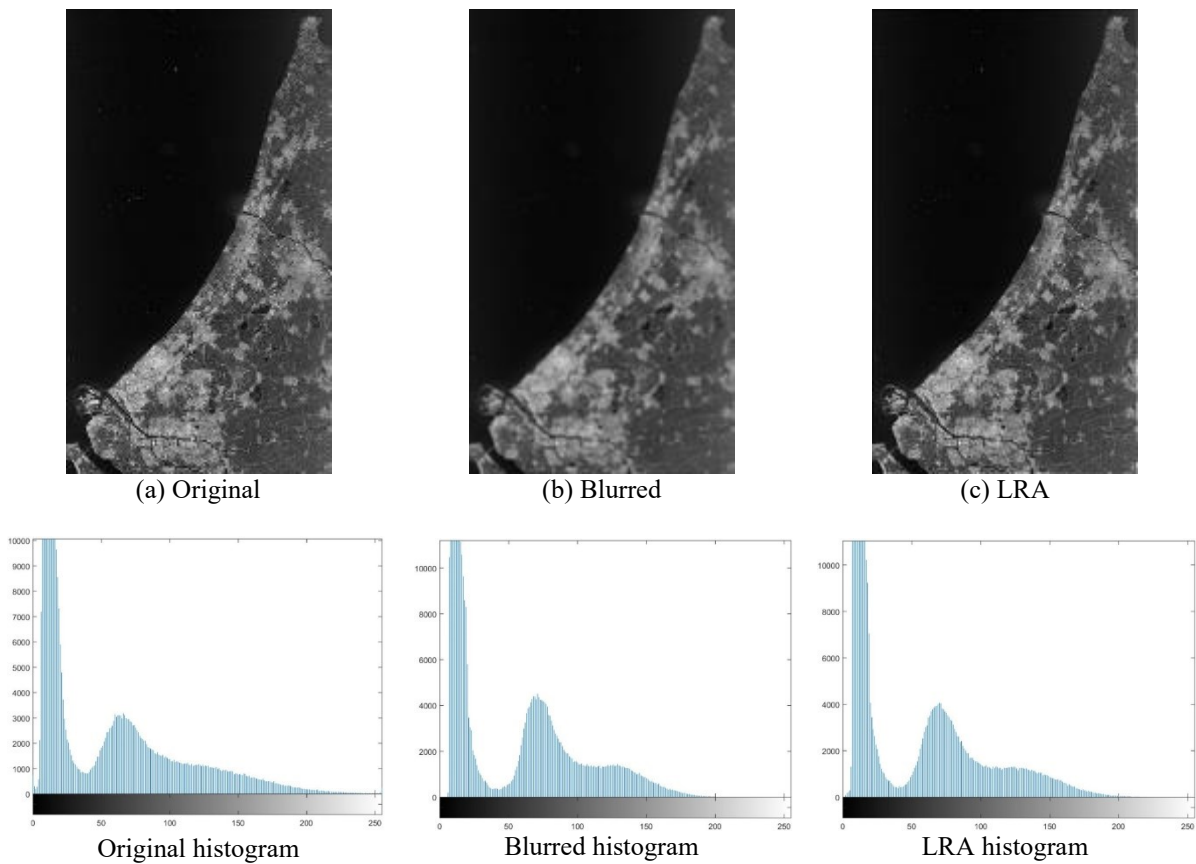
Table 2.4: The resultant metrics of the deblurred by blind deconvolution methods, for the out of focus blur case.

Netherlands	ISNR	RMSE	PSNR
AMF	0.94	29.41	18.73
GMF	0.96	25.85	19.85
HMF	0.95	25.88	19.84
CHMF	0.98	25.38	20.01
MeF	0.89	25.26	20.05
DWT	1.35	23.93	20.52
BF	0.97	25.44	19.99
ALF	0.85	25.88	19.84

Regarding the results shown in the Figure 2.18 and in the Table 2.3 we can see that the LRA has shown the best results in visual and metrics, whereas the CLS has shown the worst results obtained among the rest non-blind methods introduced. Regarding the results shown in the Figure 2.19 and in the Table 2.4 we can see that the DWT has shown the best results in visual and metrics, whereas the AMF has shown the worst results obtained among the rest blind methods introduced.

2.4.1.1.c Atmospheric turbulence blur case

In this section, we will simulate the “Radar image of the Netherlands” image with atmospheric turbulence blur with $\sigma^2=5$. We present in Figures 2.20 (a), (b) and 2.21 (a), (b), the original “Radar image of the Netherlands” image and the corrupted image by the atmospheric turbulence blur with $\sigma^2=5$ respectively. After that, we will deblur the blurred image using the blind and non-blind deconvolution methods. The final step will be to implement our proposed method by combining the best image resulted from the non-blind convolution methods with the best one obtained from the blind convolution methods by the fusion technique.



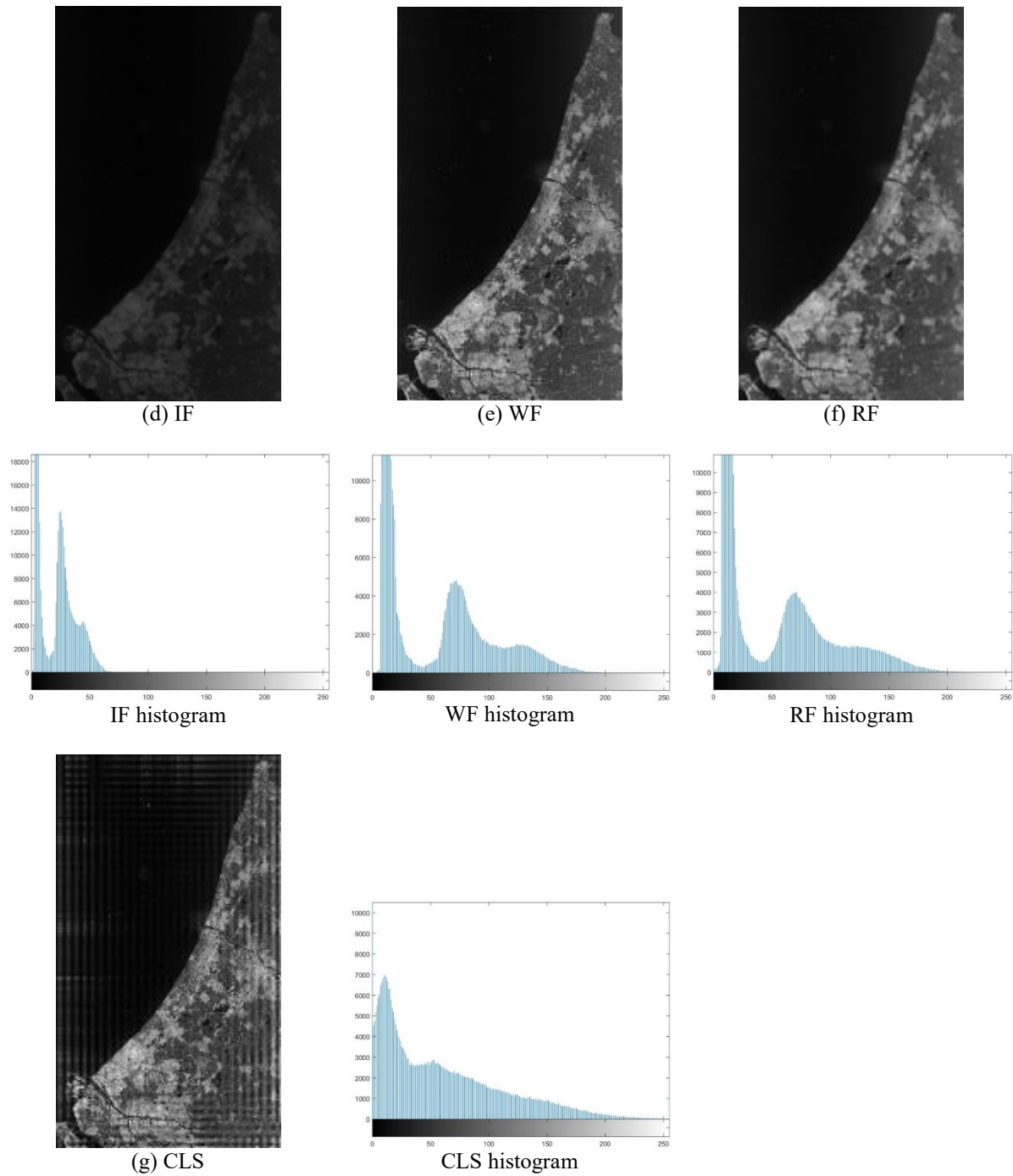
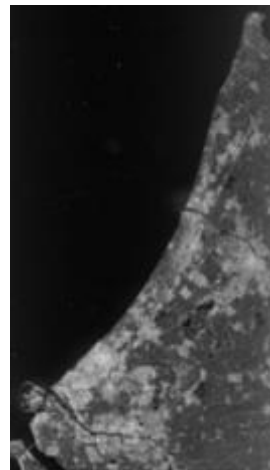


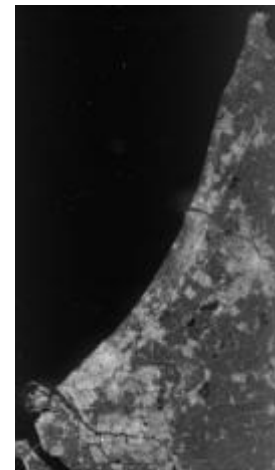
Figure 2.20: The resultant deblurred images by the non-blind deconvolution methods and the corresponding histogram for each deblurred image, for the atmospheric turbulence blur case.



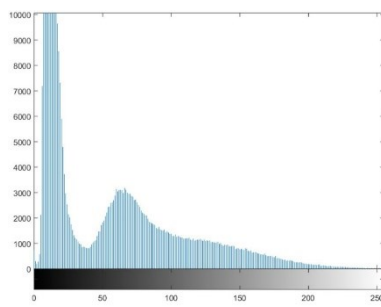
(a) Original



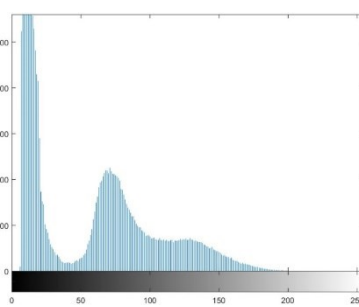
(b) Blurred



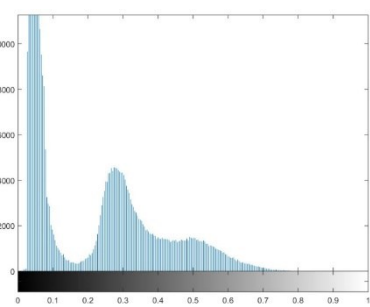
(c) AMF



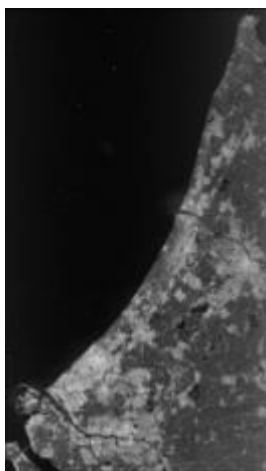
Original histogram



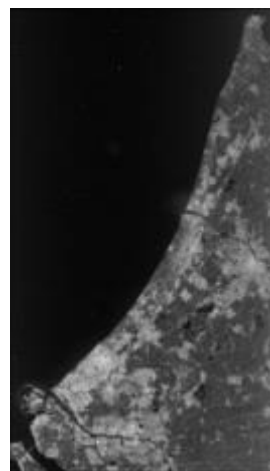
Blurred histogram



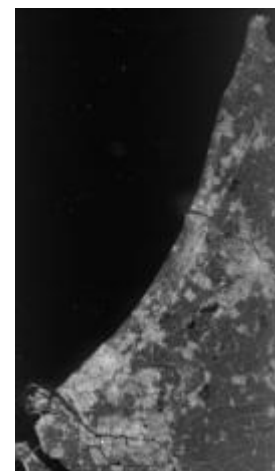
AMF histogram



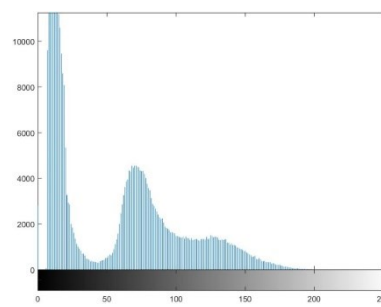
(d) GMF



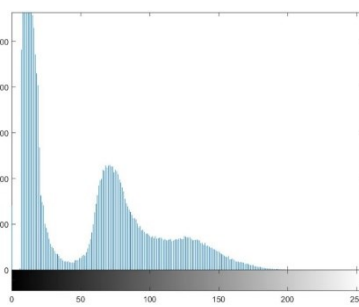
(e) HMF



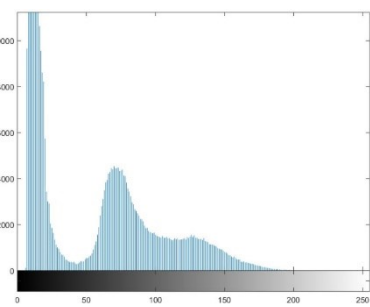
(f) CHMF



GMF histogram



HMF histogram



CHMF histogram

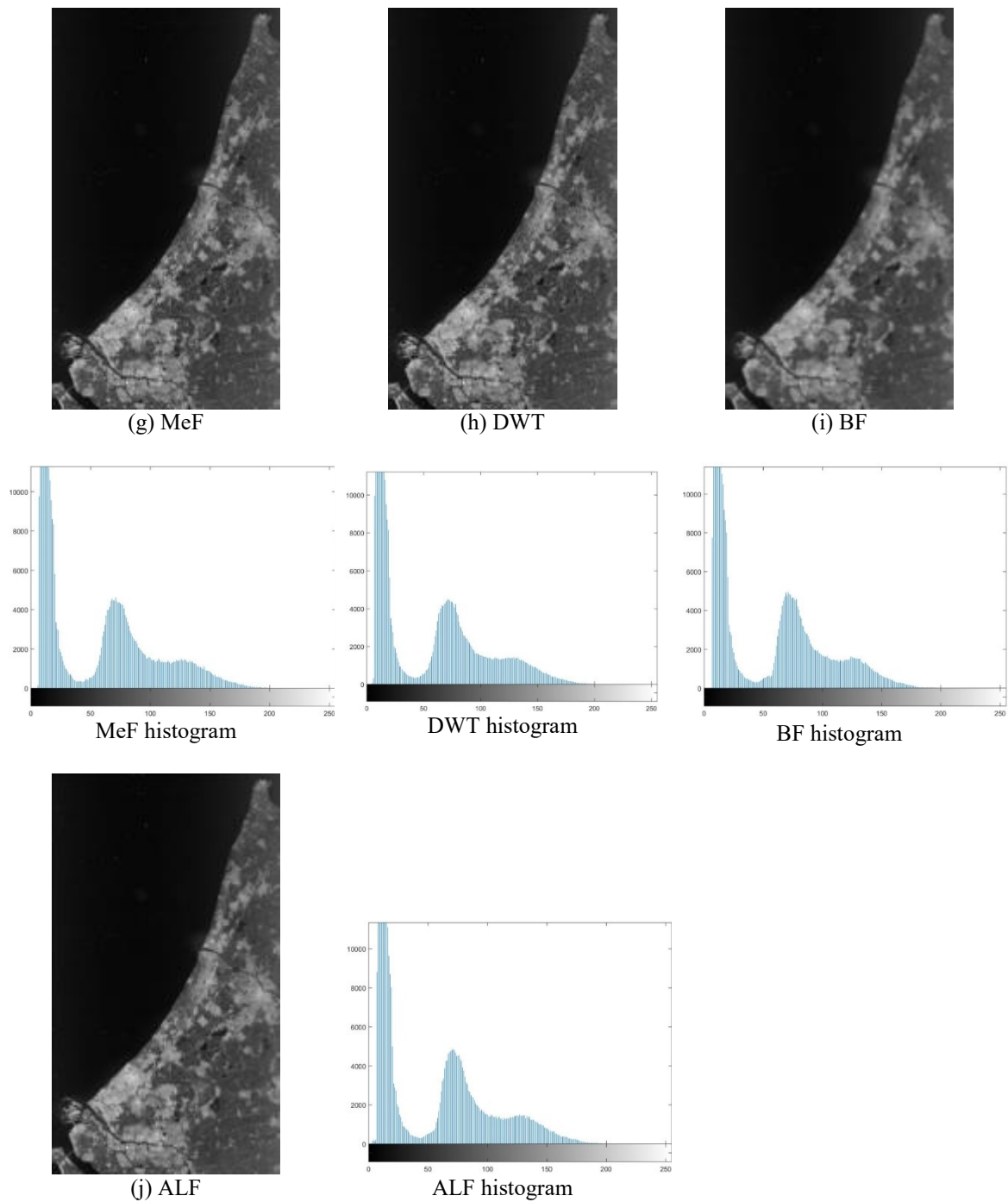


Figure 2.21: The resultant deblurred images by the blind deconvolution methods, and the corresponding histogram for each deblurred image, for the atmospheric turbulence blur case.

Table 2.5: The resultant metrics of the deblurred by non-blind deconvolution methods, for the atmospheric turbulence blur case.

Netherlands	ISNR	RMSE	PSNR
LRA	1.45	28.15	19.11
IF	0.18	49.95	14.13
WF	0.92	46.18	14.81
RF	0.28	48.47	14.39
CLS	0.17	52.66	13.67

Table 2.6: The resultant metrics of the deblurred by blind deconvolution methods, for the atmospheric turbulence blur case.

Netherlands	ISNR	RMSE	PSNR
AMF	0.57	48.53	14.38
GMF	0.93	45.92	14.86
HMF	0.94	45.87	14.87
CHMF	0.98	44.87	15.06
MeF	0.99	44.77	15.08
DWT	1.32	34.59	17.32
BF	0.88	46.18	14.81
ALF	0.83	47.26	14.61

Regarding the results shown in the Figure 2.20 and in the Table 2.5 we can see that the LRA has shown the best results in visual and metrics, whereas the CLS has shown the worst results obtained among the rest non-blind methods introduced. Regarding the results shown in the Figure 2.21 and in the Table 2.6 we can see that the DWT has shown the best results in visual and metrics, whereas the AMF has shown the worst results obtained among the rest blind methods introduced.

2.4.1.2 Noise reduction in satellite images

In this section, we will examine the behavior of several deconvolution techniques in the case of noise presence only using the sentinel-2 Toulouse image shown in Figure 2.22. We will use the most common four types of noise, salt & pepper noise with density 0.06, Gaussian noise with mean of zero and variance of 0.06, speckle noise with mean of zero and variance of 0.08 and Poisson noise with mean of the value of the image pixel on the original image of Toulouse respectively. In the first step, the noisy image will be denoised using the blind and non-blind deconvolution techniques. In the second step, we will apply the different metrics, mentioned in chapter 1, to obtain the best denoised image of each techniques. In the third step, we apply the proposed method to ameliorate the result of denoising.

2.4.1.2.a Salt & Pepper noise

This type of noise is also referred to as impulsive or spike noise. The main source for the salt and pepper is errors occurred during the analog to digital conversion and transmission. The image containing the salt and pepper noise has only two possible values as dark pixels in the bright regions (low value- zero) and bright pixels in dark regions (high value- one). The probability of each is typically less than 0.1. The value of unaffected pixels remains unchanged. In this section, we will examine the restoration techniques for restoring the satellite image in

presence of salt & pepper noise only with density of 0.06. In the Figures 2.22 and 2.23, we show the denoised images using the non-blind and the blind techniques.

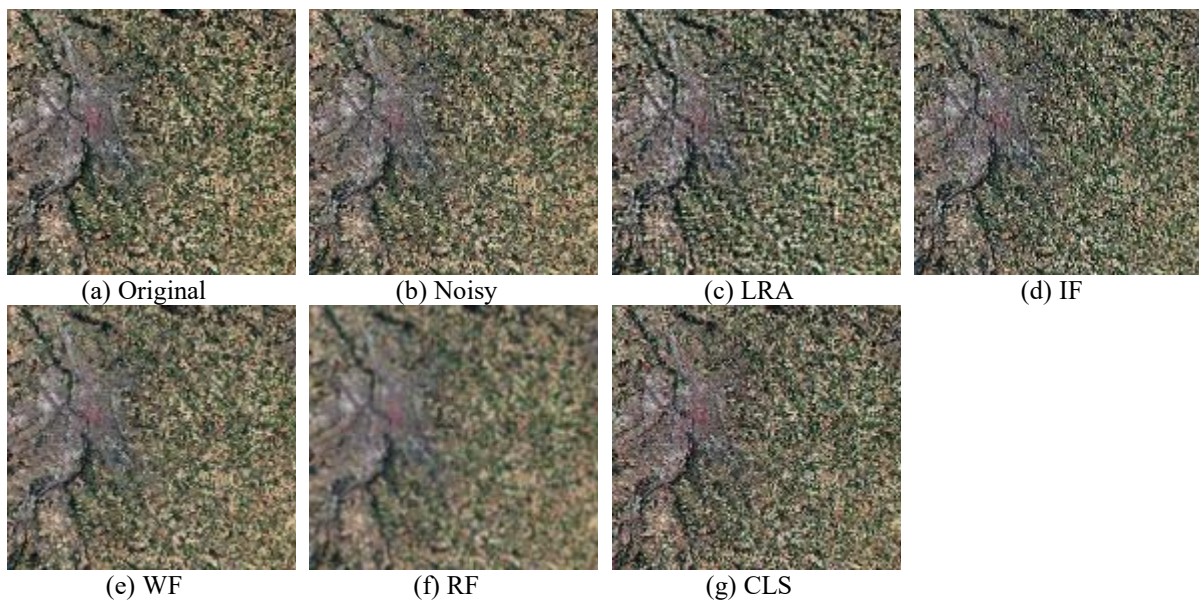


Figure 2.22: The resultant denoised images by the non-blind deconvolution methods, for the salt & pepper noise.

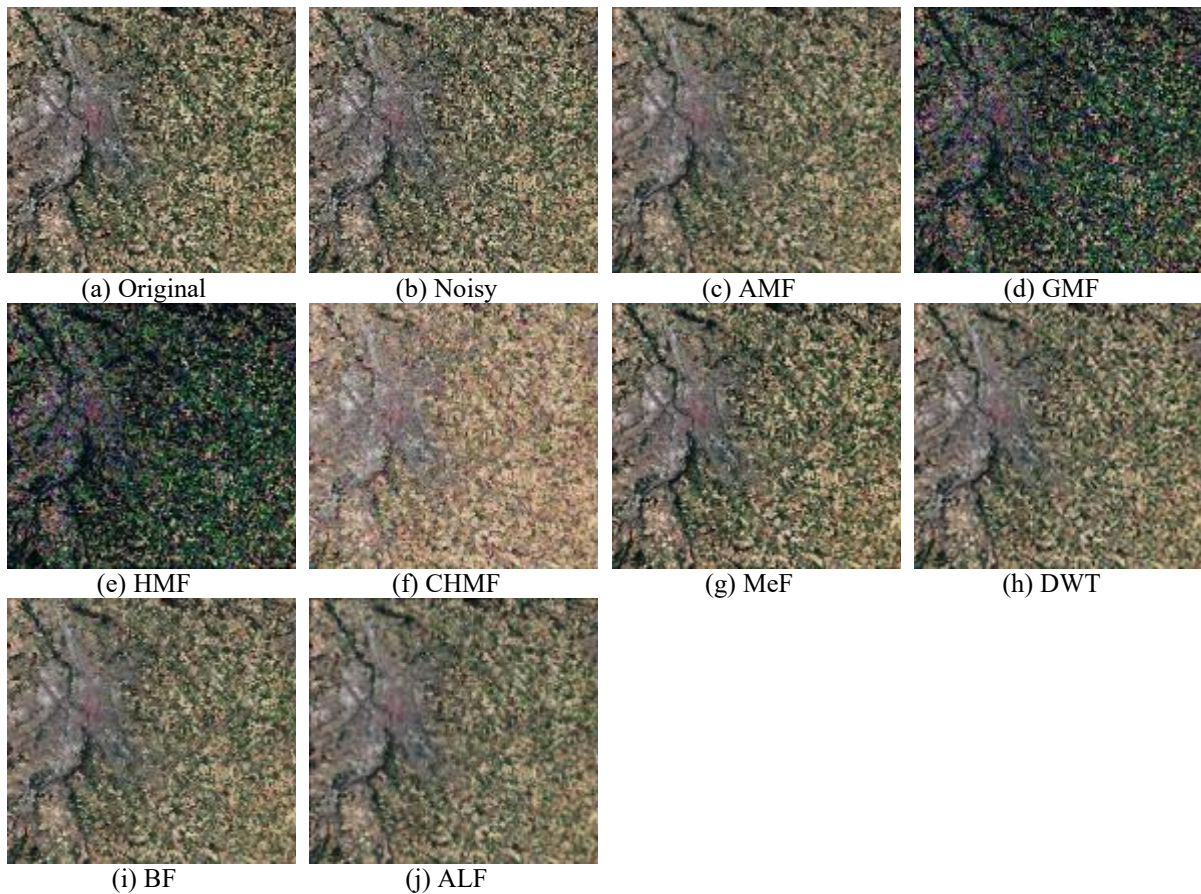


Figure 2.23: The resultant denoised image by the blind deconvolution methods for the salt & pepper noise.

Table 2.7: The resultant metrics of the denoised by non-blind deconvolution methods for the salt & pepper noise.

Toulouse	ISNR	RMSE	PSNR
LRA	0.88	44.87	13.49
IF	0.83	45.87	12.71
WF	1.12	44.77	17.17
RF	0.71	46.18	10.81
CLS	0.77	45.92	11.73

Table 2.8: The resultant metrics of the denoised by the blind deconvolution methods for the salt & pepper noise.

Toulouse	ISNR	RMSE	PSNR
AMF	1.10	36.69	16.81
GMF	0.71	72.69	10.87
HMF	0.68	76.30	10.45
CHMF	0.84	57.94	12.84
MeF	1.15	33.73	17.54
DWT	1.051	40.36	15.98
BF	1.08	37.80	16.55
ALF	1.02	42.41	15.55

Regarding the results shown in Figure 2.22 and in Table 2.7 we can see that the WF has shown the best results in visual and metrics, whereas the RF has shown the worst results obtained among the rest non-blind methods introduced.

Regarding the results shown in Figure 2.23 and in Table 2.8 we can see that the MeF has shown the best results in visual and metrics, whereas the HMF has shown the worst results obtained among the rest blind methods introduced.

2.4.1.2.b Gaussian noise

One of the most important noise that degrade the image quality is Gaussian noise that is evenly distributed over the image. When this additive noise is added to the original image, in the output noisy image every pixel is the sum of a random Gaussian distributed noise value and image pixel value. In color cameras, most amplification is performed in the blue color channel than in the green or red channel. Therefore, there is more noise in the blue channel as compared to other two channels. In this section, we will examine the restoration techniques for restoring the satellite image in presence of Gaussian noise only with mean of zero and variance of 0.08. In the Figures 2.24 and 2.25, we show the denoised images.

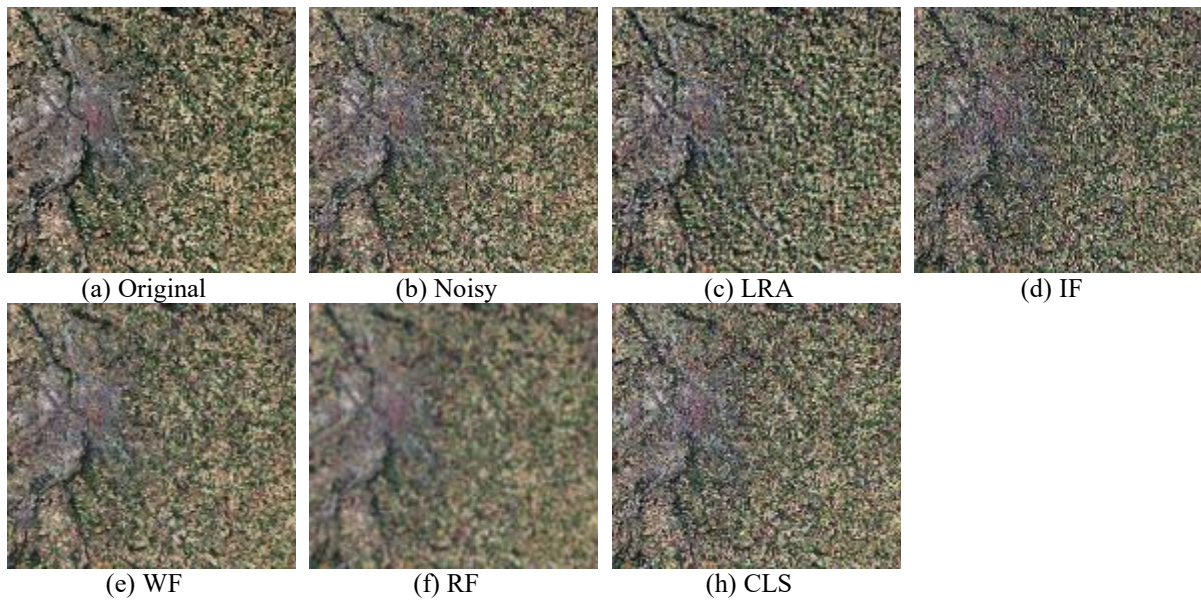


Figure 2.24: The resultant denoised images by the non-blind deconvolution methods, for the Gaussian noise.

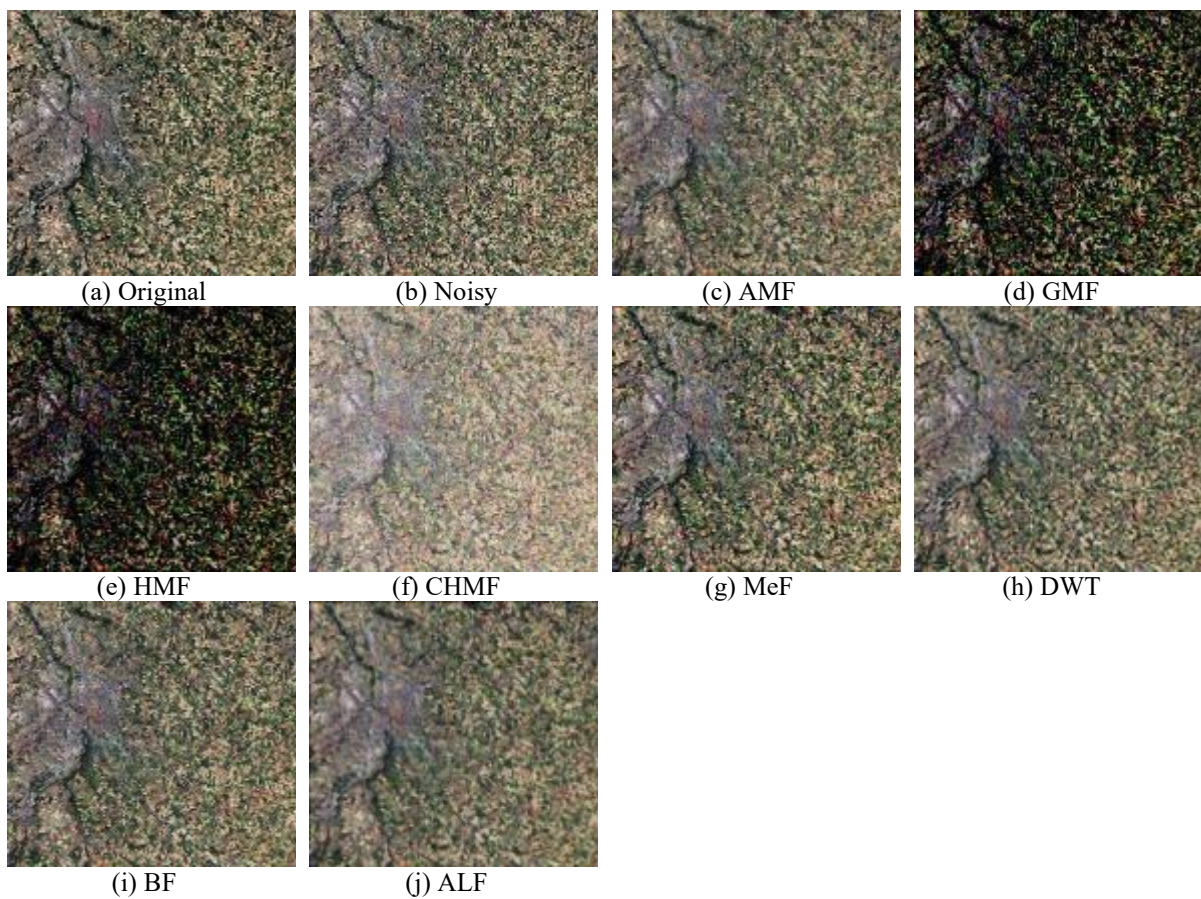


Figure 2.25: The resultant denoised image by the blind deconvolution methods, for the Gaussian noise.

Table 2.9: The resultant metrics of the denoised by non-blind deconvolution methods, for the Gaussian noise.

Toulouse	ISNR	RMSE	PSNR
LRA	0.75	68.31	11.41
IF	0.72	71.29	11.04
WF	1.08	37.80	16.55
RF	0.89	53.09	13.6
CLS	0.8	62.66	12.16

Table 2.10: The resultant metrics of the denoised by the blind deconvolution methods, for the Gaussian noise.

Toulouse	ISNR	RMSE	PSNR
AMF	1.01	40.04	16.05
GMF	0.64	78.34	10.22
HMF	0.61	83.27	9.69
CHMF	0.74	64.49	11.91
MeF	0.97	42.61	15.51
DWT	0.92	46.94	14.67
BF	1.17	32.55	17.85
ALF	0.94	45.13	15.01

Regarding the results shown in Figure 2.24 and in Table 2.9 we can see that the WF has shown the best results in visual and metrics, whereas the IF has shown the worst results obtained among the rest non-blind methods introduced.

Regarding the results shown in Figure 2.25 and in Table 2.10 we can see that the BF has shown the best results in visual and metrics, whereas the HMF has shown the worst results obtained among the rest blind methods introduced.

2.4.1.2.c Speckle noise

This multiplicative noise signal, which follows gamma distribution, is multiplied with the original image pixels to generate the noisy image. Generally, all coherent systems such as Synthetic Aperture Radar (SAR) images, Laser, Ultrasound images suffered by this speckle noise. In this section, we will examine the restoration techniques for restoring the satellite image in presence of speckle noise only with zero mean and variance of 0.08. In the Figures 2.26 and 2.27, we show the denoised images.

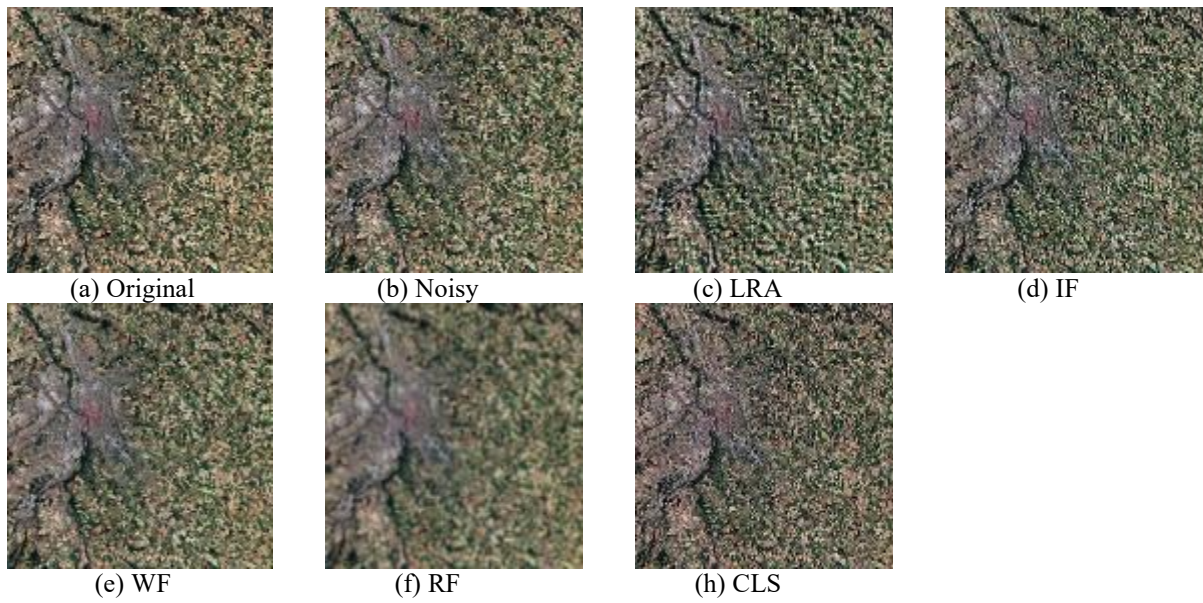


Figure 2.26: The resultant denoised images by the non-blind deconvolution methods, for the speckle noise.

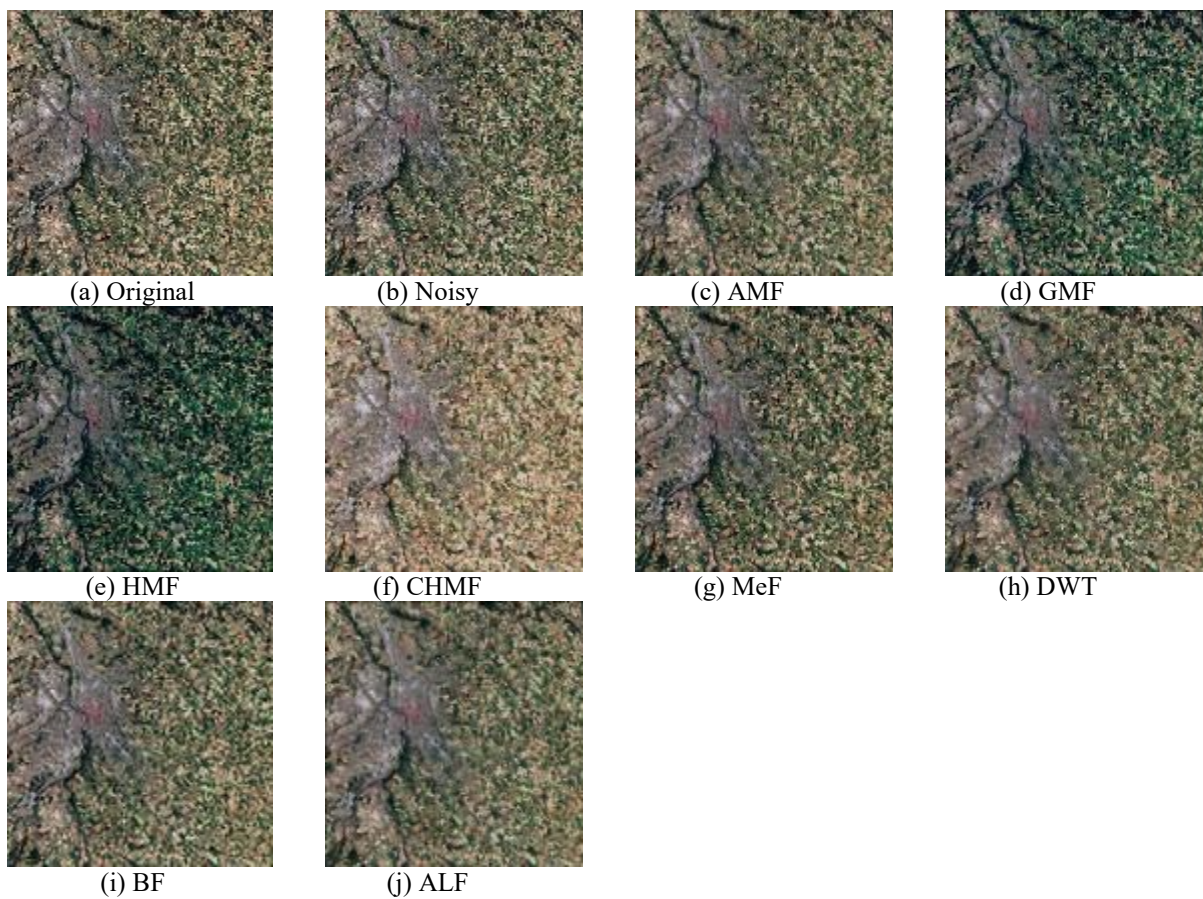


Figure 2.27: The resultant denoised images by the blind deconvolution methods, for the speckle noise.

Table 2.11: The resultant metrics of the denoised by non-blind deconvolution methods, for the speckle noise.

Toulouse	ISNR	RMSE	PSNR
LRA	0.88	50.64	14.01
IF	0.85	124.31	6.21
WF	1.20	31.12	18.24
RF	0.91	121.48	6.41
CLS	0.73	133.81	5.57

Table 2.12: The resultant metrics of the denoised by the blind deconvolution methods, for the speckle noise.

Toulouse	ISNR	RMSE	PSNR
AMF	1.06	35.81	17.02
GMF	0.89	48.87	14.32
HMF	0.81	57.48	12.91
CHMF	0.89	49.49	14.21
MeF	1.04	37.20	16.69
DWT	1.26	27.70	19.25
BF	1.06	35.97	16.98
ALF	0.99	40.97	15.85

Regarding the results shown in Figure 2.26 and in Table 2.11 we can see that the WF has shown the best results in visual and metrics, whereas the CLS has shown the worst results obtained among the rest non-blind methods introduced.

Regarding the results shown in Figure 2.27 and in Table 2.12 we can see that the DWT has shown the best results in visual and metrics, whereas the HMF has shown the worst results obtained among the rest blind methods introduced.

2.4.1.2.d Poisson noise

Fully developed speckle noise follows a Poisson distribution. This generates the Poisson noise from the data instead of adding artificial noise to the data. According to Poisson statistics, the uint8 and uint16 intensity of images must correspond to the number of photons. The double-precision images are used when the number of photons per pixel can be much larger than 65535.

In this section, we will examine the restoration techniques for restoring the satellite image in presence of Poisson noise only. In the Figures 2.28 and 2.29, we show the denoised images.

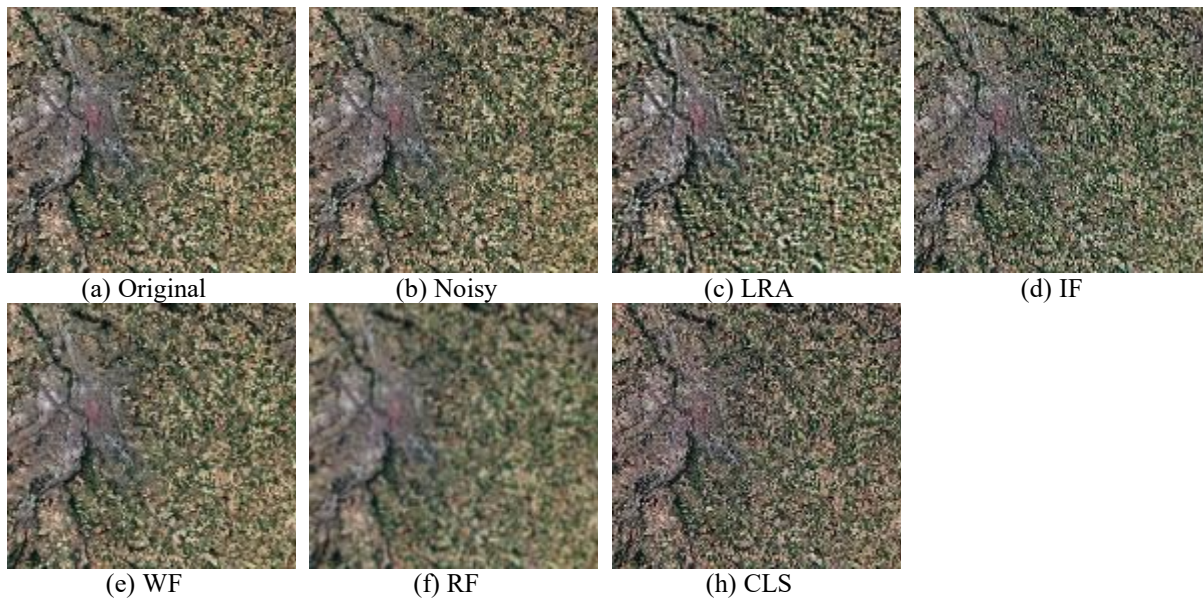


Figure 2.28: The resultant denoised images by the non-blind deconvolution methods, for the Poisson noise.

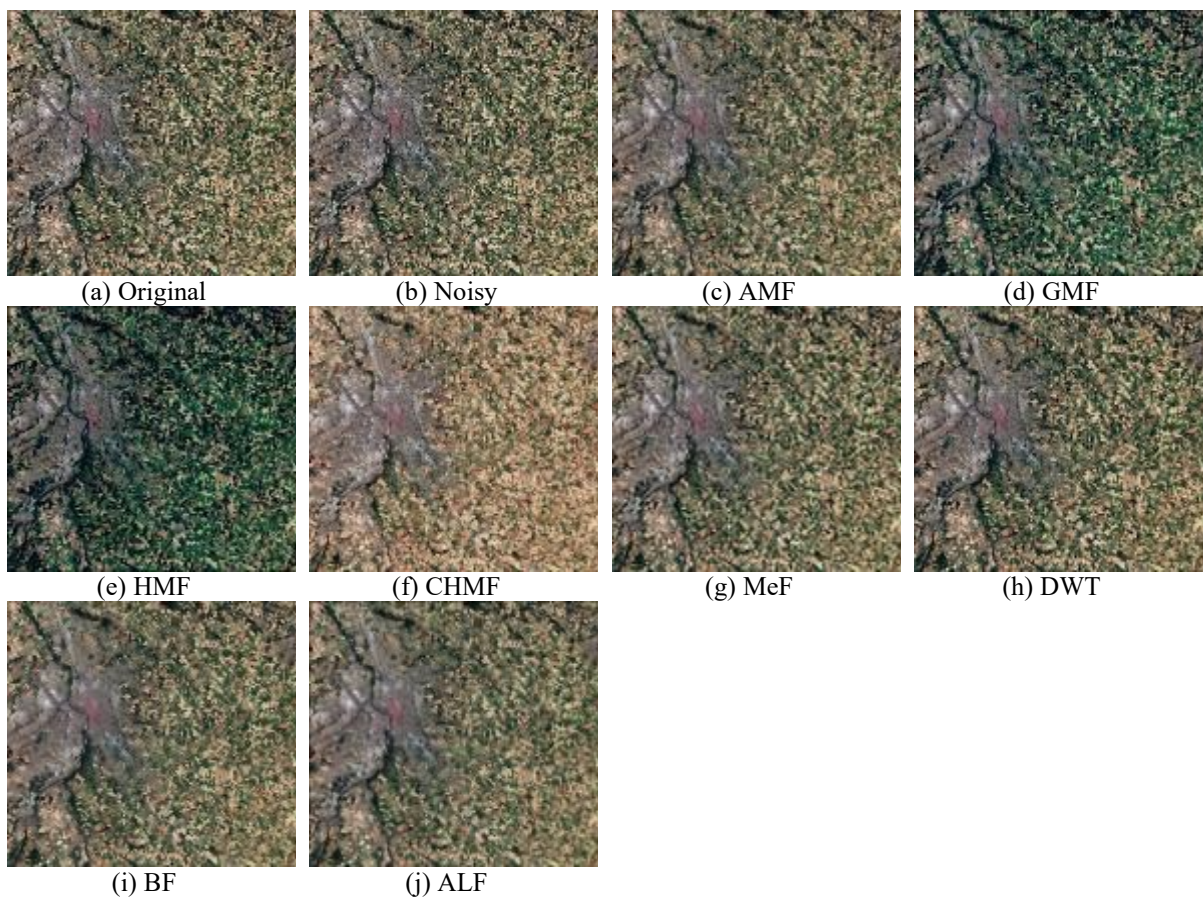


Figure 2.29: The resultant denoised image by the blind deconvolution methods, for the Poisson noise.

Table 2.13: The resultant metrics of the denoised by non-blind deconvolution methods, for the Poisson noise.

Toulouse	ISNR	RMSE	PSNR
LRA	0.99	41.40	15.76
IF	0.92	121.48	6.41
WF	1.27	27.10	19.44
RF	0.82	138.36	5.28
CLS	0.92	133.20	5.61

Table 2.14: The resultant metrics of the denoised by the blind deconvolution methods, for the Poisson noise.

Toulouse	ISNR	RMSE	PSNR
AMF	1.10	33.65	17.56
GMF	0.91	47.59	14.55
HMF	0.83	54.83	13.32
CHMF	0.93	45.66	14.91
MeF	0.96	43.75	15.28
DWT	1.12	32.58	17.84
BF	1.36	23.39	20.72
ALF	1.03	38.41	16.41

Regarding the results shown in Figure 2.28 and in Table 2.13 we can see that the WF has shown the best results in visual and metrics, whereas the RF has shown the worst results obtained among the rest non-blind methods introduced.

Regarding the results shown in Figure 2.29 and in Table 2.14 we can see that the BF has shown the best results in visual and metrics, whereas the HMF has shown the worst results obtained among the rest blind methods introduced.

2.4.1.3 Blur and noise reduction in satellite images

In this section, we will take into consideration the presence of blur plus noise. Satellite images are subject to suffer from the existence of noise, the most types of noise that affect the satellite images is the speckle noise [SHA13]. We will study the performance of the non-blind and blind deconvolution in the case of the presence of the atmospheric turbulence blur and the speckle noise. We will use the satellite image of “Southeast France” in this section.

In this section, we will examine our deconvolution methods with atmospheric turbulence blur with $\sigma^2=5$, and speckle noise presence. In this section, we will consider that speckle noise with mean of zero, and variance of 0.08. After that, we will apply the fusion combination on resulted image of the blind convolution methods with the best image resulted from the non-blind convolution methods. In the Figures 2.30 and 2.31, we show the restored images.

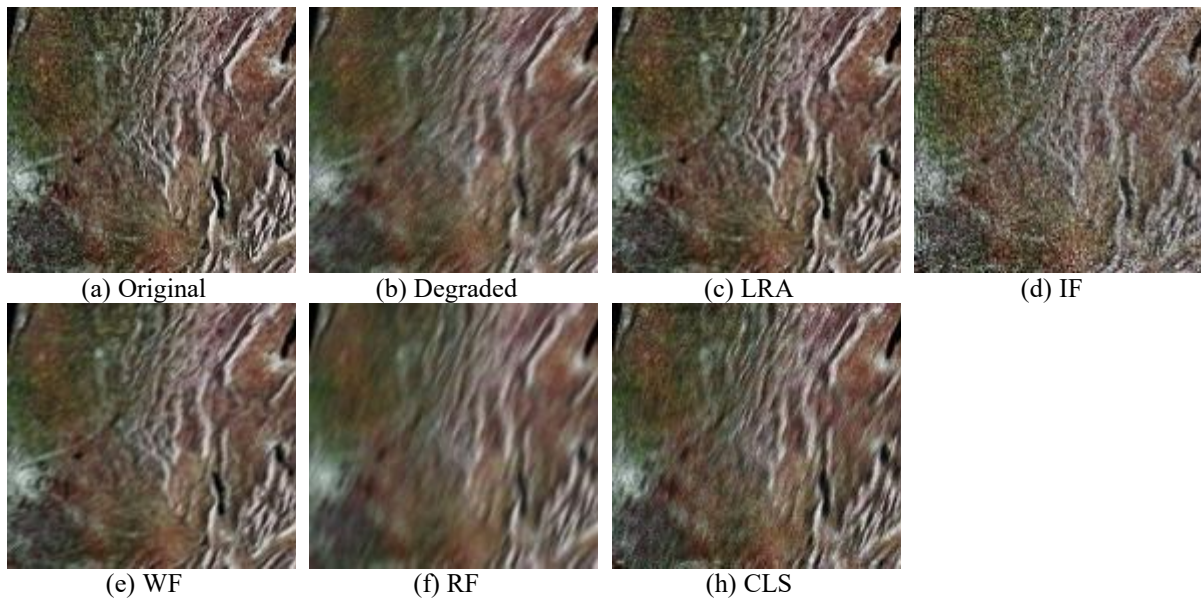


Figure 2.30: The resultant restored images by the non-blind deconvolution methods, for the case of atmospheric turbulence blur and speckle noise.

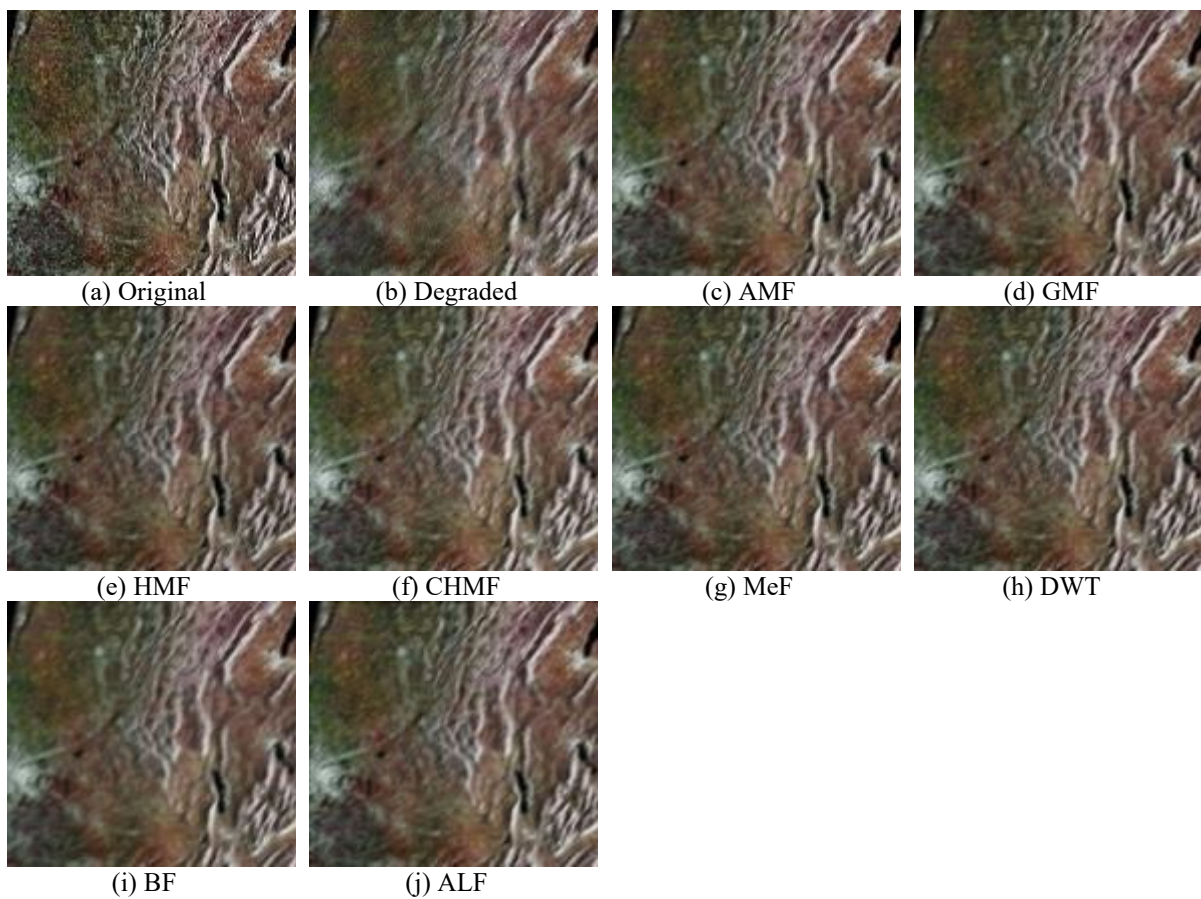


Figure 2.31: The resultant restored image by the blind deconvolution methods, for the case of linear atmospheric turbulence blur and speckle noise.

Table 2.15: The resultant metrics of the restoration with non-blind deconvolution methods, for the case of atmospheric turbulence blur and speckle noise.

Southeast France	ISNR	RMSE	PSNR
LRA	0.96	46.94	14.67
IF	0.82	59.50	12.61
WF	1.07	38.77	16.33
RF	0.86	55.53	13.21
CLS	0.79	63.10	12.1

Table 2.16: The resultant metrics of the restoration with blind deconvolution methods, for the case of atmospheric turbulence blur and speckle noise.

Southeast France	ISNR	RMSE	PSNR
AMF	1.06	39.49	16.17
GMF	1.05	40.23	16.01
HMF	1.04	40.69	15.91
CHMF	1.05	39.90	16.08
MeF	1.06	39.17	16.24
DWT	1.23	30.80	18.33
BF	1.11	36.02	16.97
ALF	1.03	41.26	15.79

Regarding the results shown in Figure 2.30 and in Table 2.15 we can see that the WF has shown the best results in visual and metrics, whereas the CLS has shown the worst results obtained among the rest non-blind methods introduced.

Regarding the results shown in Figure 2.31 and in Table 2.16 we can see that the DWT has shown the best results in visual and metrics, whereas the ALF has shown the worst results obtained among the rest blind methods introduced.

2.4.2 Evaluation of results and applying the proposed method

This study makes a comparison between the different presented image restoration algorithms non-blind image deconvolution (NBID), blind image deconvolution (BID) and the proposed method deconvolution (PMD) on the basis of performance metrics like PSNR (Peak Signal to Noise Ratio), MSE (Mean Square Error), RMSE (Root Mean Square Error) and ISNR (Improved Signal to Noise Ratio). In this section, we will apply our proposed method by choosing the image that has the best results based on the PSNR values from the two groups, non-blind and blind deconvolution methods, and then we will apply the PMD to achieve an image with better results.

2.4.2.1 Cases for the blurred satellite images

In this section, we will apply the PMD on the best results obtained from the non-blind and blind deconvolution methods in the case of the three blur types, motion, out of focus and atmospheric turbulence blur. We will illustrate the results by means of image and PSNR in order to clarify and demonstrate the efficiency of the PMD.

2.4.2.1.a The case for the Motion blur

In the case for motion blur, our results indicate that the best result obtained from the non-blind deconvolution methods was the deblurred image of the Lucy-Richardson method with PSNR of 23.07. On the other hand, the best result obtained from the blind deconvolution methods was the deblurred image of the median method with a PSNR value of 22.02. In this part, we will apply our PMD to these two images in order to obtain a better result. Fig 2.32 shows the original image of Netherlands, the Lucy-Richardson deblurred image, the median deblurred image and the PMD resultant image respectively. We can notice the improvement in the vision result. The PSNR results shown in Table 2.17 supports the improvement of the deblurred image with PSNR of 24.82 for the image obtained from the PMD.

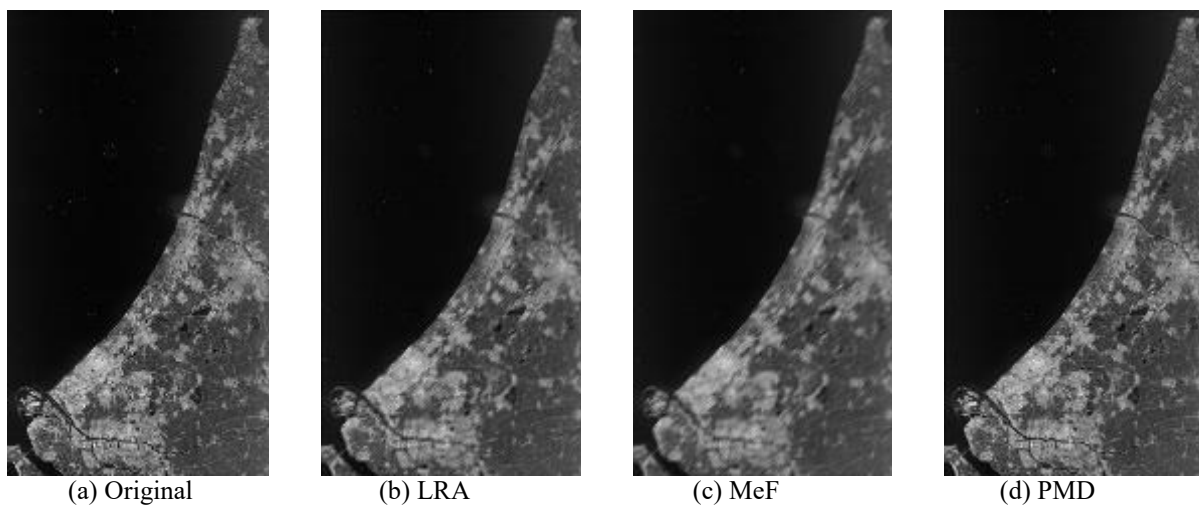


Figure 2.32: The resultant restored images for the case of motion blur.

Table 2.17: The resultant PSNR of the different methods for the case of motion blur.

Netherlands	ISNR	RMSE	PSNR
LRA	1.22	17.84	23.07
MeF	0.95	20.14	22.02
PMD	1.63	14.59	24.82

2.4.2.1.b The case for the out of focus blur

In the case for out of focus blur, our results indicate that the best result obtained from the non-blind deconvolution methods was the deblurred image of the Lucy-Richardson method with PSNR of 20.45. On the other hand, the best result obtained from the blind deconvolution methods was the deblurred image of the DWT method with a PSNR value of 20.52. In this part, we will apply our PMD to these two images in order to obtain a better result. Figure 2.33 shows the original image of Netherlands, the Lucy-Richardson deblurred image, the Wavelet deblurred image and the PMD resultant image respectively. We can notice the improvement in the vision result. The PSNR results shown in Table 2.18 supports the improvement of the deblurred image with PSNR of 23.12 for the image obtained from the PMD.

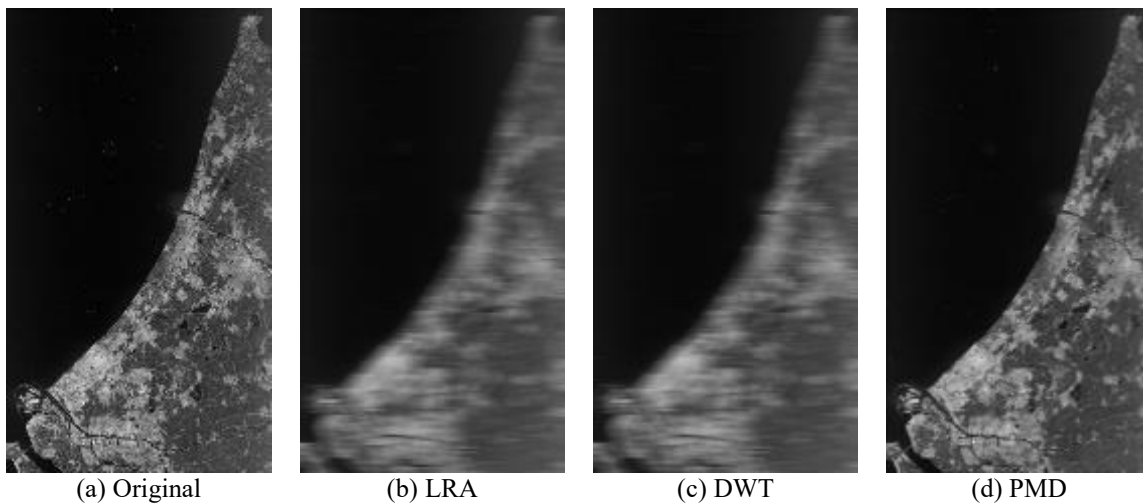


Figure 2.33: The resultant restored image for the out of focus blur.

Table 2.18: The resultant PSNR of the different methods for the out of focus blur.

Netherlands	ISNR	RMSE	PSNR
LRA	1.25	24.13	20.45
DWT	1.35	23.93	20.52
PMD	1.52	17.74	23.12

2.4.2.1.c The case for the atmospheric turbulence blur

In the case for atmospheric turbulence blur, our results indicate that the best result obtained from the non-blind deconvolution methods was the deblurred image of the Lucy-Richardson method with PSNR of 19.11. On the other hand, the best result obtained from the blind deconvolution methods was the deblurred image of the Wavelet method with a PSNR value of 17.32. In this part, we will apply our PMD to these two images in order to obtain a better result. Figure 2.34 shows the original image of Netherlands, the Lucy-Richardson deblurred image,

the wavelet deblurred image and the PMD resultant image respectively. We can notice the improvement in the vision result. The PSNR results shown in Table 2.19 supports the improvement of the deblurred image with PSNR of 22.82 for the image obtained from the PMD.

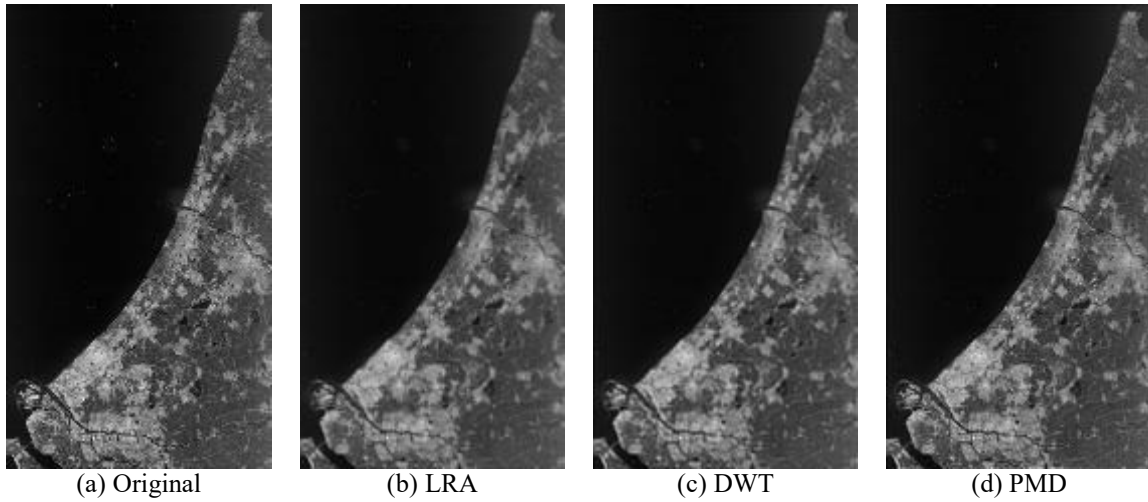


Figure 2.34: The resultant restored image, for the atmospheric turbulence blur.

Table 2.19: The resultant PSNR of the different methods, for the atmospheric turbulence blur.

Netherlands	ISNR	RMSE	PSNR
LRA	1.45	28.15	19.11
DWT	1.32	34.59	17.32
PMD	1.50	18.37	22.82

2.4.2.2 Cases for the noised only satellite images

In this section, we will apply the PMD on the best results obtained from the non-blind and blind deconvolution methods in the case of noise only presence. The four noise types, salt & pepper, Gaussian, speckle and Poisson noise are used to affect the satellite image. After denoising the noised image using the several non-blind and blind techniques, we will choose the best image from each technique and apply our method on the both images. We will illustrate the results by means of image and PSNR in order to clarify and demonstrate the efficiency of the PMD.

2.4.2.2.a The case for the Salt & Pepper noise

In the case for the salt & pepper noise, our results indicate that the best result obtained from the non-blind deconvolution methods was the denoised image of the Wiener method with PSNR of 17.17. On the other hand, the best result obtained from the blind deconvolution methods was the denoised image of the Median method with a PSNR value of 17.54. In this part, we will

apply our PMD to these two images in order to obtain a better result. Figure 2.35 shows the original satellite image of Toulouse, the wiener denoised image, and the median denoised image and the PMD resultant image respectively.

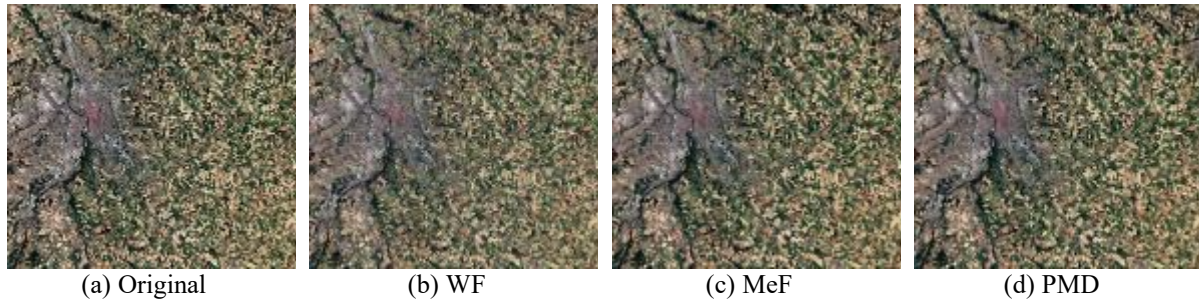


Figure 2.35: The resultant restored image, for the salt & pepper noise.

Table 2.20: The resultant PSNR of the different methods, for the salt & pepper noise.

Toulouse	ISNR	RMSE	PSNR
WF	1.12	44.77	17.17
MeF	1.15	33.73	17.54
PMD	1.24	28.58	18.98

From the results illustrated in Figure 2.35 and Table 2.20, we can notice the improvement in the vision result. The PSNR results shown in Table 2.20 supports the improvement of the denoised image with PSNR of 18.98 for the image obtained from the PMD.

2.4.2.2.b The case for Gaussian noise

In the case for the Gaussian noise, our results indicate that the best result obtained from the non-blind deconvolution methods was the denoised image of the Wiener method with PSNR of 16.55. On the other hand, the best result obtained from the blind deconvolution methods was the denoised image of the bilateral method with a PSNR value of 17.85. In this part, we will apply our PMD to these two images in order to obtain a better result. Figure 2.36 shows the original satellite image of Toulouse, the Wiener denoised image, and the bilateral denoised image and the PMD resultant image respectively.

From the results illustrated in Figure 2.36 and Table 2.21, we can notice the improvement in the vision result. The PSNR results shown in Table 2.21 supports the improvement of the denoised image with PSNR of 21.82 for the image obtained from the PMD.

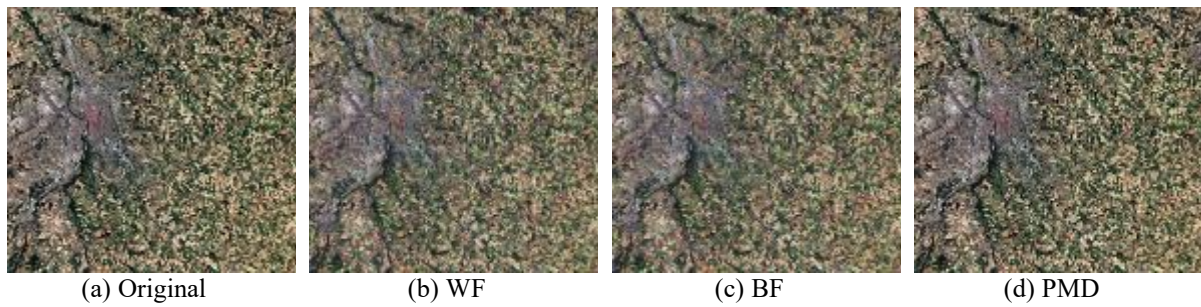


Figure 2.36: The resultant restored image for the Gaussian noise.

Table 2.21: The resultant PSNR of the different methods for the Gaussian noise.

Toulouse	ISNR	RMSE	PSNR
WF	1.08	37.80	16.55
BF	1.17	32.55	17.85
PMD	1.43	20.61	21.82

2.4.2.2.c The case for Speckle noise

In the case for the speckle noise, our results indicate that the best result obtained from the non-blind deconvolution methods was the denoised image of the Wiener method with PSNR of 18.24. On the other hand, the best result obtained from the blind deconvolution methods was the denoised image of the Wavelet method with a PSNR value of 19.25. In this part, we will apply our PMD to these two images in order to obtain a better result. Figure 2.37 shows the original satellite image of Toulouse, the Wiener denoised image, and the Wavelet denoised image and the PMD resultant image respectively.

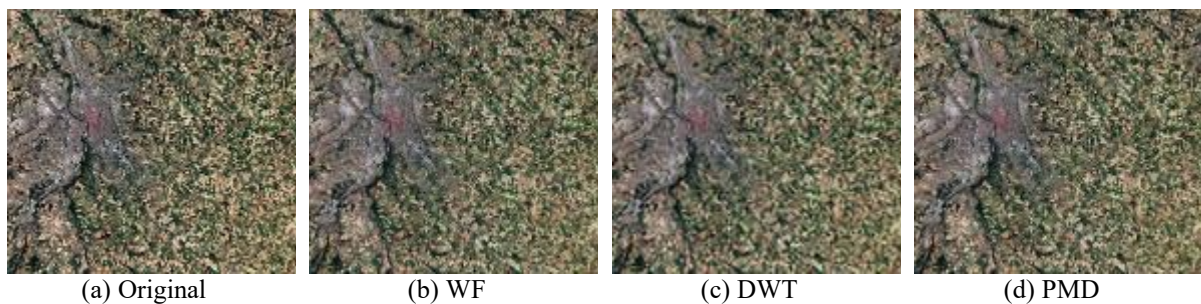


Figure 2.37: The resultant restored image for the speckle noise.

Table 2.22: The resultant PSNR of the different methods for the speckle noise.

Toulouse	ISNR	RMSE	PSNR
WF	1.20	31.12	18.24
DWT	1.26	27.70	19.25
PMD	1.38	22.59	21.02

From the results illustrated in Figure 2.37 and Table 2.22, we can notice the improvement in the vision result. The PSNR results shown in Table 2.22 supports the improvement of the denoised image with PSNR of 21.02 for the image obtained from the PMD.

2.4.2.2.d The case for Poisson noise

In the case for the Poisson noise, our results indicate that the best result obtained from the non-blind deconvolution methods was the denoised image of the wiener method with PSNR of 19.44. On the other hand, the best result obtained from the blind deconvolution methods was the denoised image of the bilateral method with a PSNR value of 20.72. In this part, we will apply our PMD to these two images in order to obtain a better result. Figure 2.38 shows the original satellite image of Toulouse, the Wiener denoised image, and the bilateral denoised image and the PMD resultant image respectively.

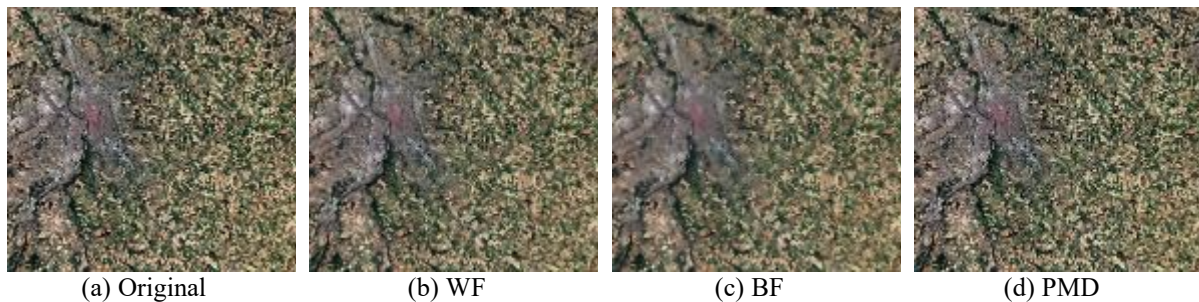


Figure 2.38: The resultant restored image for the Poisson noise.

Table 2.23: The resultant PSNR of the different methods for the Poisson noise.

Toulouse	ISNR	RMSE	PSNR
WF	1.27	27.10	19.44
BF	1.36	23.39	20.72
PMD	1.46	19.68	22.22

From the results illustrated in Figure 2.38 and Table 2.23, we can notice the improvement in the vision result. The PSNR results shown in Table 2.23 supports the improvement of the denoised image with PSNR of 22.22 for the image obtained from the PMD.

2.4.2.3 Cases for noised and blurred satellite images

In this section, we will apply the PMD on the best resultant images obtained from both the non-blind and blind deconvolution methods in the case of noise and blur. We will apply our PMD on the both images to obtain a new image with better results. We will illustrate the results by means of image and PSNR in order to clarify and demonstrate the efficiency of the PMD.

2.4.2.3.a The case for Speckle noise with Atmospheric turbulence blur

In the case for speckle noise with atmospheric turbulence blur, our results indicate that the best result obtained from the non-blind deconvolution methods was the denoised image of the Wiener method with PSNR of 16.33. On the other hand, the best result obtained from the blind deconvolution methods was the denoised image of the Wavelet method with a PSNR value of 18.33. In this part, we will apply our PMD to these two images in order to obtain a better result. Figure 2.39 shows the original satellite image of Toulouse, the Wiener denoised image, the Wavelet denoised image and the PMD resultant image respectively.

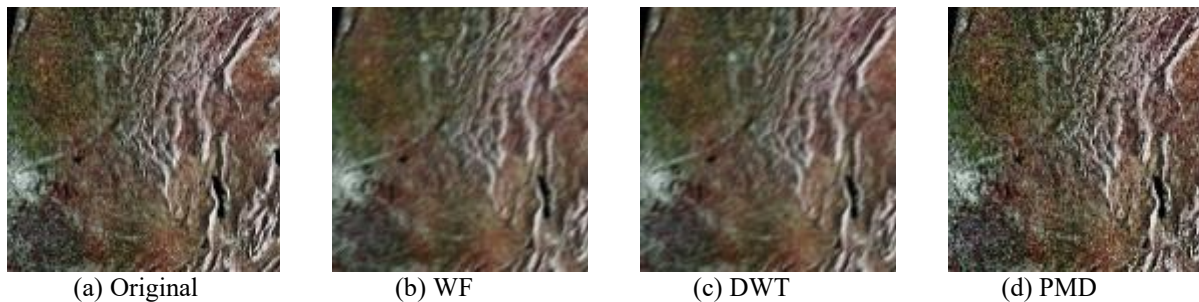


Figure 2.39: The resultant restored image for the speckle noise with atmospheric turbulence blur.

Table 2.24: The resultant PSNR of the different methods for the speckle noise with atmospheric turbulence blur.

Southeast France	ISNR	RMSE	PSNR
WF	1.07	38.77	16.33
DWT	1.23	30.80	18.33
PMD	1.32	25.18	20.08

From the results illustrated in Figure 2.39 and Table 2.24, we can notice the improvement in the vision result. The PSNR results shown in Table 2.24 supports the improvement of the denoised image with PSNR of 20.08 for the image obtained from the PMD.

Conclusion

In this chapter, we presented the comparative study based on dividing several deconvolution methods into two groups; the first is non-blind deconvolution methods and the second is the blind deconvolution methods. The simulation results of the tested satellite images indicate that our proposed method has improved the results of deblurring, denoising and restoration of the blurred, noised and degraded satellite images respectively. In this chapter, we made three kinds of comparisons; the first was a comparison of the performance of the non-blind methods and

the blind methods in the case of the presence of blur effect only on the satellite image. In the first comparison, we studied the behavior of all methods with different kinds of blur, we used three types of blur; the first is the motion blur, the second is the out of focus blur and the third is the atmospheric turbulence blur. The behavior of the methods varies according to the type of the blur. As for the non-blind methods, we notice that the LRA is the superior with the highest values of PSNR in the three types of blur among the other non-blind methods and almost among the blind methods also. On the other hand, the Wavelet and Median methods has the superiority among the other blind methods and the non-blind methods except for the LRA in cases of the blur only presence. In the second comparison, we studied the behavior of the several methods by applying it to a satellite image affected by noise only. We used four common types of noise; salt & pepper, Gaussian, speckle and Poisson noise. In this stage, the wiener method has achieved the best results among the other non-blind methods. As for the blind methods in this stage, Median has achieved the best results in the presence of the salt & pepper noise. BF was the superior in the cases of Gaussian and Poisson noise. DWT has achieved the best results in the case of speckle noise presence. The third comparison was to degrade the satellite image with a combination of speckle noise and atmospheric turbulence blur. The wiener method has still the superior compared to the other non-blind methods. The DWT has achieved the best results and it was the superior among the other blind methods. The last stage of our work was to choose the superior resultant image from each group, the non-blind and the blind methods, in each comparison stage. The two resultant image have been applied into the PMD. The vision results and the metric results have indicated that our proposed method has enhanced and improved the results by means of both image and metrics values.

References

- [Ban96] M. Banham and A. Katsaggelos, Spatially adaptive wavelet-based multiscale image restoration, *IEEE Trans. Image Processing*, Vol. 5, pp. 619-634, 1996.
- [Bel00] M. Belge, M. E. Kilmer, and E. L. Miller, Wavelet domain image restoration with adaptive edge-preserving regularity, *IEEE Trans. Image Processing*, Vol. 9, pp. 597-608, 2000.
- [Bov09] A. Bovik, *The Essential Guide to Image Processing*, London: Elsevier, 2009.
- [Boy15] A. K. Boyat, B. K. Joshi, A Review Paper: Noise Models In Digital Image Processing, *Signal & Image Processing: An International Journal (SIPIJ)*, Vol.6, No.2, April 2015.
- [Can76] M. Cannon, Blind deconvolution of spatially invariant image blurs with phase, *IEEE Trans. on Acou., speech and sig. proc.*, Vol. 24, No. 1, pp.58-63, 1976.
- [Cho14] Yoonsuk Choi, A Novel Multimodal Image Fusion Method Using Hybrid Wavelet-based Contourlet Transform, University of Nevada, Las Vegas, January 2014.
- [Das15] S. Das, J. Saikia, S. Das and N. Goni, A comparative study of different noise filtering techniques in digital images, *International Journal of Engineering Research and General Science*, Vol. 3, No. 5, pp. 180-191, 2015.
- [Des15] S. Deswal, S. Gupta and B. Bhushan, A Survey of Various Bilateral Filtering Techniques, *International Journal of Signal Processing, Image Processing and Pattern Recognition*, Vol. 8, No. 3, pp. 105-120, 2015.
- [Fig03] M. A. T. Figueiredo and R. D. Nowak, An EM Algorithm for Wavelet-Based Image Restoration, *Ieee Transactions on Image Processing*, Vol. 12, No. 8, pp. 906-916, 2003
- [Gan13] P. Ganesan V. Rajini, Comparative Study of Denoising Methods for Satellite Image Restoration Using Matlab, *International Journal of Advanced Research in Computer Science*, Vol. 4, No. 5, pp. 74-77, May 2013.
- [Gon08] R. Gonzalez, R. Woods, *Digital Image Processing*, 3rd ed.; Prentice Hall: Upper adde River, New Jersey, pp. 333–415, 2008.
- [Gup15] D. Gupta and S. Choubey, Discrete Wavelet Transform for Image Processing, *International Journal of Emerging Technology and Advanced Engineering*, Vol. 4, No. 3, pp. 598-602, 2015.
- [Hed11] P. Hedao and S. S. Godbole, Wavelet Thresholding Approach for Image Denoising, *International Journal of Network Security & Its Applications (IJNSA)*, Vol. 3, No. 4, pp. 16-21, 2011.

- [Hun73] B. R. Hunt, The Application of Constrained Least Squares Estimation to Image Restoration by Digital Computer, IEEE Trans. on Computers, Vol. C-22, No. 9, pp. 805-812 1973.
- [Kau12] A. Kaur and V. Chopra, A comparative study and analysis of image restoration techniques using different images formats, International Journal for Science and Emerging Technologies with Latest Trends, Vol. 2, No. 1, pp. 7-14, 2012.
- [Kau15] P. Kaushik, M. Chawla and G. Kumar, Detection of Noise in an Image using Blind Deconvolution Method, International Journal of scientific research and management (IJSRM), Vol. 3, Issue 7, pp. 3411-3415, 2015.
- [Mah10] D. Maheswari et. al., Noise removal in compound image using median filter, International Journal on Computer Science and Engineering, Vol. 02, No.0 4, pp. 1359-1362, 2010.
- [Mar16] B. Marhaba, M. Zribi, and W. Khoder, Image Restoration Using a Combination of Blind and Non-Blind Deconvolution Techniques, International Journal of Engineering Research & Science (IJOER), vol. 2, no. 5, pp. 225–239, 2016.
- [Mih99] M. Mihçak, I. Kozintsev, K. Ramchandran, and P. Moulin, Low-complexity image denoising based on statistical modeling of wavelet coefficients, Signal Processing Lett., Vol. 6, pp. 300–303, 1999.
- [Mis16] D. Mistry and A. Banerjee, Deblurred of Image with Wiener Filter in MATLAB, Journal of Emerging Technologies and Innovative Research (JETIR), Vol. 1, Issue 1, pp. 25-29, 2016.
- [Mou99] P. Moulin and J. Liu, “Analysis of multiresolution image denoising schemes using generalized—Gaussian and complexity priors, IEEE Trans. Inform. Theory, Vol. 45, pp. 909–919, 1999.
- [Nat13] A. Nath, Image Denoising Algorithms: A Comparative study of Different Filtration approaches used in image restoration, IEEE, International Conference on Communication Systems and Network Technologies, 2013.
- [Paj04] G. Pajares and J. M. de la Cruz, A wavelet-based image fusion tutorial, Pattern Recognition, Vol. 37, pp. 1855-1872, 2004.
- [Pri16] S. Priyanka1, Dr.A.S.Naveen kumar, Noise Removal in Remote Sensing Image Using Kalman Filter Algorithm, International Journal of Advanced Research in Computer and Communication Engineering, Vol 5, Issue 3, pp. 894-897, 2016.

- [Ran14] J. Rani and S. Kaur, Image Restoration Using Various Methods and Performance Using Various Parameters, International Journal of Advanced Research in Computer and Software Engineering, Vol. 4, No. 1, pp. 778-783, January 2014.
- [Ras17] J. Rastogi, D. Mittal, D. Singh, Comparative Study of Image Denoising algorithms in Medical and Satellite Images, International Research Journal of Engineering and Technology, Vol. 4, pp. 3024-3030, 2017.
- [Sam09] P. D. Samarasinghe and R. A. Kennedy, On Non-blind Image Restoration, 3rd International Conference on Signal Processing and Communication Systems, 2009.
- [Sha13] K.M. Sharavana Raju, Mohammad Shahnawaz Nasir, T. Meera Devi, Filtering Techniques to reduce speckle Noise and Image Quality Enhancement methods on Satellite Images. IOSR Journal of Computer Engineering, volume 15, issue 4, pp. 10-15, 2013.
- [Sin13] R. Singh and N. Gupta, Image Restoration Model with Wavelet Based Fusion, Journal of Information Engineering and Applications, Vol. 3, No. 6, pp. 21-26, 2013.
- [Smi97] .S. M. Smith and J. M. Brady, Susan - a new approach to low level image processing, Int. Journal of Computer Vision, Vol. 23, pp.45-78, 1997.
- [Tha16] A. Thakur, A. Kausar, and A. Iqbal, Comparison efficacy of restoration method for space variant motion blurred images using kalman and wiener filter, 6th International Conference -Cloud System and Big Data Engineering (Confluence), pp. 508-512, 2016.
- [Tic06] M. Tico and M. Vehvilainen, Estimation of motion blur point spread function from differently exposed image frames, Proc. 14th Eur. Signal Process. Conf., Florence, Italy, pp. 1-4, 2006.
- [Tom98] C. Tomasi and R. Manduchi, Bilateral filtering for gray and color images, Proc. Int. Conf. Computer Vision, pp. 839-846, 1998.
- [Tom08] E. Tom Bishop, Blind Image Deconvolution: Nonstationary Bayesian approaches to restoring blurred photos, The University of Edinburgh, 2008.
- [Ufa12] A. S. Ufade, B. K. Khadse and S. R. Suralkar, Restoration of Blur Image Using wavelet Based Image Fusion, International Journal of Engineering and Advanced Technology (IJEAT), Vol. 2, No. 2, pp. 159-61, 2012.
- [URL14] URL:
http://www.esa.int/spaceinimages/Images/2014/04/Radar_image_of_the_Netherlands
- [URL18] URL: http://www.esa.int/spaceinimages/Images/2018/01/Southeast_France

- [Ver13] R. Verma, Dr. Jahid Ali, A Comparative Study of Various Types of Image Noise and Efficient Noise Removal Techniques, International Journal of Advanced Research in Computer Science and Software Engineering, Vol. 3, Issue 10, pp. 617-622, October 2013.
- [Whi94] R. L. White, Image Restoration Using the Damped Richardson-Lucy Method, The Restoration of HST Images and Spectra, Vol. 2, No. 1, pp. 1-7, 1994.
- [Yar85] L. Yaroslavsky, Digital Picture Processing - An Introduction, Springer Verlag, 1985.
- [Yeo06] W. S. Yeoh, C. Zhang, Constrained Least Squares Filtering Algorithm for Ultrasound Image Deconvolution, IEEE Transactions on Biomedical Engineering Vol. 53, Issue: 10, pp. 2001-2007, 2006.
- [Zho99] Z. Zhong, Investigations of image fusion, University of Lehigh, USA, December 1999.
- [Zho00] S. Zhong and V. Cherkassky, Image Denoising using Wavelet Thresholding and Model Selection, International Conference on Image Processing, Vol. 3, pp. 262-265, 2000.
- [Zhu12] Y. Zhu, C. Huang, An Improved Median Filtering Algorithm for Image Noise Reduction, Physics Procedia, Vol. 25, pp. 609-616, 2012.

Chapter 3

Importance sampling Monte Carlo filters for satellite images restoration

Table of Contents

Introduction	111
3.1 Analytical methods for filtering	112
3.1.1 Filtering problem	112
3.1.2 Bayesian optimal filtering	114
3.1.2.1 Optimal filtering	114
3.1.2.2 Kalman filtering.....	117
3.1.2.3 The Extended Kalman Filter	120
3.1.2.4 The Unscented Kalman Filter.....	122
3.2 Monte Carlo methods for nonlinear filtering.....	125
3.2.1 Monte Carlo methods	126
3.2.2 Particle filters.....	127
3.2.2.1 The Sequential Importance Sampling Algorithm.....	127
3.2.2.2 The Sequential Importance Resampling Algorithm	131
3.2.2.3 Empirical distributions	132
3.2.3 Bayesian bootstrap filter.....	133
3.2.3.1 Definition of the Bayesian bootstrap filter	133
3.2.3.2 Fast bootstrap technique	135
3.3 Experimental results	137
3.3.1 Visual results	138
3.3.1.1 Application of filters on impulse noise	138
3.3.1.2 Application of filters on Gaussian noise	141
3.3.1.3 Application of filters on Speckle noise	143
3.3.2 Metrics results	145
3.3.2.1 French synergy image.....	145
3.3.2.2 Seville Spain image	145
3.3.2.3 Remark	146
Conclusion.....	146
References	147

Introduction

Image restoration is a major field in the image-processing domain. The problematic in image restoration has three phases. The first is the process of eliminating the blur in the image; assuming that the image is only blurred, we call that image deblurring. The second is removing the noise from the image, assuming that the image is only noised, we call that image denoising. The third phase is the case when the image is affected by blur and noise, and then the process of removing blur and noise is called restoration. However, denoising and deblurring could also be named restoration.

There are many applications in the image restoration domain, such as forensic applications, consumer photography, space imagery and others. A wide variety of approaches for image restoration, from classical to recursive, exists in the literature [Ban97]. Researchers working on image restoration have long used Kalman method in the image restoration domain [Bie83][Woo77]. However, in these implementations, stationary image and degradation models have been used exclusively, even though it is well known that images are nonstationary.

The stationary models have been used previously because of the practical constraints of memory and computation time. To avoid memory consumption and time execution problems, the reduced order model Kalman filter (ROMKF) was proposed in [Ang89]. The ROMKF is simple and easy to implement low image order state space model. A simplified model Kalman filter (SMKF) is a different method with more reduction in computational complexity for image restoration, it was proposed in [Rao01]. In scalar observation condition, an efficiency computational was observed through the benefit of a reduced update procedure [Woo77]. However, due to the presence of nonlinear orientation data, a pressing need occurred for a modification method of the Kalman filter.

Extended Kalman filter (EKF) overcome these obstacles and provides modification by linearizing all nonlinear models like the process and measurements models so the traditional Kalman filter can be applied [Sor85]. Unfortunately, two essential disadvantages were found in EKF [Koc92]. First, due to the Jacobian matrices derivation, the linear approximations to the nonlinear functions make it hard to implement. Second, the time intervals must be small; otherwise, the filter could be unstable due to this linearization [Jul95].

To surmount these problems, Julier and Uhlmann [Jul97] produced unscented Kalman filter (UKF). An importance sampling-based UKF for image denoising, which is not only computationally efficient but also performs very well, is introduced in [Wan13].

The contribution of this chapter is to establish a recursive Bootstrap filtering framework for image restoration. The bootstrap algorithm is a filtering process based on both the Bayesian state estimation and the Monte Carlo method. The bootstrap application has achieved very good results and it is superior in handling any non-linear functionality system and/or measurement noise of any distribution.

The chapter is organized as follows. Section 3.1 presents analytical methods for filtering. In the 3.2 section, Monte Carlo methods for nonlinear filtering are described. Experimental results are presented to demonstrate the accuracy of the two methods for satellite images restoration in section 3.3.

3.1 Analytical methods for filtering

In the early 60's, R.E. Kalman [Kal60] introduced his important paper representing a recursive solution for the discrete-data linear filtering problem. Following that time and with the help of the great progress in computer science, Kalman filtering has drew attention and was used in a large number of applications, especially in the field of assisted navigation [Pra13][Xin13] and image restoration [Woo81][Bie83][Tek86][Cit92][Arb04][Sub07].

The Kalman filter is developed as a group of mathematical equations, which provides an effective recursive computational, intends to estimate the state of a process, in such a manner that reduces as much as possible the mean of the squared error. The first part of this chapter is dedicated to the Kalman filter technique because this method is considered the reference for linear dynamical systems. This filter will be useful later to evaluate the performance of our different approaches.

3.1.1 Filtering problem

In the theory of stochastic processes, we can present the filtering problem as a mathematical model for a number of state estimation problems in the signal processing and the related fields. Our main objective in Kalman filtering is to obtain the most accurate estimation for the true value for a system from an incomplete or probably noised set of observations in the same system. Some approaches and special cases are quite understood: for example, in the case of Gaussian random variables the linear filters are optimal such as the Wiener filter and the Kalman-Bucy filter.

Filtering can be described as the process involving the extract of information about a quantity of interest at time t by utilizing the data have been measured up to and including t . Here, let us

take into consideration the following general stochastic filtering problem in a dynamic state-space form [Jaz70][Sor74]:

$$\dot{x}_t = f(t, x_t, u_t, w_t) \quad (3.1)$$

$$y_t = g(t, x_t, u_t, v_t) \quad (3.2)$$

where (3.1) and (3.2) are called the state and the measurement equations respectively; x_t, y_t, u_t represent the state vector, the measurement vector and the system input vector (as driving force) in a controlled environment; $f: \mathbb{R}^{N_x} \mapsto \mathbb{R}^{N_x}$ and $g: \mathbb{R}^{N_x} \mapsto \mathbb{R}^{N_y}$ are two vector-valued functions, which are potentially time varying; w_t and v_t represent the dynamical and measurement noise respectively, with appropriate dimensions.

The preceding formulation was presented in the continuous-time domain, in practice; however, we are more concerned about the discrete-time filtering. In this context, the following practical filtering problem is concerned:

$$x_{n+1} = f(x_n, w_n) \quad (3.3)$$

$$y_n = g(x_n, v_n) \quad (3.4)$$

where w_n and v_n represent random sequences white noise with unknown statistics in the discrete-time domain.

The state equation (3.3) characterizes the state transition probability $p(x_{n+1}|x_n)$, whereas the measurement equation (3.4) represents the probability $p(y_n|x_n)$ that is more related to the measurement noise model. In a special case, where a linear Gaussian dynamic system will be considered, the equations (3.3) and (3.4) will be reduced to the following:

$$x_{n+1} = F_{n+1,n}x_n + w_n \quad (3.5)$$

$$y_n = G_n x_n + v_n \quad (3.6)$$

where, $F_{n+1,n}, G_n$ represent the transition and the measurement matrix respectively.

Consider the initial density $p(x_0)$, transition density $p(x_n|x_{n-1})$, and the likelihood $p(y_n|x_n)$, the goal of the filtering is the estimation of the best current state at a time n given the observations up to time n , which is in essence amount to estimate the posterior density $p(x_n|y_{1:n})$ or $p(x_{0:n}|y_{1:n})$.

In spite of the fact that the posterior density gives a full solution of the stochastic filtering issue, the problem persists intractable because the density is a function but not a finite-dimensional point estimate.

3.1.2 Bayesian optimal filtering

Bayesian filtering is aimed to apply the Bayesian statistics and Bayes rule to probabilistic inference problems and specifically the stochastic filtering problem. To our knowledge, Ho and Lee [Lo64] were among the first authors to discuss iterative Bayesian filtering, in which they discussed in principle the sequential state estimation problem and included the Kalman filter (KF) as a special case. In the past few decades, numerous authors have investigated the Bayesian filtering in a dynamic state space framework [Sor71][Kra85][Kra88][Pol94][Wes97].

3.1.2.1 Optimal filtering

In optimal filtering algorithm, we are primarily concerned with the discrete time estimation problem. A discrete-time system model is described by the two equations below:

$$x_n = f(x_{n-1}, w_n) \tag{3.7}$$

where $f : IR^k \times IR^m \rightarrow IR^k$, w_n is the white noise system and an observation vector given by:

$$y_n = g(x_n, v_n) \tag{3.8}$$

where $g : IR^k \times IR^r \rightarrow IR^p$, and v_n is the observation white noise.

In general, the problem of the optimal filtering is to estimate the state vector at time n , given all the measurements up to and including time n , which we will denote by $Y_n = \{y_i : i = 1, \dots, n\}$. In a Bayesian perspective, we look at this problem as how to compute the distribution $p(x_n | Y_n)$, we can do this recursively in two steps.

Prediction step:

$p(x_n | Y_{n-1})$ is calculated by the filtering distribution $p(x_{n-1} | Y_{n-1})$ at time $n-1$:

$$p(x_n | Y_{n-1}) = \int p(x_n | x_{n-1}) p(x_{n-1} | Y_{n-1}) dx_{n-1} \tag{3.9}$$

where $p(x_{n-1} | Y_{n-1})$ is supposed to be known due to recursion and $p(x_n | x_{n-1})$ is given by Equation (3.7) and the known statistics of w_{n-1} :

$$p(x_n | x_{n-1}) = \int p(x_n | x_{n-1}, w_{n-1}) p(w_{n-1} | x_{n-1}) dw_{n-1} \quad (3.10)$$

Since $p(w_{n-1} | x_{n-1})$ is assumed to be just $p(w_{n-1})$ then we have:

$$p(x_n | x_{n-1}) = \int \delta(x_n - f(x_{n-1}, w_{n-1})) p(w_{n-1}) dw_{n-1} \quad (3.11)$$

Update step:

Then, as y_n measurement becomes available at time step n , we update the prior according to Bayes' rule:

$$p(x_n | Y_n) = \frac{p(y_n | x_n) p(x_n | Y_{n-1})}{p(y_n | Y_{n-1})} \quad (3.12)$$

where the normalizing denominator is given by:

$$p(y_n | Y_{n-1}) = \int p(y_n | x_n) p(x_n | Y_{n-1}) dx_n \quad (3.13)$$

The conditional pdf of y_n given x_n $p(y_n | x_n)$, is defined by the measurement model and the known statistics of v_n :

$$p(y_n | x_n) = \int \delta(y_n - g(x_n, v_n)) p(v_n) dv_n \quad (3.14)$$

where $\delta(\cdot)$ is the Dirac delta function.

In general, it is not possible that the computations in the prediction and update steps (Equations 3.9-3.12) can be taken out analytically; hence, we need to use some approximation methods such as Monte Carlo sampling. In some limited cases, however, the computations in Equations 3.9-3.12 can be taken out analytically, as will show in the following.

Criterion that measures the optimality:

An optimal filter is said to be “optimal” only in some specific sense; in other words, one should define a criterion that measures the optimality. For example, some potential criteria for measuring the optimality can be:

1. Minimum mean-squared error (MMSE): It can be defined in terms of prediction or filtering error (or equivalently the trace of state-error covariance):

$$E\left[\|x_n - \hat{x}_n\|^2 | Y_n\right] = \int \|x_n - \hat{x}_n\|^2 p(x_n | Y_n) dx_n \quad (3.15)$$

which is aimed to find the conditional mean:

$$\hat{x}_n = E[x_n | Y_n] = \int x_n p(x_n | Y_n) dx_n \quad (3.16)$$

2. Maximum a posteriori (MAP): It is aimed to find the mode of posterior probability $p(x_n | Y_n)$, which is equal to minimize a loss function:

$$\varepsilon = E\left[1 - \mathbb{I}_{x_n: \|x_n - \hat{x}_n\| \leq \zeta}(x_n)\right] \quad (3.17)$$

where $\mathbb{I}(\cdot)$ is an indicator function and ζ is a small scalar.

3. Maximum likelihood (ML): which is reduced to a special case of MAP where the prior is neglected.

Both MMSE and MAP are methods, which require an estimation of the posterior distribution (density), but the MAP method does not need to calculate the denominator (integration) and therefore it is more inexpensive computationally; whereas the MMSE requires a complete knowledge of the prior, likelihood and evidence. However, MAP estimate has a drawback, particularly in a high-dimensional space. High probability density does not imply high probability mass. A narrow spike with a very small width (support) can have a very high density, but the actual probability of estimated state (or parameter) belonging to it is small. Hence, the width of the mode is more important than its height in the high-dimensional case.

The criterion of optimality used for Bayesian filtering is the Bayes risk of MMSE. Bayesian filtering is optimal in a sense that it seeks the posterior distribution, which integrates and uses all of the available information expressed by probabilities (assuming they are quantitatively correct). However, as time proceeds, one needs infinite computing power and unlimited memory to calculate the “optimal” solution, except in some special cases (e.g. linear Gaussian or conjugate family case). Hence, in general, we can only seek a suboptimal or locally optimal solution.

3.1.2.2 Kalman filtering

Kalman filtering method [Kal60] provides an analytical solution for the filtering problem [Kal64], in which the sufficient statistics of mean and state-error correlation matrix are calculated and propagated. Kalman filter has a very nice Bayesian interpretation. For the sake of simplicity, we will consider that the measurement and dynamic noises are both Gaussian distributed with zero mean and with constant covariance.

The derivation of KF in the linear Gaussian scenario is based on the following assumptions:

- $E[w_n w_m^t] = Q_n = \Sigma_w \delta_{mn}$; $E[v_n v_m^t] = R_n = \Sigma_v \delta_{mn}$.

- The state and process noise are mutually independent:

$$E[x_n w_m^t] = 0 \text{ for } n \leq m ; E[x_n v_m^t] = 0 \text{ for all } n, m.$$

- The process and measurement noises are mutually independent:

$$E[w_n v_m^t] = 0 \text{ for all } n, m.$$

At each iteration, the KF makes a state prediction for x_n , denoted $\hat{x}_{n|n-1}$. We use the notation $n|n-1$ since we will only use measurements provided until time-step $n-1$ in order to make the prediction at time-step n . The error in the state prediction $\tilde{x}_{n|n-1}$ is described as the difference between the true state and the state prediction, as below:

$$\tilde{x}_{n|n-1} = x_n - \hat{x}_{n|n-1} \quad (3.18)$$

We can define the covariance structure for the expected error on the state prediction as the expected outer product of the state prediction error. This covariance structure is called the error covariance prediction and we denote it by $P_{n|n-1}$:

$$P_{n|n-1} = E[(\tilde{x}_{n|n-1})(\tilde{x}_{n|n-1})^t] \quad (3.19)$$

The filter will also provide an updated state estimate for x_n , given all the measurements provided up to and including time step n . We express these estimates as $\hat{x}_{n|n}$. We similarly define the state estimate error $\tilde{x}_{n|n}$ as below:

$$\tilde{x}_{n|n} = x_n - \hat{x}_{n|n} \quad (3.20)$$

The expectation of the outer product of the state estimate error represents the covariance structure of the expected errors on the state estimate, which is called the updated error covariance and is expressed by $P_{n|n}$:

$$P_{n|n} = E[(\tilde{x}_{n|n})(\tilde{x}_{n|n})^t] \quad (3.21)$$

A prediction is made at a time-step n for the underlying state of the system through enabling the state to transition forward utilizing our model for the dynamics and remarking that $E[w_n] = 0$. This serves as our state prediction:

$$\hat{x}_{n|n-1} = F_{n,n-1}\hat{x}_{n-1|n-1} \quad (3.22)$$

By expanding the expectation in Equation (3.19), this will result with the following equation for the error covariance prediction.

$$P_{n|n-1} = F_{n,n-1}P_{n-1|n-1}F_{n,n-1}^t + Q_n \quad (3.23)$$

We can modify our state prediction into the measurement space. This is a prediction for the measurement, now we can expect to observe.

$$\hat{y}_{n|n-1} = G_n\hat{x}_{n|n-1} \quad (3.24)$$

The variation between the observed and the predicted measurement is the residual measurement, which we want to minimize in this algorithm.

$$v_n = y_n - \hat{y}_{n|n-1} \quad (3.25)$$

In addition, we can calculate the associated covariance for the residual measurement, which is the expectation of the outer product of the measurement residual with itself, $E[v_n v_n^t]$. This is called the covariance residual measurement:

$$S_n = G_n P_{n|n-1} G_n^t + R_n \quad (3.26)$$

Now we will define the updated state estimate to be the prediction and few perturbations in addition, which is provided by multiplying the weighting factor times the measurement residual. The weighting factor, which is called the Kalman Gain, will be discussed below:

$$\hat{x}_{n/n} = \hat{x}_{n/n-1} + K_n v_n \quad (3.27)$$

Furthermore, the updated error covariance could be also calculated by expanding the outer product in Equation (3.21)

$$P_{n/n} = (I - K_n G_n) P_{n/n-1} \quad (3.28)$$

where I is the appropriately sized identity matrix.

Now, we must find the appropriate Kalman filter Gain K_n in order to minimize the mean square state estimation error $E\left[|\tilde{x}_{n/n}|^2\right]$. In other words, we must minimize the trace of the above updated error covariance matrix. After few calculations, we got the optimal gain, which will achieve this:

$$K_n = P_{n/n-1} G_n^t S_n^{-1} \quad (3.29)$$

The KF covariance matrices give us a measure of uncertainty in the predictions and the updated state estimate. This is a highly relevant feature for the different applications of filtering as we then know how much to be able to trust our predictions and estimates. Furthermore, because the method is recursive, then we need to produce an initial covariance that is large enough to contain the initial state in order to ensure a comprehensible performance. The underlying assumption of noise density model is a main weakness in the KF method. Anyway, the KF guarantees an accurate solution for the linear Gaussian prediction and the filtering problem.

3.1.2.3 The Extended Kalman Filter

Kalman Filter method provides a solution for the linear dynamic system represented in Equations (3.3) and (3.6). The main issue in the practical applications is that the equations defining the physical system are commonly non-linear. Consequently, non-linear extensions of KF have been considered and proposed. Example of these extensions is the Extended Kalman Filter (EKF) [Jaz70], which we will present in this section. The EKF is considered to be as a nonlinear standard Bayesian state-estimation algorithm. In EKF, the non-linear state and measurement equations are linearized using the first order Taylor series expansion. The state update function is linearized at the posterior mean of the previous time step and the measurement function at the prior mean of the current time step. In discrete time, the general dynamical system is defined by the discrete nonlinear state space equation:

$$x_n = f(x_{n-1}, u_{n-1}) + w_n \quad (3.30)$$

$$y_n = g(x_n) + v_n \quad (3.31)$$

where w_n and v_n are the process and observation noises respectively which are assumed to be zero mean multivariate Gaussian noises with covariance Q_k and R_k respectively. u_{n-1} is the control vector.

Regarding the equations (3.30) and (3.31), we note that the function f is used to calculate the prediction state using the previous estimation. In addition, we use the function g to calculate the prediction measurement from the prediction state. Anyway, the two functions f and g will not be applied directly to the covariance. Alternatively, the Jacobian matrix (partial derivatives) will be calculated, and here where the ability of the EKF to solve the non-linearity problem lies. The Jacobian will be computed with the current prediction states, and the produced matrices will be used in the KF filter equations. This is the main process to linearize the non-linearity process around the current estimation.

Given the non-linear measurement equation (3.31). The Taylor first order series approximation at the prior mean of the measurement function is:

$$g(x_n) \approx g(\hat{x}_{n/n-1}) + G_n(x_n - \hat{x}_{n/n-1}) \quad (3.32)$$

where the Jacobian of the measurement function is:

$$G_n = \left. \frac{\partial g}{\partial x} \right|_{\hat{x}_{n|n-1}} \quad (3.33)$$

The predicted state estimate is computed by:

$$\hat{x}_{n|n-1} = f(\hat{x}_{n-1|n-1}, u_{n-1}) \quad (3.34)$$

In addition, the covariance predicted estimate is given by:

$$P_{n|n-1} = F_{n-1} P_{n-1|n-1} F_{n-1}^t + Q_{n-1} \quad (3.35)$$

where the state transition matrix is defined to be the Jacobian:

$$F_{n-1} = \left. \frac{\partial f}{\partial x} \right|_{\hat{x}_{n-1|n-1}, u_{n-1}} \quad (3.36)$$

The measurement residual is calculated by:

$$v_n = y_n - g(\hat{x}_{n|n-1}) \quad (3.37)$$

And the measurement residual covariance is given by:

$$S_n = G_n P_{n|n-1} G_n^t + R_n \quad (3.38)$$

We find the optimal gain:

$$K_n = P_{n|n-1} G_n^t S_n^{-1} \quad (3.39)$$

We can now define the updated state estimate by:

$$\hat{x}_{n|n} = \hat{x}_{n|n-1} + K_n v_n \quad (3.40)$$

The estimation of the updated covariance can be get by:

$$P_{n|n} = (I - K_n G_n) P_{n|n-1} \quad (3.41)$$

From the previous equations, the EKF can be considered to provide the optimal terms by “first-order” approximations. Anyway, these approximations could produce great errors in the covariance of the transformed (Gaussian) random variable and the true posterior mean; this will

produce a sub-optimal execution and filter divergence. These are the drawbacks that we will address and solve in the following section by means of the Unscented Kalman Filter (UKF).

3.1.2.4 The Unscented Kalman Filter

The EKF has considered being the standard technique to perform recursive nonlinear estimation. As we saw in the previous section, the EKF method yet provides just an approximation to the optimal nonlinear estimation. Here, we will present an alternative method to the EKF, which will overcome the drawbacks of the EKF that were discussed earlier. This filter, called the unscented Kalman filter (UKF), was proposed by Julier et al [Jul95][Jul96][Jul97], then it was moreover developed by Wan and Van der Merwe [Van00][Van01][Wan00].

The UKF has exceeded the need of the EKF for Jacobians in order to linearize the state equations. Instead, the UKF will approximate the state equations by Gaussian random variables (GRV) which will be applied by a set of deterministic very small points (sigma points) which are carefully chosen. These sample points will determine the actual mean and covariance of the GRV. After generating these sample points through the non-linear system, these sample points will capture the actual posterior mean and the actual posterior covariance to the third order of the Taylor series for any nonlinearity [Wan00].

An augmentation of the covariance and the estimated state will occur with the covariance and the mean of the process noise in the prediction step:

$$x_{n-1|n-1}^a = \left[\hat{x}_{n-1|n-1}^t \quad E(w_n^t) \right] \quad (3.42)$$

$$P_{n-1|n-1}^a = \begin{bmatrix} P_{n-1|n-1} & 0 \\ 0 & Q_n \end{bmatrix} \quad (3.43)$$

Using the augmentation of the state and covariance, sigma points group of $(2L+1)$ will be created where L is the dimension of the augmented state:

$$\chi_{n-1|n-1}^0 = x_{n-1|n-1}^a \quad (3.44)$$

$$\chi_{n-1|n-1}^i = x_{n-1|n-1}^a + \left(\sqrt{(L+\lambda)P_{n-1|n-1}^a} \right)_i, \quad i=1, \dots, L \quad (3.45)$$

$$\chi_{n-1|n-1}^i = x_{n-1|n-1}^a - \left(\sqrt{(L+\lambda)P_{n-1|n-1}^a} \right)_{i-L}, \quad i=L+1, \dots, 2L \quad (3.46)$$

where $(\sqrt{(L + \lambda)P_{n-1|n-1}^a})_i$ is the i^{th} column of the root square matrix $(L + \lambda)P_{n-1|n-1}^a$.

The transition function f will be used to propagate the sigma points as:

$$\chi_{n|n-1}^i = f(\chi_{n-1|n-1}^i), i=0, \dots, 2L \quad (3.47)$$

The predicted state and covariance are produced through recombination of the weighted sigma points:

$$\hat{x}_{n|n-1} = \sum_{i=0}^{2L} W_s^i \chi_{n|n-1}^i \quad (3.48)$$

$$P_{n|n-1} = \sum_{i=0}^{2L} W_c^i (\chi_{n|n-1}^i - \hat{x}_{n|n-1})(\chi_{n|n-1}^i - \hat{x}_{n|n-1})^t \quad (3.49)$$

We will get the state and covariance weights using:

$$\begin{cases} W_s^0 = \frac{\lambda}{L + \lambda} \\ W_c^0 = \frac{\lambda}{L + \lambda} + (1 - \alpha^2 + \beta) \\ W_s^i = W_c^i = \frac{\lambda}{2(L + \lambda)} \\ \lambda = \alpha^2(L + \kappa) - L \end{cases} \quad (3.50)$$

Here, α and κ will manage the spread of the sigma points. β is relevant to the x distribution. In the updating step, the predicted state and covariance are augmented as in the prediction step, but in this step with the mean and covariance of the measurement noise:

$$x_{n|n-1}^a = \begin{bmatrix} \hat{x}_{n|n-1}^t & E(v_n^t) \end{bmatrix} \quad (3.51)$$

$$P_{n|n-1}^a = \begin{bmatrix} P_{n|n-1} & 0 \\ 0 & R_n \end{bmatrix} \quad (3.52)$$

As previously, a group of $(2L+1)$ sigma points is obtained from the augmentation state and covariance where L is the dimension of the augmentation state.

$$\mathcal{X}_{n|n-1}^0 = x_{n|n-1}^a \quad (3.53)$$

$$\mathcal{X}_{n|n-1}^i = x_{n|n-1}^a + (\sqrt{(L + \lambda)P_{n|n-1}^a})_i, i = 1, \dots, L, \quad (3.54)$$

$$\mathcal{X}_{n|n-1}^i = x_{n|n-1}^a - (\sqrt{(L + \lambda)P_{n|n-1}^a})_{i-L}, i = L + 1, \dots, 2L \quad (3.55)$$

In an alternative case, the augmentation of the sigma points could be implemented along the following lines if the UKF prediction has been used:

$$\mathcal{X}_{n|n-1} := \left[\mathcal{X}_{n|n-1}^t \quad E(v_n^t) \right] \pm \sqrt{(L + \lambda)R_n^a} \quad (3.56)$$

where

$$R_n^a = \begin{bmatrix} 0 & 0 \\ 0 & R_n \end{bmatrix} \quad (3.57)$$

The sigma points are calculated by the observation function g :

$$\gamma_n^i = g(\mathcal{X}_{n|n-1}^i), i = L + 1, \dots, 2L \quad (3.58)$$

In this case, the prediction measurements and covariance are generated by recombination of the weighted sigma points as:

$$\hat{y}_n = \sum_{i=0}^{2L} W_s^i \gamma_n^i \quad (3.59)$$

$$P_{y_n y_n} = \sum_{i=0}^{2L} W_c^i (\gamma_n^i - \hat{y}_n)(\gamma_n^i - \hat{y}_n)^t \quad (3.60)$$

The UKF Kalman gain is computed by:

$$K_n = P_{x_n y_n} P_{y_n y_n}^{-1} \quad (3.61)$$

where the state-measurement cross-covariance matrix is obtained by:

$$P_{x_n, y_n} = \sum_{i=0}^{2L} W_c^i (\chi_{n|n-1}^i - \hat{x}_{n|n-1})(y_n^i - \hat{y}_n)^t \quad (3.62)$$

As with the Kalman filter, the updated state is the predicted state plus the innovation weighted by the Kalman gain,

$$\hat{x}_{n/n} = \hat{x}_{n/n-1} + K_n (y_n - \hat{y}_n) \quad (3.63)$$

Moreover, we can obtain the updated covariance by subtracting the predicted measurement covariance, weighted by the Kalman gain, from the predicted covariance as follows:

$$P_{n/n} = P_{n/n-1} - K_n P_{y_n, y_n} K_n^t \quad (3.64)$$

Unlike EKF, the UKF represents a derivative-free algorithm and gives superior execution at an equivalent computational complexity. Despite the fact that the UKF has distinct improvements over the EKF, several limitations still exist. As same in the EKF, these algorithms make a Gaussian assumption on the probability density of the state random variable. In spite of the fact that this assumption is true, and various real-world applications have been successfully implemented based on this assumption. However, the Gaussian assumption will not suffice, and the UKF (or EKF) cannot be applied with confidence.

In such cases, we have to resort to further powerful, but in fact more computationally expensive, filtering criteria such as Monte Carlo and Bayesian algorithms.

3.2 Monte Carlo methods for nonlinear filtering

Several new Monte Carlo based algorithms such as hybrid Monte Carlo, quasi-Monte Carlo and Bayesian bootstrap have been reinvigorated and improved. We can view the Monte Carlo technique as a sort of stochastic sampling approach that intends to tackle the analytically stubborn complex systems.

The power of Monte Carlo methods is that they can solve the difficult numerical integration problems. In recent years, sequential Monte Carlo approaches have attracted more and more attention to the researchers from different areas, with many successful applications in signal and image processing statistics, machine learning, objects tracking, econometrics, automatic control, communications, and in other fields [Dou97]. One of the powerful advantages of the Monte Carlo sequential approaches comes from the ability to perform an on-line estimation

through the combination of the robust Monte Carlo sampling algorithms with Bayesian inference considering an acceptable computational cost.

Particularly, the sequential Monte Carlo (SMC) approach has been used in both state and parameter estimation, the state estimation is sometimes called "particle filter statistics". The Sequential Monte Carlo Method is capable to deal with the non-Gaussian posterior probability of the state in the nonlinear systems; the propagation of the conditional pdf is usually desired in such systems.

The concept of the method is to approximate the state posterior probability by generating a high number of weighted particles or samples utilizing Monte Carlo Methods. In fact, the particle filters are actually an extension to the point mass filters. However, in the particle filters, the particles will accumulate in the high probabilities areas instead of being distributed uniformly over the state.

3.2.1 Monte Carlo methods

Monte Carlo (MC) methods are computational methods that use random numbers. They are basic to many parts of computational science such as phase transitions in statistical physics, electronic structure in computational chemistry and materials science, mechanisms for chemical reactions, etc. Emerging applications include uncertainty quantification and reliability, Bayesian statistics, and nonlinear filtering.

There is a very strong relationship between theoretical analysis and development of new algorithms. Monte Carlo method, which has been proposed first by Metropolis and Ulam in 1949 [Met49], is a numerical algorithm that utilizes random numbers in solving mathematical issues that could not be solved analytically. MC methods are time-consuming methods as it uses random numbers simulation, however, with the development of computers MC methods is more easy to use than before. MC methods present a way to produce samples from a given probability distribution. Furthermore, they provide a solution to the problem of estimating expectations of distribution functions hence computing numerical approximations for integrals.

In further mathematical expressions: Let us consider a random variable X (could be multi-dimensional) with a probability mass function or probability density function $f_X(x)$ that is greater than zero on a set of values X . In this case, the supposed value of a function g of X will be:

$$E[g(X)] = \sum_{x \in \Omega} g(x) f_X(x) \quad (3.65)$$

if X is discrete, and

$$E[g(X)] = \int_{\Omega} g(x) f_X(x) dx \quad (3.66)$$

if X is continuous, where Ω is the support of f_X . Now, let us assume to have an n -sample of X 's, (x_1, \dots, x_n) , then we calculated the mean of $g(x)$ over the sample, then the Monte Carlo estimate will be as follow:

$$\tilde{g}_n(x) = \frac{1}{n} \sum_{i=1}^n g(x_i) \quad (3.67)$$

of $E[g(x)]$. We could, alternatively, express the random variable

$$\tilde{g}_n(X) = \frac{1}{n} \sum_{i=1}^n g(X) \quad (3.68)$$

which we name the Monte Carlo estimator of $E[g(x)]$.

3.2.2 Particle filters

The Particle Filter algorithm is a type of Monte Carlo techniques, which provides a solution for the state estimation problem. The important or fundamental idea of the particle filter, which is also known as the bootstrap filter, condensation algorithm, interacting particle approximations and survival of the fittest, is to represent the needed posterior density function by a set of random particles or samples. These particles will be associated with weights, now we must compute the estimates considering these samples and weights. This Monte Carlo characterization will become an equivalent representation of the posterior probability function when the number of samples becomes quite high, and the solution approaches the optimal Bayesian estimate.

3.2.2.1 The Sequential Importance Sampling Algorithm

Basically, the principle of the particle filtering methods lies on the sequential updating of a distribution utilizing importance-sampling techniques. In 1994, Kong et al [Kon94] have proposed the sequential importance sampling (SIS) algorithm, which is one type of the particle filtering methods. SIS requires the use of importance sampling to solve the recursion equation. In this section, we present the SIS method for the particle filter.

The SIS algorithm that benefits from using an importance density that is a density introduced to represent another density, which cannot be correctly, computed, i.e. the sought posterior density in the present case. Next, the desired samples will be drawn from the importance density rather of the actual density. When one will derive the SIS algorithm, it is beneficial to take into considering the full posterior distribution at time $p(x_{0:n-1} | y_{1:n-1})$, instead of the filtering distribution, $p(x_{n-1} | y_{1:n-1})$, which is just the marginal of the full posterior distribution concerning x_{n-1} .

The main principle idea in SIS is approximating the posterior distribution at $n-1$, $p(x_{0:n-1} | y_{1:n-1})$, by means of a weighted set of samples $\{x_{0:n-1}^i, \omega_{n-1}^i\}_{i=1}^N$, which also named particles, these samples (particles) will be updated recursively in order to get the posterior distribution at the next time step: $p(x_{0:n} | y_{1:n})$. SIS is based on importance sampling.

Importance sampling: The importance sampling techniques are the basis of the sequential Monte Carlo methods that are used by particle filters in solving the problem of the recursive equation. According to the Bayesian methods, we usually know the probability distribution only up to a normalizing constant. We draw samples from the proposal distribution $q(x)$ in order to approximate the target distribution $p(x)$. In general, we need to implement the importance sampling when it is easier to sample from a proposal distribution rather from directly sampling from the target distribution. To overcome the difference between the proposal and targeted distributions, we ought to give every sample x^i by a weight $\omega^i \propto \pi(x^i)/q(x^i)$ where which the function $\pi(x)$ is proportional to $p(x)$ (i.e. $p(x) \propto \pi(x)$) which we know how to evaluate. When applying to our posterior distribution at the time $n-1$, importance sampling gives:

$$p(x_{0:n-1} | y_{1:n-1}) \approx \sum_{i=1}^N \omega_{n-1}^i \delta_{x_{0:n-1}^i} \quad (3.69)$$

where $\delta_{x_{0:n-1}^i}$ is a delta function that is centered at $x_{0:n-1}^i$.

Sequential Importance Sampling: In particle filters method, the important distribution is the marginal or joint distribution of the latent variables at time n , given all observations up to that point. Even so, the complexity of the normalizing constant $p(y_n | y_{1:n-1})$ usually prevents direct calculation so we have to use the importance sampling (IS). Our purpose is to update sequentially the posterior distribution at time n meanwhile not to modify the previously

simulated states $x_{0:n-1}$. In order to implement this, let us suppose there is an importance function, $q(x_{0:n} | y_{1:n-1})$, that is easy to sample from, and that $p(x_{0:n} | y_{1:n-1}) > 0 \Rightarrow q(x_{0:n} | y_{1:n-1}) > 0$. Furthermore, assume that the importance function is chosen so that it updates recursively in time when the next observation becomes available and is of the form [Ris04]:

$$q(x_{0:n} | y_{1:n}) = q(x_n | x_{0:n-1}, y_{1:n})q(x_{0:n-1} | y_{1:n-1}) \quad (3.70)$$

so that we can simply expand each particle $x_{0:n-1}^i$ at time $n-1$ with a new state x_n^i at time n sampled from $q(x_n | x_{0:n-1}, y_{1:n})$. Now to update the weights, ω_{n-1}^i , we notice that, following the importance sampling method, the weights of the particles at time n must be as follows:

$$\omega_n^i \propto \frac{p(x_{0:n}^i | y_{1:n})}{q(x_{0:n}^i | y_{1:n})} \quad (3.71)$$

After that, assuming that a weighted particle approximation $\{\omega_{n-1}^i, x_{n-1}^i\}$ occur for $p(x_{n-1} | y_{1:n-1})$, we can use the IS to find an approximation to $p(x_n | y_{1:n-1})$ where the unnormalized weights are:

$$\omega_n^i \propto \omega_{n-1}^i \frac{p(y_n | x_n^i)p(x_n^i | x_{n-1}^i)}{q(x_n^i | x_{0:n-1}^i, y_{1:n})} \quad (3.72)$$

also, the normalized weights are given by

$$\tilde{\omega}_n^i = \frac{\omega_n^i}{\sum_{j=1}^N \omega_n^j} \quad (3.73)$$

According to the SIS algorithm, for every sequential received measurement, recursive particles and weights are propagated; this is given by algorithm 1.

Algorithm 1: The Sequential Importance Sampling Algorithm**Initialize:** At time $n=0$ 1. For $i=1, \dots, N$ (a) Sample $x_0^i \sim p(x_0)$

(b) Evaluate the importance weights up to a normalizing constant:

$$\omega_0^i = p(y_1 | x_0^i)$$

2. For $i = 1, \dots, N$ normalize the importance weights:

$$\tilde{\omega}_0^i = \frac{\omega_0^i}{\sum_{j=1}^N \omega_0^j}$$

Iterate: For n in 1 to T 1. For $i = 1, \dots, N$ (a) Sample $x_n^i \sim q(x_n | x_{n-1}^i, y_{1:n})$ and $x_{0:n}^i = (x_{0:n-1}^i, x_n^i)$

(b) Evaluate the importance weights up to a normalizing constant:

$$\omega_n^i \propto \omega_{n-1}^i \frac{p(y_n | x_n^i) p(x_n^i | x_{n-1}^i)}{q(x_n^i | x_{0:n-1}^i, y_{1:n})}$$

2. For $i = 1, \dots, N$ normalise the importance weights:

$$\tilde{\omega}_n^i = \frac{\omega_n^i}{\sum_{j=1}^N \omega_n^j}$$

Output: $\{x_n^i, \omega_n^i\}_{i=1}^N$ for $n \in \{0, T\}$.

Degeneracy of the SIS Algorithm: Ideally, the posterior distribution would be the importance density function but this is not possible. For an importance function of the form (Equation 3.70), the variance of the importance weights can only increase over time [kon94]. This has a harmful effect on the accuracy and leads to the degeneracy phenomenon. After only a few steps, nearly all the particles will have negligible weight. As a result, a large amount of computational effort will be devoted to updating a contribution, which has almost zero weight. The degeneracy phenomenon is a big problem in particle filtering. One way to reduce it is to increase the number of samples, N , which may be impractical. Degeneracy can also be

minimized through a good choice of importance function and by including a resampling step in the SIS algorithm.

In practice, iteration of the update equations in 3.70 and 3.72 leads to a degeneracy problem where only a few of the particles will have a significant weight, and all the other particles will have very small weights. Degeneracy is typically measured by an estimate of the effective sample size:

$$N_{eff} = \frac{1}{\sum_{i=1}^N (\omega_n^i)^2} \quad (3.74)$$

where a smaller N_{eff} means a larger variance for the weights, which yields to more degeneracy.

Notice that $N_{eff} \leq N$ and small N_{eff} indicates sharp degeneracy. To decrease the degeneracy, a resampling step is introduced.

3.2.2.2 The Sequential Importance Resampling Algorithm

The sequential importance resampling (SIR) algorithm, developed separately from the SIS algorithm, was first introduced by Gordon et al. [Gor93] and contains a resampling step at each iteration of the sequential importance-sampling algorithm. Since then, resampling has been shown to have both major practical and theoretical benefits [Dou08].

Mostly, all types of the particle filter methods are modifications of the basic SIS method viewed above. The SIR algorithm can be viewed as a variant of SIS in such a way that the proposal distribution $q(x_n | x_{n-1}^i, y_n)$ is considered to be the state transition distribution $p(x_n | x_{n-1}^i)$ and the resampling is done at each iteration. Thus, in the SIR algorithm, the update equations for the particles are reduced to:

$$x_n^i \sim p(x_n | x_{n-1}^i) \quad (3.75)$$

$$\omega_n^i \propto p(y_n | x_n^i) \quad (3.76)$$

In Algorithm 2, we illustrate the algorithmic steps for the sequential importance resampling method. Usually, the simple choice for the proposal distribution is $p(x_n | x_{n-1}^i)$ which is the choice of Gordon et al. [Gor93] who gave the original SIR filter. This gives weights in the

resampling algorithm of $\omega_n^i \propto p(y_n | x_n^i)$. Although resampling reduces the problem of degeneracy, but it introduces other problems, which did not exist with the SIS algorithm.

Algorithm 2: The Sequential Importance Resampling Algorithm

Initialize: At time $n=0$

1. For $i=1, \dots, N$

(a) Sample $x_0^i \sim p(x_0)$

(b) Evaluate the importance weights up to a normalizing constant:

$$\omega_0^i = p(y_1 | x_0^i)$$

2. For $i = 1, \dots, N$ normalize the importance weights:

$$\tilde{\omega}_0^i = \frac{\omega_0^i}{\sum_{j=1}^N \omega_0^j}$$

Iterate: For n in 1 to T

1. For $i = 1, \dots, N$

(a) Resample \tilde{x}_{n-1}^i by resampling from $\{x_{n-1}^i\}_{i=1}^N$ with probabilities $\{\omega_{n-1}^i\}_{i=1}^N$

(b) Set $\{x_{n-1}^i, \omega_{n-1}^i\}_{i=1}^N \rightarrow \left\{x_{n-1}^i, \frac{1}{N}\right\}_{i=1}^N$

(c) Propagate weights $\omega_n^i = \frac{p(y_n | x_n^i)p(x_n^i)}{\pi(x_n^i | x_{0:n-1}^i, y_{1:n})}$

3. For $i = 1, \dots, N$ normalise the importance weights:

$$\tilde{\omega}_n^i = \frac{\omega_n^i}{\sum_{j=1}^N \omega_n^j}$$

Output: $\{x_n^i, \omega_n^i\}_{i=1}^N$ for $n \in \{0, T\}$.

3.2.2.3 Empirical distributions

The previously explained samples can be also seen as empirical distributions of the required state pdfs, i.e. the prior:

$$p(x_n | Y_{n-1}) \approx \frac{1}{N} \sum_{i=1}^N \delta(x_n - x_n^i) \quad (3.78)$$

The resampling step includes producing a new set $\{x_n^{i*} : i = 1, \dots, N\}$ by resampling N times from an approximate discrete representation given by:

$$\begin{aligned} p(x_n | Y_n) &= \frac{p(y_n | x_n) p(x_n | Y_{n-1})}{p(y_n | Y_{n-1})} \\ &\approx p(y_n | x_n) \frac{1}{N} \sum_{i=1}^N \delta(x_n - x_n^i) / p(y_n | Y_{n-1}) \\ &= \frac{1}{N} \sum_{i=1}^N p(y_n | x_n^i) \delta(x_n - x_n^i) / p(y_n | Y_{n-1}) \\ &= \frac{1}{N} \sum_{i=1}^N p(y_n | x_n^i) \delta(x_n - x_n^i) / p(y_n | Y_{n-1}) \\ &= \sum_{i=1}^N \omega_n^i \delta(x_n - x_n^i) \end{aligned} \quad (3.79)$$

so that $\Pr(x_n^{i*} = x_n^j) = \omega_n^j$.

3.2.3 Bayesian bootstrap filter

In the following, we will explain and discuss the Bayesian bootstrap filter (BBF) and illustrate the BBF algorithm. The Bayesian approach is to construct the probability density function (pdf) of the state given all the observations up to that point. Knowledge of the pdf of the state, conditioned on all available measurements provides the most complete description of the state. The principal idea of the bootstrap filter is to express the required pdf as a set of random samples, instead of a function over state-space. As the number of samples is increased, it will provide an exact and equivalent representation of the required pdf.

3.2.3.1 Definition of the Bayesian bootstrap filter

In 90's, Gordon has proposed a new filtering method [Gor93], based on Bayesian state estimation and Monte-Carlo algorithm, the proposed method called bootstrap filter. The great advantage of the bootstrap filter was its capability to manage any non-linearity function and system and/or measurement noise of any distribution. Regarding the non-linear problems, it is hard to get the analytical solutions for the Equations (3.12) and (3.14), here comes the role of the Monte Carlo methods to outwit these difficulties.

The bootstrap filter is a recursive method which works by estimation of the posterior $p(x_n | Y_n)$ from several numbers of samples associated with weights. Assume that we have several independent samples $\{x_{n-1}(i) : i = 1, \dots, N\}$ obtained from the pdf $p(x_{n-1} | Y_{n-1})$. In the bootstrap algorithm, these samples will be propagated and updated within the Bayesian recursion to get a set of values $\{x_n(i) : i = 1, \dots, N\}$, these values are approximately distributed as $p(x_n | Y_n)$. Hence, the method is an approximate simulation of the prediction and update stage for the recursive Bayesian filter. We can illustrate the filter procedure as the following:

Prediction step: Each sample from the pdf $p(x_{n-1} | Y_{n-1})$ is passed through the system model to obtain samples from the prior at time step n :

$$x_n^*(i) = f(x_{n-1}(i), w_{n-1}(i)) \quad (3.80)$$

where $w_{n-1}(i)$ is a sample drawn from the pdf of the system noise $p_w(w_{n-1})$.

Update step: When the measurement y_n is received; the likelihood of each prior sample will be evaluated and the normalized weight for each sample will be obtained:

$$q_i = \frac{p(y_n | x_n^*(i))}{\sum_{j=1}^N p(y_n | x_n^*(j))} \quad (3.81)$$

Thus define a discrete distribution over $\{x_n^*(i) : i = 1, \dots, N\}$, with probability mass q_i associated with each $x_n^*(i)$. Now resample N times from the discrete distribution to generate samples $\{x_n(i) : i = 1, \dots, N\}$, so that for any j $\Pr(x_n(j) = x_n^*(i)) = q_i$, it can be contended that the samples $x_n(i)$ are approximately distributed as the required pdf $p(x_n | Y_n)$.

The above steps of prediction and update form a single iteration of the recursive algorithm. By repeating this procedure, we can get $\{x_n(i) : i = 1, \dots, N\}$ at every time step recursively. To initiate the algorithm, N samples $x_1^*(i)$ are drawn from the known initial pdf $p(x_1 | Y_0) \equiv p(x_1)$.

The resampling portion of the update process is implemented by drawing a random sample u_i from the uniform $(0,1]$ distribution. When

$$\sum_{j=0}^{M-1} q_j < u_i \leq \sum_{j=0}^M q_j \quad (3.82)$$

where $q_0=0$, we choose $x_n(i) = x_n^*(M)$ for making up the posterior.

If N is large, this process takes a very long time to complete, and the problem is further exacerbated when a large number of samples is simulated over many time instants. However, examining the structure of the resampling process, a faster method is proposed in [Bea97], which can still generate useful results. The faster method is based on the expected number of times each prior sample should appear in the posterior. It is described in the next section.

3.2.3.2 Fast bootstrap technique

It is trivial to see that the main limitation of the bootstrap filter is that for large N . It is also easy to observe that the resampling step is where the program spends the most time. The resampling step takes at most N^2 time, which means that doubling the number of samples squares the amount of time needed. As a result, the procedure may become intractable for large sample sizes in real time applications. Gordon et al. [Gor93] suggest that the use of massively parallel computers raises the possibility of real time operation with very large sample sets. A slightly different algorithm than Beadle [Bea97] in suggests the Bootstrap order to speed up the resampling process. In this algorithm, the author proposes a new procedure for the resampling step in which samples are picked into the posterior in groups rather than one at a time as in the weighted bootstrap. Beadle's fast bootstrap algorithm works by generating samples into the posterior based on the expected number of times each value in the prior should be resampled to the posterior. The weighted bootstrap provides a possibly small, but finite, probability of resampling any value $x_n^*(i)$ for $i=1, \dots, N$, from the prior into the posterior. The probability of resampling a particular $x_n^*(M)$ is q_M . To implement this, the value of $x_n^*(M)$ is selected each time a random variable U uniformly distributed on $(0,1]$ satisfies:

$$\sum_{j=0}^{M-1} q_j < U \leq \sum_{j=0}^M q_j \quad (3.83)$$

Thus, the probability of selecting $x_j^*(M)$ is the same as U lying in the interval bounded as shown above. Equivalently, this probability can be expressed as U lying in the range,

$$0 < U \leq q_M \quad (3.84)$$

If M is large, this process takes a very long time to complete, and the problem is further exacerbated when a large number of samples are needed. To overcome the problem, Beadle and

Djuric [Bea97] had proposed a fast bootstrap algorithm. It is based on the expected number of times at which a prior sample appears in the posterior at each time instant, as described below. With a sequence of m trials, the weighted bootstrap resampling procedure can be analyzed as a sequence of Bernoulli trials. Thus, the probability of ‘success’ on a single trial (i.e. selecting some $x_j^*(M)$ in to the posterior) is $p = q_M$ and the probability of “failure” $q = 1 - q_M$. It is therefore easy to see that the probability of selecting some value $x_j^*(M)$ exactly L times in N trials is given by the binomial distribution of order N . Thus, the expected number of times any prior sample $x_j^*(M)$ should appear in the posterior is Nq_j .

Therefore, the way this fast bootstrap algorithm is implemented is to assign a sampling probability of $1/N$ to the N samples. Then at a fixed time j , we pick one of the prior samples from the set $\{x_j^*(i)\}$, say $x_j^*(M)$ and place $\lfloor Nq_M \rfloor$ samples of the $x_j^*(M)$ value into the posterior, (where $\lfloor \cdot \rfloor$ denotes the largest integer function), rather than just picking one value at a time as in the weighted bootstrap method. This method is repeated until a total of N samples have been generated. Then the resampling is stopped, and the posterior samples are projected ahead using the given system model. The resample and projection scheme is repeated until the desired number of observed data has been processed.

Algorithm 3: Bayesian bootstrap filter Algorithm

1. Initializing, at time $n=0$

FOR $i=1: N$, sample $x_0(i) \sim p(x_0)$ and set $n=1$

2. Importance sampling step

(a) FOR $i=1: N$, sample $x_n^*(i) \sim p(x_n|x_{n-1}(i))$ and set $x_{0:n}^*(i) = (x_{0:n-1}(i), x_n^*(i))$.

(b) FOR $i=1: N$, evaluate the normalized importance weights q_i .

3. Selection step

(a) Resample with replacement N particles $(x_{0:n}(i), i = 1, \dots, N)$ from the set

$(x_{0:n}^*(i), i = 1, \dots, N)$ according to the importance weights.

(b) Set $n \leftarrow n+1$ and go to step 2.

3.3 Experimental results

The performance of the techniques that have been cited in this chapter is investigated with various simulations. The comparison of the different filters KF, EKF, UKF and BBF are implemented on satellite images. This section deals with images degraded by different noises and the results after denoising the images using the mentioned filters. Here, we use the mathematical image model given in chapter 1 section 1.3. Here, we adopt a causal image model proposed in [Zha05]:

$$s(m, n) = a_1 s(m, n-1) + a_2 s(m-1, n) + a_3 s(m-1, n-1) \quad (3.85)$$

For implementation of different filters KF, EKF, UKF and BBF a state independent output equation and a state space difference equation as follows:

$$x(m, n) = Cx(m, n-1) + Eu(m, n) + Dw(m, n) \quad (3.86)$$

$$y(m, n) = Hx(m, n) + v(m, n) \quad (3.87)$$

where $x(m, n) = [s(m, n), s(m, n-1), s(m-1, n+1), s(m-1, n)]^T$ and the following system matrices is formulated by

$$C = \begin{bmatrix} a_1 & 0 & a_2 & a_3 \\ 1 & 0 & 0 & 0 \\ 0 & 0 & 0 & 0 \\ 0 & 0 & 1 & 0 \end{bmatrix}, \quad E = \begin{bmatrix} 0 \\ 0 \\ 1 \\ 0 \end{bmatrix}, \quad H = [1 \quad 0 \quad 0 \quad 0] \text{ and } D = \begin{bmatrix} 1 & 0 \\ 0 & 0 \\ 0 & 1 \\ 0 & 0 \end{bmatrix}.$$

The input term $u(m, n)$ is introduced as the recent estimate of pixel $s(m-1, n+1)$. The variables $w(m, n)$ and $v(m, n)$ denotes the process noise and the measurement noise, respectively. The image model coefficients a_1, a_2, a_3 are identified using the Least Squares method.

In this section, to evaluate the performance of the BBF algorithm with respect to the other filters, we choose two satellite images from the European Space Agency (ESA), which has authorized us to use in our work. The first image given in Figure 3.1.a is: “French synergy: contains modified Copernicus Sentinel data (2016), processed by ESA”, capital of the Charente-Maritime department in western France, La Rochelle and surroundings are featured in this Sentinel-2A image, captured on 26 December 2015. The second image given in Figure 3.2.a is

“Seville, Spain: contains modified Copernicus Sentinel data (2015), processed by ESA A”. The western area of Spain’s Province of Seville and its capital with the same name (right) is pictured in this image from the Sentinel-2A satellite, which was captured by the Copernicus Sentinel-2A satellite on 26 July 2016. In our implementation we used the two images in gray level with size of 512×697 pixels and 512×680 pixels respectively. The values of coefficients a_1, a_2 and a_3 related to the two images is given in Table 3.1.

Table 3.1: The values of the images coefficients.

Image	a_1	a_2	a_3
French synergy	0.6382	0.5233	-0.1624
Seville, Spain	0.5512	0.5449	-0.1072

3.3.1 Visual results

3.3.1.1 Application of filters on impulse noise

The simulations are done on a real sentinel satellite remote sensing images. We simulated the original Images with impulse noise with 0.06 density. The original and Noisy images are shown in Figure 3.1 (a), Figure 3.2 (a) and Figure 3.1 (b), Figure 3.2 (b) respectively.

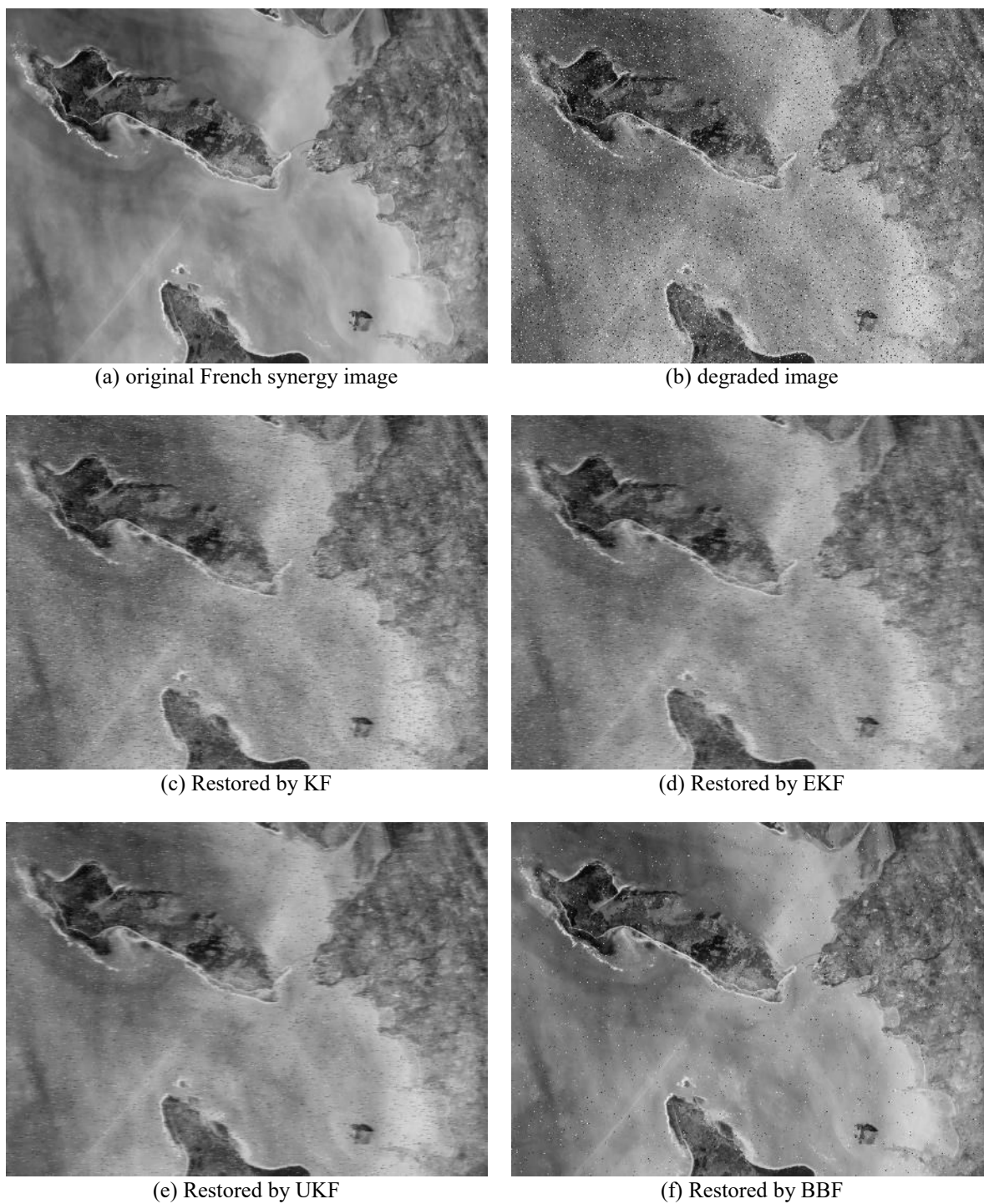


Figure 3.1: Restoration of the French synergy image degraded by impulse noise.

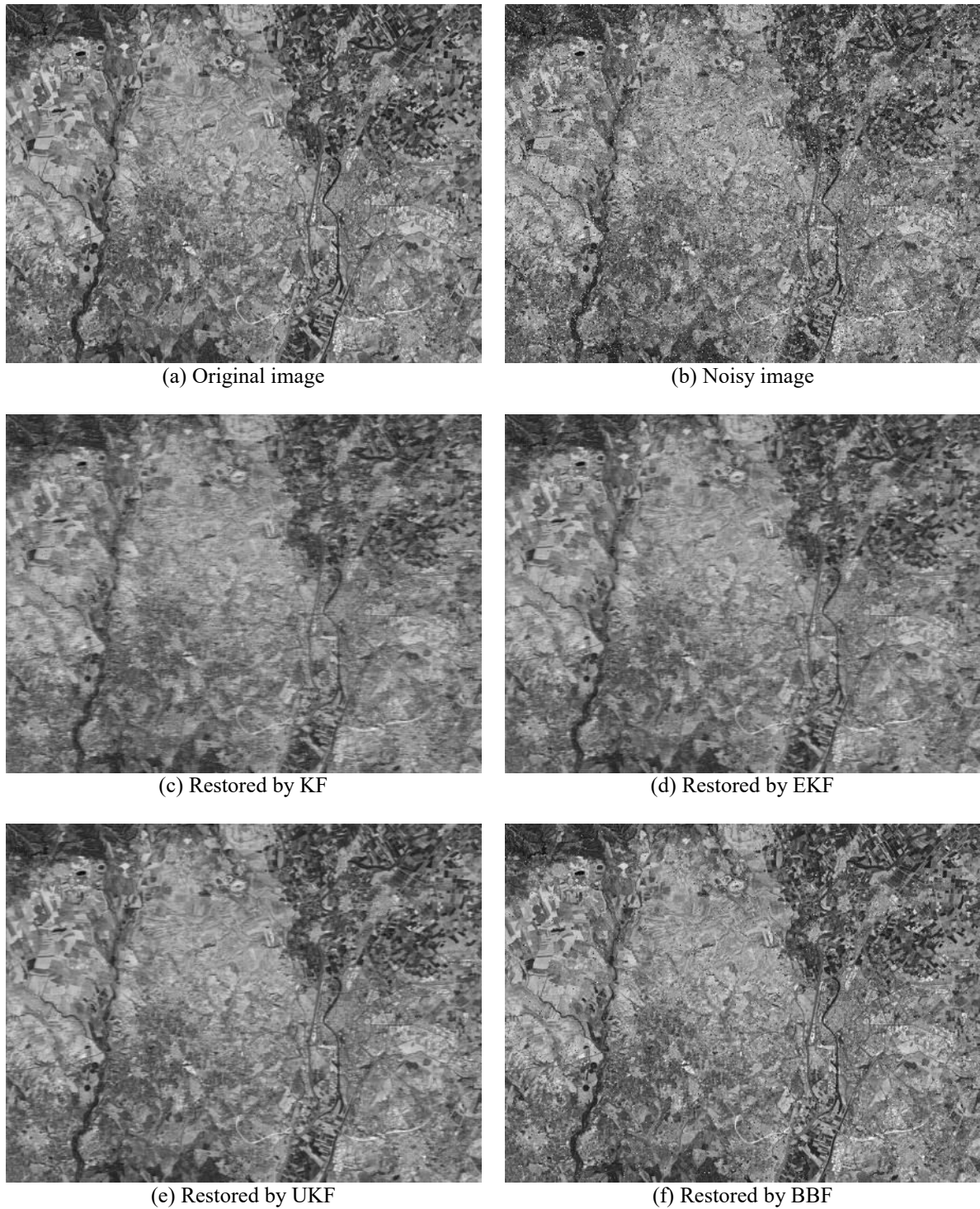


Figure 3.2: Restoration of the Seville Spain image degraded by the impulse noise.

In the figures 3.1 and 3.2, we illustrated our results on denoising the noisy French synergy and Seville Spain Images respectively. In this part of our work, we have denoised both original images with impulse noise of density 0.06. The denoised images indicate that the EKF and UKF gave better results than KF. However, according to the resultant denoised images, the BBF has the best results among the other filters.

3.3.1.2 Application of filters on Gaussian noise

Here, we simulated the original Images with Gaussian noise of a zero mean and variance of 0.03. The original and Noisy images are shown in Figure 3.3 (a), Figure 3.4 (a) and Figure 3.3 (b), Figure 3.4 (b) respectively.

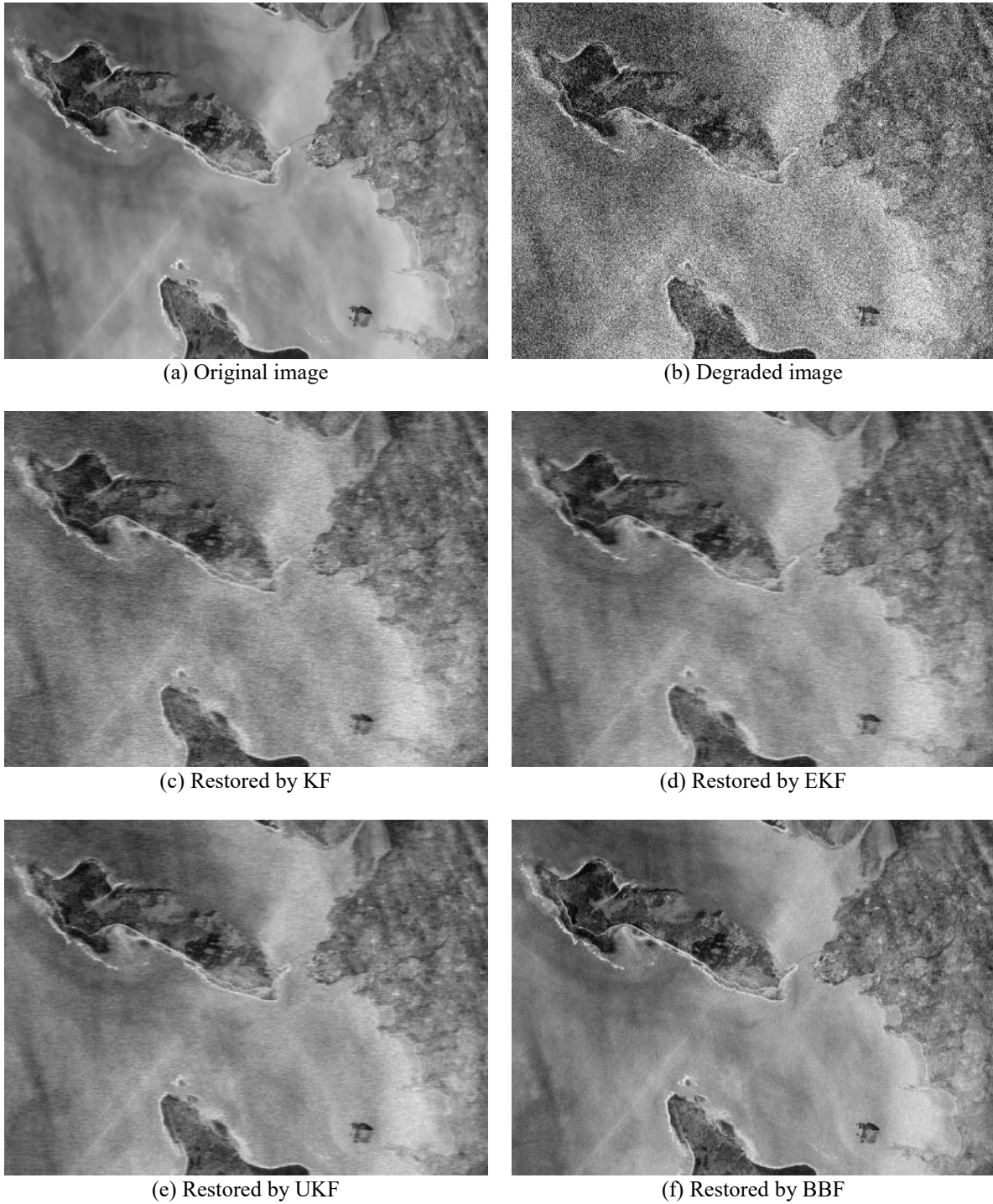


Figure 3.3: Restoration of the French synergy image degraded by the Gaussian noise.

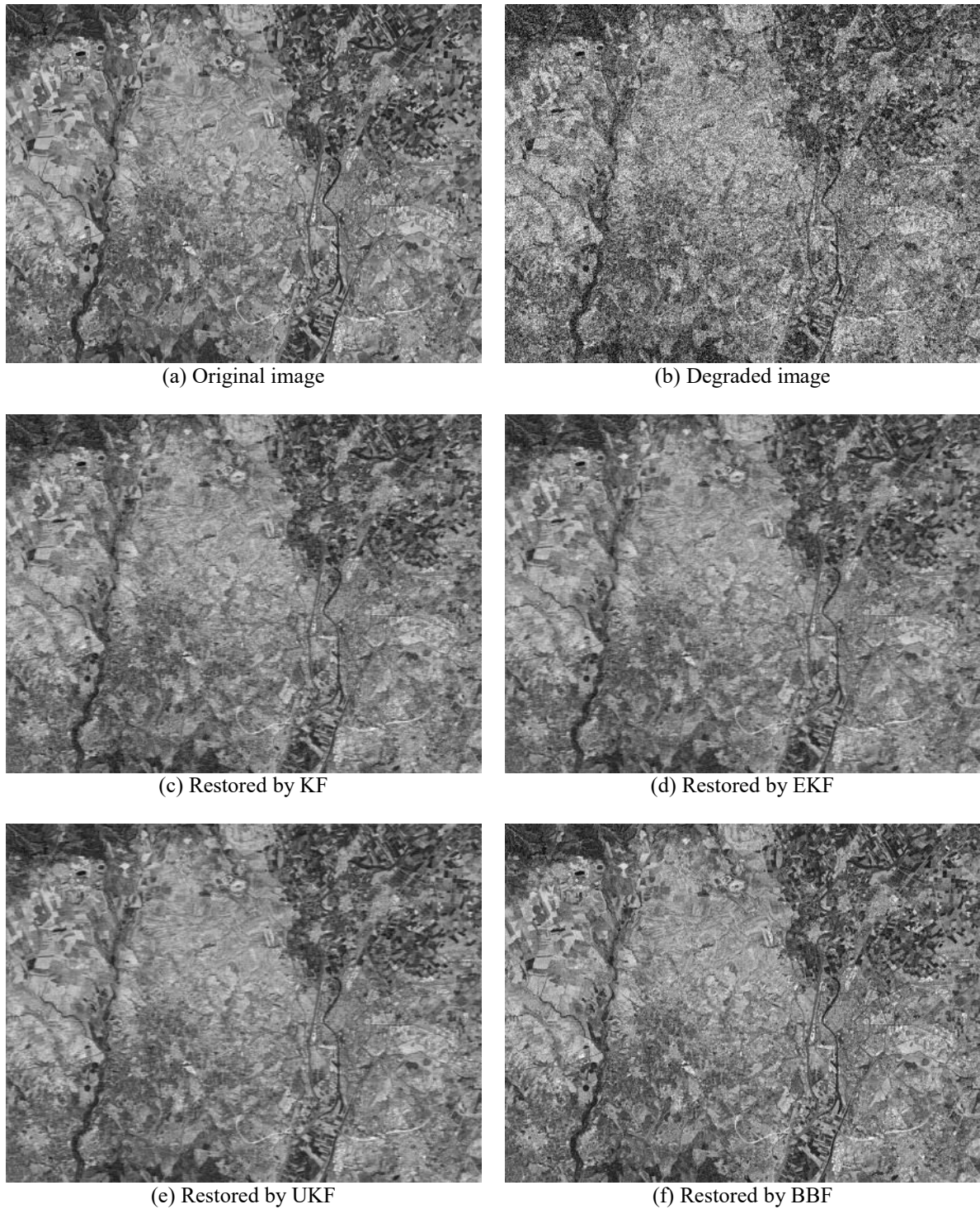


Figure 3.4: Restoration of the Seville Spain image degraded by the Gaussian noise.

Here, in the figures 3.3 and 3.4, we have shown our results on denoising the noisy French synergy and Seville Spain Images respectively. In this part of our work, we have corrupted both images with a Gaussian noise of 0 mean and variance of 0.03. The denoised images show that the EKF and UKF gave better results than KF. However, according to the resulted denoised images, the BBF has the best results among the other filters.

3.3.1.3 Application of filters on Speckle noise

In this part, we simulated the original Images with speckle noise of a zero mean and variance of 0.05. The original and Noisy images are shown in Figure 3.5 (a), Figure 3.6 (a) and Figure 3.5 (b), Figure 3.6 (b) respectively.

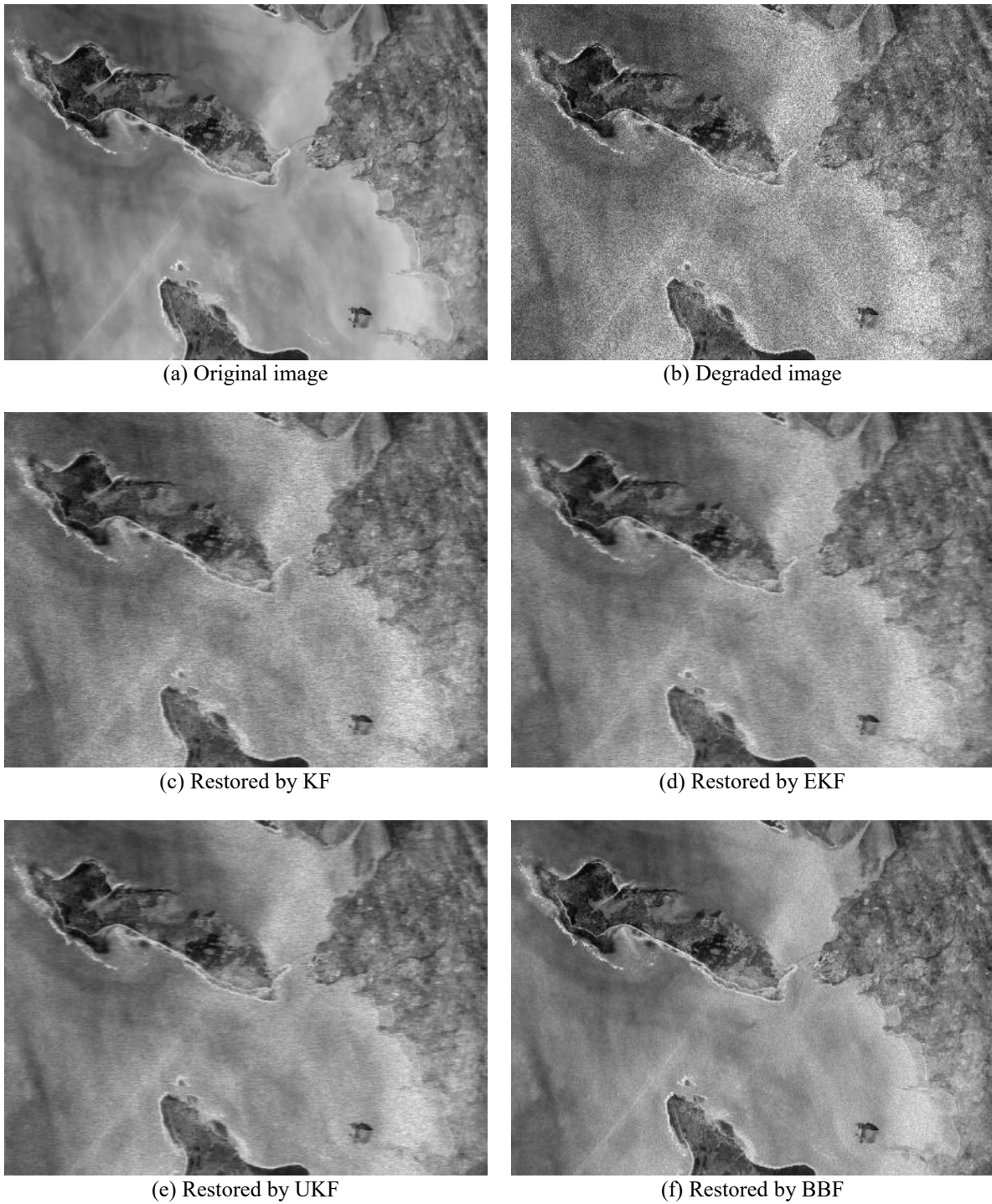


Figure 3.5: Restoration of the French synergy image degraded by the speckle noise.

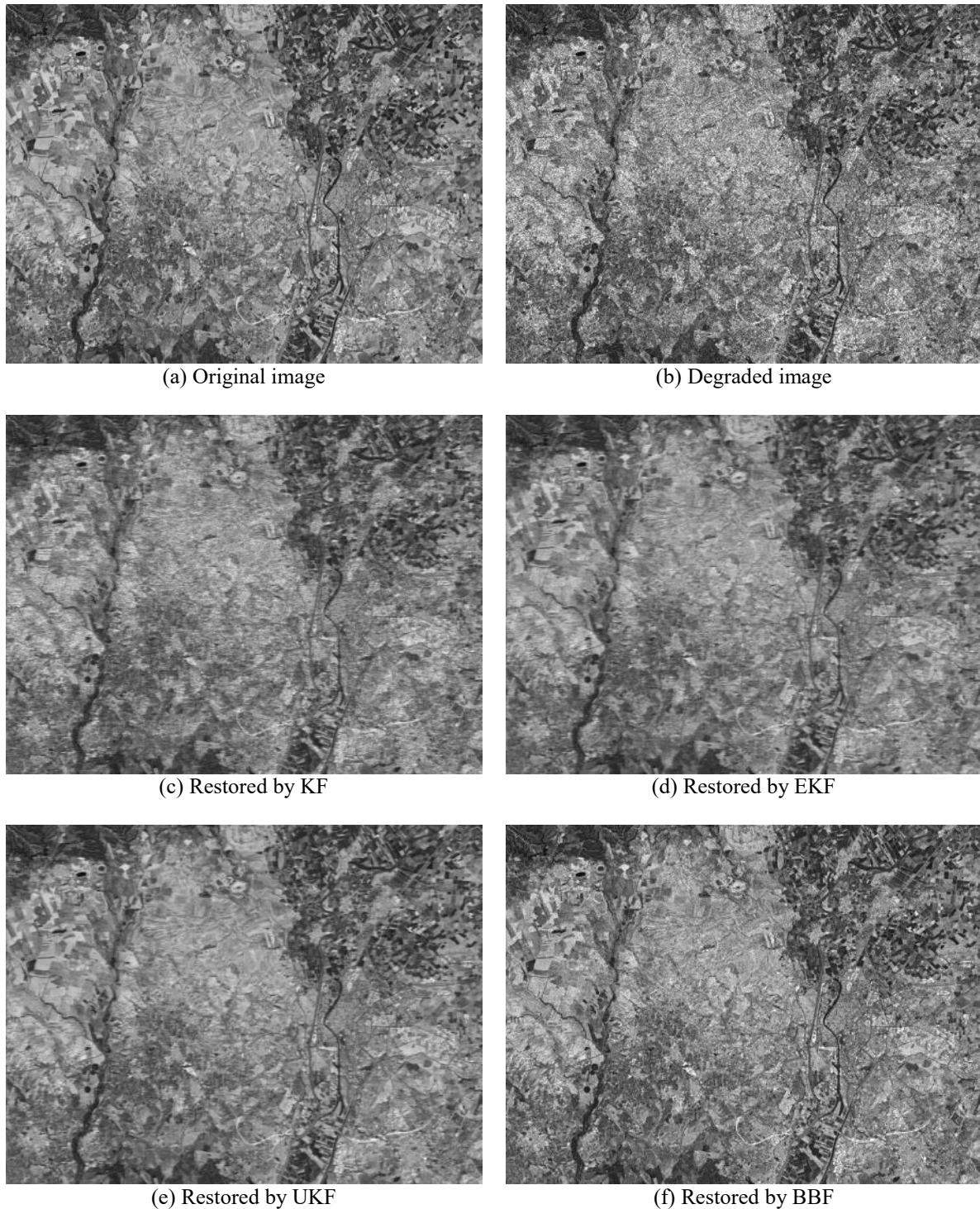


Figure 3.6: Restoration of the Seville Spain image degraded by the speckle noise.

In the figures 3.5 and 3.6, we have shown our results on denoising the noisy French synergy and Seville Spain Images respectively. Here, we have corrupted both images with a speckle noise of 0 mean and variance of 0.05. The denoised images show that the EKF and UKF gave better results than KF. However, according to the resulted denoised images, the BBF has the best results among the other filters.

3.3.2 Metrics results

In the previous section we corrupted the French synergy and the Seville Spain images with the most common types of noise, impulse, Gaussian and speckle then, we have shown the resulted denoised images using KF, EKF, UKF and BBF. Now in this section, we will show our metric results with means of ISNR (M_1), RMSE (M_2) PSNR (M_3). We will use both, tables and line charts in order to illustrate our numerical results that have been obtained of denoising the both images by the mentioned filters.

3.3.2.1 French synergy image

Here, we will show the metric results that we obtained from the denoised SAR image results in Table 3.2 for all types of noise using the KF, EKF, UKF, and BBF restoration methods for the French synergy image.

Table 3.2: The metric results obtained from the denoised French synergy image.

Filters	KF			EKF			UKF			BBF		
	M_1	M_2	M_3									
Salt & Pepper	5.26	16.75	23.62	5.57	15.42	24.34	6.33	12.62	26.08	6.84	11.03	27.25
Gaussian	5.41	16.09	23.97	5.93	14.04	25.15	6.46	12.19	26.38	7.26	9.85	28.23
Speckle	5.05	17.70	23.14	5.64	15.17	24.48	6.00	13.76	25.33	6.36	12.53	26.14

From the Table 3.2, we can notice that the BBF has achieved the best results among the other filters used which support the image results that have been shown in the previous section.

3.3.2.2 Seville Spain image

Now, we will show the denoised ISNR, RMSE and PSNR results in Table 3.3 for all types of noise using the KF, EKF, UKF, and BBF for the Seville Spain image.

Table 3.3: The metric results obtained from the denoised Seville Spain image.

Filters	KF			EKF			UKF			BBF		
	M_1	M_2	M_3									
Salt & Pepper	4.20	22.21	21.17	5.06	17.68	23.15	5.95	13.95	25.21	6.54	11.93	26.57
Gaussian	4.91	18.37	22.82	5.15	17.26	23.36	5.46	15.90	24.07	6.00	13.79	25.31
Speckle	4.33	21.43	21.48	4.54	20.30	21.95	4.92	18.32	22.84	6.18	13.14	25.73

From the Table 3.3, we can notice that the BBF has achieved the best results among the other filters used which support the image results that have been shown in the previous section.

3.3.2.3 Remark

We have carried out our practical experiments using MATLAB software running on Dell CORE i5 machine with 16 Gb. During our work with BBF, we took the number of samples $N=500$, the process time for the BBF to restore the satellite image was approximately 1526 seconds. The introduced fast technique applied to the BBF algorithm to restore the satellite images has reduced the process time to approximately 87 seconds, meanwhile, the results produced was, approximately, same as the results produced from the BBF.

Conclusion

The restoration process is a very important and necessary task in the digital image processing. Various noise models available can distort the satellite images up to any extent. In this chapter, we analyzed that analytical methods for filtering and Monte Carlo methods for nonlinear filtering with resample are too computational complex for image restoration. Hence, we adopted the Bayesian bootstrap filter to the area of image restoration to mitigate the computational problem found in conventional Kalman filter, Extended Kaman filter and Unscented Kalman filter. In this chapter we studied the BBF algorithm for satellite image restoration. This filter has shown interesting results among the other used filters. A comparison with other restoration methods, KF, EKF, and UKF was presented in this chapter. The efficiency of the BBF performed based on ISNR, MSE and PSNR. Our visual and metrics results indicate the high performance of BBF in restoring degraded satellite images compared with the results obtained from the other filters. In this chapter, we also proposed the usage of FBBF in the satellite image restoration, where the FBBF has performed the same results as the BBF but with a noticeable reduction in consumed time. Using the resampling process, BBF algorithm has introduced a solution for the degeneracy phenomenon which is a big problem in particle filtering, yet this resampling process noticed to produce another problem as the number of sampling is increased. In the resampling step, the samples will be distributed in a discrete manner, this problem, if it was not solved properly, will yield to sample collapse or what is known as losing diversity among the samples. To solve the problem of losing diversity among the particles we will propose in chapter 4 a new method in the resampling stage.

References

- [Ang89] D. L. Angwin and H. Kaufman, Image restoration using reduced order models, *Signal Processing*, Vol.16, pp. 186-193, 1989.
- [Arb04] D. Arbel, E. Cohen, M. Citroen, D. G. Blumberg, and N. S. Kopeik, Landsat TM Satellite Image Restoration Using Kalman Filters, Vol. 70, No. 1, pp. 91-100, January 2004.
- [Ban97] M. R. Banham and A. K. Katsaggelos, Digital Image Restoration, *IEEE Signal Processing Magazine*, pp. 24-41, 1997.
- [Bea97] E. R. Beadle, P. M. Djuric, A fast-weighted Bayesian bootstrap filter for nonlinear model state estimation, *IEEE Transactions on Aerospace and Electronic Systems*, Vol. 33, Issue: 1, pp. 338 – 343, 1997.
- [Bie83] J. Biemond, J. Rieske and J. Gerbrands, A fast Kalman filter for images degraded by both blur and noise, *IEEE Trans. Acoust. Speech Signal Process.*, Vol. 31, pp. 1248-1256, October 1983.
- [Cit92] S. Citrin, and M. R. A. Sadjadi, A Full-Plane Block Kalman Filter for Image Restoration, *IEEE Tran. On Image Processing*, Vol. I, No.4, pp. 488-495, October 1992.
- [Dou97] A. Doucet, Monte Carlo methods for Bayesian estimation of hidden Markov models: Application to radiation signals, Ph.D. thesis, Univ. Paris-Sud Orsay, 1997.
- [Dou08] A. Doucet and A. M. Johansen, A Tutorial on Particle Filtering and Smoothing: Fifteen years later. Technical report, Institute of Statistical Mathematics, Japan and Department of Statistics, University of Warwick, 2008.
- [Gor93] N. J. Gordon, D. J. Salmond and A. F. M. Smith, Novel approach to nonlinear/non-Gaussian Bayesian state estimation, *IEE Proceedings-F*, Vol. 140, No. 2, pp. 107-113, 1993.
- [Gor95] N. J. Gordon, D. J. Salmond and C. Ewing, Bayesian State Estimation for Tracking and Guidance Using the Bootstrap Filter, *Journal of Guidance. Control and Dynamics*, Vol. IS. No. 6, pp. 1434-1443, 1995.
- [Ho64] Y. C. Ho and R. C. K. Lee, A Bayesian approach to problems in stochastic estimation and control, *IEEE Trans. Automat. Contr.*, vol. 9, pp. 333-339, Oct. 1964.
- [Jai89] A. K. Jain, *Fundamentals of Digital image processing*, Englewoods Cliffs, NJ: Prentice Hall, (1989).

- [Jaz70] A. H. Jazwinski, *Stochastic Processes and Filtering Theory*, New York: Academic Press, 1970.
- [Jul95] S. J. Julier, J. K. Uhlmann, and H. F. Durrant-Whyte, "A new approach for filtering nonlinear systems," in *American Control Conference*, Vol. 3, pp. 1628–1632, 1995.
- [Jul96] S. J. Julier and J. K. Uhlmann, *A General Method for Approximating Nonlinear Transformations of Probability Distributions*. Technical report, RRG, Dept. of Engineering Science, University of Oxford, 1996.
- [Jul97] S. J. Julier and J. K. Uhlmann, "A New extension of the Kalman filter to nonlinear systems," in *AeroSense'97*, pp. 182–193, 1997.
- [Kal60] R. E. Kalman, "A New Approach to Linear Filtering and Prediction Problems," *Journal Transactions of the ASME-Journal of Basic Engineering*, Vol. 82, Series D, pp. 35-45, 1960.
- [Kal64] R. E. Kalman, "When is a linear control system optimal?," *Trans. ASME, Ser. D, J. Basic Eng.*, Vol. 86, pp. 51-60, 1964.
- [Koc92] S. Koch H. Kaufman, "Image Restoration Using Extended Kalman Filters," *IFAC Proceedings*, Vol. 25, Issue 14, July, pp. 477-480, 1992.
- [Kon94] A. Kong, J. S. Liu and W. H. Wong, "Sequential imputations and Bayesian missing data problems." *Journal of the American statistical association*, 89 (425), pp. 278–288, 1994.
- [Kra85] S. C. Kramer, *The Bayesian approach to recursive state estimation: Implementation and application*, Ph.D. thesis, UC San Diego, 1985.
- [Kra88] S. C. Kramer and H. W. Sorenson, "Recursive Bayesian estimation using piece-wise constant approximations," *Automatica*, Vol. 24, pp. 789-901, 1988.
- [Met49] N. C. Metropolis and S. M. Ulam, "The Monte-Carlo Method," *J. Amer. Stat. Assoc.*, 44: pp. 335–341, 1949.
- [Pol94] A. Pole, M. West, and P. J. Harrison, *Applied Bayesian Forecasting and Time Series Analysis*. New York: Chapman-Hall, 1994.
- [Pra13] K. Praveena, A. Ravikumar, "Design of Inertial Navigation System using Kalman Filter," *International Journal of Engineering Inventions*, Vol. 2, Issue 12, pp. 76-82, December 2013.
- [Rao01] K. D. Rao, M. N. S. Swamy, and E. I. Plotkin, "Image restoration using an hybrid approach based on DWT and SMKF," *IEEE Proc. Int. Image Proc. Conf.*, pp. 249-252, 2001.

- [Ris04] B. Ristic, S. Arulampalam and N. Gordon, Beyond the Kalman Filter: Particle filters for tracking applications, Artech House, 2004.
- [Sor71] H. W. Sorenson and D. L. Alspach, Recursive Bayesian estimation using Gaussian sums, *Automatica*, Vol. 7, pp. 465-479, 1971.
- [Sor74] H. W. Sorenson, On the development of practical nonlinear filters, *Inform. Sci.*, Vol. 7, pp. 253–270, 1974.
- [Sor85] H. Sorenson, Kalman filtering theory and applications. IEEE Press, 1985.
- [Sub07] G. R. K. S. Subrahmanyam, A. N. Rajagopalan, and R. Aravind Importance Sampling Kalman Filter for Image Estimation, *IEEE Signal Processing Letters*, Vol. 14, No. 7, pp. 453-456, 2007.
- [Tek86] A. M. Tekalp, H. Kaufman, and J. W. Woods, Identification of image and blur parameters for the restoration of non-causal blurs. *IEEE Transactions on Acoustic, Speech and Signal Processing*, ASSP-4(4), pp. 963-971, August 1986.
- [Van00] R. Van der Merwe et al, The unscented kalman filter, Technical Report CUED/F-INFENG/TR 380, Cambridge University Engineering Department, Cambridge, England, 2000.
- [Van01] R. Van der Merwe and E. A. Wan, Efficient derivative-free kalman filters for online learning, In To appear in European Symposium on Artificial Neural Networks, (ESANN), Bruges, Belgium, 2001.
- [Wan00] E. Wan, R. Van Der Merwe, The unscented kalman filter for nonlinear estimation, in: Adaptive Systems for Signal Processing, Communications, and Control Symposium 2000. AS-SPCC. The IEEE 2000, pp. 153-158, 2000.
- [Wan13] R. Wang and S. Li, A novel algorithm for image denoising based on unscented Kalman filtering, *Int J Information and Communication Technology*, Vol. 5, Nos. 3/4, pp. 343-353, 2013.
- [Wes97] M. West and J. Harrison, Bayesian Forecasting and Dynamic Models, 2nd ed., New York: Springer, 1997.
- [Woo77] J. W. Woods and C.W. Radewan, Kalman filtering in two dimensions, *IEEE Trans. Inf. Theory*, Vol. 23, pp. 473-482, 1977.
- [Woo81] J. W. Woods and V. K. Ingle, Kalman filtering in two dimensions: Further results, *IEEE Transactions on Acoustic, Speech and Signal Processing*, ASSP-29 (2), pp. 188-197, 1981.

- [Xin13] Y. Xincun, O. Yongzhong, S. Fuping and F. Hui, Kalman filter applied in underwater integrated navigation system, *Geodesy and Geodynamics*, Vol. 4 No.1, pp. 46-50, 2013.
- [Zha05] Y. Zhai et al, Image restoration using a hybrid combination of particle filtering and wavelet denoising, *IEEE International Conference on Image Processing*, pp. 790-793, 2005.

Chapter 4

Reduction of speckle noise in SAR images

Table of Contents

Introduction	155
4.1 Nonparametric multivariate density estimation.....	156
4.1.1 Kernel density estimation	157
4.1.2 Kernel-diffeomorphism estimator	159
4.1.2.1 Case of one dimension.....	159
4.2 A proposed method to reduce the speckle noise	162
4.2.1 Description of SAR images	163
4.2.2 SAR image mathematical model	165
4.2.3 Nonparametric Bayesian bootstrap filtering.....	167
4.2.4 Image Denoising Using Discrete Wavelet Transform (DWT).....	168
4.2.4.1 DWT Process:.....	168
4.2.4.2 Thresholding Process.....	170
4.3 Experimental results	170
4.3.1 Results of SAR image Sydney Australia.....	172
4.3.2 Results of SAR image City of Paris	176
Conclusion.....	180
References	182

Introduction

Satellite images and medical images, are usually degraded by noise during image acquisition and/or transmission process. Noise can be introduced into an image depending on how the image is created in several ways. Satellite image containing the noise signals lead to a distorted image, which could not be understood and studied properly. Noise can be defined as any disturbance that changes the original signal information. Image noise is a random, usually unwanted variation in brightness or color information in an image [Sal10]. Noise affects the pixels of the original image, resulting in a distorted output image.

There are several types of noise that may be introduced in the image pixel, the three mainly types, as impulsive noise (salt & pepper), additive noise (Gaussian Noise) and multiplicative noise (Speckle Noise). Reducing noise from the medical images, satellite images etc. is a main challenge for the researchers in digital image processing. Noise reduction helps the possibility of better interpretation of the content of the image. Depending on the nature of the noise, such as additive or multiplicative noise, there are several approaches for removing the noise from an image. Images that degraded due to multiplicative noise effects are usually harder to be denoised than ones affected by an additive noise, that is because of the nature of the multiplicative noise.

In general, SAR images are subject to be affected by speckle noise more than other types of noise [Zhu13]. There are several speckle reduction filters in the literature as lee [Lee80], kuan [Kua85] [Kua87] and frost [Fro82] filters, they are still common used filters [Ahi11]. There are also many filters which can be used to reduce speckle noise such as, median filter, wiener filter and Kalman filter [Ond16] [Pri16].

In our work, we introduced a novel method, which reduces speckle noise in synthetic aperture radar (SAR) images retaining the original content of these images. This method is based on the nonparametric multivariate density estimation [Bou10][Hwa94][Lof65] and the Bayesian bootstrap filter [Mar17][Mar18b]. In order to facilitate the process of density estimation, the nonparametric approach must rely in general on the assumption that the underlying density is smooth. Many nonparametric density estimators are motivated as extensions of the classical histogram [Rub14][Kol13][Jar09][Tar70]. The multivariate nonparametric density estimation of posterior density is used in the resampling step of the Bayesian bootstrap filter. This estimation technique makes it possible to regularize the bootstrap filter, which means drawing the samples continuously rather than discretely. The chapter is organized as follows. Section 4.1 presents a nonparametric multivariate density estimation. In

the section 4.2, a proposed method to reduce the speckle noise is introduced. Experimental results are presented to demonstrate the accuracy of the proposed method for SAR images denoising in section 4.3.

4.1 Nonparametric multivariate density estimation

In signal-processing applications, most algorithms work properly if the probability densities of the multivariate signals (or noises) are known. Unfortunately, in reality, these densities are usually not available, and parametric or non-parametric estimation of the densities becomes critically needed. Regarding data generating, the non-parametric density estimation methods have simplest and less difficult assumptions about distributing the data than the assumptions made by the parametric density estimation [Sco92]. An estimator of an unknown probability density, regression curve, or other function of interest is shape constrained if it is restricted to produce estimates having some desired qualitative features. Qualitative features that might be of interest include monotonicity, unimodality, or convexity, for example. Parametric estimators may be considered shape constrained to a high degree, as their qualitative characteristics are pre-established. Nonparametric function estimators, conversely, have a low degree of shape restriction, their qualitative features being determined primarily by the data. A probability density function (pdf), $f(x)$, of a p -dimensional data x is a continuous and smooth function which satisfies the following positivity and integrate-to-one constraints:

$$f(x) \geq 0, \quad \int_{\mathbb{R}^p} f(x) dx = 1 \quad (4.1)$$

We generally consider the analysis of a p -variate random sample $\{x_n, n=1, \dots, N\}$ from an unknown density function, $f(x)$, where $x \in \mathbb{R}^p$. It is worth reminding ourselves that (theoretically) for the analysis of a random sample, perfect knowledge of the density functions $f(x)$ means that anything we may need to know can be computed. In practice, the computation may be quite complicated if the dimension of the data is high, but the greatest challenge comes from not knowing a parametric form for the density $f(x)$. In [Fis32], Fisher referred to this step in data analysis as the problem of specification. Nonparametric methodology provides a consistent approach for approximating in a large class of unknown densities, at a cost of less efficient estimation when the correct parametric form is known. Of course, if an incorrect parametric form is specified, then bias will persist. Kernel density estimation is the most widely used practical method for accurate nonparametric density estimation. Numerous articles have

been written on its properties, applications, and extensions [Sil86][Sco92]. In this chapter, we are interested to use this method for estimation of posterior density in the resampling step of the Bayesian bootstrap filter.

4.1.1 Kernel density estimation

To estimate the unknown density function f , one can use parametric or nonparametric methods. The parametric ones, e.g., the maximum likelihood method, require assumptions on the form of the unknown density. Then, the only problem is to estimate the parameters. But sometimes, having no additional information about the distribution, we should use nonparametric methods, like the histogram or the kernel estimator. The kernel density estimator (KDE), introduced in [Ros56] (in the univariate case), is characterized by two components: the bandwidth $h(n)$ and the kernel K . We consider its multivariate version, $p \geq 1$ (see e.g., [Sil86]). Multivariate kernel density estimation is an important technique in multivariate data analysis and has a wide range of applications [Sco92]. However, its widespread usefulness has been limited by the difficulty in computing an optimal data-driven bandwidth. We remedy this deficiency in this section.

Definition 4.1: Let $X = (X_1, X_2, \dots, X_p)^T$ denote a p -dimensional random vector with density $f(x)$ defined on \mathbb{R}^p , and let $\{x_1, x_2, \dots, x_n\}$ be an independent random samples drawn from $f(x)$. The general form of the kernel estimator of $f(x)$ is [Wan93]:

$$\hat{f}_H(x) = \frac{1}{n} \sum_{i=1}^n K_H(x - x_i) \quad (4.2)$$

where $K_H(x) = |H|^{-1/2} K(H^{-1/2}x)$, $K(\cdot)$ is a multivariate kernel function with $K \geq 0$ and $\int_{\mathbb{R}^p} K(t) dt = 1$, and H is asymmetric positive definite $p \times p$ matrix known as the bandwidth matrix.

The choice of the kernel function K is not crucial to the accuracy of kernel density estimators, so we use the standard multivariate normal kernel throughout:

$$K_H(x) = (2\pi)^{-p/2} |H|^{-1/2} \exp\left[-\frac{1}{2} x^T H^{-1} x\right] \quad (4.3)$$

where H plays the role of the covariance matrix. On the other hand, the choice of the bandwidth matrix H is the single most important factor affecting its accuracy since it controls the amount and orientation of smoothing induced.

The bandwidth matrix can be restricted to a class of positive definite diagonal matrices, and then the corresponding kernel function is known as a product kernel. However, there is much to be gained by choosing a full bandwidth matrix, where the corresponding kernel smoothing is equivalent to pre-rotating the data by an optimal amount and then using a diagonal bandwidth matrix. It has been widely recognized that the performance of a kernel density estimator is primarily determined by the choice of bandwidth, and only in a minor way by the choice of kernel function. A large body of literature exists on bandwidth selection for univariate kernel density estimation [Mar87][Jon96]. However, the literature on bandwidth selection for multivariate data is very limited. In [Sai94], authors discussed the performance of bootstrap and cross-validation methods for bandwidth selection in multivariate density estimation and found that the complexity of finding an optimal bandwidth grows prohibitively as the dimension of data increases. A less variable cross-validation algorithm using the plug-in method, which requires auxiliary smoothing parameters, is presented in [Wan94]. The technology for choosing these auxiliary smoothing parameters is not well developed. An alternative plug-in algorithm for bandwidth selection for bivariate data is presented in [Duo03]. This plug-in method has the advantage that it always produces a finite bandwidth matrix and requires computation of fewer pilot bandwidths. However, it cannot be directly extended to the general multivariate setting.

The most commonly used optimality criterion for selecting a bandwidth matrix is the mean integrated squared error (*MISE*) given by:

$$MISE(H) = E \left[\int (\hat{f}_H(x) - f(x))^2 dx \right] \quad (4.4)$$

When data are observed from the multivariate normal density and the diagonal bandwidth matrix [Sco92][Bow97], denoted by $H = \text{diagonal}(h_1, h_2, \dots, h_p)$ is employed. The optimal bandwidth that minimizes *MISE* can be approximated by:

$$h_i = \sigma_i \left\{ \frac{4}{(p+2)n} \right\}^{1/(p+4)} \quad (4.5)$$

for $i=1, 2, \dots, p$, where σ_i is the standard deviation of the i^{th} variate, and can be replaced by its sample estimator in practical implementations.

Example 4.1: We consider estimating the density of the Gaussian mixture f given by:

$$f(x) = \frac{1}{4\pi} e^{-\frac{1}{2}(x_1^2+x_2^2)} + \frac{1}{4\pi} e^{-\frac{1}{2}((x_1-2)^2+x_2^2)} \quad (4.6)$$

from 500 randomly generated points. We employ the Matlab routine for 2-dimensional data. The routine is an automatic bandwidth selection method specifically designed for a second order Gaussian kernel [Bot10]. The Figure 4.1 shows the joint density estimate that results from using the automatically selected bandwidth.

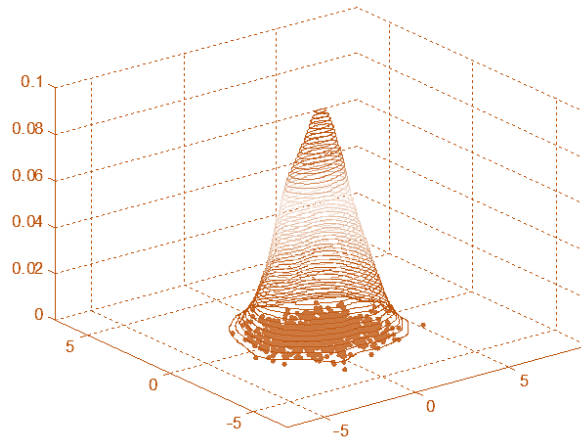


Figure 4.1: Kernel density estimate with diagonal bandwidth for synthetic normal mixture data.

4.1.2 Kernel-diffeomorphism estimator

The kernel density estimation method is not so attractive when the density has its support confined to a bounded space U of IR^p . A new nonparametric probability density function (pdf) estimator called the ‘kernel-diffeomorphism estimator’, which suppress border convergence difficulties by using an appropriate regular change of variable have been suggested in [Sao97].

4.1.2.1 Case of one dimension

Given a sequence of independent samples X_1, X_2, \dots, X_N identically distributed as a random variable X with pdf f_X , we can form a sequence of estimators of f_X such that $\hat{f}_{X,N}$ depends only on the first N observations. Let F be the set of all continuous and bounded pdfs of random variables whose support is confined to the real interval $I=[a, b]$.

Definition 4.2: A kernel-diffeomorphism estimator is an estimator $\hat{f}_{X,N}$ of the form:

$$\hat{f}_{X,N}(x) = \frac{|\phi'(x)|}{Nh_N} \sum_{n=1}^N K\left(\frac{\phi(x) - \phi(X_n)}{h_N}\right) \quad (4.7)$$

with:

- (a) a pdf K , called kernel;
- (b) a sequence of positive real number h_N , called bandwidth; and
- (c) a regular C^l -diffeomorphism ϕ from $]a, b[$ to IR (i.e. its first derivative $\phi'(x)$ tends to infinity when x tends to the lower or the higher bound).

We give the two important families of diffeomorphism:

$$i. \phi_{a,b} :]a, b[\rightarrow IR \quad \text{and} \quad ii. \phi_{a,b} :]a, b[\rightarrow IR$$

$$x \mapsto \log\{(x-a)/(b-x)\} \quad \text{and} \quad x \mapsto tg\{\alpha(x-\beta)\}$$

where $\alpha = \pi/(b-a)$ and $\beta = (a+b)/2$.

Example 4.2: In order to test the estimator, we generate 1000 samples following the beta distribution. The analytical expression pdf of beta where p and $q > -1$ is given by:

$$f_{p,q}(x) = \begin{cases} \frac{x^p (1-x)^q (p+q+1)!}{p!q!} & \text{if } 0 \leq x \leq 1 \\ 0 & \text{if } x < 0 \text{ or } x > 1 \end{cases} \quad (4.8)$$

In order to show that the estimator is better than the classic Kernel method, we choose the parameters $p=0.5$ and $q=5$. Figure 4.2 shows the pdf estimation in the case where the Gaussian Kernel and the logarithmic diffeomorphism are used. The curves $\hat{f}_{p,q,G}$ and $\hat{f}_{p,q,\phi}$ represent respectively the Gaussian Kernel and the logarithmic diffeomorphism estimators of beta pdf $f_{p,q}(x)$. We see from Figure 4.2 that the kernel-diffeomorphism method estimates the pdf $f_{p,q}(x)$ better than the kernel method.

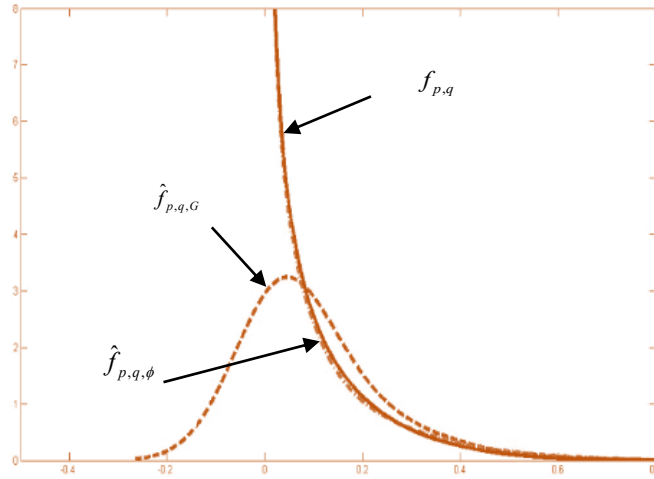


Figure 4.2: Estimation of pdf $f_{p,q}(x)$.

4.1.2.2 Case of p -dimension

Given a sequence of independent samples X_1, X_2, \dots, X_N identically distributed as the random variable X with a pdf f_X , the observations are in a bounded space U of IR^d ($d \geq 2$). Let us recall the generalized definition of the kernel-diffeomorphism estimator.

Definition 4.3: A d -dimensional kernel-diffeomorphism estimator is an estimator $\hat{f}_{X,N}$ of the form:

$$\hat{f}_{X,N}(x) = \frac{|\det\{\phi'(x)\}|}{N h_{1,N} h_{2,N} \dots h_{d,N}} \sum_{n=1}^N K \left(\frac{\phi_1(x) - \phi_1(X_n)}{h_{1,N}}, \dots, \frac{\phi_d(x) - \phi_d(X_n)}{h_{d,N}} \right) \quad (4.9)$$

with a d -dimensional pdf K , called kernel; a d -dimensional vector of positive real numbers $h_N = (h_{1,N}, \dots, h_{d,N})$, the generalized bandwidth; and a regular C^1 -diffeomorphism $\phi(x) = (\phi_1(x), \dots, \phi_d(x))$ from U to IR^d .

The C^1 -diffeomorphism is called regular if $|\det\{\phi'(x)\}|$ tends to infinity as x tends to the bound of the open space U . The K is called regular if it is a square integrated density.

Example 4.3: Let f_X be a d -dimensional beta distribution (of the first kind) whose components are independent with parameters $p = q = 1$:

$$f_X(x) = 6^d \prod_{i=1}^d x_i (1-x_i) \text{ where, } x = (x_1, x_2, \dots, x_d) \in (]0,1[)^d \quad (4.10)$$

As a kernel, we can choose the product kernel of the form: $K(x) = \prod_{i=1}^p K_i(x_i)$, with (for $i=1, \dots, p$):

$$K_i(x_i) = \begin{cases} \frac{3}{4\sqrt{5}}(1 - x_i^2/5) & \text{if } |x_i| < \sqrt{5} \\ 0 & \text{if } |x_i| \geq \sqrt{5} \end{cases} \quad (4.11)$$

As a diffeomorphism, we take:

$$\begin{aligned} \phi: U = (]0,1[)^p &\rightarrow IR^p \\ x &\mapsto \phi(x) = \left(\text{Log} \frac{1-x_1}{x_1}, \dots, \text{Log} \frac{1-x_p}{x_p} \right) \end{aligned} \quad (4.12)$$

$$\text{Then, } |\det\{\phi'(x)\}| = \prod_{i=1}^p \frac{1}{x_i(1-x_i)}.$$

For further information about this estimator, we can see the paper [Sao97].

4.2 A proposed method to reduce the speckle noise

Speckle noise is one of or the main defects that distorts SAR images [Zhu13]. Restoration of SAR images corrupted by the speckle noise has indeed attracted the attention of many researchers. Several filters have been introduced in the past for the reduction of speckle noise. In this work, we propose a novel approach, utilizing a hybrid combination between the Nonparametric BBF (NBBF) [Mar17][Mar18b] and the DWT [Mal98] to suppress speckle noise in SAR images. Here, we will first generate the noisy image by degrading the original image with the multiplicative speckle noise. Second, the degraded image will be entered to the NBBF in order to reduce the speckle noise. Third, we apply the DWT method to the output filtered image by the NBBF. Fourth, we apply thresholding process [Guo00] on the output coefficients by the DWT. Finally, we apply the IDWT to get our output restored image. In Figure 4.3 we show the flow chart diagram of the proposed algorithm.

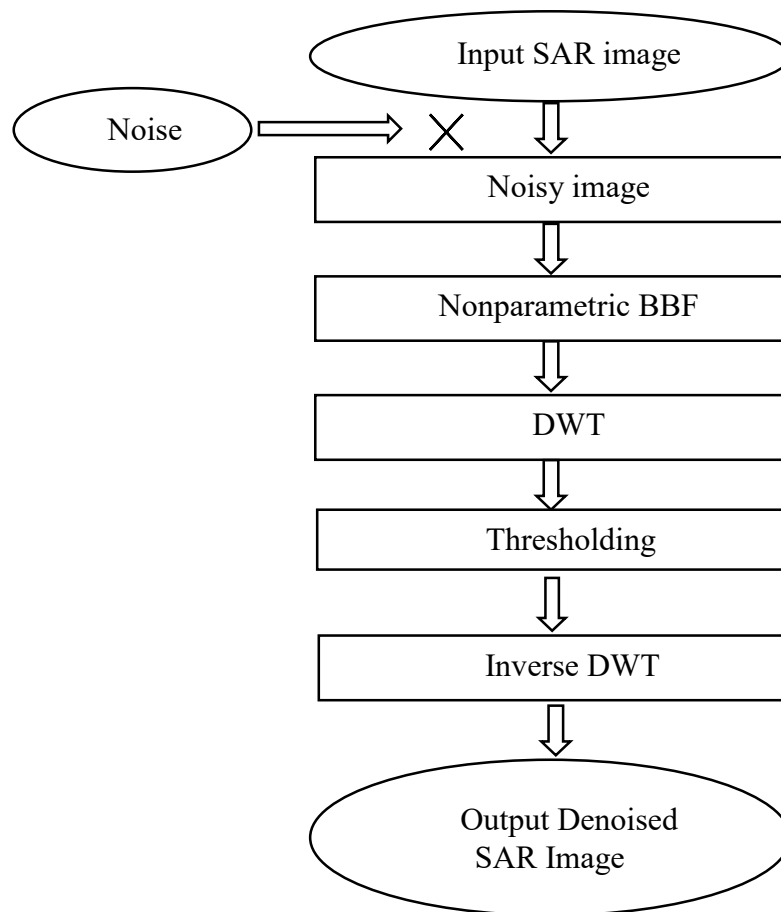


Figure 4.3: The Proposed algorithm.

4.2.1 Discription of SAR images

Synthetic Aperture Radar (SAR) images can be obtained from satellites such as European Remote Sensing Satellite (ERS), Japanese Earth Resource Satellite (JERS) and RADARSAT. Since radar interacts with the ground features in ways different from the optical radiation, special care has to be taken when interpreting radar images. We present an example of an ERS SAR image in Figure 4.4. SAR provides high-resolution, day-and-night and weather-independent images for a multitude of applications ranging from geoscience and climate change research, environmental and Earth system monitoring, 2-D and 3-D mapping, change detection, 4-D mapping (space and time), security-related applications up to planetary exploration. Besides the advantages, it suffers from a major problem caused by random phase fluctuations of the return electromagnetic signals. These fluctuations appear as noise in the processed image and known as speckle noise.



Figure 4.4: ERS SAR image.

Speckle noise in SAR is generally more serious, causing difficulties for image interpretation hence it is required to be restored, but because of multiplicative nature, it requires different treatment than additive noise. Speckle noise occurs as granular pattern formed by the interference of randomly scattered energy which occurs when object illuminated by coherent radiation have rough surface. Speckle noise causes difficulties for image interpretation and further processing of the image. The speckle is multiplicative in nature, which makes the process of noise removal more complicated. The ideal speckle reduction technique preserves the edges and other textural information. We present in Figure 4.5 a noised SAR image. This image is extracted from the above SAR image, showing the clearing areas between the river and the coastline. The image appears "grainy" due to the presence of speckles.

Over the last three decades, several different methods have been proposed for the reduction of speckle, or despeckling, in SAR images. A number of filtering algorithms dealing with multiplicative noise have been proposed. The most notable include the Lee [Lee80], Kuan [Kua85], and Frost [Fro82] filters. These filters which aim at minimizing the mean square error (MSE), are derived from the speckle model, i.e., assuming speckle is a multiplicative noise random variable, with mean of one. Goal of this chapter is to making a novel method to reduce the speckle noise for SAR images based on non-parametric Bayesian bootstrap filter and discrete wavelet transform.

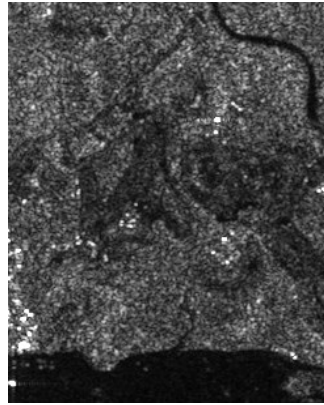


Figure 4.5: Noised SAR image.

4.2.2 SAR image mathematical model

A SAR image is a mean intensity estimate of the radar reflectivity of the region which is being imaged. We will model the discrete original image $s(m, n)$, with size $N_l \times N_c$, by a 2-D auto-regressive (AR) process of low order [Jai81]:

$$s(m, n) = \sum_{(k,l) \in \Gamma} c_{k,l} s(m-k, n-l) + w(m, n) \quad (4.13)$$

where m and n represent the row and the column of a pixel respectively, $c_{k,l}$ are the coefficients of image model, Γ is the nonsymmetric half plane (NSHP) model support [Ang89], and $w(m, n)$ is a zero-mean homogeneous Gaussian distributed process with covariance $\sigma_w^2(m, n)$, which is independent of $s(m, n)$.

A state vector $x(m, n)$ at location (m, n) can be defined by:

$$x(m, n) = \begin{bmatrix} s(m, n), s(m-1, n), \dots, s(1, n); \\ s(N, n-1), \dots, s(1, n-1); \dots; \\ s(N, n-M), \dots, s(m-M, n-M) \end{bmatrix}^T \quad (4.14)$$

This state was determined assuming an image of N pixels wide and scanned from left to right, top to bottom.

Speckle noise severely impedes automatic scene segmentation and interpretation, and limits the resolution of SAR images as well as their utility. If s represents the original image and v is speckle noise, then the degraded observation y is given by the relation:

$$y(m, n) = s(m, n) \cdot v(m, n) \quad (4.15)$$

Noise v is assumed to be independent of s with unit mean and variance σ_v^2 . The multiplicative nature of speckle complicates the noise reduction process in SAR. A speckle suppression filter should effectively filter homogeneous areas, retain image texture and edges (both straight and curved), and preserve features (linear as well as point-type). The image model, which describes the evolution of the state with space and the statistical characteristics of the image at spatial indices m and n , is defined as:

$$x(m, n) = f(x(m-1, n), w(m-1, n)) \quad (4.16)$$

where f is the nonlinear function of the state vector $x(m, n)$ and $w(m-1, n)$ is a process noise sequence independent of the system states.

The pdf of w is assumed to be known as $p_w(w)$. The Bayesian filtering algorithm seeks filtered of $x(m, n)$ based on the sequence of all available measurements $Y_{m,n} = \{y(i, n)\}_{i=1}^m$ up to time step m from the posterior conditional pdf $p(x(m, n) | Y_{m,n})$. The distribution of the initial condition $x(1, n)$ is assumed to be given by $p(x(1, n) | Y_{0,n}) = p(x(1, n))$. The a posterior conditional pdf $p(x(m, n) | Y_{m,n})$ and the filtered conditional pdf $p(x(m, n) | Y_{m-1,n})$ evolve in the following manner:

$$p(x(m, n) | Y_{m-1,n}) = \int p(x(m, n) | x(m-1, n)) p(x(m-1, n) | Y_{m-1,n}) dx(m-1, n) \quad (4.17)$$

and

$$p(x(m, n) | Y_{m,n}) = \frac{p(y(m, n) | x(m, n)) p(x(m, n) | Y_{m-1,n})}{\int p(y(m, n) | x(m, n)) p(x(m, n) | Y_{m-1,n}) dx(m, n)} \quad (4.18)$$

A large number of numerical methods for evaluating the Bayesian filtering have been proposed. In this work, we introduce a new method, which will be explained in the next subsection.

4.2.3 Nonparametric Bayesian bootstrap filtering

Bayesian bootstrap filtering (BBF) is a powerful technique since it is not restricted by model assumptions of linearity and/or Gaussian noise. The bootstrap filter is a recursive algorithm to estimate the posterior pdf $p(x(m, n) | Y_{m,n})$ from a set of samples. Assuming that we have a set of random samples $\{x_i(m-1, n) : i = 1, \dots, N_b\}$ that are independently drawn from the pdf $p(x(m-1, n) | Y_{m-1,n})$, where N_b is the number of bootstrap samples. Bootstrap filter performs approximate Bayesian estimation by predicting and updating a set of samples, representing the system probability density functions. The filter procedure is as follows:

Prediction: Each sample from pdf $p(x(m-1, n) | Y_{m-1,n})$ is passed through (4.15) to obtain a new sample $x_i^*(m, n)$ at location (m, n) .

Update: On receipt of the measurement $y(m, n)$, evaluate the likelihood of each prior sample and obtain the normalized weight q_i for each sample:

$$q_i = \frac{p(y(m, n) | x_i^*(m, n))}{\sum_{j=1}^N p(y(m, n) | x_j^*(m, n))} \quad (4.19)$$

This defines a discrete distribution over $\{x_i^*(m, n) : i = 1, \dots, N_b\}$ with probability mass q_i associated with element $x_i^*(m, n)$. Now resample N times from the discrete distribution to generate samples $\{x_i(m-1, n) : i = 1, \dots, N_b\}$, so that for any j , $\Pr\{x_j(m, n) = x_i^*(m, n)\} = q_i$. The samples are approximately distributed as the required pdf $p(x(m, n) | Y_{m,n})$.

In the update step of BBF, the resampling from the discrete distribution was suggested as a method to reduce the degeneracy problem, which is prevalent in BBF. On the other hand, the resampling procedure was noticed to produce other problems, particularly, the problem of losing diversity among the particles. To resolve this problem, we suggested regularizing the BBF [Mar17][Mar18a]. This regularization is established at the level of the resampling stage, where the samples are drawn from a continuous distribution rather than a discrete one.

By using a nonparametric multivariate density estimation given in section 4.1, samples are drawn from a continuous approximation of the posterior density $p(x(m, n) | Y_{m,n})$.

Nonparametric bootstrap update: As before, define a discrete distribution over $\{x_i^*(m, n) : i = 1, \dots, N_b\}$, with probability mass q_i associated with element $x_i^*(m, n)$. However, instead of resampling directly from this discrete sample set we now use the set of weighted points and the multivariate kernel density or the multivariate kernel-diffeomorphism density to generate samples from the approximation:

$$p(x(m, n) | Y_{m,n}) \approx \sum_{i=1}^{N_b} q_i K_H(x(m, n) - x_i(m, n)) \quad (4.20)$$

Or

$$p(x(m, n) | Y_{m,n}) \approx \frac{|\det\{\phi'(x(m, n))\}|}{N_b (h_{N_b})^p} \sum_{i=1}^{N_b} q_i K\left(\frac{\phi(x(m, n)) - \phi(x_i(m, n))}{h_{N_b}}\right) \quad (4.21)$$

We can now declare the algorithm in details as follow.

Nonparametric Bayesian bootstrap filter algorithm

1. Initializing, $m=1$.

- FOR $i=1: N_b$, draw samples $x_i(1, n)$, from the proposal distribution $x_i(m, n) \sim p(x(1, n))$

2. Importance sampling step

- FOR $i=1: N_b$, draw samples $x_i^*(1, n)$, from the transition PDF $x_i(m, n) \sim$

$$p(x(m, n) | x_i(m-1, n)) \text{ and set } x_i^*(1:m, n) = (x_i(1:m-1, n), x_i^*(m, n)).$$

- FOR $i=1: N_b$, compute the normalized importance weights given by (4.19).

3. Selection step

- Resample with replacement N_b particles $x_i(1:m, n); i = 1, \dots, N_b$ from the set

$$x_i^*(1:m, n); i = 1, \dots, N_b \text{ according to the importance weights using (4.20) or (4.21).}$$

Set $m \leftarrow m+1$ and go to step 2.

4.2.4 Image Denoising Using Discrete Wavelet Transform (DWT)

4.2.4.1 DWT Process:

The DWT is based on sub-band coding which generates a fast computation of Wavelet Transform. It is easy to implement, requires less computation time and the resources required are considerably decreased. In DWT, digital filtering techniques are used which gives time scale

representation of the digital signal. The signal $x(n)$ to be analyzed is passed through filters at different cut off frequencies and at different scales. The term “Wavelet” means a small wave. This smallness specifies the condition that the window function is of fixed length. A wave is defined as an oscillating function of space or time and it is periodic whereas wavelets are localized waves. Wavelets are suited to transient signals and their energy concentrated in time. To analyze signals, Fourier transform and Short-Time Fourier Transform (STFT) use waves and Wavelet transform uses wavelets of finite energy. This Wavelets transform has proved to be a useful tool in various application of image and signal processing [Luk14].

The pixel or signal $x(n)$ is processed by passing it through a series of filters. First, it is passed through a low pass filter with impulse response $g(n)$ giving the approximation coefficient:

$$y_{high}[k] = \sum_n x[n].g[2k - n] \quad (4.22)$$

The signal is decomposed simultaneously using a high pass filter $h(n)$ as a result of which the detailed coefficient is obtained:

$$y_{low}[k] = \sum_n x[n].h[2k - n] \quad (4.23)$$

Since an image is a 2-dimensional signal, it is represented as $x(M, N)$. Each row is filtered and sampled to obtain two $x(N, M/2)$ images. Then each column is filtered and down sampled to obtain four $x(N/2, M/2)$ images. The resultant is one-dimensional scaling function $\phi(x, y)$ and two dimensional wavelet functions $\psi^H(x, y)$, $\psi^V(x, y)$ and $\psi^D(x, y)$ which represent the sub bands of the image. Now, we use the concept of Mean Square Difference of Slope (MSDS) to remove the artifacts. We have two MSDS namely $MSDS_1$ and $MSDS_2$ of which $MSDS_1$ is comprised of vertical and horizontal blocks:

$$MSDS_1 = \varepsilon(\psi^H(x, y)) + \varepsilon(\psi^V(x, y)) = \varepsilon_H + \varepsilon_V \quad (4.24)$$

Similar, the $MSDS_2$ involves the usage of the diagonal components:

$$MSDS_2 = \varepsilon(\psi^D(x, y)) = \varepsilon_D \quad (4.25)$$

The intensity slopes of all adjacent blocks are:

$$MSDS_t = MSDS_1 + MSDS_2 \quad (4.26)$$

On global minimization of $MSDS_t$, we can reduce the blocking artifacts. On de-quantization and application of Inverse Discrete Transform, the original image is restored.

4.2.4.2 Thresholding Process

The Small coefficients in the sub-bands are dominated by noise, while coefficients with large absolute value carry more original image information than noise. Replacing noisy coefficients (small coefficients below certain value) by zero and an inverse wavelet transform may lead to reconstruction that has lesser noise. Normally Hard Thresholding and Soft Thresholding techniques are used for such denoising process. Hard and Soft thresholding [Don95][Hed11] [Vij12] with threshold λ are defined as follows. The threshold λ is chosen according to the signal energy and the noise variance σ^2 . The hard thresholding operator is defined as:

$$\begin{aligned} D(U, \lambda) &= U \text{ for all } |U| > \lambda \\ &= 0 \text{ otherwise} \end{aligned} \quad (4.27)$$

The soft thresholding operator on the other hand is defined as:

$$\begin{aligned} D(U, \lambda) &= 0 \text{ for all } |U| \leq \lambda \\ &= \text{sgn}(U)(|U| - \lambda) \text{ otherwise} \end{aligned} \quad (4.28)$$

The DWT denoising procedure will go as follows:

1. Transform the noisy image into orthogonal domain by discrete 2D wavelet transform.
2. Apply hard or soft thresholding the noisy detail coefficients of the wavelet transform.
3. Perform inverse discrete wavelet transform to obtain the denoised image.

Here, the threshold plays an important role in the denoising process. Normally, hard thresholding and soft thresholding techniques are used for such denoising process. Hard thresholding is a keep or kill rule whereas soft thresholding shrinks the coefficients [Tas00] above the threshold in absolute value. It is a shrink or kill rule.

4.3 Experimental results

The performance of the proposed method is examined by using two satellite SAR images with several speckle noise simulations. Denoising is carried out for SAR image with Speckle noise of variance $\sigma_v^2 = 0.02, 0.03, 0.04, 0.05, 0.06, 0.07$ and 0.08 . For objective evaluation, the signal to noise ratio of each denoised image has been calculated using ISNR, RMSE and PSNR. The

first image shown in Figure 4.6.a is the upper part of the Terra SAR-X image (911×512 pixels) of Sydney Australia. It is provided by the German Aerospace Center (DLR) in July 9, 2007, which shows Botany Bay, located south of the airport [ESA07]. The second image shown in Figure 4.7.a is the city of Paris image (687×512 pixels) acquired by the SAR satellite Sentinel-1A on Tuesday, May 31, 2016 [Den16]. In order for us to implement the proposed method over a given noised satellite images, we have used the state dynamical model given by (4.29),

$$x(m,n) = Cx(m,n-1) + Eu(m,n) + Dw(m,n) \quad (4.29)$$

where

$$x(m,n) = \begin{bmatrix} s(m,n) \\ s(m-1,n) \\ s(m+2,n-1) \\ s(m+1,n-1) \\ s(m,n-1) \end{bmatrix}, \quad C = \begin{bmatrix} a_4 & 0 & a_3 & a_2 & a_1 \\ 1 & 0 & 0 & 0 & 0 \\ 0 & 0 & 0 & 0 & 0 \\ 0 & 0 & 1 & 0 & 0 \\ 0 & 0 & 0 & 1 & 0 \end{bmatrix}, \quad E = \begin{bmatrix} 0 \\ 0 \\ 1 \\ 0 \\ 0 \end{bmatrix} \quad \text{and} \quad D = \begin{bmatrix} 1 & 0 \\ 0 & 0 \\ 0 & 1 \\ 0 & 0 \\ 0 & 0 \end{bmatrix}.$$

The input term $u(m,n)$ is introduced as the recent estimate of the pixel $s(m-1, n+1)$. We have adopted a causal image model proposed in [Jai81] using a non-symmetric half plane (NSHP) region of the support shown below [Jai89]:

$$s(m,n) = a_1 s(m-1, n-1) + a_2 s(m, n-1) + a_3 s(m+1, n-1) + a_4 s(m-1, n) \quad (4.30)$$

where a_1, a_2, a_3 and a_4 are the model coefficients given in Table 4.1, which are identified using the Least Squares method [cha76]. In our work we will use the BBF with $N_b=500$.

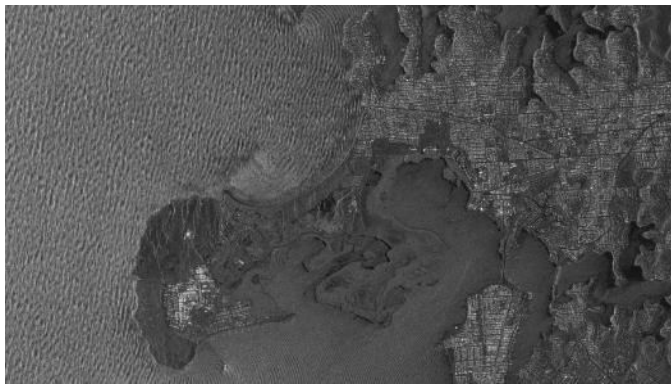
Table 4.1: Model coefficients for the used SAR images.

Image	a_1	a_2	a_3	a_4
Sydney Australia	-0.1698	0.03651	0.1230	0.6762
City of Paris	-0.0904	0.4006	0.1514	0.5304

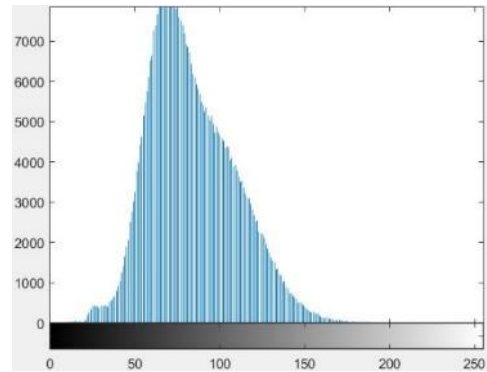
In order to be able to quantify the improvement achieved by our method, we have first degraded original “noiseless” images with synthetic speckle in a controlled manner. To evaluate the proposed filter’s capability in minimizing speckle effects while preserving image contents and details, a number of established filters were applied to both the SAR images, including the BBF.

4.3.1 Results of SAR image Sydney Australia

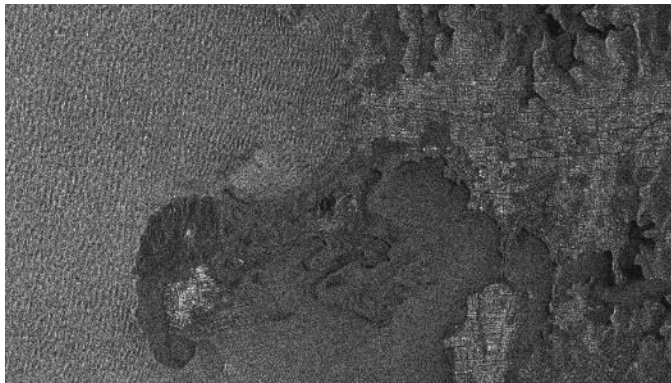
In this section we will introduce a simulate noisy image of the image of Sydney Australia with a multiplicative noise - speckle noise-, then we will denoise the simulated noisy image with our proposed methods and other several basic filters in order to show the superiority of our proposed filter. The mean of the speckle noise is taken to be unity with several values of the speckle noise variance $\sigma_v^2 = 0.02, 0.03, 0.04, 0.05, 0.06, 0.07$ and 0.08 . In Figure 4.6, we illustrate the visual results for restoring the Sydney Australia image that was degraded by speckle noise of variance $\sigma_v^2 = 0.08$. We will show the results by means of the numerics: ISNR, RMSE and PSNR in Tables 4.2, 4.3 and 4.4 respectively.



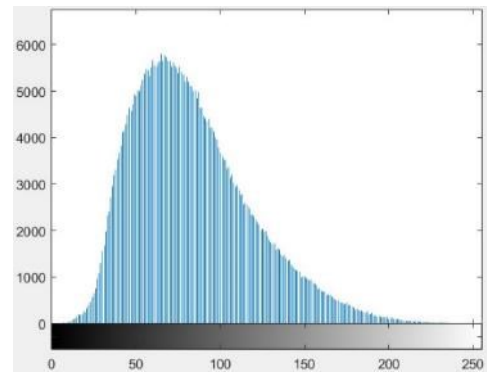
(a) Original 'Sydney, Australia' image



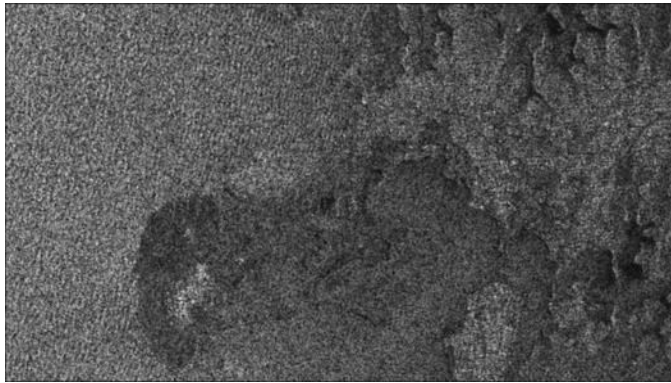
Histogram for image (a)



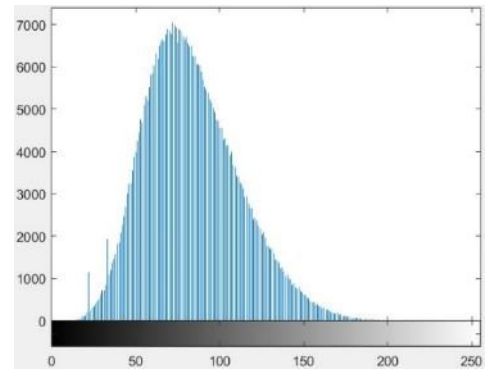
(b) Degraded image



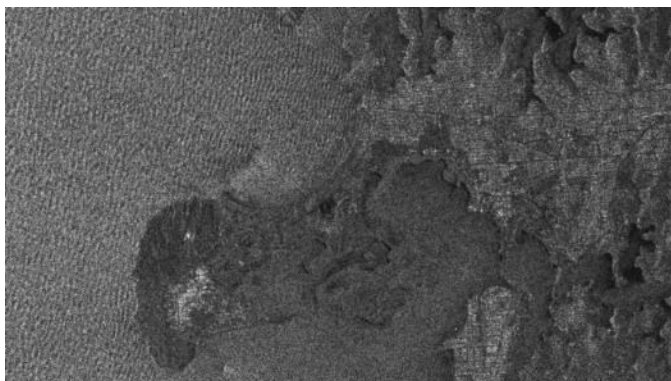
Histogram for the image (b)



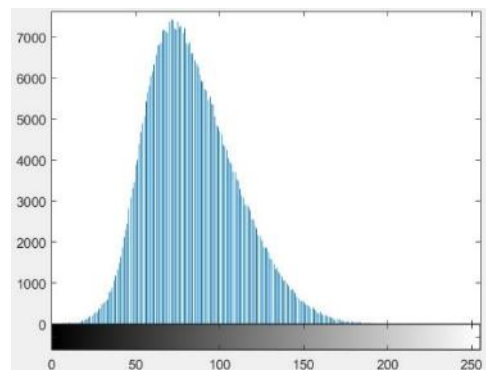
(c) Restored image by kuan filter



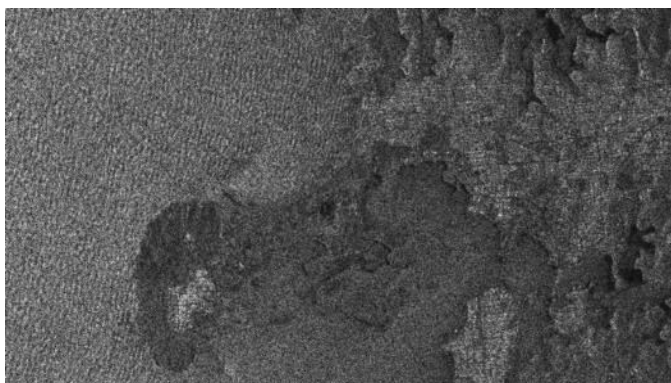
Histogram for the image (c)



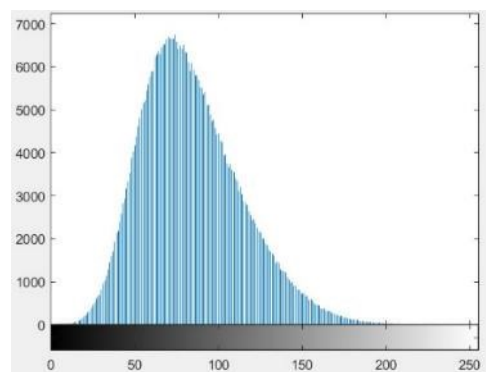
(d) Restored image by frost filter



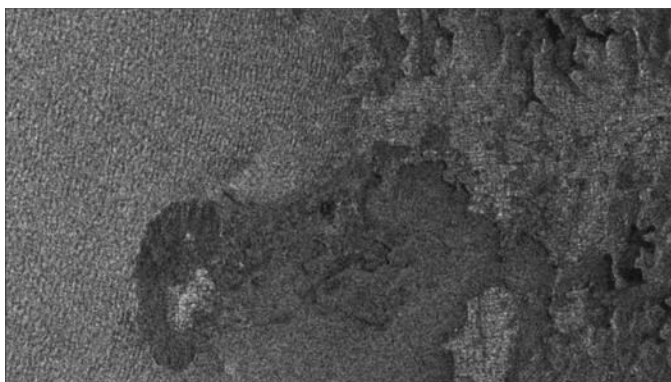
Histogram for the image (d)



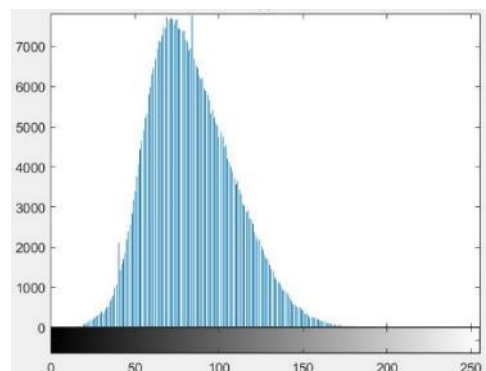
(e) Restored image by lee filter



Histogram for the image (e)



(f) Restored image by wiener filter



Histogram for the image (f)

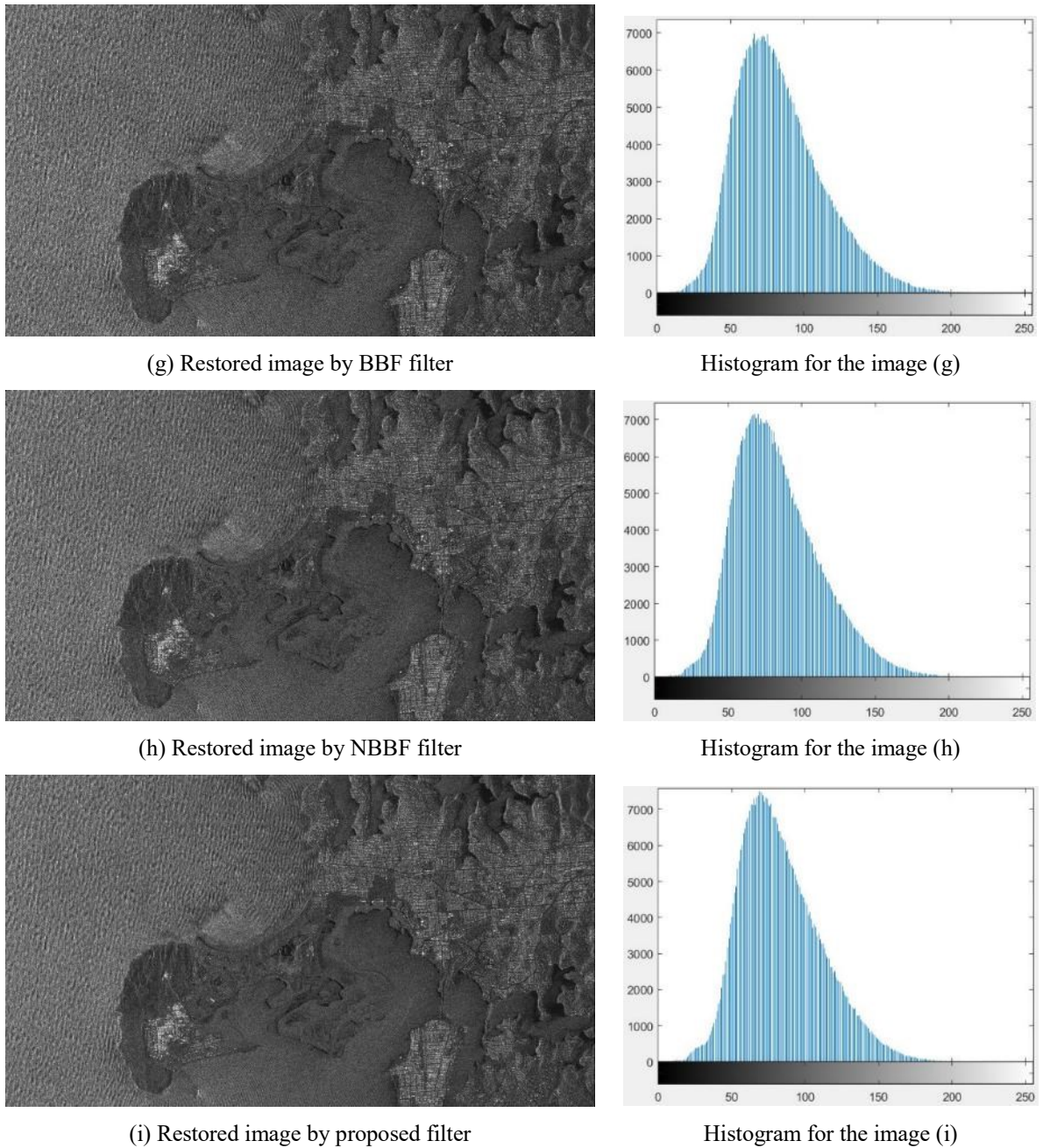


Figure 4.6: Denoising of ‘Sydney, Australia’ image corrupted by speckle noise of variance of 0.08.

Table 4.2: Comparison of the ISNR resultant values of the proposed, NBBF, BBF and the other basic filters for denoising the SAR image of Sydney corrupted by Speckle noise.

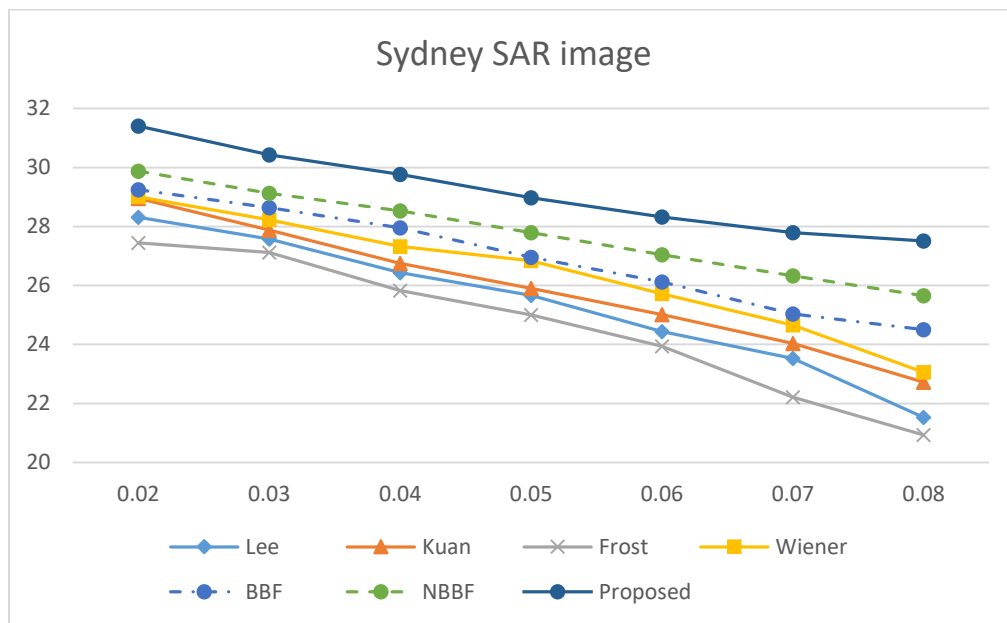
σ_v^2	0.02	0.03	0.04	0.05	0.06	0.07	0.08
Kuan	7.30	6.98	6.49	6.15	5.62	5.22	4.35
Frost	7.58	7.11	6.62	6.26	5.87	5.44	4.87
Lee	6.93	6.78	6.22	5.86	5.40	4.65	4.09
Wiener	7.60	7.26	6.87	6.66	6.17	5.71	5.02
BBF	7.71	7.44	7.15	6.71	6.35	5.88	5.65
NBBF	7.98	7.66	7.39	7.09	6.75	6.44	6.14
Proposed	8.65	8.22	7.93	7.59	7.31	7.07	6.95

Table 4.3: Comparison of the RMSE resultant values of the proposed, NBBF, BBF and the other basic filters for denoising the SAR image of Sydney corrupted by Speckle noise.

σ_v^2	0.02	0.03	0.04	0.05	0.06	0.07	0.08
Kuan	9.75	10.62	12.11	13.23	15.24	16.92	21.31
Frost	9.07	10.26	11.68	12.87	14.26	15.96	18.58
Lee	10.78	11.19	12.99	14.29	16.14	19.70	22.83
Wiener	9.01	9.85	10.93	11.56	13.15	14.86	17.86
BBF	8.76	9.40	10.16	11.40	12.56	14.22	15.12
NBBF	8.15	8.88	9.52	10.32	11.28	12.26	13.26
Proposed	6.83	7.65	8.25	9.04	9.74	10.36	10.70

Table 4.4: Comparison of the PSNR resultant values of the proposed, NBBF, BBF and the other basic filters for denoising the SAR image of Sydney corrupted by Speckle noise.

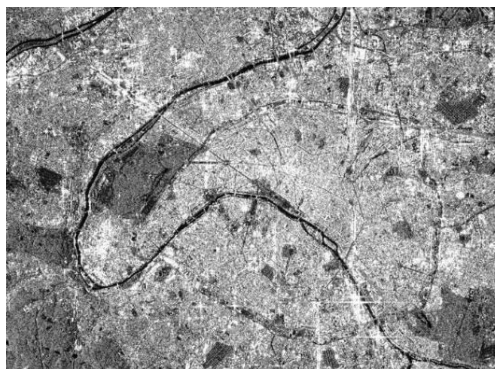
σ_v^2	0.02	0.03	0.04	0.05	0.06	0.07	0.08
Kuan	28.32	27.58	26.44	25.67	24.44	23.53	21.53
Frost	28.95	27.88	26.75	25.91	25.02	24.04	22.72
Lee	27.45	27.12	25.83	25	23.94	22.21	20.93
Wiener	29.01	28.23	27.33	26.84	25.72	24.66	23.06
BBF	29.25	28.64	27.96	26.96	26.12	25.04	24.51
NBBF	29.88	29.13	28.53	27.83	27.05	26.33	25.65
Proposed	31.41	30.43	29.77	28.98	28.33	27.79	27.51

Line Chart 4.1: PSNR results for denoising the SAR image of Sydney by the several filters.

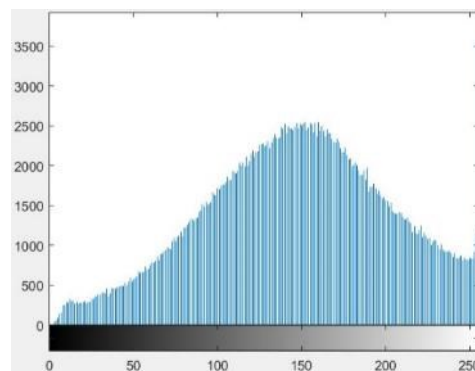
We can notice from the visual results for the SAR image of Sydney the improvements of our proposed method over the other methods introduced, as well as the increasing in the ISNR, PSNR and the decreasing of the RMSE values for the proposed method over the other methods.

4.3.2 Results of SAR image City of Paris

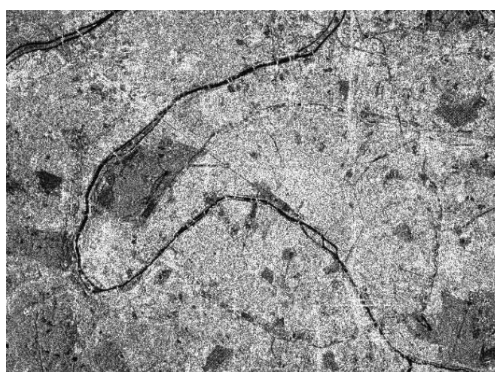
In this section we will introduce a simulate noisy image of the image of city of Paris with a multiplicative noise - speckle noise-, then we will denoise the simulated noisy image with our proposed methods and other several basic filters in order to show the superiority of our proposed filter. The mean of the speckle noise is taken to be unity with several values of the speckle noise variance $\sigma_v^2=0.02, 0.03, 0.04, 0.05, 0.06, 0.07$ and 0.08 . In Figure 4.7, we illustrate the visual results for restoring the Paris city image that was degraded by speckle noise of variance $\sigma_v^2=0.08$. We will show the results by means of the numerics: ISNR, RMSE and PSNR in Tables 4.5, 4.6 and 4.7 respectively.



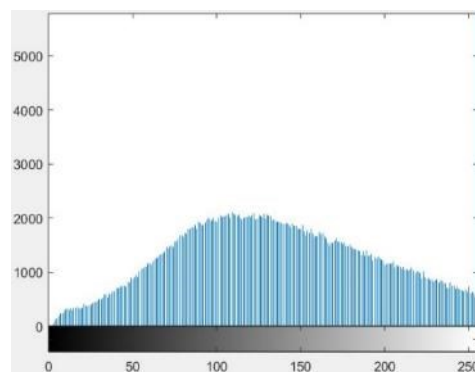
(a) Original 'city of Paris' image



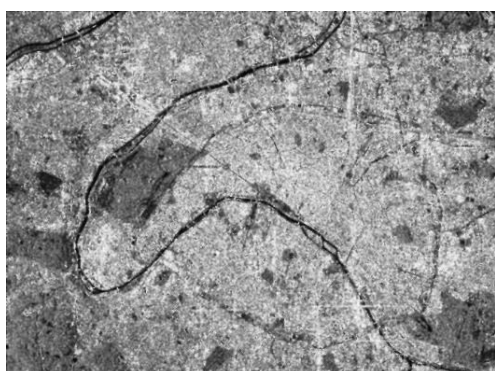
Histogram of image (a)



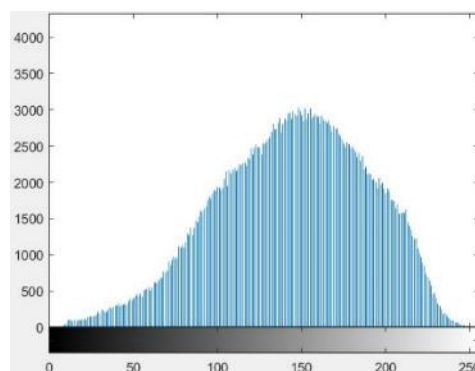
(b) Degraded image



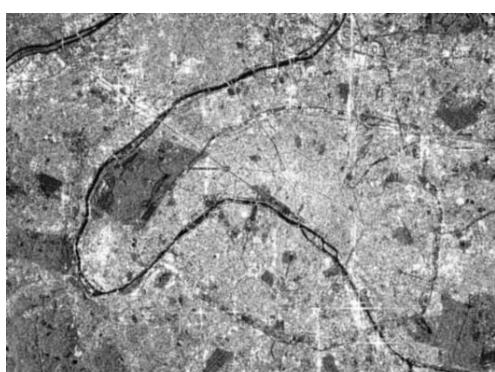
Histogram of image (b)



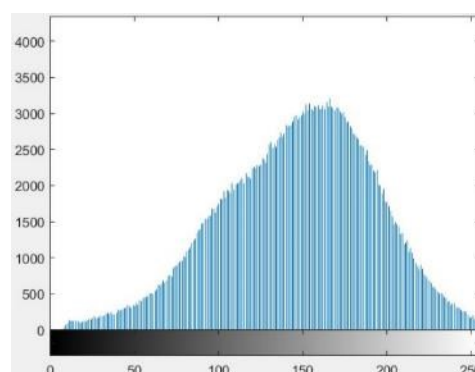
(c) Restored image by kuan filter



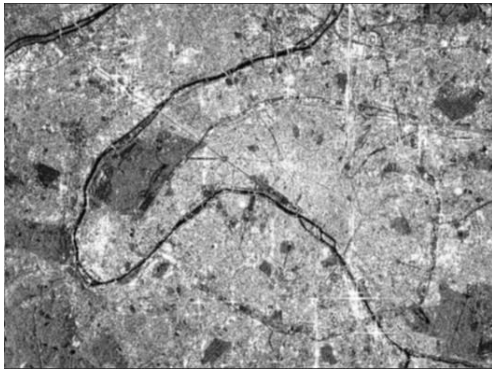
Histogram of image (c)



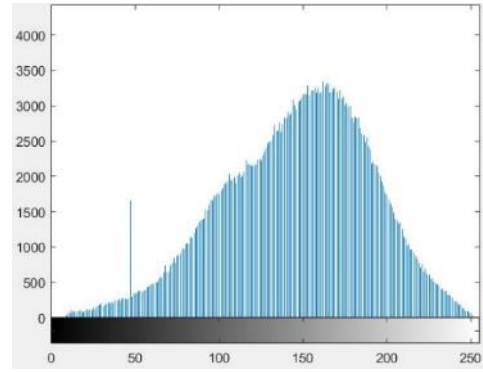
(d) Restored image by frost filter



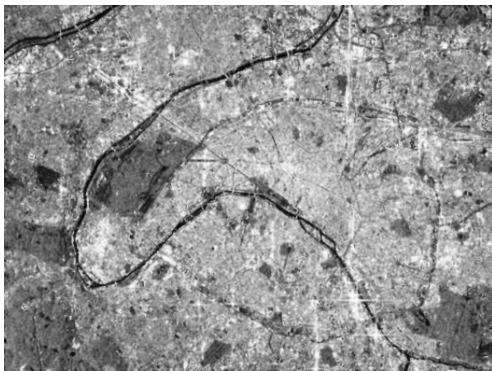
Histogram of image (d)



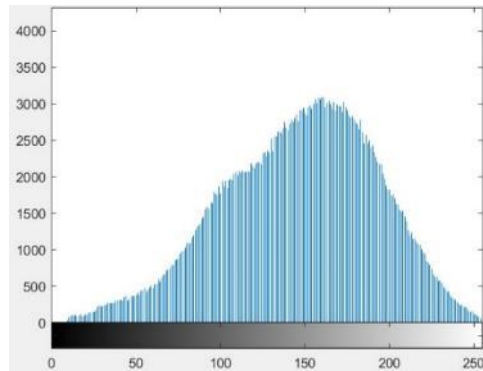
(e) Restored image by lee filter



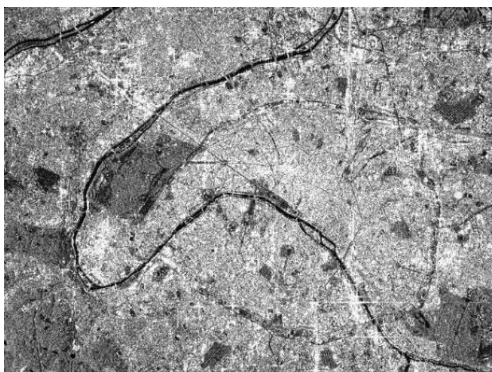
Histogram of image (e)



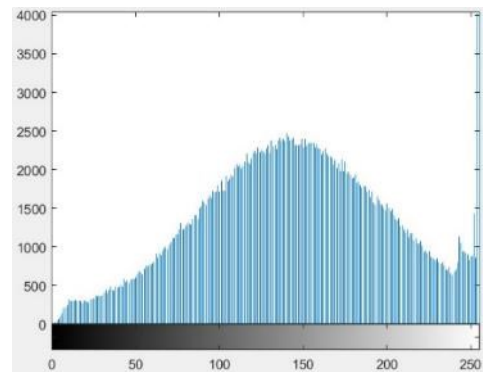
(f) Restored image by wiener filter



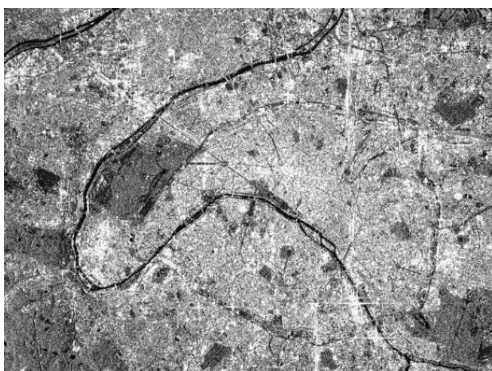
Histogram of image (f)



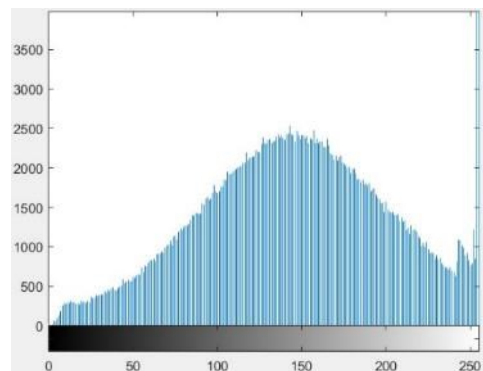
(g) Restored image by BBF filter



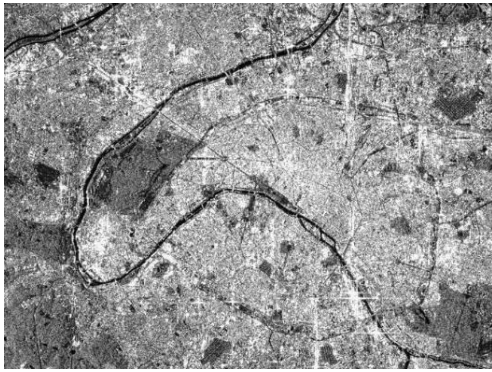
Histogram of image (g)



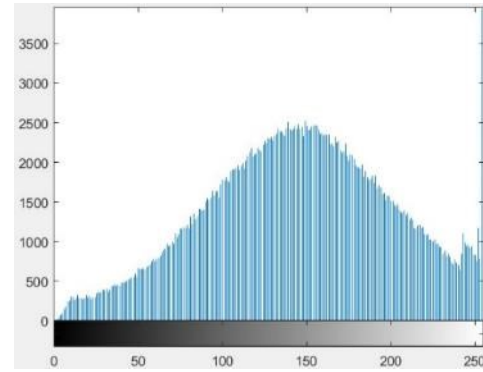
(h) Restored image by NBBF filter



Histogram of image (h)



(i) Restored image by the proposed filter



Histogram of image (i)

Figure 4.7: Denoising of ‘city of Paris’ image corrupted by speckle noise of variance of 0.08.**Table 4.5:** Comparison of ISNR resultant values of the proposed, NBBF, BBF and other basic filters for denoising the SAR image of Paris corrupted by Speckle noise.

σ_v^2	0.02	0.03	0.04	0.05	0.06	0.07	0.08
Kuan	6.23	5.88	5.57	4.95	4.40	3.94	3.37
Frost	6.48	6.05	5.77	5.16	4.91	4.13	3.46
Lee	6.09	5.77	5.42	4.69	4.23	3.82	3.33
Wiener	6.71	6.19	5.82	5.32	5.42	4.79	4.15
BBF	6.81	6.33	6.21	5.82	5.51	5.18	4.84
NBBF	6.92	6.63	6.30	5.91	5.59	5.49	5.08
Proposed	7.12	6.90	6.53	6.29	5.80	5.70	5.27

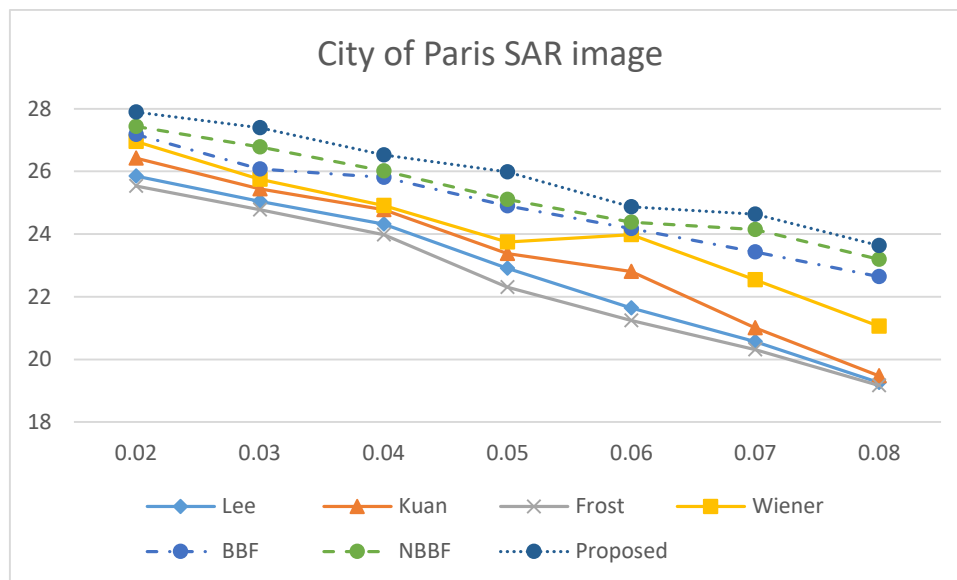
Table 4.6: Comparison of RMSE resultant values of the proposed, NBBF, BBF and other basic filters for denoising the SAR image of Paris corrupted by Speckle noise.

σ_v^2	0.02	0.03	0.04	0.05	0.06	0.07	0.08
Kuan	12.96	14.22	15.45	18.18	21.04	23.80	27.67
Frost	12.13	13.58	14.66	17.22	18.39	22.62	26.98
Lee	13.44	14.66	16.07	19.48	22.03	24.52	27.96
Wiener	11.42	13.11	14.44	16.50	16.07	18.97	22.49
BBF	11.12	12.62	13.02	14.45	15.70	17.12	18.75
NBBF	10.80	11.64	12.72	14.11	15.35	15.78	17.60
Proposed	10.24	10.85	11.98	12.76	14.50	14.91	16.73

Table 4.7: Comparison of PSNR resultant values of the proposed, NBBF, BBF and other basic filters for denoising the SAR image of Paris corrupted by Speckle noise.

σ_v^2	0.02	0.03	0.04	0.05	0.06	0.07	0.08
Kuan	25.85	25.04	24.32	22.91	21.64	20.57	19.26
Frost	26.42	25.44	24.78	23.38	22.81	21.01	19.48
Lee	25.53	24.78	23.98	22.31	21.24	20.31	19.17
Wiener	26.95	25.75	24.91	23.75	23.98	22.54	21.06
BBF	27.18	26.08	25.81	24.9	24.18	23.43	22.64
NBBF	27.43	26.78	26.01	25.11	24.38	24.14	23.19
Proposed	27.89	27.39	26.53	25.98	24.87	24.63	23.63

Line Chart 4.2: PSNR results for denoising the image of the city of Paris SAR image by the several filters.



Here we can notice from the visual results for the SAR image of Paris the improvements of our proposed method over the other methods introduced, as well as the increasing in the ISNR, PSNR and the decreasing of the RMSE values for the proposed method over the other methods.

Conclusion

In this chapter, a novel approach for speckle noise reduction in SAR image is introduced. The proposed method is a combination between the novel NBBF and the DWT which introduce a superior method to reduce the effect of the multiplicative - speckle - noise in the SAR images. At first we improved the performance of the BBF by regularizing the process in the resampling stage using the nonparametric multivariate density estimation which solved the problem of losing diversity among the particles, this regularization process has yields into an enhancement

in the restoration results. After that we input the result obtained from our NBBF into the DWT restoration stage. In addition, this procedure has improved the overall restoration results and we have obtained a better image restoration results by the means of visual and metric results. We compared our method with several basic speckle reduction methods in SAR images: Frost, Lee, Kuan and Wiener. The steps made was to simulate a noisy image from the original SAR image with speckle noise with unity mean and several values of the variance σ_v^2 0.02, 0.03, 0.04, 0.05, 0.06, 0.07 and 0.08. As we mentioned before, we have gained an attractive improvement in the restoration images visually. Furthermore, the increase in the ISNR, PSNR and the decreasing in the RMSE values indicates that there is a marked improvement in the restored image quality provided by our proposed methods.

References

- [Ahi11] R. Ahirwar and A. Choubey, A Novel Wavelet-based Denoising Method of SAR Image Using Interscale Dependency, 2011 International Conference on Computational Intelligence and Communication Systems, pp. 52-57, Oct. 2011.
- [Al-10] S. S. Al-amri et al, A Comparative Study of Removal Noise from Remote Sensing Image, International Journal of Computer Science Issues, Vol. 7, Issue, 1, No. 1, pp. 32-36, January 2010.
- [ANG89] D. L. Angwin and H. Kaufman, Image Restoration Using Reduced Order Models, Signal Processing Vol.16, pp. 21-28, 1989.
- [Bou10] T. Bouezmarni, J. V.K. Rombouts, Nonparametric density estimation for multivariate bounded data, Journal of Statistical Planning and Inference 140, pp. 139-152, 2010.
- [Bot10] Z. I. Botev, J. F. Grotowski and D. P. Kroese, Kernel density estimation via diffusion, Annals of Statistics, Vol. 38 (5), pp. 2916-2957, 2010.
- [Bow97] A. W. Bowman and A. Azzalini, Applied Smoothing Techniques for Data Analysis, London: Oxford University Press, 1997.
- [Cha76] A. Charnes, E. L. Frome, P. L. Yu, The Equivalence of Generalized Least Squares and Maximum Likelihood Estimates in the Exponential Family, Journal of the American Statistical Association, Vol. 71, No. 353, pp. 169-171, 1976.
- [Den16] Gil Denis, «Un autre regard sur la terre», URL: <http://www.un-autre-regard-sur-la-terre.org/>
- [Don95] D. L. Donoho, "De-noising by soft-thresholding," in IEEE Transactions on Information Theory, vol. 41, no. 3, pp. 613-627, May 1995.
- [Duo03] T. Duong and M. L. Hazelton, (), Plug-in Bandwidth Selectors for Bivariate Kernel Density Estimation, Journal of Nonparametric Statistics, 15, pp. 17-30, 2003.
- [ESA07] ESA. "Image gallery: TerraSAR-X. 2007. URL: <http://www.dlr.de/dlr/en/desktopdefault.aspx/tabid-10422/#gallery/331>
- [Fis32] R. A. Fisher, Statistical Methods for Research Workers, Fourth Edition, Oliver and Boyd, Edinburgh, 1932.
- [Fro82] V. S. Frost, J. A. Stiles, K. S. Schanmugan, J. C. Holzman, A model for radar images and its application to adaptive digital filtering of multiplicative noise, IEEE Transaction on Pattern Analysis and Machine Intelligence, Vol. 4 (2), pp. 157-166, 1982.
- [Guo00] D. Guo et al, A Study of Wavelet Thresholding Denoising, Proceedings of ICSP2000, pp. 329-332, 2000.

- [Hed11] P. Hedao1 and S. S. Godbole, Wavelet thresholding approach for image denoising, International Journal of Network Security & Its Applications (IJNSA), Vol.3, No.4, 2011.
- [Hwa94] J. N. Hwang, S. R. Lay and A. Lippman, Nonparametric multivariate density estimation: a comparative study, IEEE Transactions on Signal Processing, Vol. 42, Issue 10, pp. 2795-2810, 1994.
- [Jai81] A. K. Jain, Advances in mathematical models for image processing, Proceedings of the IEEE, Vol. 69, no. 5, pp. 502-528, 1981.
- [Jai89] A. K. Jain, Fundamentals of Digital image processing, Englewoods Cliffs, NJ: Prentice Hall, 1989.
- [Jar09] J. Jarnicka, Multivariate kernel density estimation with a parametric support, Opuscula Math., Vol. 29, No. 1, pp. 41-55, 2009.
- [Jon96] M. C. Jones, J. S. Marron and S. J. Sheather, A Brief Survey of Bandwidth Selection for Density Estimation, Journal of the American Statistical Association, 91, pp. 401-407, 1996.
- [Kol13] J. Koloda, A. M. Peinado, V. Sánchez, On the application of multivariate kernel density estimation to image error concealment, IEEE International Conference on Acoustics, Speech and Signal Processing (ICASSP), 2013.
- [Kua85] D. T. Kuan, A. A. Sawchuk, T. C. Strand and P. Chavel, "Adaptive Noise Smoothing Filter for Images with Signal-Dependent Noise," in IEEE Transactions on Pattern Analysis and Machine Intelligence, vol. PAMI-7, no. 2, pp. 165-177, 1985.
- [Kua87] D. T. Kuan et al, Adaptive restoration of images with speckle, IEEE Transactions on Acoustics, Speech, and Signal Processing, Vol. 35 (3), pp. 373–383, 1987.
- [Kum13] S. Kumar and Y. K. Jain, Performance Evaluation and Analysis of Image Restoration Technique using DWT, International Journal of Computer Applications, Vol. 72, No.18, pp. 11-20, 2013.
- [Lee80] J. S. Lee, Digital image enhancement and noise filtering by use of local statistics, IEEE Transactions on Pattern Analysis and Machine Intelligence Vol. 2 (2), pp. 165-168, 1980.
- [Lof65] D. O. Loftsgaarden, C. P. Quesenberry, A Nonparametric Estimate of a Multivariate Density Function, Annals of Mathematical Statistics, Vol. 36, Issue 3, pp. 1049-1051, Jun. 1965.

- [Luk14] B. Lukose and P. Roobini, Image Denoising Using Discrete Wavelet Transform, International Journal of Advances in Computer Science and Technology, Vol. 3, No. 7, pp. 395-398, July 2014.
- [Mal98] S. Mallat, A Wavelet Tour of Signal Processing, New York: Academic, 1998.
- [Mar87] J. S. Marron, A Comparison of Cross-Validation Techniques in Density Estimation, Annals of Statistics, 15, pp. 152-162, 1987.
- [Mar17] B. Marhaba and M. Zribi, Regularized bootstrap filter for image restoration, 11th International Conferences Computer Graphics, Visualization, Computer Vision and Image Processing and Big Data Analytics, Data Mining and Computational Intelligence, pp. 117-123, 2017.
- [Mar18a] B. Marhaba and M. Zribi, The bootstrap Kernel-Diffeomorphism Filter for Satellite Image Restoration, IEEE 22nd International Symposium on Consumer Technologies, Russia, pp. 80 - 84, 2018.
- [Mar18b] B. Marhaba and M. Zribi, Reduction of speckle noise in SAR images using hybrid combination of Bootstrap filtering and DWT, International Conference on Computer and Applications (ICCA), Beirut, pp. 377-382, 2018.
- [Ond16] B. Ondela, S. Pareyani, Analysis of Filters for the Reduction of Speckle Noise in Images, International Journal of Advanced Research in Computer and Communication Engineering, Vol. 5, Special Issue 3, pp. 97-101, 2016.
- [Pri16] S. Priyanka, A. S. Naveen kumar, Noise Removal in Remote Sensing Image Using Kalman Filter Algorithm, International Journal of Advanced Research in Computer and Communication Engineering Vol. 5, Issue 3, pp. 894-897, 2016.
- [Ros56] M. Rosenblatt, Remarks on some nonparametric estimates of a density function, Ann. Math. Statist. 27, pp. 827-837, 1956.
- [Rub14] E. L. Rubio, A Histogram Transform for Probability Density Function Estimation, IEEE Transactions on Pattern Analysis and Machine Intelligence, Vol. 36, Issue 4, pp. 644-656, 2014.
- [Sai94] S. R. Sain, K. A. Baggerly and D. W. Scott, Cross-Validation of Multivariate Densities, Journal of the American Statistical Association, 89, pp. 807-817, 1994.
- [Sao97] S. Saoudi, F. Ghorbel and A. Hillion, Some Statistical Properties of the Kernel-Diffeomorphism Estimator, Applied Stochastic Models and Data Analysis, Vol. 13, pp. 39-58, 1997.
- [Sil86] B. W. Silverman, Density Estimation for Statistics and Data Analysis, Chapman & Hall/CR, New York, 1986.

- [Sco92] D. W. Scott, *Multivariate density estimation: Theory, practice, and visualization*, Wiley Series in Probability and Mathematical Statistics, New York: Wiley, 1992.
- [Tar70] M. Tarter and R. Kronmal, On Multivariate Density Estimates Based on Orthogonal Expansions, *The Annals of Mathematical Statistics*, Vol. 41, No. 2, pp. 718-722, Apr. 1970.
- [Tas00] C. Taswell, "The what, how, and why of wavelet shrinkage denoising," in *Computing in Science & Engineering*, vol. 2, no. 3, pp. 12-19, May-June 2000.
- [Vij12] M. Vijay and L.S. Devi, Speckle Noise Reduction in Satellite Images Using Spatially Adaptive Wavelet Thresholding, *International Journal of Computer Science and Information Technologies*, Vol. 3 (2) , pp. 3432-3435, 2012.
- [Wan93] M. P. Wand and M. C. Jones, Comparison of Smoothing Parameterizations in Bivariate Kernel Density Estimation, *Journal of the American Statistical Association*, 88, pp. 520-528, 1993.
- [Wan94] M. P. Wand and M. C. Jones, Multivariate Plugin Bandwidth Selection, *Computational Statistics*, 9, pp. 97-116, 1994.
- [Woo77] J. W. Woods and C.W. Radewan, Kalman filtering in two dimensions, *IEEE Trans. Inf. Theory*, Vol. 23, pp. 473-482, 1977.
- [Zhu13] Junling Zhu, Jianguo Wen and Yafeng Zhang, A New Algorithm for SAR Image Despeckling Using an Enhanced Lee Filter and Median Filter, *6th International Congress on Image and Signal Processing (CISP)*, pp. 224-228, 2013.

General Conclusion and Perspectives

There are several types of imagery that researchers concern to study the restoration techniques among, such as satellite, medical, consumer cameras etc. In our thesis, we chose to study and apply the restoration techniques on the satellite images, which is important in many fields such as security, planet health, changing lands and water bodies. In order to benefit of the satellite images to the maximum extent and to take advantage of the data in it, then use these data effectively in studies in different areas, these images should be clear so that researchers can analyze the information in satellite images and take data fully and correctly. Unfortunately, satellite images are subject to many distortion effects during the acquisition process and during the transmission channels, these effects appear in the image in the form of blur and/or noise. The result of this noise and/or blur appears as an annoying loss of a large part of the valuable information without which researchers cannot take advantage of these images. Image restoration techniques can process the degraded satellite images and remove the defects due to noise and/or blur and output an image, which is as close as to the original image retaining the useful information and details. The image restoration field is one of the most important fields in the image-processing domain. A wide variety of approaches for image restoration, from classical to recursive, exists in the literature.

In our work, we have presented linear and nonlinear techniques in satellite images restoration. Regarding the obtained results, we found that nonlinear restoration techniques are superior to the linear restoration techniques by: edge preserving, sharpness and more powerful with the non-Gaussian noise assumptions. In the rest of our work, we have been particularly interested in nonlinear filtering techniques in a statistical framework. The main objective of our work is to propose a novel nonlinear filtering techniques that guaranties a resultant restored image is clearer than the previous proposed methods. Here, we introduced the mathematical models for the original and degraded (observed) images that we will adopt for the restoration of satellite images. The model of the original image is the output of a linear 2-D autoregressive (AR) process, which is very conducive for recursive filtering in 2-D. The observed satellite image is modeled as the output of a 2-D spatially varying linear system, which is characterized by its point-spread function (PSF). We have chosen as a nonlinear filter, the Bayesian bootstrap filter (BBF) for resolving the problem of degradation in the satellite images. The bootstrap algorithm is a filtering process based on both the Bayesian state estimation and the Monte Carlo (MC) methods. The BBF is a recursive algorithm to estimate the posterior probability density function (pdf) from a set of samples for Bayesian image restoration. Although the resampling

step in BBF has reduced the degeneracy problem which is prevalent in particle filters, it has introduced other problems, and in particular, the problem of loss of diversity among the particles. This arises because in the resampling stage, samples are drawn from a discrete distribution. Here, we have proposed a modification in the resampling stage of the BBF based on nonparametric multivariate density estimation, as a potential solution to the above problem. This modification occurred at the resampling stage, which involves changing the sampling process from a discrete distribution to a continuous approximation of the posterior density using the nonparametric methods. We called the filters obtained by this modification nonparametric BBF (NBBF). Comprehensive experiments were carried out in order to confirm the effectiveness of the proposed nonlinear filters on the quality of the restored satellite images by means of Peak Signal to Noise Ratio (PSNR). Finally, we have reduced the speckle noise in satellite SAR images by proposing a method that combines the NBBF and discrete wavelet transform (DWT) approach.

Future Work

We believe it would be very worthy to study and involve some of the nonparametric density estimators that we did not use in our work, such as orthogonal series density estimation and B-spline density estimator, in the image restoration process to estimate the posterior probability density estimation. We also believe it is a very important step to study and analyses the convergence and stability of the proposed. Also, it would be a very good idea to extend the proposed NBBF scheme to the non-causal image model. Another interesting topic is to involve the proposed NBBF in the domain of coupling image restoration with image segmentation. Finally, we see that the NBBF would achieve a very interesting results when implementing it in video restoration field.

Appendix

1.A Sentinel-1

1.A.1 Spectral Bands and Resolution

Sentinel-1 carries a single C-band synthetic aperture radar instrument operating at a center frequency of 5.405 GHz. It includes a right-looking active phased array antenna providing fast scanning in elevation and azimuth, data storage capacity of 1 410 Gb and 520 Mbit/s X-band downlink capacity. Denoting the transmit and receive polarizations by a pair of symbols, a radar system using H and V linear polarizations can thus have the following channels:

- HH - for horizontal transmit and horizontal receive, (**HH**)
- VV - for vertical transmit and vertical receive, (**VV**)
- HV - for horizontal transmit and vertical receive (**HV**), and
- VH - for vertical transmit and horizontal receive (**VH**).

The C-SAR instrument supports operation in dual polarization (HH+HV, VV+VH) implemented through one transmit chain (switchable to H or V) and two parallel receive chains for H and V polarization. Dual polarization data is useful for land cover classification and sea-ice applications.

Sentinel-1 operates in four exclusive acquisition modes:

- Strip map (SM)
- Interferometric Wide swath (IW)
- Extra-Wide swath (EW)
- Wave mode (WV).

Spatial resolutions depend on the acquisition mode and the level of processing.

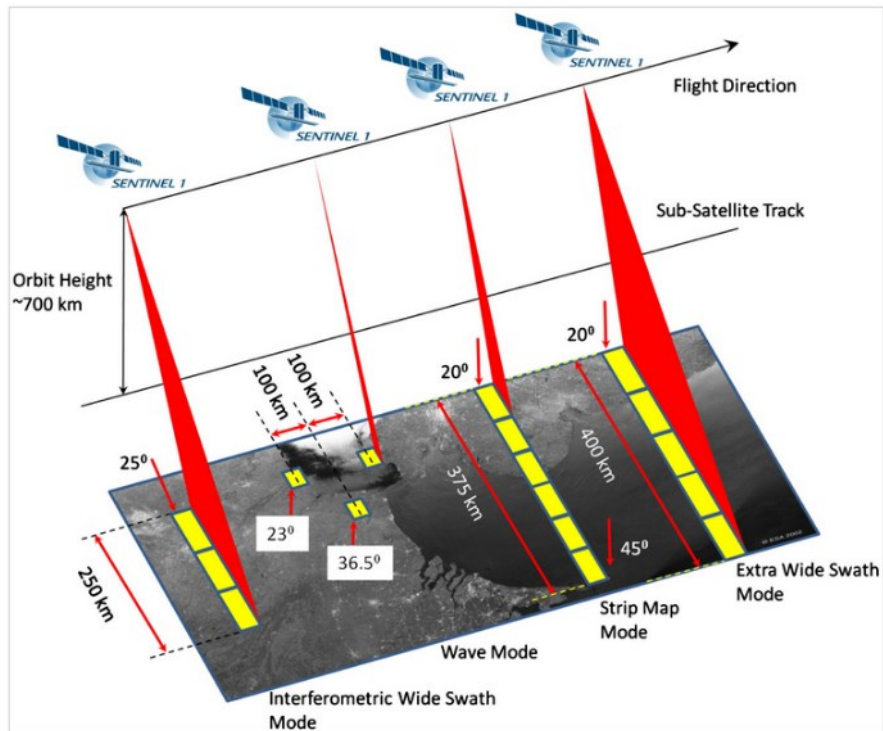


Figure 1.A.1: Sentinel-1 Modes.

1.A.1.a Level-1 Single Look Complex

Single Look Complex products (SLC) have spatial resolutions that depend on acquisition mode. In Table 1 below for SLC SM/IW/EW products, the spatial resolutions and pixel spacing are provided at the lowest and highest incidence angles. For SLC WV products, the spatial resolution and pixel spacing are provided for the WV1 and WV2 imagettes. The SM and WV SLC products are sampled at the natural pixel spacing, meaning that the pixel spacing is determined in azimuth by the pulse repetition frequency (PRF) and in range by the radar range sampling frequency. Thus, there will be slight variations around the orbit. Note that spatial resolution is a measure of the system's ability to distinguish between adjacent targets while pixel spacing is the distance between adjacent pixels in an image, measured in meters. The equivalent number of independent looks (ENL) for a given product type is intended to correspond to the number of equally weighted, statistically independent looks which would produce the same speckle statistics as the processing used to generate the product. IW and EW SLC products have all bursts in all sub-swaths are re-sampled to a common pixel spacing grid in range and azimuth.

Table 1.A.1: Acquisition resolution Level-1 SLC.

Mode	Resolution rg × az	Pixel spacing rg × az	Number of looks	ENL
SM	1.7 × 4.3 m to 3.6 × 4.9 m	1.5 × 3.6 m to 3.1 × 4.1 m	1 × 1	1
IW	2.7 × 22 m to 3.5 × 22 m	2.3 × 14.1 m	1 × 1	1
EW	7.9 × 43 m to 15 × 43 m	5.9 × 19.9 m	1 × 1	1
WV	2.0 × 4.8 m and 3.1 × 4.8 m	1.7 × 4.1 m and 2.7 × 4.1 m	1 × 1	1

1.A.1.b Level-1 Ground Range Detected

Level-1 GRD products are available in one of three spatial resolutions:

- Full Resolution (FR) for SM mode
- High Resolution (HR) for SM, IW and EW modes
- Medium Resolution (MR) for SM, IW, EW and WV modes.

The spatial resolution of GRD products in the tables below corresponds to the mid-range value at mid-orbit altitude, averaged over all swaths (SM/WV) or sub-swaths (IW/EW). The range resolution is ground range. The equivalent number of looks (ENL) for IW and EW GRD products corresponds to an average over all sub-swaths.

Table 1.A.2: Full resolution Level-1 GRD.

Mode	Resolution rg × az	Pixel spacing rg × az	Number of looks	ENL
SM	9 × 9 m	3.5 × 3.5 m	2 × 2	3.7

Table 1.A.3: High resolution Level-1 GRD.

Mode	Resolution rg × az	Pixel spacing rg × az	Number of looks	ENL
SM	23 × 23 m	10 × 10 m	6 × 6	29.7
IW	20 × 22 m	10 × 10 m	5 × 1	4.4
EW	50 × 50 m	25 × 25 m	3 × 1	2.7

Table 1.A.4: Medium resolution Level-1 GRD.

Mode	Resolution rg × az	Pixel spacing rg × az	Number of looks	ENL
SM	84 × 84 m	40 × 40 m	22 × 22	398.4
IW	88 × 87 m	40 × 40 m	22 × 5	81.8
EW	93 × 87 m	40 × 40 m	6 × 2	10.7
WV	52 × 51 m	25 × 25 m	13 × 13	123.7

1.A.1.c Level-2 Ocean

For Level-2 OCN products, the swell spectra (OSW) are provided at a spatial resolution of 20 km by 20 km. The wind fields (OWI) and surface radial velocity (RVL) components have a spatial resolution of 1 km by 1 km (for SM/IW/EW). For WV, the results are average on the 20x20km grid, giving only 1 value by vignettes.

1.A.2 Sentinel-1 data

The Sentinel-1 mission represents a completely new approach to SAR mission design by ESA in direct response to the operational needs for SAR data expressed under the EU-ESA GMES (Global Monitoring for Environment and Security) program. The mission ensures continuity of C-band SAR data to applications and builds on ESA's heritage and experience with the ERS and Envisat SAR instruments, notably in maintaining key instrument characteristics such as stability and accurate well-calibrated data products.

1.A.2.a Sentinel-1 data products

Sentinel data products are made available systematically and free of charge to all data users including the general public, scientific and commercial users. The data will be delivered within an hour of reception for Near Real-Time (NRT) emergency response, within three hours for NRT priority areas and within 24 hours for systematically archived data. All data products are distributed in the Sentinel Standard Archive Format for Europe (SAFE) format. Each mode can potentially produce products at SAR Level-0, Level-1 SLC, Level-1 GRD, and Level-2 OCN. Data products are available in single polarization (VV or HH) for Wave mode and dual polarization (VV+VH or HH+HV) or single polarization (HH or VV) for SM, IW and EW modes.

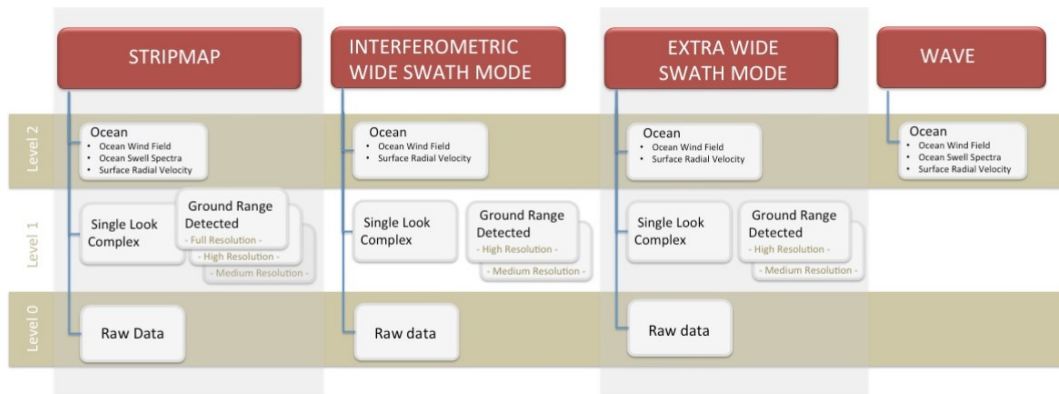


Figure 1.A.2: Graphical Representation of Sentinel-1 Core Products.

Level-0: The SAR Level-0 products consist of compressed and unfocused SAR raw data. Level-0 products are the basis from which all other high-level products are produced. Level-0 data is compressed using Flexible Dynamic Block Adaptive Quantization (FDBAQ), which provides a variable bit rate coding that increases the number of bits allocated to bright scatterers. For the data to be usable, it will need to be decompressed and processed using focusing software. Level-0 data includes noise, internal calibration and echo source packets as well as orbit and attitude information. Level-0 products are stored in the long-term archives. They can be processed to generate any type of product during the mission lifetime and for 25 years after the end of the space segment operations. Level-0 products are available to data users for only the SM, IW and EW modes.

Level-1: Level-1 data are the generally available products intended for most data users. Level-1 products are produced as Single Look Complex (SLC) and Ground Range Detected (GRD). Level-1 Single Look Complex (SLC) products consist of focused SAR data georeferenced using orbit and attitude data from the satellite and provided in zero-Doppler slant-range geometry. The products include a single look in each dimension using the full transmit signal bandwidth and consist of complex samples preserving the phase information. Level-1 Ground Range Detected (GRD) products consist of focused SAR data that has been detected, multi-looked and projected to ground range using an Earth ellipsoid model. Phase information is lost. The resulting product has approximately square spatial resolution pixels and square pixel spacing with reduced speckle at the cost of worse spatial resolution.

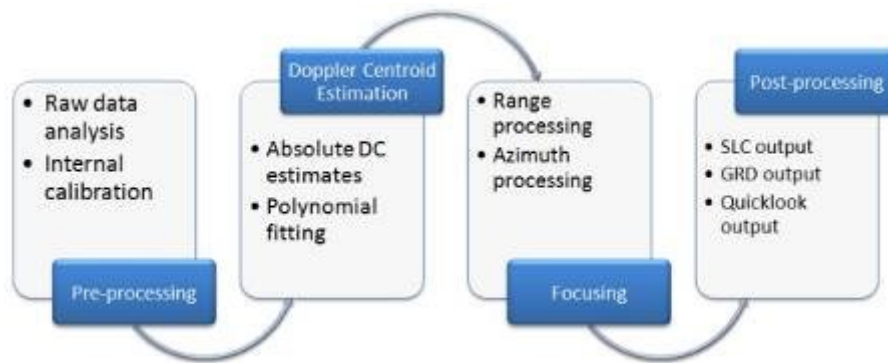


Figure 1.A.3: Level-1 Processing Flow.

Level-2: Level-2 consists of geolocated geophysical products derived from Level-1. Level-2 OCN products include components for Ocean Swell spectra (OSW) providing continuity with ERS and ASAR WV and two new components: Ocean Wind Fields (OWI) and Surface Radial Velocities (RVL). The OSW component is a two-dimensional ocean surface swell spectrum and includes an estimate of wind speed and direction per swell spectrum. The OSW component provides continuity measurement of SAR swell spectra at C-band. The OSW is generated from Stripmap and Wave modes only and is not available from the TOPSAR IW and EW modes. For Stripmap mode, there are multiple spectra derived from the Level-1 SLC image. For Wave mode, there is one spectrum per vignette. The OWI is a ground range gridded estimate of the surface wind speed and direction at 10 m above the surface derived from internally generated Level-1 GRD images of SM, IW or EW modes. The RVL surface radial velocity component is a ground range gridded difference between the measured Level-2 Doppler grid and the Level-1 calculated geometrical Doppler. The RVL component provides continuity of the ASAR Doppler grid.

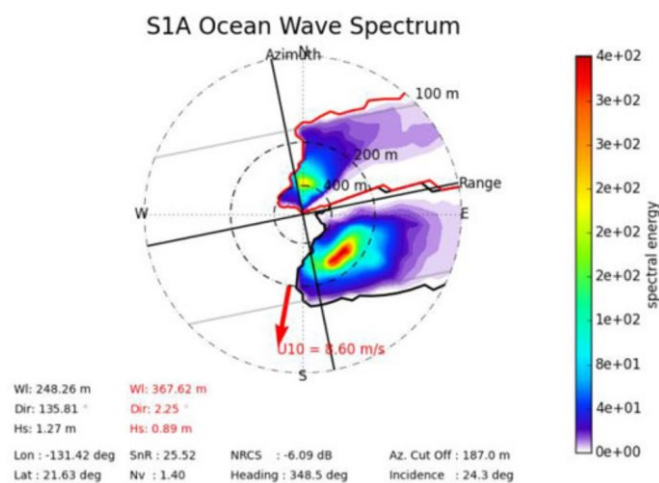


Figure 1.A.4: Example of Ocean Wave Spectrum presenting two swell partitions Copernicus Sentinel data (2016).

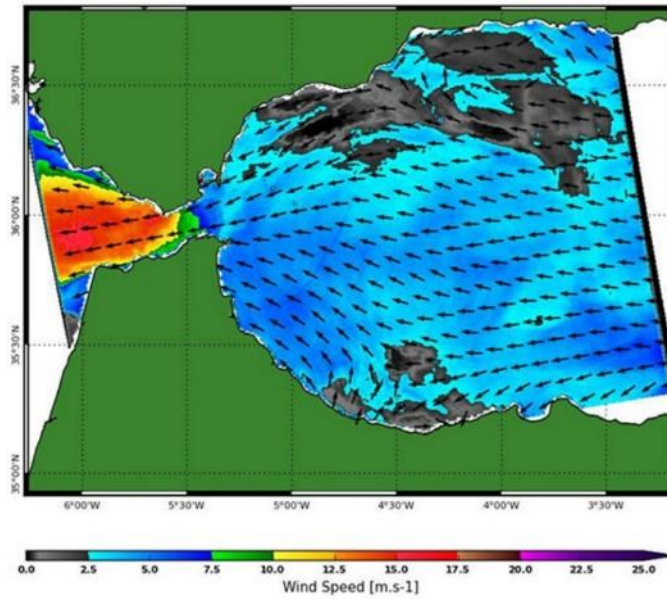


Figure 1.A.5: Example of SAR wind measurement over Gibraltar Copernicus Sentinel data (2017).

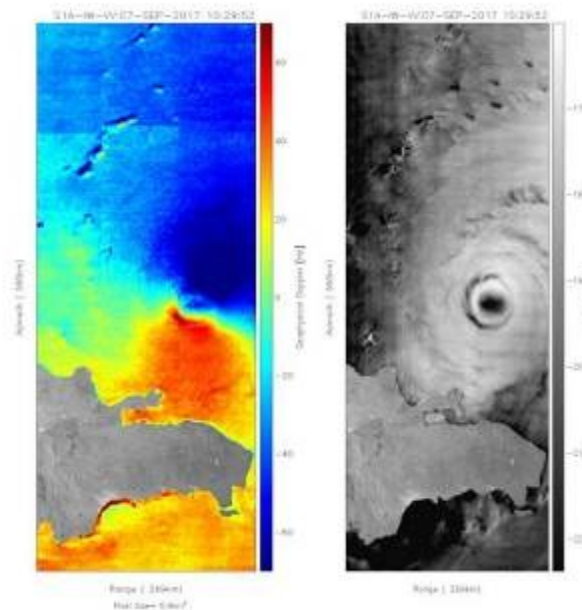


Figure 1.A.6: Surface Radial Velocity (RVL): Doppler anomaly over Irma Hurricane Copernicus Sentinel data (2017).

1.A.2.b Sentinel-1 data formats

Sentinel data products are distributed using a Sentinel-specific variation of the Standard Archive Format for Europe (SAFE) format specification. The SAFE format has been designed to act as a common format for archiving and conveying data within ESA Earth Observation archiving facilities. SAFE was recommended for the harmonization of the GMES missions by the GMES Product Harmonization Study. The Sentinel-SAFE format wraps a folder containing image data in a binary data format and product metadata in XML. This flexibility allows the

format to be scalable enough to represent all levels of Sentinel products. A Sentinel product refers to a directory folder that contains a collection of information. It includes:

- A 'manifest. Safe' file which holds the general product information in XML.
- Subfolders for measurement datasets containing image data in various binary formats.
- A preview folder containing 'quick looks' in PNG format, Google Earth overlays in KML format and HTML preview files.
- An annotation folder containing the product metadata in XML as well as calibration data.
- A support folder containing the XML schemes describing the product XML.

Products from all processing levels (Level-0, Level-1 and Level-2) are delivered in Sentinel-SAFE format. The data delivered is packaged as a file structure containing a manifest file in XML format listing general product metadata and subfolders for measurement data, annotations, previews and support files. The manifest file is an XML file containing the mandatory product metadata common to all Sentinel-1 products.



Figure 1.A.7: Product Folder File Structure for Level-1 Products.

Annotated data sets contain metadata describing the properties and characteristics of the measurement data or how they were generated. For each band of data, a product annotation data set contains metadata describing the main characteristics corresponding to that band such as the state of the platform during acquisition, image properties, polarization, Doppler information, swath merging and geographic location. Calibration annotations contain calibration information and the beta nought, sigma nought, gamma and digital number look-up tables that can be used for absolute product calibration. Noise data annotations contain the estimated thermal noise look-up tables. Annotated data sets are provided in XML format. Level-2 products do not contain annotation data sets as all product metadata is contained within the netCDF product file. In the preview folder, quick look data sets are power detected, averaged and decimated to produce a lower resolution version of the image. Single polarization products are represented with a greyscale image. Dual polarization products are represented by a single composite color image in RGB with the red channel (R) representing the first polarization, the green channel (G) represents the second polarization and the blue channel (B) represents an average of the absolute values of the two polarizations. Level-2 OCN products do not contain quick looks. Representation data sets found in the support folder contain information about the format or syntax of the measurement, annotated data sets, and can be used to validate and exploit these data. Representation data sets are provided as XML schemas. Measurement data sets contain the binary information of the actual acquired or processed data. For Level-0 this is the instrument data, for Level-1, it is the processed images and for Level-2, it is the derived data. There is one measurement data set per polarization and per swath. TOPSAR SLC products contain one complex measurement dataset in Geo TIFF format per swath per polarization. Level-1 GRD products contain one detected measurement dataset in Geo TIFF format per polarization. Measurement data sets are provided in Geo TIFF format for Level-1 products and netCDF format for Level-2 products. The Level-2 OCN products in netCDF format include both the annotation and measurement datasets described as netCDF attributes dimensions and variables in one self-describing, self-contained file.

1.A.3 Applications

Sentinel-1 provides data feeding services for applications in the Copernicus priority areas of maritime monitoring, land monitoring and emergency management. We can categorize these applications under three categories.

1.A.3.a Maritime Monitoring

(i) Ice Monitoring

High-resolution ice charting services supply ice classification and iceberg data to national coast guards, navies and shipping companies, to assist in assuring safe year-round navigation in the ice-covered Arctic and sub-Arctic zones. For sea-ice, information on ice concentration, extent, type, thickness and drift velocity can be determined. The location, size and drift of icebergs can also be collected. Sentinel-1 dual polarization data can significantly improve ice classification and discrimination. Through the detection of changes in the Arctic sea-ice extent, Sentinel-1 can be used to assess environmental impacts on coastal areas and transportation. In Figure 1.A.8, we presented an Advanced Synthetic Aperture Radar (ASAR) image on March 12th and March 16th 2011 of the Sulzberger Ice Shelf in Antarctica (newly formed icebergs can clearly be seen in the second image).

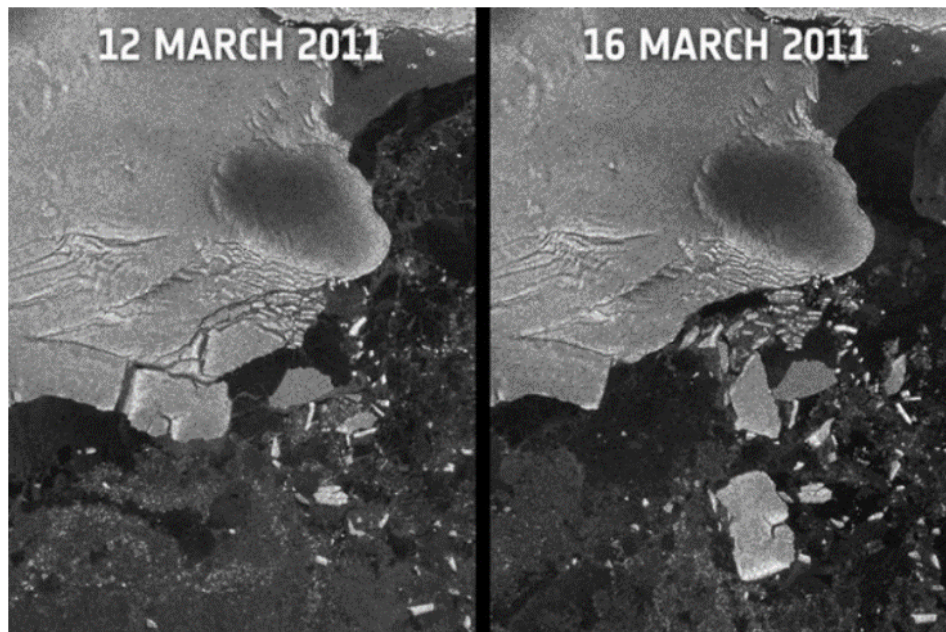


Figure 1.A.8: ASAR image on March 12th and March 16th 2011 of the Sulzberger Ice Shelf.

(ii) Ship Monitoring

Sentinel-1 uses wide area coverage with improved revisit times and is able to potentially detect smaller ships than ENVISAT ASAR. The mission's ability to observe in all weather and in day or nighttime makes it ideal for precise cueing and location of ship activities at sea, allowing for more efficient and cost-effective use of other security assets, such as patrol aircraft and ships. Data relevant to ship detection are transmitted by the satellite in real-time for reception by local collaborative ground stations supporting European and national services. In Figure 1.A.9, we

presented ASAR Image Showing the Ships for the International Fleet Review Assembling in the Solent between the Isle of Wight and Portsmouth on June 26th 2005.



Figure 1.A.9: ASAR Image Showing the Ships for the International Fleet Review Assembling.

(iii) Oil Pollution Monitoring

Oil detection applications are used for gathering evidence of illegal discharges, analyzing the spread of oil spills and prospecting for oil reserves by highlighting naturally occurring seepage. Oil slicks are distinctly visible in SAR imagery as characteristically dark features. Most oil slicks are caused by ships emptying bilge before entering port. Detections can be correlated with Automatic Identification System (AIS) or Long-Range Identification and Tracking (LRIT) information broadcasts from ships to determine sources and prosecute offenders. Data relevant to oil spill monitoring are transmitted by the satellite in real-time for reception by local collaborative ground stations supporting European and national services.

Likewise, detection of naturally occurring oil seepage from the ocean floor can provide clues for oil prospecting. In Figure 1.A.10, we presented ASAR Image on May 2nd 2010 showing the Deepwater Horizon Oil Spill in the Gulf of Mexico near the Delta National Wildlife Refuge.



Figure 1.A.10: ASAR Image Showing the Deepwater Horizon Oil Spill.

1.A.3.b Land Monitoring

(i) Forestry

Sentinel-1 can play an important role in sustainable forest management with clear-cut and partial-cut detection, forest type classification, biomass estimation and disturbance detection. For climate change, mapping of forest fire scars can be an important part of mapping the carbon history of a forest and plays a critical role in the estimation of carbon emissions.

Land cover maps can be used to support forest management and the monitoring of illegal timber harvesting worldwide. In Figure 1.A.11, we presented a Sentinel-1 SAR polarimetric color composite of an crop area near New Amsterdam city (yellow: forest/dense woody vegetation; dark blue: water/humid soil; shades of brown: crop fields; very bright blue: settlements).

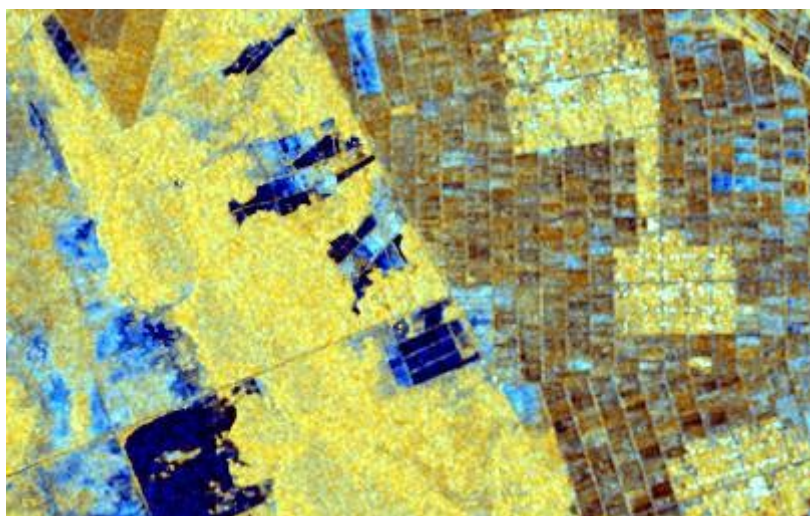


Figure 1.A.11: SAR polarimetric color composite of an crop area near New Amsterdam city.

(ii) Agriculture

Monitoring of crop conditions, soil properties and mapping tillage activities help to assess land use, predict harvests, monitor seasonal changes and assist in implementing policy for sustainable development. Sentinel-1 will also be used for monitoring the changes of agricultural production and productivity of pastures caused by drought and monitoring the decline of land productivity and soil degradation due to excessive cultivation and pasturage and improper irrigation. Agricultural maps enable provision of independent and objective estimates of the extent of cultivation in a given country or growing season, which can be used to support efforts to ensure food security in vulnerable areas. In Figure 1.A.12, we presented a color composite of three SAR images taken over the AGRISAR Test Site within a period of 2½ weeks at the beginning of the growing season (the different colors reflect the crop type and change in crop condition during this short time period).

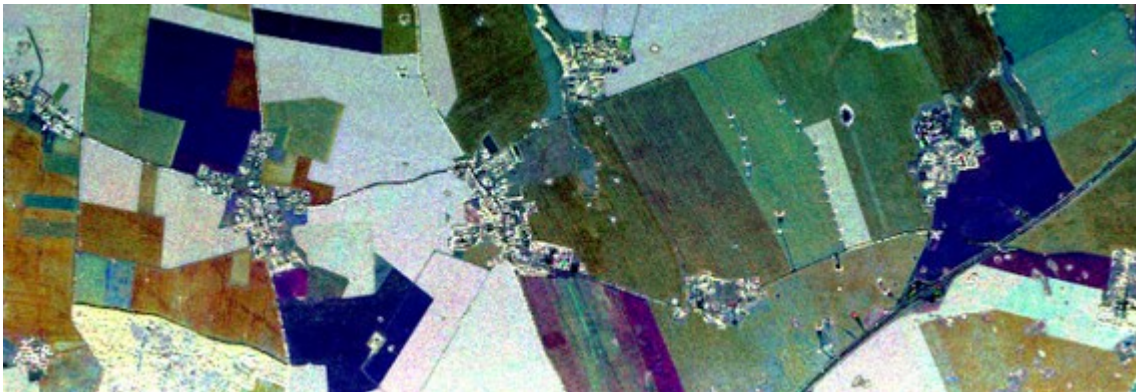


Figure 1.A.12: Color Composite of Three SAR Images.

(iii) Urban Deformation Mapping

Interferometric SAR can detect surface movements with an accuracy of a few millimeters per year and can provide an accurate tool for monitoring of land subsidence, structural damage and underground construction to improve safety and reduce economic loss. In Figure 1.A.13, we presented a Subsidence Monitoring of Venice; Italy with Sentinel-1 (provides the means for continuous monitoring of ground movement with an accuracy of a few millimeters per year).

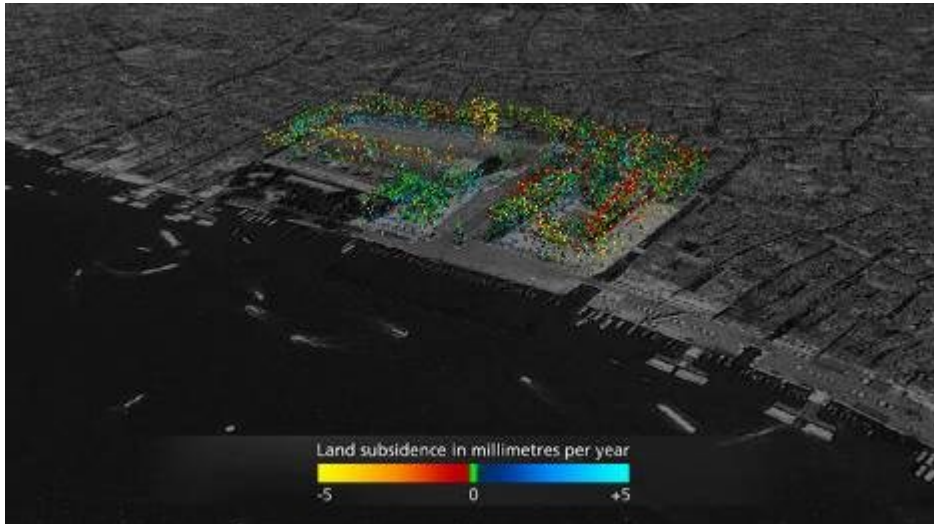


Figure 1.A.13: Subsidence Monitoring of Venice, Italy.

1.A.3.c Emergency Management

(i) Flood Monitoring

Flooding is the world's most costly type of natural disaster. Across the developing world, floods can strike with deadly regularity, destroying housing, agriculture and communications.

Developed nations are hardly immune: the floods that struck Europe in 2002 cost dozens of lives and billions of Euros. Some 85% of all European civil protection measures are concerned with floods, and the damage done by flooding is set to grow further in future. Extensive building along riverbanks and flood plains leaves more property under threat and climatologists project an increase in extreme weather events including floods. Well in advance of any flood occurring, satellites can help civil protection planners anticipate where a river would be most prone to burst its banks, and take action accordingly. Satellite data can provide highly detailed digital elevation models of areas at risk that can serve as the basis of computerized flood simulations. During a flood event, near-real-time images are a management tool for authorities coping with the disaster. One of the biggest problems is obtaining a clear picture of the overall extent of the flood. Wide area satellite images can show an entire flood within a single picture, with radar instruments especially well-suited for differentiating between waterlogged and dry land. A sequence of satellite images can show if the flood is growing or diminishing over time, and highlight further areas coming under threat of inundation. Simply comparing before and after images of the flooded region makes possible a rapid and authoritative damage assessment estimate, factoring in different land cover types to quantify the cost of the flood.



Figure 1.A.14: Flood in the north of Italy.

Furthermore, high-resolution digital elevation models (DEMs) generated through Sentinel-1's interferometric modes can be used to conduct run-off and inundation analysis in areas previously lacking elevation data.

(ii) Earthquake Analysis

In SAR provides the unique ability to produce medium and high-resolution maps of earthquake deformations. Through the persistent monitoring of earthquake-prone areas, active fault lines can be discovered and potential risks can be studied. The Interferometric Wide swath mode will make it easier to monitor very large-scale earthquakes. We presented in Figure 1.A.15 ASAR coseismic interferogram of the 2011 Tohoku-oki earthquake in Japan processed by JPL/Caltech ARIA project using ROI_PAC. One color cycle represents 50 cm of motion in the radar line of sight.

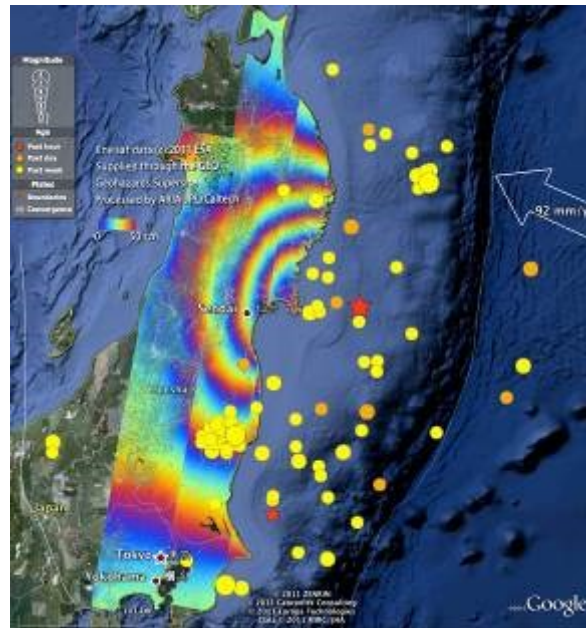


Figure 1.A.15: ASAR coseismic interferogram of Tohoku-oki.

(iii) Landslide and Volcano Monitoring

SAR interferometry can locate areas prone to landslides and monitor surface deformation to provide early warning of potential disasters and monitoring of critical infrastructure. Pre-eruption uplift and post eruption volcanic shrinkage can be monitored with similar interferometric techniques and can complement in-situ networks from volcano observatories. InSAR monitoring can help detect first signs of increasing levels of volcanic activity, preceding earthquakes and other precursors that may signal eruptions. We presented in Figure 1.A.16 ASAR interferogram image over the Kenyan section of the Great Rift Valley shows small surface displacements that are not visible to the naked eye of the Longonot Volcano. Interferogram images appear as rainbow-colored interference patterns.

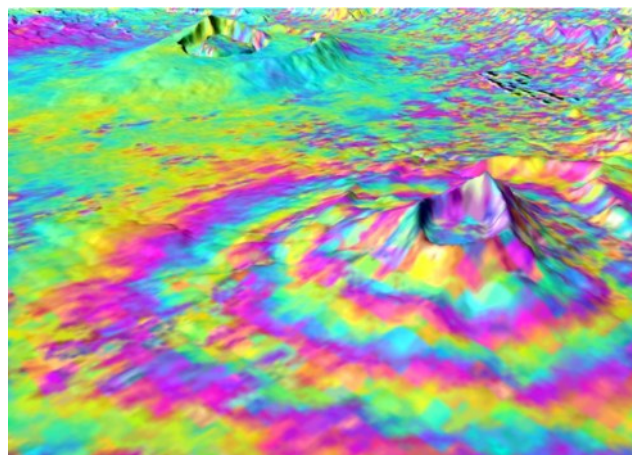


Figure 1.A.16: ASAR interferogram image over the Kenyan section of the Great Rift Valley.

1.B Sentinel-2

1.B.1 Spectral Bands and Resolution

The Sentinel-2 Multi-Spectral Instrument (MSI) acquires 13 spectral bands ranging from Visible and Near-Infrared (VNIR) to Shortwave Infrared (SWIR) wavelengths along a 290-km orbital swath. The MSI sensor data are complementary to data acquired by the U.S. Geological Survey (USGS) Landsat 8 Operational Land Imager (OLI) and Landsat 7 Enhanced Thematic Mapper Plus (ETM+). A collaborative effort between ESA and the USGS provides for the public access and redistribution of global acquisitions of ESA's Sentinel-2 data at no cost through secondary U.S.-based portals, in addition to direct user access from ESA.

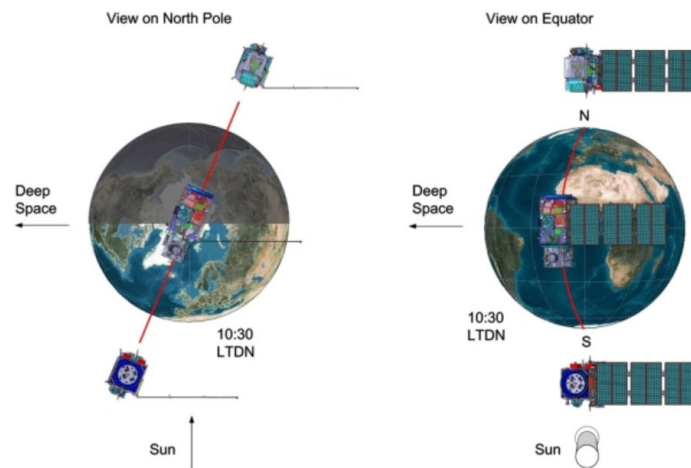


Figure 1.B.1: The Twin-Satellite sentinel-2 Orbital Configuration.

The twin satellites of sentinel-2 will provide continuity of Spot and Landsat type image data, contribute to ongoing multispectral observations and benefit Copernicus services.

The MSI measures reflected radiance through the atmosphere within 13 spectral bands. The spatial resolution is dependent on the particular spectral band (Figure 1.B.2):

- 4 bands at 10 meter: blue (490 nm), green (560 nm), red (665 nm), and near infrared (842 nm).
- 6 bands at 20 meter: 4 narrow bands for vegetation characterization (705 nm, 740 nm, 783 nm, and 865 nm) and 2 larger SWIR bands (1,610 nm and 2,190 nm) for applications such as snow/ice/cloud detection or vegetation moisture stress assessment.
- 3 bands at 60 meter: mainly for cloud screening and atmospheric corrections (443 nm for aerosols, 945 nm for water vapor, and 1375 nm for cirrus detection).

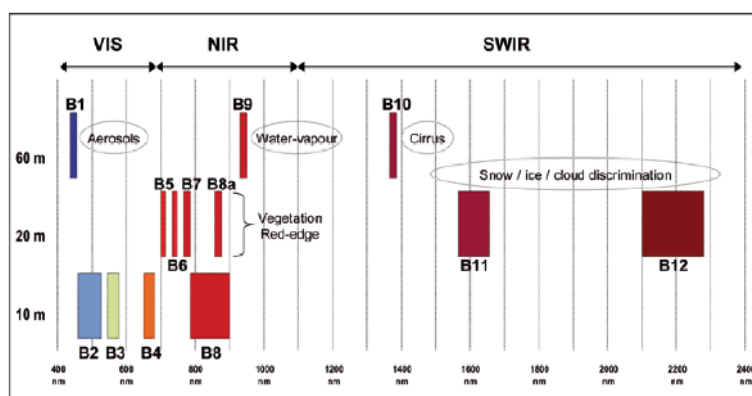


Figure 1.B.2: Spectral bands versus spatial resolution.

Table 1.B.1: Sentinel-2 Radiometric and Spatial Resolutions.

Sentinel-2 Bands	Central Wavelength (nm)	Bandwidth (nm)	Spatial Resolution (m)
Band 1-Coastal aerosol	443	20	60
Band 2-Blue	490	65	10
Band 3-Green	560	35	10
Band 4-Red	665	30	10
Band 5-Vegetation Red Edge	705	15	20
Band 6-Vegetation Red Edge	740	15	20
Band 7-Vegetation Red Edge	783	20	20
Band 8-NIR	842	115	10
Band 8A-Narrow NIR	865	20	20
Band 9-Water vapour	945	20	60
Band 10-SWIR-Cirrus	1375	30	60
Band 11-SWIR	1610	90	20
Band 12-SWIR	2190	180	20
Band TCI*	RGB	Composite	10

*Data acquired after December 5, 2016 include a full resolution True-Colour Image as an RGB (red, green, blue) composite image created from bands 4, 3, 2.

1.B.2 Sentinel-2 data

Sentinel-2 is a constellation of two Earth observation satellites, developed under the direction of the European Space Agency, as part of the European Commission's ambitious Copernicus Earth observation program. The full Copernicus program, which consists of several different Sentinel missions, is the most comprehensive systematic Earth Observation program ever created, providing land, ocean, and atmosphere observations, with continuity out to 2030. The wide-swath, multi-spectral imaging capabilities of the Sentinel-2 satellites provide an unprecedented view of our Earth, covering all of the Earth's landmasses, large islands, and waterways. Sentinel-2 data is ideal for agriculture, forestry, and other land management applications. For example, it can be used to study leaf area as well as chlorophyll and water

content; to map forest cover and soils; and to monitor inland waterways and coastal areas. Images of natural disasters such as floods and volcanic eruptions can be used for disaster mapping and humanitarian relief efforts. Satellite data is provided in multiple levels typically ranging from 0 to 3, where 0 is unprocessed instrument and payload data at full resolution, and 3 means derived information, like a single percentage number. Level-0 and Level-1A processing are performed by the ground segment and are in general not accessible to users. Level-1B and Level-1C processing is performed routinely by the S-2 ground segment and the results are available to users.

Level-1B products represent Top-Of-Atmosphere calibrated radiances (TOA) in sensor geometry, and include radiometric corrections and the refinement of the physical geometrical viewing model (which is not applied at this level). Products are available as JPEG2000 lossless compressed images plus associated metadata, all capsuled within a SAFE file container (basically a zip-file, more details about SAFE in a later post). Level-1B is composed of granules (see also Figure below), one granule represents a sub-image (one for each band) of the satellite track, with a size of 25 km across-track and approx. 23 km along-track on ground. Each Level-1B granule has a data volume of approximately 27 MB. Level-1B products require expert knowledge of orthorectification techniques.

Level-1C products are radiometric and geometric corrected TOA products. The corrections include orthorectification and spatial registration on a global reference system (combined UTM projection and WGS84 ellipsoid) with sub-pixel accuracy. Level-1C images are delivered in tiles of 100×100 km (see also Figure below), each of which is approximately 500 MB. Products are available as JPEG2000 lossless compressed images plus associated metadata, all capsuled again within a SAFE file container. Currently, this type of data is the main target for almost all users.

Level-2 products are Bottom-Of-Atmosphere (BOA) corrected orthophotos. In addition, they contain an Aerosol Optical Thickness (AOT) map, a Water Vapor (WV) map, and a Scene Classification Map (SCM) together with Quality Indicators (QI) for cloud and snow probabilities at 60 m resolution. They are resampled and generated with an equal spatial resolution for all bands, based on the requested resolution (10 m, 20 m, or 60 m). Unfortunately, the ground segment currently not routinely generates Level-2 products but have to be generated by the users themselves (e.g. by using the Sentinel toolbox, provided by ESA free). However,

the provisioning of Level-2 products, as a systematically generated core product of the ground segment, is currently assessed.

1.B.2.a Sentinel-2 Data Structure

These Sentinel-2 images are processed to Level-1C, which means they are orthorectified, map-projected images containing top-of-atmosphere reflectance data. The images are stored in the JPEG 2000 file format, with each spectral band stored as a separate image for easy access. Images are organized in the Sentinel-2 tiling grid, which is based on the Military grid reference system that divides the Earth into square tiles of approximately 100 km on each side. A single image tile acquired at a particular point in time is referred to as a “granule.” Cloud Storage organizes granules in the following effective directory structure:

Datatakes and Datastrips: A satellite flies over an area and scans the Earth surface. For the Sentinels this is named a “datatake” – the continuous acquisition of an image from one Sentinel-2 satellite in a given MSI imaging mode. The maximum length of an imaging datatake is 15,000 km (e.g. the continuous observation from northern Russia to southern Africa). Since it is not possible for a single ground receiving station to cover such an area the term “datastrip” is introduced: within a given datatake, a portion of image downlinked during a pass to a given station is termed a “datastrip”. If a particular orbit is acquired by more than one station, a datatake is composed of one or more datastrips. The maximum length of a datastrip downlinked to a ground station is approximately 5,000 km.

Granules and Tiles: Now back to Level-1C products. In the whole concept of providing orthorectified, spatially co-registered (to a global reference system) data to users a confusion has been introduced. Specifically by allowing the usage of the same expression for different things. In order to avoid this confusion we will strictly use the term “granules” for the 25×23 km sub-images at Level-1B and the term “tiles” for 100×100 km sub-images a Level-1C and higher. The figure below (Courtesy of ESA) shall provide an impression of the meaning of these two terms. The underlying datastrip (the satellite image) forms the basis.

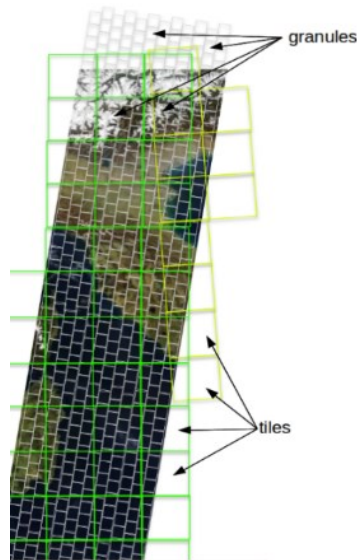


Figure 1.B.3: Sentinel-2 Granules and Tiles.

1.B.2.b Sentinel-2 Data access

The USGS Earth Resources Observation and Science (EROS) Center repackages Sentinel-2 products on a per tile basis while preserving the Sentinel Standard Archive Format for Europe (SAFE) format specification, which allows for the distribution of a user-friendly file size that is approximately 650 MB. Each Level-1C product is a 100 km×100 km tile with a UTM/WGS84 (Universal Transverse Mercator/World Geodetic System 1984) projection and datum. The Sentinel-2 tiling grid is referenced to the U.S. Military Grid Reference System (MGRS). Tiles can be fully or partially covered by image data. Partially covered tiles correspond to those at the edge of the swath. The download package from the USGS includes one file for each of the 13 spectral bands plus metadata. Update: Data acquired after December 5, 2016 are distributed from ESA in a single tile basis with a shorter naming convention and include a full-resolution True-Color Image. Previously offered Sentinel-2 data in the EROS archive will be replaced as data with the True-Color Image become available from ESA. Users may see temporary scene duplication in search results.

Products are available for download in a zip file, which includes image data, quality indicators, auxiliary data, and metadata. Sentinel image data are in Geographic Markup Language JPEG2000 (GMLJP2) format. GML provides the encoding necessary for georeferencing the image. Sentinel-2 data are intended for scientific use within a Geographic Information System (GIS) or other special application software that supports the GMLJP2 format. ESA offers the Sentinel 2 Toolbox, an open source software product, for the visualization, analysis, and processing of GMLJP2 files/Sentinel-2 data and other high-resolution remote sensing data.

Full Resolution Browse (FRB) images in Georeferenced Tagged Image File Format (GeoTIFF) are also available from the USGS for Sentinel-2 tiles. This product is a simulated natural color composite image created from three selected bands (11, 8A, 4) with a ground resolution of 20 meters. All Sentinel-2 data products are provided free of charge to all data users, including the general public, and scientific and commercial users under the terms and conditions prescribed by the European Commission's Copernicus Programme. The image data can be used easily with any software that recognizes JPEG 2000 image files. The additional metadata files can be used with the Sentinel-2 Toolbox, an open source toolbox developed for the European Space Agency (ESA). This toolbox includes visualization, analysis, and processing tools for Sentinel-2 data.

1.B.3 Applications

Sentinel-2 will serve a wide range of applications related to Earth's land surface and coastal zones. The mission will mainly provide information for agricultural and forestry practices and for helping manage food security. Satellite images will be used to determine various plant indices such as leaf area chlorophyll and water content indexes. This is particularly important for effective yield prediction and applications related to Earth's vegetation. As well as monitoring plant growth, Sentinel-2 can be used to map changes in land cover and to monitor the world's forests. It will also provide information on pollution in lakes and coastal waters. Images of floods, volcanic eruptions and landslides contribute to disaster mapping and help humanitarian relief efforts.

Examples for applications include:

- Monitoring land cover change for environmental monitoring
- Agricultural applications, such as crop monitoring and management to help food security
 - Detailed vegetation and forest monitoring and parameter generation (e.g. leaf area index, chlorophyll concentration, carbon mass estimations)
 - Observation of coastal zones (marine environmental monitoring, coastal zone mapping)
 - Inland water monitoring
 - Glacier monitoring, ice extent mapping, snow cover monitoring
 - Flood mapping and management (risk analysis, loss assessment, disaster management during floods)

The Sentinel Monitoring web application offers an easy way to observe and analyses land changes based on archived Sentinel-2 data.

1.B.4 Sentinel-2 Image Quality

The Sentinel-2 products will take advantage of the stringent radiometric and geometric image quality requirements. These requirements constrain the stability of the platform and the instrument, the ground processing and the in-orbit calibration. Table 1.2 shows the spectral band characteristics and the required signal-to-noise ratios for the reference radiances (L_{ref}). An accurate knowledge of the band equivalent wavelength is very important as an error of 1 nm can induce errors of several percent on the reflectance, especially in the blue part (atmospheric scattering) and the near infrared part of the spectrum (vegetation red edge). The equivalent wavelength therefore needs to be known with an uncertainty below 1 nm. Obtaining a physical value (radiance or reflectance) from the numerical output provided by the instrument requires knowledge of the instrument sensitivity. Any error on the absolute calibration measurement will directly affect the accuracy of this physical value. This is why a maximum 5% absolute calibration knowledge uncertainty was required for the mission, with an objective of 3%. In the same way, the cross-band and multitemporal calibration knowledge accuracies were set to 3% as an objective and 1%, respectively. Moreover, the nonlinearity of the instrument response will be known with an accuracy of better than 1% and will have to be stable enough that the detector non-uniformity can be calibrated at two radiance levels in flight.

Table 1.B.2: Band parameter for each spectral band.

Band number	Spatial Sample Distance (m)	Central wavelength (nm)	Bandwidth (nm)	Radiance sensibility range $L_{min} < L_{ref} < L_{max}$ ($W.m^{-2}.sr^{-1}.\mu m^{-1}$)	SNR Specification (at L_{ref})
1	60	443	20	16 < 129 < 588	129
2	10	490	65	11.5 < 128 < 615.5	154
3	10	560	35	6.5 < 128 < 559	168
4	10	665	30	3.5 < 108 < 484	142
5	20	705	15	2.5 < 74.5 < 449.5	117
6	20	740	15	2 < 68 < 413	89
7	20	783	20	1.5 < 67 < 387	105
8	10	842	115	1 < 103 < 308	174
8a	20	865	20	1 < 52.5 < 308	72
9	60	945	20	0.5 < 9 < 233	114
10	60	1 375	30	0.05 < 6 < 45	50
11	20	1 610	90	0.5 < 4 < 70	100
12	20	2 190	180	0.1 < 1.5 < 24.5	100

The geometric image quality requirements are summarized in Table 1.B.3. The accuracy of the image location, 20 m without ground control points (GCPs), is very good with regard to the pixel size and should be sufficient for most applications. However, from the Level-1 processing description, most of the Sentinel-2 images will benefit from GCPs and will satisfy the 12.5 m maximum geolocation accuracy.

Table 1.B.3: Sentinel-2 geometric image quality requirements.

Geometric image quality requirements	Ground processing hypothesis
A priori accuracy of image location: 2 km max (3 σ)	No processing
Accuracy of image location: 20 m (3 σ)	After image processing without GCPs
Accuracy of image location: 12.5 m (3 σ)	After image processing with GCPs
Multitemporal registration: 3 m (2 σ) for 10 m bands 6 m (2 σ) for 20 m bands 18 m (2 σ) for 60 m bands	After image processing with GCPs
Multispectral registration for any pair of spectral bands: 3 m (3 σ) for 10 m bands 6 m (3 σ) for 20 m bands 18 m (3 σ) for 60 m bands	After image processing with GCPs

2.A Point Spread Function

The most of the blurring processes can be approximated by convolution integrals, also known as Fredholm integral equations. A Point-Spread Function (PSF) or impulse response characterizes the blurring. The PSF is the output of the imaging system for an input point source. All the blurring processes considered in this section are linear and have a spatially invariant PSF [Tic06]. In the discrete image processing, we can replace the convolution integral by a sum. The blurry image $g(m, n)$ is achieved from the original image $f(m, n)$ using this convolution:

$$g(m, n) = \sum_{a=-\infty}^{+\infty} \sum_{b=-\infty}^{+\infty} h(-a, -b) f(m + a, n + b) \quad (2.1)$$

The function $h(m, n)$ represent the discrete PSF in the imaging system. We are also interested in the Discrete Fourier Transform (DFT) representation of the point-spread function, which is given by:

$$H(u, v) = \sum_{m=0}^{M-1} \sum_{n=0}^{N-1} h(m, n) e^{-2i\pi(\frac{um}{M} + \frac{vn}{N})} \quad (2.2)$$

where $u = \left[-\frac{M}{2}\right] + 1, \dots, \left[\frac{M}{2}\right]$ and $v = \left[-\frac{N}{2}\right] + 1, \dots, \left[\frac{N}{2}\right]$.

$H(u, v)$ provides a kit of coefficients for plane waves of different frequencies and orientations. These plane waves, named spatial frequency components, will rebuild the PSF exactly when multiplied by the coefficients $H(u, v)$ and summed. The function $H(u, v)$ is referred to as the system frequency response or the transfer function. By analyzing $|H(u, v)|$, we can instantly determine which spatial frequency components are attenuated or passed by the imaging system.

2.A.1 PSF generation

The PSFs forming the H_T groups, which are used in computing the error in the restoration models, are achieved by sampling continuous trajectories on a pixel grid. Every trajectory is formed of a particle position, which follow a random motion 2-D within a continuous domain.

At each iteration, the initial velocity vector of the particle is affected with deterministic inertial component and a Gaussian distribution, heading toward the current position of the

particle. In addition, there is little chance of an impulse disturbance to reverse the velocity of the particle, simulating a sudden movement, which occurs when the user presses the camera button or tries to compensate for camera shake.

After each iteration, the velocity is normalized to ensure that each trajectory corresponding to equal exposures has equal length. Gaussian, inertial, and impulsive perturbation is ruled by its own parameter, and every set of H_T contains the PSFs that are sampled from trajectories generated by parameters spanning a significant range of values. If all of the perturbation parameters are zero, then the generated trajectories will be rectilinear.

Every PSF $h_T \in H_T$ is composed of discrete values which are calculated by means of a trajectory sampling on a regular pixel grid using sub-pixel linear interpolation. The corresponding groups are obtained at different exposure times by estimating the values of each PSF by a fixed factor.

Recall that restoring the image refers to removing or reducing the known deterioration in an image. This includes the removal of the blur for the images degraded due to sensor constraints or the environment, noise filtering, and correction of geometric or nonlinear distortions due to sensors. It describes the response of the imaging system to an input point. Input point, representing a single pixel in the "ideal" image, will be recreated as something other than a single pixel in the "real" image.

“Point Spread Functions” describe the 2D distribution of light at the focal level of the telescope for the sources of astronomical points. Optical designers have worked very hard in order to reduce the PSF size for large telescopes. A good PSF evaluation is critical, especially for telescopes that are intended to have "near-diffraction" limited performance. This clearly includes space telescopes. However, it also includes large ground telescopes equipped with "active" or "adaptive" optical systems, which can significantly reduce the impact of the aerial vision on the PSF.

3.A Mean filter

3.A.1 Arithmetic mean filter

This type of mean filter is the simplest type of the other mean filters. Assuming that S_{xy} is the group of coordinates in a rectangular window with size $m \times n$, centered at a point (x, y) . The arithmetic mean filtering (AMF) process is to calculate the average value of the degraded image pixel $g(x, y)$ in the area defined by S_{xy} . The value of the restored image pixel at any point (x, y) is simply the arithmetic mean calculated using the pixels in the region defined by S . This will be applied as in the equation below:

$$\hat{f}(x, y) = \frac{1}{m \times n} \sum_{(s,l) \in S_{xy}} g(s, l) \quad (3.1)$$

The normalization factor $m \times n$ preserves the range of values of the original image. A convolution mask in which all coefficients have a value of $\frac{1}{m \times n}$ can perform this process. As the mean filter simply smoothest local variations in a degraded image, the degradation caused by blur and/or noise is reduced.

3.A.2 Geometric mean filter

Another type of the mean filtering is the geometric mean filter (GMF). GMF is also an average filtering but here the algorithm is performed as shown below:

$$\hat{f}(x, y) = \left[\prod_{(s,l) \in S_{xy}} g(s, l) \right]^{\frac{1}{mn}} \quad (3.2)$$

Each pixel will be restored by this method will take a value given by the product of the pixels in the sub-image window raised to the power $\frac{1}{m \times n}$. The geometric mean filter obtains smoothing equivalent to the arithmetic mean filter, but resultant images tend to lose some details during the process.

3.A.3 Harmonic mean filter

The third type to of mean filtering that we will study is the harmonic mean filtering (HMF). The harmonic mean method will replace the value for every single pixel by the harmonic mean

pixel values of the surrounding region. The harmonic mean values are obtained by the expression:

$$\hat{f}(x, y) = \frac{mn}{\sum_{(s,l) \in S_{xy}} \frac{1}{g(s,l)}} \quad (3.3)$$

The harmonic mean filter operates in a good manner for salt noise reduction; on the other hand, it fails with the pepper noise. It performs well also with other types of noise such as Gaussian noise.

3.A.4 Contraharmonic mean filter

The last type of mean filters, which we will study here, is the contraharmonic mean filtering (CHMF). CHMF is a non-linear filter, which restores the image based on average filtering. The CHMF procedure produces a restored image based on the equation:

$$\hat{f}(x, y) = \frac{\sum_{(s,l) \in S_{xy}} g(s,l)^{Q+1}}{\sum_{(s,l) \in S_{xy}} g(s,l)^Q} \quad (3.4)$$

where Q is representing the order of the filter.

CHMF is capable of eliminating or practically reducing the impact of salt and pepper noise. When Q has positive values, CHMF will eliminate the pepper noise. On the other hand, the filter will omit the salt noise in the case when Q has negative values. The filter is not capable of removing both the salt and pepper noise at the same time. From (3.4) we can notice the filter will behave as an arithmetic mean filter when $Q=0$, whereas when $Q=-1$ it will behave as a harmonic mean filter.

